

NASA-CR-191304

NASA-CR-191,304

RESEARCH REPORT No. OU-AME-91-2

COMPUTATIONAL ANALYSIS of HYPERSONIC
FLOWS PAST ELLIPTIC-CONE WAVERIDERS

Bok-Hyun Yoon
and
Maurice L. Rasmussen

am
he

NASA-CR-191304
19930005578



SCREEN IMAGE USER=*EBB SESSION=TA0BL14 3/ 2/93-11:19:33-AM

DISPLAY 93N14767/2

93N14767*# ISSUE 4 PAGE 781 CATEGORY 2

RPT#: NASA-CR-191304 NAS 1.26:191304 OU-AME-91-2 CNT#: NAG1-886

91/01/00 306 PAGES UNCLASSIFIED DOCUMENT

UTTL: Computational analysis of hypersonic flows past elliptic-cone waveriders

AUTH: A/YOON, BOK-HYUN; B/RASMUSSEN, MAURICE L.

CORP: Oklahoma Univ., Norman. CSS: (School of Aerospace and Mechanical Engineering.)

SAP: Avail: CASI HC A14/MF A03

CIO: UNITED STATES

MAJS: /*AERODYNAMIC CONFIGURATIONS/*BOW WAVES/*HYPERSONIC FLOW/*INVISCID FLOW/*
LEADING EDGES/*SHAPES/*SHOCK WAVES/*WAVERIDERS

MINS: / ALGORITHMS/ ANGLE OF ATTACK/ FLOW DISTRIBUTION/ HYPERSONIC FLIGHT/
HYPERSONIC VEHICLES/ MACH NUMBER

ABA: Author

ABS: A comprehensive study for the inviscid numerical calculation of the hypersonic flow past a class of elliptic-cone derived waveriders is presented. The theoretical background associated with hypersonic small-disturbance theory (HSDT) is reviewed. Several approximation formulas for the waverider compression surface are established. A CFD algorithm is used to calculate flow fields for the on-design case and a variety of off-design cases. The results are compared with HSDT, experiment, and other available CFD results. For the waverider shape used

ENTER:

MORE

SCREEN IMAGE USER=*EBB

SESSION=TAOBL14

3/ 2/93-11:20:17-AM

DISPLAY 93N14767/2

in previous investigations, the bow shock for the on-design condition stands off from the leading-edge tip of the waverider. It was found that this occurs because the tip was too thick according to the approximating shape formula that was used to describe the compression surface. When this was corrected, the bow shock became closer to attached as it should be. At Mach numbers greater than the design condition, a lambda-shock configuration develops near the tip of the compression surface. At negative angles of attack, other complicated shock patterns occur near the leading-edge tip. These heretofore unknown flow patterns show the power and utility of CFD for investigating novel hypersonic configurations such as waveriders.

ENTER:

UNIVERSITY of OKLAHOMA
SCHOOL of AEROSPACE and MECHANICAL ENGINEERING
RESEARCH REPORT No. OU-AME-91-2

COMPUTATIONAL ANALYSIS of HYPERSONIC
FLOWS PAST ELLIPTIC-CONE WAVERIDERS

by

Bok-Hyun Yoon
and
Maurice L. Rasmussen

(NASA-CR-191304) COMPUTATIONAL
ANALYSIS OF HYPERSONIC FLOWS PAST
ELLIPTIC-CONE WAVERIDERS (Oklahoma
Univ.) 306 p

N93-14767

Unclass

G3/02 0132234

January 1991

LIBRARY COPY

MAR 07 1991

LANGLEY RESEARCH CENTER
LIBRARY NASA
HAMPTON, VIRGINIA

ACKNOWLEDGMENTS

This work is a slightly modified version of the doctoral dissertation of Bok-Hyun Yoon. The authors especially acknowledge the discussions, advice, and contributions of Professors Ron Cox and George Emanuel. This work was supported by NASA Langley Grant No. NAG-1-886.

ABSTRACT

A comprehensive study for the inviscid numerical calculation of the hypersonic flow past a class of elliptic-cone derived waveriders is presented. The theoretical background associated with hypersonic small-disturbance theory (HSDT) is reviewed. Several approximation formulas for the waverider compression surface are established. A CFD algorithm due to Lawrence is used to calculate flow fields for the on-design case and a variety of off-design cases. The results are compared with HSDT, experiment, and other available CFD results. For the waverider shape used in previous investigations, the bow shock for the on-design condition stands off from the leading-edge tip of the waverider. It was found that this occurs because the tip was too thick according to the approximating shape formula that was used to describe the compression surface. When this was corrected, the bow shock became closer to attached as it should be. At Mach numbers greater than the design condition, a lambda-shock configuration develops near the tip of the compression surface. At negative angles of attack, other complicated shock patterns occur near the leading-edge tip. These heretofore unknown flow patterns show the power and utility of CFD for investigating novel hypersonic configurations such as waveriders.

TABLE OF CONTENTS

	Page
ACKNOWLEDGEMENTS.....	ii
ABSTRACT.....	iii
TABLE OF CONTENTS.....	iv
LIST OF FIGURES.....	v
NOMENCLATURE.....	vi
 Chapter	
I. INTRODUCTION.....	1
II. ELLIPTIC-CONE DERIVED WAVERIDER.....	6
III. GOVERNING EQUATIONS.....	14
IV. SOLUTION PROCEDURE.....	22
V. GEOMETRICAL CONSIDERATIONS.....	29
VI. CIRCULAR AND ELLIPTIC-CONE FLOW SOLUTIONS.....	39
VII. WAVERIDER FLOW SOLUTIONS.....	44
VIII. CONCLUDING REMARKS.....	72
REFERENCES.....	75
 Appendix	
A. APPROXIMATE ANALYTICAL SOLUTION.....	80
B. NUMERICAL ALGORITHM.....	89
C. GEOMETRY OF LEADING EDGE.....	102
FIGURES.....	104

LIST OF FIGURES

Figure	Page
1-1. Model of Aero-Space Plane	104
2-1. Spherical Polar Coordinates (r, θ, ϕ)	105
2-2. Construction of Elliptic-Cone Waverider	106
2-3. Waverider Configuration	107
2-4. Waverider Type- <i>A</i>	108
2-5. Waverider Type- <i>B</i>	109
3-1. Coordinate Systems	110
3-2. Initial Conditions for Velocity	111
3-3. Boundary Conditions	112
3-4. Reflection Condition	113
5-1. Elliptic Grid Generation	114
5-2. <i>O</i> -Type Grid	115
5-3. Magnified <i>O</i> -Type Grid	116
5-4. Fan-Type Grid	117
5-5. Magnified Fan-Type Grid	118
5-6. Adaptive Grid	119
5-7. Magnified Adaptive Grid	120

5-8. Finite-Volume Element	121
6-1. Solution to Elliptic-Cone Flow	122-130
6-1a. Grid for Elliptic-Cone Flow (for WR Type- <i>B</i>)	122
6-1b. Cross-Plane Velocity Distribution	123
6-1c. Azimuthal Velocity Component	124
6-1d. Wall Pressure Distribution	125
6-1e. Pressure near Lower Symmetry Plane	126
6-1f. Wall Pressure Comparison	127
6-1g. Comparison of Pressure near Lower Symmetry Plane	128
6-1h. Pressure Contours	129
6-1i. Mach Number Contours	130
6-2. Entropy Contours	131-132
6-2a. Entropy Contours ($\delta = 12^\circ$ Elliptic Cone)	131
6-2b. Entropy Contours ($\delta = 18.62^\circ$ Elliptic Cone)	132
6-3. Shock Comparisons	133-134
6-3a. Shock Comparison ($\delta = 12^\circ$ Elliptic Cone)	133
6-3b. Shock Comparison ($\delta = 18.62^\circ$ Elliptic Cone)	134
7-1. On-design Solutions (WR Type-A1O)	135-143
7-1a. Grid for Type-A1O Waverider	135
7-1b. Cross-Plane Velocity Distribution	136
7-1c. Magnified Cross-Plane Velocity near Tip	137
7-1d. Shock Location Comparison	138

7-1e. Azimuthal Velocity Component	139
7-1f. Wall Pressure Distribution	140
7-1g. Pressure near Lower Symmetry Plane	141
7-1h. Pressure Contours	142
7-1i. Mach Number Contours	143
7-2. On-design Solutions (WR Type- <i>A2F</i>)	144-151
7-2a. Grid for Type- <i>A2F</i> Waverider	144
7-2a'. Magnified Fan-grid for Tip Region	145
7-2b. Cross-Plane Velocity Distribution	146
7-2c. Magnified Cross-Plane Velocity near Tip	147
7-2d. Shock Location Comparison	148
7-2e. Azimuthal Velocity Component	149
7-2f. Wall Pressure Distribution	150
7-2g. Pressure near Lower Symmetry Plane	151
7-3. On-design Solutions (WR Type- <i>B1O</i>)	152-163
7-3a. Grid for Type- <i>B1O</i> Waverider	152
7-3b. Cross-Plane Velocity Distribution	153
7-3c. Magnified Cross-Plane Velocity near Tip	154
7-3d. Shock Location Comparison	155
7-3e. Azimuthal Velocity Component	156
7-3f. Wall Pressure Distribution	157
7-3g. Pressure near Lower Symmetry Plane	158

7-3h. Pressure Contours	159
7-3i. Mach Number Contours	160
7-3j. Wall Pressure Coefficients	161
7-3k. Mesh Size Effect (Shock)	162
7-3l. Mesh Size Effect (Leading Edge)	163
7-4. On-design Solutions (WR Type- <i>B2F</i>)	164-170
7-4a. Grid for Type- <i>B2F</i> Waverider	164
7-4b. Cross-Plane Velocity Distribution	165
7-4c. Magnified Cross-Plane Velocity near Tip	166
7-4d. Shock Location Comparison	167
7-4e. Azimuthal Velocity Component	168
7-4f. Wall Pressure Distribution	169
7-4g. Pressure near Lower Symmetry Plane	170
7-5. HSDT and Euler Solutions (WR Type- <i>A1O</i>)	171-176
7-5a. u : Radial Velocity Component	171
7-5b. v : Polar Velocity Component	172
7-5c. w : Azimuthal Velocity Component	173
7-5d. p : Pressure Distribution	174
7-5e. ρ : Density Distribution	175
7-5f. T : Temperature Distribution	176
7-6. HSDT and Euler Solutions (WR Type- <i>B1O</i>)	177-182
7-6a. u : Radial Velocity Component	177

7-6b. v : Polar Velocity Component	178
7-6c. w : Azimuthal Velocity Component	179
7-6d. p : Pressure Distribution	180
7-6e. ρ : Density Distribution	181
7-6f. T : Temperature Distribution	182
7-7. Off-Design Solution ($M_\infty = 3, \alpha = 0^\circ$)	183-188
7-7a. Cross-Plane Velocity Distribution	183
7-7b. Wall Pressure Distribution	184
7-7c. Pressure near Lower Symmetry Plane	185
7-7d. Azimuthal Velocity Component	186
7-7e. Pressure Contours	187
7-7f. Mach Number Contours	188
7-8. Off-Design Solution ($M_\infty = 4.5, \alpha = 0^\circ$)	189-193
7-8a. Cross-Plane Velocity Distribution	189
7-8b. Magnified Cross-Plane Velocity near Tip	190
7-8c. Wall Pressure Distribution	191
7-8d. Pressure near Lower Symmetry Plane	192
7-8e. Azimuthal Velocity Component	193
7-9. Off-Design Solution ($M_\infty = 5, \alpha = 0^\circ$)	194-201
7-9a. Cross-Plane Velocity Distribution	194
7-9b. Magnified Cross-Plane Velocity near Tip	195
7-9c. Total Pressure Contours	196

7-9d. Wall Pressure Distribution	197
7-9e. Pressure near Lower Symmetry Plane	198
7-9f. Azimuthal Velocity Component	199
7-9g. Pressure Contours	200
7-9h. Mach Number Contours	201
7-10. Off-Design Solution ($M_\infty = 10, \alpha = 0^\circ$)	202-207
7-10a. Cross-Plane Velocity Distribution	202
7-10b. Total Pressure Contours	203
7-10c. Schematic Diagram of Lambda Shock	204
7-10d. Wall Pressure Distribution	205
7-10e. Pressure near Lower Symmetry Plane	206
7-10f. Azimuthal Velocity Component	207
7-11. Pressure Comparisons at Off-Design Conditons ($M_\infty \neq 4, \alpha = 0^\circ$)	208-209
7-11a. Pressure near Lower Symmetry Plane	208
7-11b. Wall Pressure	209
7-12. Off-Design Solution ($M_\infty = 4, \alpha = +3^\circ$)	210-215
7-12a. Cross-Plane Velocity Distribution	210
7-12b. Magnified Cross-Plane Velocity near Tip	211
7-12c. Wall Pressure Distribution	212
7-12d. Pressure near Lower Symmetry Plane	213
7-12e. Pressure near Upper Symmetry Plane	214
7-12f. Azimuthal Velocity Componen	215

7-13. Off-Design Solution ($M_\infty = 4, \alpha = +10^\circ$)	216-221
7-13a. Cross-Plane Velocity Distribution	216
7-13b. Magnified Cross-Plane Velocity near Tip	217
7-13c. Wall Pressure Distribution	218
7-13d. Pressure near Lower Symmetry Plane	219
7-13e. Pressure near Upper Symmetry Plane	220
7-13f. Azimuthal Velocity Component	221
7-14. Off-Design Solution ($M_\infty = 4, \alpha = -2^\circ$)	222-227
7-14a. Cross-Plane Velocity Distribution	222
7-14b. Magnified Cross-Plane Velocity near Tip	223
7-14c. Wall Pressure Distribution	224
7-14d. Pressure near Lower Symmetry Plane	225
7-14e. Pressure near Upper Symmetry Plane	226
7-14f. Azimuthal Velocity Component	227
7-15. Off-Design Solution ($M_\infty = 4, \alpha = -4^\circ$)	228-233
7-15a. Cross-Plane Velocity Distribution	228
7-15b. Magnified Cross-Plane Velocity near Tip	229
7-15c. Wall Pressure Distribution	230
7-15d. Pressure near Lower Symmetry Plane	231
7-15e. Pressure near Upper Symmetry Plane	232
7-15f. Azimuthal Velocity Component	233
7-16. Off-Design Solution ($M_\infty = 4, \alpha = -8^\circ$)	234-240

7-16a. Cross-Plane Velocity Distribution	234
7-16b. Magnified Cross-Plane Velocity near Tip	235
7-16c. Total Pressure Contours	236
7-16d. Wall Pressure Distribution	237
7-16e. Pressure near Lower Symmetry Plane	238
7-16f. Pressure near Upper Symmetry Plan	239
7-16g. Azimuthal Velocity Component	240
7-17. Off-Design Solution ($M_\infty = 4, \alpha = -12^\circ$)	241-246
7-17a. Cross-Plane Velocity Distribution	241
7-17b. Magnified Cross-Plane Velocity near Tip	242
7-17c. Wall Pressure Distribution	243
7-17d. Pressure near Lower Symmetry Plane	244
7-17e. Pressure near Upper Symmetry Plane	245
7-17f. Azimuthal Velocity Component	246
7-18. Pressure Comparisons at Off-Design Conditons ($M_\infty = 4, \alpha \neq 0^\circ$)	247-248
7-18a. Pressure near Lower Symmetry Plane	247
7-18b. Wall Pressure	248
7-19. Off-Design Solution ($M_\infty = 5, \alpha = +4^\circ$)	249-254
7-19a. Cross-Plane Velocity Distribution	249
7-19b. Magnified Cross-Plane Velocity near Tip	250
7-19c. Wall Pressure Distribution	251
7-19d. Pressure near Lower Symmetry Plane	252

7-19e. Pressure near Upper Symmetry Plane	253
7-19f. Azimuthal Velocity Component	254
7-20. Off-Design Solution ($M_\infty = 5, \alpha = -4^\circ$)	255-260
7-20a. Cross-Plane Velocity Distribution	255
7-20b. Magnified Cross-Plane Velocity near Tip	256
7-20c. Wall Pressure Distribution	257
7-20d. Pressure near Lower Symmetry Plane	258
7-20e. Pressure near Upper Symmetry Plane	259
7-20f. Azimuthal Velocity Component	260
7-21. Off-Design Solution ($M_\infty = 3, \alpha = +4^\circ$)	261-266
7-21a. Cross-Plane Velocity Distribution	261
7-21b. Magnified Cross-Plane Velocity near Tip	262
7-21c. Wall Pressure Distribution	263
7-21d. Pressure near Lower Symmetry Plane	264
7-21e. Pressure near Upper Symmetry Plane	265
7-21f. Azimuthal Velocity Component	266
7-22. Off-Design Solution ($M_\infty = 3, \alpha = -4^\circ$)	267-272
7-22a. Cross-Plane Velocity Distribution	267
7-22b. Magnified Cross-Plane Velocity near Tip	268
7-22c. Wall Pressure Distribution	269
7-22d. Pressure near Lower Symmetry Plane	270
7-22e. Pressure near Upper Symmetry Plane	271

7-22f. Azimuthal Velocity Component	272
7-23. Pressure Comparisons at Off-Design Conditons ($M_\infty \neq 4, \alpha \neq 0^\circ$)	273-274
7-23a. Pressure near Lower Symmetry Plane	273
7-23b. Wall Pressure	274
7-24. Entropy Contours	275-276
7-24a. Entropy Contours for Waverider Type- <i>B1F</i>	275
7-24b. Entropy Contours for Waverider Type- <i>B1O</i>	276
7-25. Aerodynamic Quantities (WR Type- <i>B1O</i> : α, M_∞)	277-284
7-25a. Lift Coefficient vs. M_∞	277
7-25b. Drag Coefficient vs. M_∞	278
7-25c. Lift/Drag Ratio vs. M_∞	279
7-25d. Normal-force Coefficient vs. α	280
7-25e. Axial-force Coefficient vs. α	281
7-25f. Lift Coefficient vs. α	282
7-25g. Drag Coefficient vs. α	283
7-25h. Lift/Drag Ratio vs. α	284

NOMENCLATURE

English Symbols

a	Semimajor axis of outer ellipse
A	Axial force
A^*	Flux Jacobian matrix of \hat{E}^* , Eq.(B-12)
b	Semiminor axis of outer ellipse
B	Flux Jacobian matrix, Eq.(B-37,38)
c_v	Specific heat at constant volume
\tilde{C}	Flux Jacobian matrix, Eq.(B-32)
C_A	Axial-force coefficient
C_D	Drag coefficient
C_L	Lift coefficient
C_N	Normal-force coefficient
D	Drag
e	Internal energy per unit mass
e	Defined in Eq.(A-35)
E_t	Total energy
\vec{F}	Force vector

g_2	Shock eccentricity parameter for elliptic cone
h	Enthalpy
h_t	Total enthalpy
H_2	Defined in Eq.(A-23)
\tilde{H}	Defined in Eq.(B-3)
\hat{H}	General expression for either \hat{F} or \hat{G} flow
\hat{H}	General expression for cross flow difference
J	Jacobian
J	$a_0(\delta)^2/a_0(\beta)^2$
K_δ	Hypersonic similarity parameter($\equiv M_\infty\delta$)
K_β	$M_\infty\beta$
L	Lift
M_∞	Freestream Mach number
\hat{n}	Outward unit normal vector
N	Normal force
$O()$	Expression for denoting order
p	Pressure
\bar{p}	Pressure with dimension
P	Source term of Poisson's equation for η
\bar{P}	Rate of production of \bar{U}
P_2	Dimensionless pressure for elliptic cone
q_∞	Dynamic pressure

Q	Source term of Poisson's equation for ζ
\vec{r}	Position vector
R_2	Dimensionless density for elliptic cone
$\tilde{R}, \tilde{R}^{-1}$	Right and left eigen vector matrices
s	Entropy
\vec{s}	Displacement vector
S	Area
S_2	Dimensionless entropy for elliptic cone
S_b	Waverider base plane area
\vec{S}	Area vector
t	time
T	Temperature
\bar{T}	Temperature with dimension
\bar{U}	Conservative variable column matrix
U	See Eq.(A-23)
U_H^*	Homogeneous solution of U as a function of z
U_P^*	Particular solution of U as a function of z
z	θ_0/δ
a_1, a_2, a_3	Parameters specifying outer ellipse boundary
U, U^*, U^{**}	Defined in Eqs.(A-22)
ΔV	Cell volume
ΔV	Leading edge tip angle

\vec{V}_∞	Freestream velocity
a, b	Exponential of P and Q source terms of Poisson's equation
$\hat{e}_r, \hat{e}_\theta, \hat{e}_\phi$	Base vectors in r, θ , and ϕ -directions
$\hat{E}, \hat{F}, \hat{G}$	Flows in ξ, η , and ζ -directions
$\bar{E}, \bar{F}, \bar{G}$	Cartesian fluxes in the x, y , and z -directions
\hat{F}, \hat{G}	Cross flow expressions in η and ζ directions
$\hat{i}, \hat{j}, \hat{k}$	Cartesian base vectors
$l_\alpha, m_\alpha, n_\alpha$	x, y, z components of $\Delta \vec{S}_\alpha$
u, v, w	Cartesian velocity components
$\bar{u}, \bar{v}, \bar{w}$	Cartesian velocity components with dimensions
u_0, v_0, w_0	Velocity components for unperturbed basic cone in spherical coordinates
u_2, v_2, w_2	Perturbed velocity components of basic cone in spherical coordinates
$\hat{U}, \hat{V}, \hat{W}$	Contravariant velocity components
$p(\xi), q(\xi)$	Components of P and Q source terms of Poisson's equation
x, y, z	Cartesian coordinates
x', y', z'	Rotated Cartesian coordinates

Greek Symbols

α	Angle of attack
β	Shock angle
β	Compression parameter
β	Angle of yaw
γ	Ratio of specific heats

Γ_1, Γ_2	Inner and outer boundary of grid
δ	Half cone angle
δ	Differential operator
Δ	Forward differential operator
ϵ	Density ratio across shock
ϵ_2	Small perturbation parameter
η_0	Defined in Eq.(A-20)
ϕ	Accuracy parameter in Chakravarthy's scheme
ϕ	Azimuthal angle
ϕ_s	Waverider anhedral angle
θ	Conical angle
$\theta_c(\phi)$	Defined in Eq.(A-14)
$\theta_0(\phi)$	Stretched variable, Eq.(A-20)
$\theta_s(\phi)$	Defined in Eq.(A-15)
Θ_2	Defined in Eq.(A-29)
$\tilde{\Lambda}$	Eigenvalue matrix
ρ	Density
$\bar{\rho}$	Density with dimension
σ	Ratio of β to δ
∇	Gradient operator
ξ, η, ζ	Generalized curvilinear coordinates
r, θ, ϕ	Spherical coordinates

Subscripts

0	Unperturbed quantity
2	Perturbed quantity
c	Basic elliptic cone
i	Inviscid
j	Index number for ϕ
k	Index number for η
l	Index number for ζ
m	General expression for either k or l
max	Maximum value
r	Radial component of any variable
r	Reference
s	Shock
v	Viscous
w	Wall
α	Index number for six interfaces of hexahedron
κ	General expression for either η or ζ
θ	Polar component of any variable
ϕ	Azimuthal component of any variable
∞	Freestream condition

Superscripts

0	Values for previous marching step
-----	-----------------------------------

<i>I</i>	First order discretized form
<i>II</i>	Second order discretized form
<i>n</i>	Index number for ξ -coordinate

Chapter I

INTRODUCTION

The design of trans-atmospheric and aero-space vehicles has been of great interest in recent years. The National Aero-Space Plane (NASP) is an example of the current effort to develop technologies to design a vehicle that will fly into orbit while taking off and landing like a conventional airplane. A simple generic diagram of an aero-space plane configuration is shown in Fig.(1-1). The generic configuration is divided into three parts: a forebody, a scramjet propulsion unit, and an afterbody. All of these parts are to be blended together as a smooth, interacting entity. Besides these basic parts, of course, there may also be wings and tails taking part in the overall configuration.

One concept for the design of the forebody part of such a configuration is that of a waverider. A waverider shape offers a high lift and a small drag, and, in addition, provides favorable flow properties for the inlet of the scramjet propulsion unit. This investigation is directed towards a general study of the aerodynamics and flow fields associated with a special class of waverider configurations.

The concept of a waverider has been around for some time. A good history of the original concepts and a discussion of some possible aerodynamic applications can be found in Küchemann[1]. A waverider is constructed by identifying the stream surfaces of known supersonic flow fields as new solid surfaces that are connected in such a way as to form a new aerodynamic configuration. The flow field and aerodynamic properties of the waverider configuration are thus well known from the basic flows from which they were obtained. This basic flow and geometric configuration

are called the on-design conditions. When the waverider shape is held fixed, and either or both of the Mach number and orientation of the oncoming flow are varied, the varied conditions are said to be the off-design conditions. Whereas the underlying concept of waveriders is that the on-design conditions are easy to calculate, the off-design conditions are usually very difficult to calculate. The development of Computational Fluid Dynamics (CFD) possibly provides the only practical means for studying the off-design properties of waverider configurations.

The first CFD analyses of waverider flow fields were made by Jones et al.[2] and Jones[3,4]. These studies considered the elliptic-cone derived waveriders of Rasmussen[5] for which experimental results were available (Rasmussen et al.[6] and Jischke et al.[7]). The CFD calculations associated with Jones were simplified by using the full potential equations to describe the flow fields. Also, because the elliptic-cone waveriders are conical together with their inviscid flow fields even at off-design conditions, the similarity properties of conical flows could be fully utilized. In spite of the fact that the related elliptic-cone flow fields were slightly rotational, the irrotational potential-flow calculations provided fairly good agreement with experimental results and with the perturbation-analysis results upon which the elliptic-cone waveriders were based. This was probably due to the fact that the waveriders were actually not very slender, such that the viscous drag was small compared to the wave drag, and that the vorticity produced by small perturbations from axisymmetric flow was small.

The purpose of the present study is to deal with the flow fields and aerodynamics of the elliptic-cone derived waveriders by CFD methods utilizing the complete Euler equations. Both the fluid dynamics and aerodynamics of the waverider flow fields are of interest together with the numerics of the CFD solution method. It was also desired to obtain results for viscous effects and heat transfer by utilizing the Parabolized Navier-Stokes (PNS) equations. Whereas the inviscid flow-field studies

were successful, the studies involving the viscous effects did not lead to success. In addition to a broad description of the inviscid-flow results, some of the difficulties associated with the viscous-flow numerics will be addressed.

Just recently, after the completion of the present work, several other papers have appeared that deal with the calculation of waverider flow fields by CFD methods. Long[8] used the Euler equations to analyze an elliptic-cone waverider and a modified psuedo-waverider. Both configurations were fitted with afterbodies in their base regions. The only off-design results that were reported were for varied freestream Mach numbers. Jones and Dougherty[9] studied round-nosed, sharp-edged non-conical waveriders derived from axisymmetric conical flow fields. The Euler equations were used with emphasis on the grid generation to account properly for the flow near the sharp leading edges. Only on-design conditions were treated. Liao et al.[10] studied elliptic-cone derived waveriders by a CFD Navier-Stokes simulation. These calculations considered the design Mach number fixed ($M_\infty = 4$), but varied the angle of attack. Although local skin-friction coefficients were calculated, the overall lift and drag were not. Because the shock is spread out over several grid elements, it was noticed that there was some flow spillage around the sharp edges of the waverider where in principle the shock should be attached. This was also noticed by Jones and Dougherty, as well as within the present investigation. Whereas these recent investigations have some regions of commonality with the present investigation, the present study is concerned primarily with the broad, overall description of the flow past a class of elliptic-cone derived waveriders, both on-design and off-design. The results are related to the numerics of the CFD calculation scheme, and thus this is of interest also. The intent and the results of the present investigation are different and more comprehensive than the aforementioned papers.

The above three studies used existing codes based on unsteady 3-D equations with super computers like the Cray-2. On the other hand, in this study the steady-flow equations are utilized. Thus, the computational dimension can be reduced by one and the calculation can be made more effective and economical than the previous investigations.

Some of the difficulties involved in this problem lie in handling the singularity produced by the sharp leading edge. The elliptic-cone waverider has two very sharp leading edges, and a bow shock is attached at the edges at the on-design condition in the ideal inviscid case. This can cause difficulties in both grid generating and numerical integrating procedures. For example, a slightly deteriorated grid structure near the tip will result in the divergence of the numerical calculations. Therefore, for this type of problem, both procedures should be carried out with great care in order to get successful results.

Because of the particular boundary geometry and the importance of the flow near the body wall, the utilization of body-fitted coordinates is necessary. Among various methods for grid generation, an elliptic grid generator, which is a widely used scheme, is utilized, because it produces a very smooth grid. Although the overall geometry of the waverider looks simple, a lot of effort should be exerted to get a desirable grid structure especially near the tip. For that purpose Roberts' stretching[11], Sorenson's[12] method, and Anderson's adaptive grid method[13] are adopted.

Numerous numerical algorithms and methods can be considered for numerical integration and discretizing the Euler equations which are used in this study. In this investigation, Lawrence's STARS3D code based on his algorithm, which is a steady version of Roe's[14] approximate Riemann solver and is in the class of upwind schemes, is utilized to solve the hypersonic flows past elliptic-cone waveriders. The upwind schemes can be classified into two categories; Flux Vector Splitting

(FVS)[15] and Flux Difference Splitting (FDS). The FVS divides any flux into the positive and negative parts according to the sign of its relevant eigenvalues first and then discretizes them by using one-sided differences. The FDS determines a flux difference for two corresponding cell interfaces first and then discretizes the flux difference according to the relevant eigenvalues. Lawrence et al.[16] applied a Total Variation Diminishing (TVD) [17,18] schemes of Chakravarthy et al.[19,20] to the PNS equations to develop an algorithm which is in the category of the FDS. The TVD schemes have attracted much attention in the field of hypersonic flows, since they have some desirable properties associated with the handling of discontinuities like a shock in view of the stability and built-in dissipation. This algorithm uses the Finite Volume Method (FVM) to discretize the governing equations and an Alternating Directional Implicit method to integrate in space. The FVM, which is acquiring popularity recently over the conventional Finite Difference Method, is reported to have some advantages for the problems with irregular boundaries. In order to calculate inviscid flows, which were only possible for this problem with this code, the option for an inviscid flow was used.

Despite the difficulties due to the singularities involved in the elliptic-cone waverider flow, the complete compressible inviscid solutions are sought without modifying the sharp geometry. To confirm the validity of numerical results for the hypersonic flow past waveriders, analytic approximate solutions obtained by means of the Hypersonic Small Disturbance Theory (HSDT) are calculated and compared with computational values. The HSDT result, which is possible to get only at the on-design condition, is used for checking the trends of the CFD results but not necessarily for seeking complete agreement. The main goal of this investigation is the study of the flow behavior around waveriders at off-design conditions where analytical solutions do not currently exist.

Chapter II

ELLIPTIC-CONE DERIVED WAVERIDER

In this chapter we describe the development of an elliptic-cone waverider. Although such waveriders can be obtained from the basic supersonic flow past any elliptic cone, we shall be concerned with those cones having small eccentricities. In these cases, approximate results can be obtained by perturbation methods and hypersonic small-disturbance theory[5]. We shall outline the basic results here and leave the details for **Appendix A**.

2.1 Perturbation Expansions

We introduce spherical polar coordinates (r, θ, ϕ) as shown in Fig.(2-1). A flow or a body is said to be conical if it does not depend on the radial coordinate r . We assume that a basic axisymmetric conical flow has been established. The basic circular-cone semi-vertex angle is δ and the corresponding attached shock semi-vertex angle is β . The uniform freestream flow, denoted by the subscript ∞ , is in the z direction, which is the axis of symmetry of the basic circular cone. We assume (along with Rasmussen[5]) that the basic axisymmetric flow is perturbed by introducing an elliptic-cone perturbation in the cone body shape. The elliptic-cone body is thus described by

$$\theta_c(\phi) = \delta[1 - \epsilon_2 \cos 2\phi + O(\epsilon_2^2)], \quad (2-1)$$

where ϵ_2 is a small-perturbation parameter that is a measure of the eccentricity. The corresponding shock shape is assumed to be

$$\theta_s(\phi) = \delta[\sigma - \epsilon_2 g_2 \cos 2\phi + O(\epsilon_2^2)]. \quad (2-2)$$

Here $\sigma \equiv \beta/\delta$ is the ratio of the basic-shock angle to the basic-cone angle. The shock eccentricity factor g_2 is to be determined as part of the perturbation solution.

To account for a singular behavior in the solution near the surface of the perturbed cone, Rasmussen[21,22] introduced a new stretched variable θ_0 to replace the polar angle θ :

$$\frac{\theta_0 - \delta}{\beta - \delta} = \frac{\theta - \theta_c(\phi)}{\theta_s(\phi) - \theta_c(\phi)}. \quad (2-3)$$

Thus, for the new independent variable, $\theta_0 = \delta$ at the perturbed cone and $\theta_0 = \beta$ at the perturbed shock. The radial velocity $u(\theta, \phi)$, polar velocity $v(\theta, \phi)$, azimuthal velocity $w(\theta, \phi)$, pressure $p(\theta, \phi)$, density $\rho(\theta, \phi)$, and entropy $s(\theta, \phi)$ were then expanded in the series forms

$$u(\theta, \phi) = u_0(\theta_0) + \epsilon_2 u_2(\theta_0) \cos 2\phi + O(\epsilon_2^2), \quad (2-4a)$$

$$v(\theta, \phi) = v_0(\theta_0) + \epsilon_2 v_2(\theta_0) \cos 2\phi + O(\epsilon_2^2), \quad (2-4b)$$

$$w(\theta, \phi) = \epsilon_2 w_2(\theta_0) \sin 2\phi + O(\epsilon_2^2), \quad (2-4c)$$

$$p(\theta, \phi) = p_0(\theta_0) [1 + \epsilon_2 P_2(\theta_0) \cos 2\phi] + O(\epsilon_2^2), \quad (2-4d)$$

$$\rho(\theta, \phi) = \rho_0(\theta_0) [1 + \epsilon_2 R_2(\theta_0) \cos 2\phi] + O(\epsilon_2^2), \quad (2-4e)$$

$$s(\theta, \phi) = s_0 + c_v \epsilon_2 S_2(\theta_0) \cos 2\phi + O(\epsilon_2^2). \quad (2-4f)$$

Here the subscript 0 denotes the unperturbed basic-cone quantity, and the subscript 2 denotes the perturbation quantities. These expansions are a variation of the original expansions by Rasmussen and Lee[23]. An approximate solution for the above variables was obtained within the framework of hypersonic small-disturbance

theory. The results are valid for large freestream Mach numbers M_∞ and small cone angles δ such that the similarity parameter $K_\delta \equiv M_\infty \delta$ is held fixed at an arbitrary value. When $K_\delta \rightarrow 0$, the linear-theory limit is obtained, and when $K_\delta \rightarrow \infty$ the hypersonic limit is obtained.

2.2 Conical Stream Surfaces

A streamline is described by the vector equation

$$\vec{V} \times d\vec{s} = 0, \quad (2-5a)$$

where $d\vec{s}$ is a differential element of distance measured along the streamline. In spherical coordinates this becomes

$$\frac{dr}{u} = \frac{rd\theta}{v} = \frac{r \sin \theta d\phi}{w}. \quad (2-5b)$$

Consistent with the first-order perturbations and hypersonic small-disturbance theory[21,22], this reduces to

$$\frac{dr}{rV_\infty} = \frac{d\theta_0}{v_0(\theta_0)} = \frac{\theta_0 d\phi}{\epsilon_2 w_2(\theta_0) \sin 2\phi}. \quad (2-5c)$$

The second and third members of this equation describe the family of conical stream surfaces. The variables can be separated, and we have

$$\frac{\epsilon_2 w_2(\theta_0) d\theta_0}{\theta_0 v_0(\theta_0)} = \frac{d\phi}{\sin 2\phi}. \quad (2-6)$$

An accurate approximation for $v_0(\theta_0)$ is (see **Appendix A**):

$$v_0(\theta_0) = -V_\infty \theta_0 \left(1 - \frac{\delta^2}{\theta_0^2} \right). \quad (2-7)$$

If we denote by $\phi = \phi_s$ the azimuthal location where the conical stream surface intersects the shock $\theta_0 = \beta$, then Eq.(2-6) together with Eq.(2-7) can be integrated to give

$$-\epsilon_2 \int_\beta^{\theta_0} \frac{w_2(\theta_0)}{V_\infty} \frac{d\theta_0}{\theta_0^2 - \delta^2} = \int_{\phi_s}^\phi \frac{d\phi}{\sin 2\phi} = \frac{1}{2} \ln \left[\frac{\tan \phi}{\tan \phi_s} \right]. \quad (2-8)$$

This is done in two different ways. The first way captures the behavior in the vortical layer, that is, near $\theta_0 = \delta$. It yields a simple result and is the basis for the actual construction of the waveriders in Refs. [6, 7, 26]. The azimuthal velocity $w_2(\theta_0)$ is a complicated function (see **Appendix A**), and the integral on the left side of Eq.(2-8) must be evaluated numerically as it stands. It is thus useful to find an approximation for this integral. Since the integral is singular at $\theta_0 = \delta$, most of the value of the integral comes when θ_0 is near δ , that is, near the surface of the perturbed cone. Thus we can set $w_2(\theta_0) \cong w_2(\delta)$. This is a good approximation when $w_2(\theta_0)$ varies slowly across the shock layer; otherwise there may be some error in the shape near the leading edge. Correspondingly, in the integral we can set $\theta_0^2 - \delta^2 = (\theta_0 + \delta)(\theta_0 - \delta) \cong 2\delta(\theta_0 - \delta)$. When this is done the integral can be approximated simply, and we obtain

$$\left(\frac{-\epsilon_2 w_2(\delta)}{\delta V_\infty} \right) \ln \left[\frac{\theta_0 - \delta}{\beta - \delta} \right] = \left[\frac{\tan \phi}{\tan \phi_s} \right]. \quad (2-9)$$

Let us define a new small parameter e by

$$e \equiv -\frac{\epsilon_2 w_2(\delta)}{\delta V_\infty}. \quad (2-10)$$

This parameter is positive since w_2 is negative when ϵ_2 is positive, and vice versa. Equation (2-9) can now be solved for $\theta_0(\phi)$ and written in the form

$$\frac{\theta_0(\phi)}{\delta} = 1 + (\sigma - 1) \left[\frac{\tan \phi}{\tan \phi_s} \right]^{1/e}. \quad (2-11)$$

In terms of the physical variable $\theta(\phi)$, obtained from Eq.(2-3), this can be rewritten as

$$\frac{\theta(\phi)}{\delta} = \frac{\theta_c(\phi)}{\delta} + \left[\frac{\theta_s(\phi)}{\delta} - \frac{\theta_c(\phi)}{\delta} \right] \left[\frac{\tan \phi}{\tan \phi_s} \right]^{1/e}. \quad (2-12)$$

Equation (2-12) describes the conical stream surfaces generated by hypersonic flows past elliptic cones. It is valid for small eccentricities, that is, for small ϵ_2 . Since all

of the streamlines that comprise a conical stream surfaces pass through a common ray along the conical shock, they all have the same entropy. Thus, a conical stream surface is also a constant-entropy surface.

It was first established by Ferri[24] that the surface of a conical solid body in a supersonic conical flow must be a constant-entropy surface. In general, except for axisymmetric shocks, the entropy must vary azimuthally immediately downstream of a conical shock. Thus, whereas Eqs.(2-4) may hold in the vicinity of the shock, they cannot hold in general near the surface of a conical body. Equations (2-4) are thus said to be the outer expansions, and another set of perturbation expansions must hold near the surface of the body. They are called the inner expansions, and they describe what is said to be the vortical layer. The vortical layer has been studied by means of matched asymptotic expansions [21,22,25]. It is found that the outer expansion for the pressure in Eq.(2-4d) is uniformly valid across the vortical layer to all orders, and the first-order azimuthal velocity in Eq.(2-4c) is uniformly valid to the lowest order. As might be expected, therefore, the approximation in Eq.(2-12) for a constant-entropy surface is also found to be uniformly valid across the whole shock layer.

Although Eq.(2-12) is a uniformly-valid approximation for a conical stream surface across the shock layer, it is a composite solution, and thus it is not unique. There are other approximate formulas that are correct to the same order of accuracy in ϵ_2 . Another possible approximation is

$$\left(\frac{\theta(\phi)}{\delta}\right)^2 = \left(\frac{\theta_c(\phi)}{\delta}\right)^2 + \left[\left(\frac{\theta_s(\phi)}{\delta}\right)^2 - \left(\frac{\theta_c(\phi)}{\delta}\right)^2 \right] \left[\frac{\tan \phi}{\tan \phi_s} \right]^{1/\epsilon}. \quad (2-13)$$

This gives approximately the same result as Eq.(2-12) since $(\theta + \theta_c)$ and $(\theta_s + \theta_c)$ are nearly the same for slender cones in hypersonic flow. Equation (2-12) was used in Refs.[6,7] and Eq.(2-13) was used in Ref.[26]. A better representation for a conical

stream surface can be obtained by approximating the combination $w_2(\theta_0)/(\theta_0 + \delta)$ by a linear variation with θ_0 from the body to the shock. Thus we would have

$$\frac{w_2(\theta_0)}{V_\infty(\theta_0 + \delta)} \simeq \frac{w_2(\delta)}{2V_\infty\delta} + \left[\frac{w_2(\beta)}{V_\infty(\beta + \delta)} - \frac{w_2(\delta)}{2V_\infty\delta} \right] \left(\frac{\theta_0 - \delta}{\beta - \delta} \right). \quad (2-14)$$

If we substitute this approximation into Eq.(2-8), then upon integration we obtain

$$\left(\frac{\theta_0 - \delta}{\beta - \delta} \right) \exp \left[\left\{ \frac{2w_2(\beta)}{(\sigma + 1)w_2(\delta)} - 1 \right\} \left(\frac{\theta_0 - \beta}{\beta - \delta} \right) \right] = \left[\frac{\tan \phi}{\tan \phi_s} \right]^{1/e}. \quad (2-15)$$

If the exponential term in this expression were ignored, then this result would be the same as Eqs.(2-9) or (2-11). Equation (2-15) is more accurate near the shock.

2.3 Construction of an Elliptic-Cone Derived Waverider

A conical constant-entropy stream surface, such as given by Eqs.(2-12), (2-13) or (2-15), is used as a lower compression surface in a new waverider configuration. The complementary upper freestream surfaces are taken to be a pair of triangular plane surfaces that pass through the axis of symmetry (z -axis) of the basic cone and intersect the elliptic-cone shock at the angle $\phi = \pm\phi_s$. A cross-section plane, perpendicular to the axis of symmetry, is shown in Fig.(2-2). The angle ϕ_s where the upper freestream planes intersect the lower conical stream surface is said to be the anhedral angle. A perspective lower rear view of an elliptic-cone waverider is shown in Fig.(2-3).

For the on-design condition, the flow is aligned with the upper freestream surfaces, and the shock is attached to the sharp leading-edge tip at $\phi = \phi_s$. This orientation is said to be at zero angle of attack $\alpha = 0$. After the body shape is fixed based on the on-design conditions, the off-design conditions can occur by changing the freestream Mach number and/or by changing the orientation of the waverider ($\alpha \neq 0$). We shall not consider non-zero yawing (or sideslip) angle. Thus the flows considered will be right/left symmetric with respect to the vertical plane of

symmetry of the waverider. For Mach numbers less than the design Mach number, the bow shock will detach from the sharp leading edge of the waverider.

2.4 Specific Waverider Shapes

Two basic elliptic-cone waveriders are considered, denoted by A and B . For both cases, the on-design Mach number is $M_\infty = 4$ and the eccentricity is $\epsilon_2 = 0.1$. The pertinent functions of $K_\delta \equiv M_\infty \delta$ are determined from the formulas given in Appendix A.

Table (2-1)

Parameters	Waverider A	Waverider B
δ	12°	18.62°
ϕ_s	60°	70°
K_δ	0.838	1.30
σ	1.62	1.34
g_2	0.382	0.597
$1/e$	6.132	7.611

The parameters for Waverider B correspond to the shape tested in Refs.[6,7]. Waverider A corresponds to the shape tested in Ref.[26], except that the eccentricity was $\epsilon_2 = 0.05$ in Ref.[26], which led to a corresponding value of $1/e = 12.264$. This large value of $1/e$ produces a very sharp leading edge on the waverider, and the initial efforts at calculating the flow led to numerical instabilities which were subsequently overcome. Consequently, the larger value of ϵ_2 was selected for the present study.

For each of the foregoing sets of parameters for models A and B , the compression surfaces were calculated according to Eqs.(2-12) and (2-15). The models with compression surfaces calculated according to Eq.(2-12) are denoted by $A1$ and $B1$, whereas the models with compression surfaces denoted by Eq.(2-15) are denoted by $A2$ and $B2$. The two compression surfaces for models $A1$ and $A2$ are shown in Fig.(2-4). The two compression curves are considerably different in the concave region where the winglet blends into the body and outward towards the leading-edge tip. Figure (2-5) shows a comparison of the compression surfaces $B1$ and $B2$.

An analysis for the leading-edge tip angles is given in **Appendix C**. The waverider types *A2* and *B2* have considerably thinner leading-edge tips. The two types of representations will be used to test the influence of variations in the waverider shape on the flow-field properties.

Chapter III

GOVERNING EQUATIONS

Three coordinate systems (Cartesian, Spherical, and Generalized coordinates) involved in the ensuing numerical investigation are shown in Fig.(3-1). The new Cartesian coordinates are labeled differently from those defined in Chapter II. The streamwise direction is x unlike z in the previous definition. For the numerical calculation we will use this new coordinate system throughout as well as the generalized coordinate system. The rotated coordinates (x', y', z') are for aerodynamic force calculations which will be considered in Chapter IV. The waveriders studied here have conical geometry and thus to describe them spherical coordinates are also utilized.

The Euler equations in Cartesian coordinates are introduced first in a strong conservation-law form. Although governing equations in this coordinate system are not utilized directly for numerical integration, their components are involved in the computational process. For example, the initial conditions are imposed by means of Cartesian velocity components. Then the unsteady Euler equations are transformed in generalized curvilinear coordinates. This would be necessary for high-speed flow problems with a complicated boundary geometry. If the governing equations are expressed in a body-fitted coordinate system, then the imposition of boundary conditions becomes relatively easy, but the equations themselves have more complicated forms. In this investigation the steady Euler equations in the body-fitted coordinates are numerically integrated by means of a space marching

shceme. For a steady problem this would be more economical and desirable with respect to the CPU time than using the unsteady equations.

Finally, in the last two sections initial and boundary conditions for the waverider problem will be presented. Despite the unusual shape of the waverider it is easy to implemet those conditions. A computer code written based on a body-fitted coordinate system can be used for a large class of similar body shapes. That is, we can solve for elliptic-cone and waverider flows with the same code written for a circular cone based on the body-fitted coordinates. In other words, the imposition of the initial and boundary conditions for the flows of a circular cone, an elliptic cone, and a waverider, is the same inspite of the geometrical difference among them. Considering both of the body-fitted and Cartesian coordinates are body-fixed coordinates, we can distinguish the waverider flow problem from the other flow problem of such as a circular or elliptic cone by the generated grid, but not by the initial or boundary conditions.

3.1 Governing Equations in Cartesian Coordinates

The unsteady Euler equations without source terms (such as a body force) can be written in a strong conservation-law form in a Cartesian coordinate system $(x_i : x, y, z)$ as

$$\frac{\partial \bar{U}}{\partial t} + \sum_{i=1}^3 \frac{\partial \bar{E}^i}{\partial x_i} = 0, \quad (\bar{E}^i : \bar{E}, \bar{F}, \bar{G}), \quad (3-1)$$

where

$$\bar{U} = \{\rho, \rho u, \rho v, \rho w, E_t\}^T, \\ \bar{E}^i = \begin{Bmatrix} \rho u_i \\ \rho u_i u + \delta_{i1} p \\ \rho u_i v + \delta_{i2} p \\ \rho u_i w + \delta_{i3} p \\ (E_t + p) u_i \end{Bmatrix},$$

$$E_t = \rho \left[e + \frac{1}{2}(u^2 + v^2 + w^2) \right],$$

where u_i are Cartesian velocity components (u, v, w), e is internal energy per unit mass, and δ_{ij} denotes the Kronecker delta function. The ideal gas model is used here for simplicity:

$$p = (\gamma - 1)\rho e = \frac{1}{\gamma M_\infty^2} \rho T. \quad (3-2)$$

All the above equations are nondimensionalized by taking the freestream values as reference parameters. The nondimensional variables are,

$$\begin{aligned} \rho &= \frac{\bar{\rho}}{\bar{\rho}_\infty}, \quad u = \frac{\bar{u}}{\bar{V}_\infty}, \quad v = \frac{\bar{v}}{\bar{V}_\infty}, \quad w = \frac{\bar{w}}{\bar{V}_\infty}, \\ p &= \frac{\bar{p}}{\bar{\rho}_\infty \bar{V}_\infty^2}, \quad e = \frac{\bar{e}}{\bar{V}_\infty^2}, \quad T = \frac{\bar{T}}{\bar{T}_\infty}, \end{aligned} \quad (3-3)$$

where the bar denotes a dimensional quantity.

3.2 Governing Equations in Generalized Curvilinear Coordinates

The Euler equations in a generalized curvilinear coordinate system can be obtained through the following transformation;

$$\xi^i = \xi^i(x, y, z), \quad (\xi^i : \xi, \eta, \zeta), \quad i = 1, 2, 3, \quad (3-4)$$

where $\xi(= \xi^1)$ is taken as the radial direction. The $\eta(= \xi^2)$ is in the crosswise direction and $\zeta(= \xi^3)$ is in the normal direction to the waverider body wall. These coordinates will be generated numerically. The η and ζ coordinates are orthogonal at the body boundary but not near the leading edges and for the rest of the flow field. Especially in case that the ξ and η coordinates are taken to be fixed at the body wall, the generalized coordinates are said to be body-fitted coordinates. If we utilize the chain rule, the governing equations in a new coordinate system can be expressed in the strong conservation-law form again[11]:

$$\frac{\partial \hat{U}}{\partial t} + \sum_{i=1}^3 \frac{\partial \hat{E}^i}{\partial \xi^i} = 0, \quad (\hat{E}^i : \hat{E}, \hat{F}, \hat{G}), \quad (3-5)$$

where

$$\hat{U} = \frac{\bar{U}}{J}, \quad (3-6)$$

$$\begin{Bmatrix} \hat{E} \\ \hat{F} \\ \hat{G} \end{Bmatrix} = \frac{1}{J}[A] \begin{Bmatrix} \bar{E} \\ \bar{F} \\ \bar{G} \end{Bmatrix}, \quad (3-7)$$

where $[A]$ is defined by

$$[A] \equiv \begin{bmatrix} \xi_x & \xi_y & \xi_z \\ \eta_x & \eta_y & \eta_z \\ \zeta_x & \zeta_y & \zeta_z \end{bmatrix}$$

and the Jacobian J is defined by the determinant of $[A]$ as

$$J \equiv |A| \equiv \frac{\partial(\xi, \eta, \zeta)}{\partial(x, y, z)}. \quad (3-8)$$

If we examine Eq.(3-7), then we can see that all the information for the fluxes of Cartesian coordinates and the flows of generalized coordinates are exchanged by means of the metrics and the Jacobian. It is to be noted here that the metrics appear in a special form such that they are divided by the Jacobian. The metrics in this form, as well as the Jacobian, have geometrical meanings. The Jacobian is equal to the inverse of the cell volume and the metrics combined with the Jacobian are area element vectors, as will be explained later. Thus, once an appropriate grid is generated, both the metrics and the Jacobian can be determined from the geometric consideration of the grid. Therefore, the explicit form of the transformation function is not necessary. Even for a special case where we can identify a transformation function, it is not necessarily desirable to use the metrics and the Jacobian calculated by this function in a numerical analysis.

3.3 Steady Hyperbolic Equations

In this study we use the steady Euler equations which are obtained from Eq.(3-5). They are written as

$$\frac{\partial \hat{E}}{\partial \xi} + \frac{\partial \hat{F}}{\partial \eta} + \frac{\partial \hat{G}}{\partial \zeta} = 0. \quad (3-9)$$

To numerically integrate the governing equations in space they are to be of a hyperbolic type. The steady Euler equations become hyperbolic in the ξ direction, if we impose a restriction such that the eigenvalues of the pertinent flux Jacobian matrices $(\partial \hat{F}/\partial \hat{E}, \partial \hat{G}/\partial \hat{E})$ should be real[47]. The restriction requires supersonic inviscid flow in the streamwise direction everywhere. Fortunately, the waverider problem investigated here has such a characteristic except for the case with a very high angle of attack and thus we can use the steady equations with space marching technique. The ξ coordinate in the steady equations plays the role of the time variable in the unsteady equations.

3.4 Initial Conditions

To start the numerical integration of the Euler equations by space marching, the initial flow values at a starting point of ξ must be specified. Since the waverider has sharp leading edges and there is no inviscid subsonic region expected for a mild angle of attack, the supersonic freestream values can be used as initial conditions (ICs). Even though the final form of the equations is expressed in the body-fitted coordinates to fit the unusual geometry of the waverider, the imposition of ICs for the velocity can be achieved easily by the utilization of the Cartesian velocity components. The initial velocity components are:

$$\begin{aligned} u_{k,l}^1 &= V_\infty \cos \alpha \cos \beta, \\ v_{k,l}^1 &= V_\infty \sin \alpha, \\ w_{k,l}^1 &= V_\infty \cos \alpha \sin \beta. \end{aligned} \quad (3-10a, b, c)$$

The effects of the angles of attack α and yaw β are implemented in this procedure by the above relation as shown in Fig.(3-2). For a special case without angles of attack and yaw where the freestream flow is in the x direction, the only nonvanishing velocity component is $u_{k,l}^1 = V_\infty$. Thus keeping and using the Cartesian velocity components in generalized curvilinear coordinates makes it easy to impose starting values, even for the particular shape of the waverider geometry. For the other flow variables such as pressure, density, and temperature, freestream values are used. The initial converged solution is sought at the position $x = 0.05$ where the step-back procedure is taken until we meet any given criterion. Since we deal with the inviscid problem only and thus the flow is conical, we don't need to integrate further downstream by space marching.

3.5 Boundary Conditions

The boundary conditions (BCs) without yaw ($\beta = 0$) are composed of three parts as shown in Fig.(3-3); the far-field away from the bow shock, the upper and lower parts of the symmetry plane, and the body wall. For the case with angle of yaw, the symmetry condition cannot be used and thus the whole flow region must be included in the calculation instead of the half domain.

Far-Field

In a supersonic flow the flow downstream of a shock does not influence the upstream flow. Thus we can use the freestream values for the region which is far away from an expected bow shock located around the lower portion of a waverider. The outer boundary values (denoted by $l = l_{max}$) are set equal to those of the freestream as

$$\bar{U}_{l_{max}} = \bar{U}_{freestream}. \quad (3-11)$$

When the angle of attack is such that an expansion wave exists above the waverider, the far-field conditions must be imposed outside the Mach cone emanating from the apex of the waverider.

Symmetry Planes

The waverider configuration studied in this work is symmetric about the plane $z = 0$ and the flow around it will be also symmetric as long as its symmetry plane is aligned with the freestream flow direction ($\beta = 0$). To impose this condition two additional neighboring grid points are necessary across both the upper and lower symmetry planes, since the numerical algorithm used is the second order in the crosswise directions. Let

$$X = \begin{bmatrix} 1 & 0 & 0 & 0 & 0 \\ 0 & 1 & 0 & 0 & 0 \\ 0 & 0 & 1 & 0 & 0 \\ 0 & 0 & 0 & -1 & 0 \\ 0 & 0 & 0 & 0 & 1 \end{bmatrix}, \quad (3-12)$$

then

$$\begin{aligned} \bar{U}_{k=1} &= X\bar{U}_{k=4}, & \bar{U}_{k=k_{max}+2} &= X\bar{U}_{k=k_{max}-1}, \\ \bar{U}_{k=2} &= X\bar{U}_{k=3}, & \bar{U}_{k=k_{max}+1} &= X\bar{U}_{k=k_{max}}. \end{aligned} \quad (3-13)$$

Here the -1 in X plays the role of changing the sign of w across the symmetry line. The above relations show simply the reflection condition which is shown in Fig.(3-4).

Wall

Since the finite-volume method is used, the wall surface is composed of cell interfaces obtained by the primary grids. Thus, fluxes at the wall instead of flow variables should be specified. For inviscid flow the contravariant velocity \hat{W} in the ζ -direction is zero. That is,

$$\vec{V} \cdot \hat{n} = 0, \Rightarrow \hat{W} \equiv \frac{\zeta_x}{J}u + \frac{\zeta_y}{J}v + \frac{\zeta_z}{J}w = 0, \quad (3-14)$$

where

$$\hat{n} = \frac{\nabla\zeta}{|\nabla\zeta|}. \quad (3-15)$$

As a consequence, all the inviscid normal fluxes to the wall vanish except for the pressure term.

Chapter IV

PROBLEM SOLVING PROCEDURE

The first part of this chapter describes the problem concerning waveriders, and the solving procedure is presented. Then the characteristics and difficulties involved in the problem are set forth. Finally a simplified relation for aerodynamic forces is presented.

4.1 Problem Description

A waverider, a lifting body with high lift-drag ratio, is chosen as the forebody of a generic aero-space plane, as mentioned earlier. This study is to numerically solve the compressible flows past waveriders at supersonic speeds at both on- and off-design conditions. Because for supersonic flows the downstream flow does not affect the upstream flow, unlike subsonic flows, a waverider forebody can be studied independently of any downstream or afterbody configuration.

Jones[2,3] solved numerically supersonic flows past waveriders by means of the full potential method[27] and obtained quite successful results. They are not strictly valid when the vorticity is sufficiently large, which occurs for a fixed finite eccentricity ϵ_2 when K_δ becomes sufficiently large. In this investigation the complete Euler equations in a steady form are utilized. Since there are no restrictions on rotationality, unlike the potential method, we can calculate for arbitrary hypersonic flow regimes.

Composition of Program Packages

The whole computer code is composed of three packages of program files. They are:

- (1) AGRID : generating grid
- (2) STARS3D : solving for flows
- (3) CPLOT : plotting various graphs and obtaining approximate solutions for waveriders

AGRID is the code that produces body-fitted coordinates. This can generate algebraic, hyperbolic, and elliptic grids. The details about elliptic grid generation are presented in **Chapter V**. The STARS3D code developed by Lawrence[28] at NASA, whose algorithm is described in **Appendix B**, is used to solve hypersonic flows past circular cones, elliptic cones, or waveriders with various conditions. This code was about 7,700 lines long, but it was reduced to 5,000 lines through modification for grids and COMMON block structure and removing some unnecessary subroutines. The CPU time was about 2.25 hours on the IBM 3081 for an 83x41 mesh. The CPLOT code is used for plotting the various variables obtained by running STARS3D through either a SURFACEII or a FORTRAN basic graphic routine. This also calculates approximate solutions by means of the HSDT. In addition PLOT3D developed by NASA is utilized for entropy contours and other plots.

4.2 Problem Characteristics

The numerical calculation of flows past waveriders involves difficulties that fall into at least three categories which are somewhat interrelated. The first category is associated with the singular nature of the waverider shape at the sharp leading edge. The second category is associated with the large gradients in the flow arising from the bow shock wave, the large gradients near the sharp leading edge especially

when the freestream Mach number is slightly less than the design Mach number, and possibly large gradients arising from vortical layers. The third category is the numerical algorithm itself, including the implementation of the wall boundary condition.

The upper surface of the elliptic-cone derived waverider is a flat delta-shaped surface that intersects the lower curved compression surface along a straight line that forms the sharp leading edge of the waverider. The singular behavior of this leading edge presents difficulties in constructing a desired smoothly-varying grid structure near the leading edge. Several grid-construction schemes will be studied: an *O*-type grid, a fan-type grid, and an adaptive grid. If the grid is too skewed or if the grid cell volumes change size too rapidly, the numerical integration process will diverge. An adaptive grid could be considered to be used for the computation. This, however, would yield a grid skewness both for the sharp leading edge region and for the bow shock region. As a test case, an adaptive grid was used with the hopes for an improved shock structure, but it did not lead to a successful converged solution.

For the on-design condition, a conical bow shock is attached at the leading edge. The upper surface of the waverider is a freestream surface, and the lower surface is a high-pressure, high-density compression surface. As is the usual case for hypersonic flows, there is a large change in flow properties across the bow shock. For the waverider problem, however, there is an additional problem. This manifests itself dramatically when the freestream Mach number decreases slightly from the design Mach number. In this case the bow shock detaches from the leading edge, and a large gradient in the flow is established around the sharp leading edge of the waverider. The same sort of behavior would occur if the location of the leading edge were perturbed, either by design or by a slight error in the representation of the waverider surface. Since the numerical shock structure itself is spread over a

few grid elements, the representation of the flow near the sharp leading edge is very sensitive to small changes or errors.

Since the asymmetric inviscid flow to be calculated is conical, a vortical layer exists that is pronounced near the symmetry plane of the compression surface. In principle, the compression surface of the waverider for the on-design flow is a constant-entropy surface since it is formed from a conical stream surface from a basic flow past an elliptic cone. There will thus be large gradients in the entropy, density, and temperature near the symmetry plane on the compression surface. There will also be corresponding large gradients in the entropy around the sharp leading edge.

In this study we do not deal with viscous flows. If viscous flows were to be considered, however, the vortical-layer effects would be mitigated. In their place, nevertheless, large gradients due to viscous boundary layers would occur. These would produce further interactions of large gradients at the leading edge.

The third category involves the numerical algorithm together with the way of the boundary condition imposition based on the finite-volume method. There is always some error involved in the numerical computation scheme. The boundary condition for the waverider surface pressure is imposed by means of the pressure at a half grid element away from the waverider wall. At the sharp leading edge, this is a potential source of difficulty. Except for the grid generation, the numerical algorithm used by the Lawrence code in this investigation is unmodified. For inviscid flows, pressure blips near the wall are detected even for the case of axisymmetric flow past a circular cone. For the related PNS viscous flows, wall pressure oscillations in the stream direction have been noted[28]. It is possible that a more accurate means of imposing the boundary conditions is needed. This will be discussed more later. The Lawrence code initializes the space marching operation by a step-back procedure using the freestream conditions as initial conditions. For the conical

inviscid problem this converges to the desired solution since the flow does not change in the radial direction. The situation is very much changed when viscous effects are involved since strong viscous interactions then occur at the vertex of the waverider.

When the waverider is inclined to the freestream, that is, when it is at a nonzero angle of attack, it is possible that other flow features will arise that can cause numerical instabilities when the angle of attack is large enough. Such features might be the detachment of the bow shock, the occurrence of imbedded shocks, or the occurrence of vortical motions.

4.3 Aerodynamic Forces

The normal-force and axial-force coefficients (C_N, C_A) are defined as

$$C_N = \frac{N}{q_\infty S_b}, \quad C_A = \frac{A}{q_\infty S_b}, \quad (4-1)$$

where N and A are normal- and axial-forces respectively, S_b is a waverider base plane area, and q_∞ is the dynamic pressure of freestream flow. The base plane S_b is used for a reference area in order to compare with experimental data which use S_b also.

$$q_\infty = \frac{1}{2} \rho_\infty V_\infty^2 = \frac{1}{2} \gamma p_\infty M_\infty^2, \quad (4-2)$$

$$S_b = l^2 \int_{\phi=0}^{\phi=\phi_*} \tan^2[\theta(\phi)] d\phi,$$

where l is the length of the waverider. The pressure force acting on a waverider can be expressed by

$$\vec{F} = - \int \int_S p d\vec{S} = - \int \int_S (p - p_\infty) \hat{n} dS, \quad (4-3)$$

where \hat{n} is an outward unit normal vector and S is a closed surface domain which embraces the whole waverider body. They are composed of three parts, i.e., a freestream upper-surface, a compression under-surface, and a base plane. Now consider the definitions of normal- and axial-forces, and metrics.

$$N \equiv \hat{j} \cdot \vec{F}, \quad A \equiv \hat{i} \cdot \vec{F}, \quad d\vec{S} = \frac{1}{J} \nabla \zeta, \quad (4-4)$$

where \hat{i} and \hat{j} are base vectors of body oriented coordinates. If the pressure of the base plane surface is assumed to have the freestream value, then the integration for the base plane vanishes by the second expression of \vec{F} in Eq.(4-3). Therefore, the N and A in discretized form can now be expressed by

$$N = 2 \sum_{i,j} [(p_\infty - p) \frac{\zeta_y}{J}]_{i,j}, \quad A = 2 \sum_{i,j} [(p_\infty - p) \frac{\zeta_x}{J}]_{i,j}, \quad 1 \leq i \leq i_{max}, 1 \leq j \leq j_{max}, \quad (4-5)$$

where the subscripts i, j are for η, ζ coordinates respectively and $p_{i,j}$ denote the wall pressures on the waverider upper and lower surfaces with excluding the base plane. Note that the signs of both $\frac{\zeta_x}{J}$ and $\frac{\zeta_y}{J}$ are negative for the lower compression surface where $p > p_\infty$ and thus N and A become positive. The C_N and C_A for the whole waverider body now become

$$C_N = \frac{2}{\gamma M_\infty^2} \frac{\sum_{i,j} [(1 - p/p_\infty) \frac{\zeta_y}{J}]_{i,j}}{S_b}, \quad (4-6)$$

$$C_A = \frac{2}{\gamma M_\infty^2} \frac{\sum_{i,j} [(1 - p/p_\infty) \frac{\zeta_x}{J}]_{i,j}}{S_b}.$$

To get these coefficients the summation should be carried out for the whole forebody geometry. However, for an inviscid flow over a conical body like the waveriders studied here a simpler calculation can be done and its procedure is presented in the following. From the grid constructed for this problem, we can let

$$\Delta \vec{S}_j \equiv \sum_{i=1}^{i_{max}} (\nabla \zeta / J)_{i,j}. \quad (4-7)$$

For an inviscid flow we can apply the conical approximation such as

$$p_{i_1,j} = p_{i_2,j} \equiv p_j, \quad (4-8)$$

where $1 \leq i_1, i_2 \leq i_{max}$. By means of Eqs.(4-7) and (4-8), the normal-force and axial-force coefficients can be obtained as

$$\begin{aligned} C_N &= \frac{2}{\gamma M_\infty^2 S_b} \sum_j \left[1 - \left(\frac{p_j}{p_\infty} \right) \right] (\Delta S_y)_j, \\ C_A &= \frac{2}{\gamma M_\infty^2 S_b} \sum_j \left[1 - \left(\frac{p_j}{p_\infty} \right) \right] (\Delta S_x)_j. \end{aligned} \quad (4-9)$$

The ratio N/A can be easily obtained by Eq.(4-9) as

$$N/A = \frac{\sum_j \left[1 - \left(\frac{p_j}{p_\infty} \right) \right] (\zeta_y)_{i_{max},j}}{\sum_j \left[1 - \left(\frac{p_j}{p_\infty} \right) \right] (\zeta_x)_{i_{max},j}} = \frac{\sum_j \left[1 - \left(\frac{p_j}{p_\infty} \right) \right] (\Delta S_y)_j}{\sum_j \left[1 - \left(\frac{p_j}{p_\infty} \right) \right] (\Delta S_x)_j}. \quad (4-10)$$

This means that to calculate N/A for the forebody with conical geometry it is sufficient to consider a special portion of the forebody separated by two cross sections instead of the whole forebody. C_L and C_D for nonzero angle of attack are calculated by the following relation:

$$\begin{Bmatrix} C_L \\ C_D \end{Bmatrix} = \begin{bmatrix} \cos \alpha & -\sin \alpha \\ \sin \alpha & \cos \alpha \end{bmatrix} \begin{Bmatrix} C_N \\ C_A \end{Bmatrix}, \quad (4-11)$$

where C_N and C_A are based on the Cartesian coordinates (x, y, z) fixed to the waverider body. The rotated Cartesian coordinates for C_L and C_D , (x', y', z') are shown in Fig.(3-1). Now L/D can be easily obtained from Eq.(4-11).

Chapter V

GEOMETRICAL CONSIDERATIONS

A generalized curvilinear coordinate system is of common use nowadays in solving numerically fluid-flow problems with complicated boundaries. If we use body-fitted coordinates with two coordinates on the body, the boundary conditions can be imposed easily and accurately. Even though there exist grid generating codes such as GRAPE[12] and EAGLE[29], it would be more desirable to write a code for the waverider problem, because the elliptic-cone waverider studied here has a geometrical singularity and thus we have to control the grid as much as we need.

Among various requirements of grid, smoothness and good grid control are basically important. Thompson's[30] elliptic grid generation, which can produce very smooth grids, is one of the most widely used schemes. The grids can be controlled by the inhomogeneous source terms called control functions in the Poisson's equations which are used for grid construction. In determining control functions to generate a required grid for an elliptic-cone waverider two factors are taken into account: an orthogonal grid near the wall and a very sharp tip. To overcome the difficulty due to double singularities we introduce a Fan-type grid which was found quite efficient there. In order to capture a bow shock more accurately we may utilize an adaptive grid. To get a more desirable grid structure near the tip the boundary points are redistributed by means of a stretching function. Finally, the metrics, Jacobian, and conical grid are described in brief.

5.1 Elliptic Grid Generation

The set of equations for 2-D elliptic grid generation is

$$\eta_{zz} + \eta_{yy} = P(\eta, \zeta), \quad \zeta_{zz} + \zeta_{yy} = Q(\eta, \zeta). \quad (5-1a, b)$$

subject to the Dirichlet BCs such as

$$\begin{aligned} \Gamma_1; z = f_1(\eta, \zeta_1), y = g_1(\eta, \zeta_1), \\ \Gamma_2; z = f_2(\eta, \zeta_2), y = g_2(\eta, \zeta_2), \end{aligned} \quad (5-2a, b)$$

where f_1, g_1, f_2 , and g_2 are functions specified for the inner ($\zeta = \zeta_1$) and outer ($\zeta = \zeta_2$) boundaries. P and Q are called control functions which control the grid shape. The solution of the above system has the form

$$\eta = \eta(z, y), \quad \zeta = \zeta(z, y), \quad (5-3a, b)$$

in a physical domain. But our purpose is to use η, ζ as new coordinates and accordingly they are to be used as independent variables instead of dependent variables. Therefore, we need the solution in the form

$$z = z(\eta, \zeta), \quad y = y(\eta, \zeta), \quad (5-4a, b)$$

in a computational domain. Figure (5-1) shows the physical and computational domains related to the elliptic grid generation. If we interchange the dependent and independent variables by means of the Jacobian theory (or chain rule), then the elliptic grid generator becomes

$$\alpha z_{\eta\eta} - 2\beta z_{\eta\zeta} + \gamma z_{\zeta\zeta} = -\frac{1}{J^2}(Pz_\eta + Qz_\zeta), \quad (5-5a)$$

$$\alpha y_{\eta\eta} - 2\beta y_{\eta\zeta} + \gamma y_{\zeta\zeta} = -\frac{1}{J^2}(Py_\eta + Qy_\zeta), \quad (5-5b)$$

where

$$\alpha \equiv z_\zeta^2 + y_\zeta^2, \quad \beta \equiv z_\eta z_\zeta + y_\eta y_\zeta, \quad \gamma \equiv z_\eta^2 + y_\eta^2. \quad (5-6a, b, c)$$

and the Jacobian J is defined as

$$J \equiv \frac{\partial(\eta, \zeta)}{\partial(z, y)}. \quad (5-7)$$

5.2 Control Functions

In determining control functions two factors are taken into account. One is grid control near the wall and the other is an adaptive grid. In this study the above two separated effects are combined together as

$$P \equiv P_W + P_A, \quad Q \equiv Q_W + Q_A, \quad (5-8)$$

where the subscript W stands for wall and A for adaptive. The P_W and Q_W can be determined only by geometric constraints, while P_A and Q_A are affected by flow solutions.

Grid Control near Wall

To control the grid near the wall two constraints by Sorenson[12] are imposed. They are orthogonality and the first grid spacing from the wall;

$$z_\eta z_\zeta + y_\eta y_\zeta|_w = 0, \quad (5-9)$$

$$(z_\zeta^2 + y_\zeta^2)^{1/2}|_w \equiv \Delta s_1 = \text{specified}, \quad (5-10)$$

where $\Delta\eta = \Delta\zeta = 1$ as usual and Δs_1 is the first grid spacing from the wall. Except for $z_{\zeta\zeta}$ and $y_{\zeta\zeta}$ at the wall all the other necessary derivatives can be determined if the inner wall boundary are specified. The second derivatives in ζ are approximated by using the one-sided differences which contain previous iteration values. The source terms are assumed to have the following forms.

$$P_W(\eta, \zeta) = p(\eta)e^{-a\zeta}, \quad Q_W(\eta, \zeta) = q(\eta)e^{-b\zeta}. \quad (5-11a, b)$$

The above constraints can decide the $p(\eta)$, $q(\eta)$ and the parameters, a and b , are specified. If a larger value of a or b is used, the effect of constraints decay very quickly. On the other hand for a smaller value it decays slowly. In solving the set of equations, the Successive Line Over-Relaxation (SLOR) method is utilized. Near the sharp corners, numerical instability may often occur. To remedy the problem, various methods including under relaxation and mixed finite difference schemes based on the sign of P and Q are used.

Adaptive Grid

To improve the resolution in regions where rapid flow variations occur, and/or to reduce the global error, an adaptive grid may be utilized. The basic idea of adaptive grid which provides automatic adjustment to the flow pattern can be obtained by equidistribution principle which for 1-D case can be expressed by

$$x_\eta w = (\Delta x)w = \text{const.} \quad (5 - 12)$$

This means simply that the mesh size is smaller when a weight function w is larger and vice versa. If we differentiate it once with respect to η and compare with the Poisson elliptic grid generating equation for 1-D, it can be easily seen that the control function P is related to $\frac{1}{w} \frac{\partial w}{\partial \eta}$. Thomas et al.[31] introduced control function as

$$P_A = (\eta_z^2 + \eta_y^2)\phi(\eta, \zeta), \quad Q_A = (\zeta_z^2 + \zeta_y^2)\psi(\eta, \zeta). \quad (5 - 13a, b)$$

Anderson[13] related these ϕ and ψ to the weight function w as

$$\phi = \frac{1}{w} \frac{\partial w}{\partial \eta}, \quad \psi = \frac{1}{w} \frac{\partial w}{\partial \zeta}. \quad (5 - 14a, b)$$

In this study w is determined by

$$w = 1 + A|\nabla p|/|\nabla p|_{\max}, \quad (5 - 15)$$

where A is a constant and the number 1 is introduced to avoid infinite grid spacing in regions where the pressure gradient vanishes. The pressure gradient in Eq.(5-15) can be obtained by

$$\begin{aligned}\frac{\partial p}{\partial z} &= (y_\zeta \frac{\partial p}{\partial \eta} - y_\eta \frac{\partial p}{\partial \zeta})/\sqrt{g}, \\ \frac{\partial p}{\partial y} &= (-z_\zeta \frac{\partial p}{\partial \eta} + z_\eta \frac{\partial p}{\partial \zeta})/\sqrt{g},\end{aligned}\tag{5-16a,b}$$

where $\sqrt{g} = \frac{1}{J}$. Note that the pressure obtained by numerical integration is defined at cell center points and thus it is necessary to express it at primary grid points before calculating pressure gradients. If we use the weight function based on the above definition directly, then the grid might become rough. Thus, we adapt the following smoothing

$$\begin{aligned}\bar{w}(k, l) &= \frac{1}{16} \{4w(k, l) + 2w(k, l+1) + 2w(k+1, l) + 2w(k-1, l) + 2w(k, l-1) \\ &\quad + w(k-1, l-1) + w(k-1, l+1) + w(k+1, l-1) + w(k+1, l+1)\}.\end{aligned}\tag{5-17}$$

Since the source terms are defined by Eqs.(5-11,13), the Poisson equations are set up as

$$\begin{aligned}&\alpha \vec{r}_{\eta\eta} - 2\beta \vec{r}_{\eta\zeta} + \gamma \vec{r}_{\zeta\zeta} \\ &= - \left\{ \left[\frac{1}{J^2} p(\eta) e^{-a\zeta} + \alpha \phi(\eta, \zeta) \right] \vec{r}_\eta + \left[\frac{1}{J^2} q(\eta) e^{-b\zeta} + \gamma \psi(\eta, \zeta) \right] \vec{r}_\zeta \right\},\end{aligned}\tag{5-18}$$

where $\vec{r} = (z, y)^T$. The Eq.(5-18) is the final form which is numerically solved to get a desired elliptic grid for a waverider.

5.3 Boundary Conditions

To generate body-fitted coordinates by solving elliptic partial differential equations two boundary conditions at inner and outer boundaries should be specified.

Inner Boundary : Waverider

The compression under-surface of the elliptic-cone waverider, $\theta_w = \theta_w(\phi)$, is constructed in spherical coordinates by either Eq.(2-12) or (2-13).

For $-\phi_s \leq \phi \leq \phi_s$, the lower compression surface is given by

$$y = -x \tan \theta_w \cos \phi, \quad z = x \tan \theta_w \sin \phi, \quad 0 \leq \phi \leq \phi_s, \quad (5-19a, b)$$

$$y = -x \tan \theta_w \cos \phi, \quad z = -x \tan \theta_w \sin \phi, \quad -\phi_s \leq \phi \leq 0. \quad (5-20a, b)$$

For $\phi_s < \phi < 2\pi - \phi_s$, two planes which are aligned with the freestream flow are used to define a waverider configuration.

$$y_s \leq y \leq 0, \quad z = -\frac{z_s}{y_s}y, \quad \phi_s \leq \phi \leq \pi, \quad (5-21a, b)$$

$$y_s \leq y \leq 0, \quad z = \frac{z_s}{y_s}y, \quad -\pi \leq \phi \leq -\phi_s. \quad (5-22a, b)$$

Outer Boundary : Ellipse

The outer boundary is defined as an adjustable ellipse.

$$\frac{(y + y_0)^2}{b^2} + \frac{z^2}{a^2} = 1. \quad (5-23)$$

where

$$y_0 = a_1 H, \quad a = a_2 H, \quad b = a_3 H, \quad H \equiv \tan \theta|_{\phi=0}. \quad (5-24a, b, c, d)$$

where a_1, a_2 , and a_3 are parameters determining the outer boundary shape.

Redistribution of Boundary Points

The inner and outer boundary points around the tip are redistributed by using Roberts' stretching[11] which is more desirable than an exponential stretching, since for the region where the clustering is not wanted we can get more uniform stretching.

The arc length, S , is defined by

$$S = \frac{(\beta + 1) - (\beta - 1)\left(\frac{\beta+1}{\beta-1}\right)^{1-\bar{\zeta}}}{1 + \left(\frac{\beta+1}{\beta-1}\right)^{1-\bar{\zeta}}} S_t, \quad (5-25)$$

where $0 < \beta < \infty$ and $\bar{\zeta} = \frac{1}{\zeta_{max}-1}$. As $\beta \rightarrow 0$, more clustered grid near $S = 0$ can be obtained. As $\beta \rightarrow \infty$, they become uniform. Based on the arc lengths we can get

the clustered grid as we like. This is done by redistributing the x and y coordinates along the wall line by means of the interpolation according to the calculated arc lengths.

Grid Types

By changing the inner boundary values with slight modifications, we can obtain different types of grids such as *O*-type, Fan-type, and adaptive grids.

The grid structure near the sharp tip plays a very important role especially in respect to the convergence in numerical calculations. The smoothness is the general requirement of any grid for body-fitted coordinates. To get such a grid the grid lines and the variation of grid cell volumes should be smooth. If we adapt *O*-type grid, which is shown in Figs.(5-2,3) and obtained for the location $x = 1$, the grid structure near the tip will be skewed so much that the grid line smoothness can be spoiled. This cannot be improved by clustering η grid lines, while the cell volume variation is not too bad. Because of the convex surface with an infinite transverse curvature at the tip, constant ζ lines near the tip region are clustered and thus grid spacings along η line which comes out of the tip are small. To adjust them we impose a positive source at the tip which is determined by trial and error.

To improve the smoothness we introduce another type of grid, a Fan-type grid, shown in Figs.(5-4,5) where several rays come out of the same tip point. The grid points are calculated at the position $x = 1$. This type of grid will not cause any problem in numerically integrating the governing partial differential equations, since we are using a finite-volume scheme and there is no flux into the body due to the zero cell area at the tip. However, it is desirable to get at least four triangular grid cells, considering that the numerical algorithm is 2nd order accurate in the crosswise direction, and thus four cells are involved to calculate a flux. The grid used here has six triangular cells. This can represent the flow differences near the tip

properly. But there is a difficulty still in constructing this type grid, since increasing ray number will make the cell areas smaller and thus the smooth variation of cell areas deteriorates. This can be alleviated by introducing a point source at the tip and adjusting the η grid line spacings near the tip. The Fan-type grid is more appropriate to get a finer grid in the η direction, while the O -type grid is more desirable for a finer grid in the ζ direction.

The adaptive grid for a Type- B waverider obtained by the Eq.(5-18) is shown in Fig.(5-6) and its magnified figure is shown in Fig.(5-7). Both figures are obtained for the location $x = 0.05$ where the numerical calculations are made. As can be seen, the grid is skewed very much near the clustered region. Even though the adaptive grid may improve the resolution of the shock in general, it doesn't seem to be very desirable for the problem which has sharp leading edges where numerical instability can occur frequently.

5.4 Jacobian and Metrics

The Jacobian and metrics have their geometrical meanings and they can be determined by the grid geometry in Fig.(5-8). The indices (n, k, l) are for (ξ, η, ζ) coordinates respectively. The vertices denoted by the solid circles (\bullet) are called primary grid points and the cell center points denoted by X are called secondary grid points.

Jacobian and Cell Volume Element

Under the definition of the Jacobian J ,

$$J \equiv \frac{\partial(\xi, \eta, \zeta)}{\partial(x, y, z)}, \quad (5-26)$$

the J is related to the cell volume in the physical domain inversely, i.e.,

$$J \equiv \frac{1}{\Delta V}, \quad (5-27)$$

where $\Delta\xi = \Delta\eta = \Delta\zeta = 1$ is set as usual. Therefore, the Jacobian can be obtained from the geometry of the grid. There can be various ways to determine the cell volume. In this investigation it is calculated by using the following relation[32],

$$\frac{1}{J} = \frac{1}{3}(\Delta\vec{S}_{k,l}^{n+1} + \Delta\vec{S}_{k+1/2,l}^{n+1/2} + \Delta\vec{S}_{k,l+1/2}^{n+1/2}) \cdot (\vec{r}_{k+1/2,l+1/2}^{n+1} - \vec{r}_{k-1/2,l-1/2}^n), \quad (5-28)$$

where \vec{r} represents a position vector for the primary grid points shown in Fig.(5-8). For example, the point C in the figure is corresponding to $\vec{r}_{k+1/2,l+1/2}^{n+1}$. The magnitude of the area element $\Delta\vec{S}_{k,l}^{n+1}$ is equivalent to the area of $ABCD$ and its direction is in the normal to the area with the the positive ξ -direction. Whereas the fluxes are defined at the cell interfaces like $\Delta\vec{S}_{k,l}^{n+1}$ in the finite volume method, the flow variables are defined at the cell center point. In the Lawrence algorithm, the marching level is raised from $(n + 1/2)$ to $(n + 1)$ as shown in Fig.(5-8) . Therefore, the point $(n + 1, k, l)$ is located at the center of the area element $ABCD$ instead of the center point of the cell.

Metrics and Cell Area Element

The comparison of the discretized equation(B-11) based on the finite volume method with its corresponding differential equation(3-5) in steady state can provide a useful relation which shows the physical explanation for metrics. For example, the ξ metrics is expressed by means of the geometrical quantity, the area vector, as

$$\frac{1}{J} \nabla_{\xi} |_{k,l}^{n+1} = \Delta\vec{S}_{k,l}^{n+1}. \quad (5-29)$$

Therefore, once a grid are generated by any means, the metrics combined with the Jacobian can also be determined through their corresponding area element vectors. The area vector $\Delta\vec{S}_{k,l}^{n+1}$ can be calculated by the cross product of two vectors as

$$\begin{aligned} \Delta\vec{S}_{k,l}^{n+1} &= \frac{1}{2}(\vec{AC} \times \vec{BD}) \\ &= \frac{1}{2}(\vec{r}_{k+1/2,l+1/2}^{n+1} - \vec{r}_{k-1/2,l-1/2}^{n+1}) \times (\vec{r}_{k-1/2,l+1/2}^{n+1} - \vec{r}_{k+1/2,l-1/2}^{n+1}). \end{aligned} \quad (5-30)$$

Note that the sign of the area element is decided by its corresponding outward unit normal \hat{n} and the metrics in FVM are defined at cell interfaces.

Conical Grid

So far we described only 2-D grid, while the problem is 3-D. We can easily construct the desired 3-D grid through contraction or expansion of the generated 2-D grid, since the elliptic-cone waverider has a conical shape. Since the $\xi = \text{constant}$ plane is perpendicular to the x -axis, for the grid constructed here we have

$$\xi_y = \xi_z = 0. \quad (5 - 31)$$

Chapter VI

CIRCULAR- AND ELLIPTIC-CONE FLOW SOLUTIONS

In this chapter, in order to confirm the validity of the code STARS3D which is used for this study and also to check the accuracy of the HSDT approximate method, we calculate some inviscid flow variables for circular cones and compare them with known exact solutions. As a second means of comparison, the solution of the flow past an elliptic cone is obtained by numerically integrating the complete Euler equations. Considering any waverider investigated here is constructed from the known compressible flow field past an elliptic cone at a supersonic speed, it will be profitable to obtain a flow solution about the elliptic cone in order to facilitate the understanding of waverider physics. In studying hypersonic flows it is important to note that for any asymmetric supersonic or hypersonic conical flow there exists a vortical layer near the body surface where the entropy changes very rapidly. For checking the vortical layer we present entropy contours. Finally to enhance the understanding of the waverider flows especially near the leading edges, the shock locations by both the HSDT and numerical integration for elliptic cones are calculated and presented.

6.1 Circular-Cone Flow

As test cases we calculate the shock angles β and normalized wall pressure p_w/p_∞ of inviscid circular-cone flows for several values of the basic circular-cone half angle δ . For the calculation $M_\infty = 4$ and $\gamma = 1.4$ are used. The numerical data are from STARS3D code and the approximate analytic data from the HSDT

by means of Eqs.(A-6,7,12). The numerical shock position is determined by the location of the largest pressure gradient. The shock is captured with one internal grid point and it is a very clean shock without any wiggles before and after the shock. For $\delta = 12.5^\circ, 17.5^\circ$, and 20.0° Sims tables[33] render exact solutions which are shown in Table (6-1).

Table (6-1)

δ	β or p_w	Sims	STARS3D	HSDT	ΔE_{N-E}	ΔE_{A-E}
12.5°	β	19.65°	19.72°	19.90°	+0.36%	+1.27%
	p_w/p_∞	2.307	2.306	2.331	-0.04%	+1.04%
17.5°	β	24.08°	24.16°	24.07°	+0.33%	-0.04%
	p_w/p_∞	3.368	3.365	3.382	-0.09%	+0.42%
20.0°	β	26.49°	26.42°	26.34°	-0.25%	-0.55%
	p_w/p_∞	4.006	4.002	4.014	-0.10%	+0.20%

As can be seen, the maximum percentage errors of the numerical values to the exact values (denoted by ΔE_{N-E}) for the surface pressure and the shock angles are 0.1% and 0.36% respectively for the given range of δ . These indicate that the computational results are very dependable, and thus that the STARS3D code can be utilized for other similar flow calculations with confidence. On the other hand, the maximum percentage errors of the approximate analytic values to the exact values (denoted by ΔE_{A-E}) for both the surface pressure and the shock angle are slightly larger than 1%.

Table (6-2) is for two values of δ that are used to generate perturbed elliptic-cone flows. For the smaller δ case the relative error of the analytic shock to the numerical shock (denoted by ΔE_{A-N}) is positive. But for the larger δ case the error is negative. The wall pressure data of the HSDT show consistently larger values than the exact values in Table (6-1) and the numerical values in Table (6-2).

Table (6-2)

δ	β or p_w	STARS3D	HSDT	ΔE_{A-N}
12.0°	β	19.30°	19.52°	+1.14%
	p_w/p_∞	2.217	2.241	+1.10%
18.62°	β	25.19°	25.07°	-0.48%
	p_w/p_∞	3.641	3.657	+0.44%

6.2 Flow Field past an Elliptic Cone

Figures (6-1) show the solution to the compressible supersonic flow past an elliptic cone at $M_\infty = 4$ and $\alpha = 0^\circ$. It is obtained by numerically integrating the Euler equations. For the reason of comparison each physical variable is normalized by its corresponding freestream value. The elliptic-cone geometry is decided by the half basic cone angle $\delta = 18.62^\circ$ and small perturbation parameter $\epsilon_2 = 0.1$ (see Eq.(2-1)). This specific geometry with the given flow condition is introduced so that it is consistent with its corresponding waverider Type-*B* at the on-design condition. Figure (6-1a) shows the grid (63x63 mesh) for the elliptic cone. Figure (6-1b) shows the disturbance velocity parallel to the $y - z$ plane, that is, $\vec{V} = V_y \hat{j} + V_z \hat{k}$. The dots indicate that the flow is in the x -direction without any disturbance due to the body. Between the dotted and arrow areas we can see a distinct boundary where a bow shock is located (roughly speaking). Through this shock the freestream flow is deflected. If we take a close look at the shock location, it can be seen that the shock stand-off is larger near the vertical minor axis than the horizontal major axis. This is in agreement with Eqs.(2-1,2) for the HSDT $g_2 = 0.597$ and $\sigma = 1.34$. The azimuthal velocity component shown in Fig. (6-1c) goes to zero as ϕ approaches 0° , 90° , or 180° . Its maximum absolute value occurs at $\phi \cong 45^\circ$. It is to be noted here that flow variables are not given at symmetry lines where primary grid points are defined. Since the FVM is used in this study, they are defined at secondary

grid points. The sign of w is negative as shown in Fig. (6-1c). That is because of the positive pressure gradient from the vertical minor axis toward the horizontal major axis, as can be seen in Fig. (6-1d). The pressure is a maximum at the major axis. Figure (6-1e) shows the pressure distribution near the lower minor axis from the freestream side to the wall side. A very sharp and clean shock is captured with one internal grid point. Figure (6-1f) shows a comparison of the pressure on the cone surface obtained by the numerical integration of the Euler equations and by the HSDT. At the minor- and major-axes the two sets of data are very close. The HSDT result in the middle of the figure is about 3 percent greater than the numerical result. Figure (6-1g) shows a comparison of the pressure distribution across the shock layer near the minor-axis symmetry plane. The HSDT shock is located more closely to the cone body than that by the numerical calculation. Figures (6-1h,i) show the pressure and Mach number contours. In both figures a bow shock is identified by coalesced lines.

6.3 Entropy and Vortical Layer

Figures (6-2a,b) show the entropy contours for the elliptic cones with $\delta = 12^\circ$ and 18.62° . Each of them corresponds to the Type-*A* or Type-*B* waverider. The constant entropy surfaces are getting closer as they approach the cone surface and they have a common tendency to embrace the body near the minor axis. This means the entropy near the wall changes very rapidly in the normal direction to the wall. A region with a rapid entropy change also has a large vorticity according to Crocco's equation. The region of the rapid change near the wall is called the vortical layer. According to an analysis by Ferri [24] vortical singularities exist at the minor axes of an elliptic cone where multiple values of entropy occur. In order to delineate the vortical layer distinctly, of course, we need accurate entropy values on the wall and symmetry lines. In this respect a finite-difference method (FDM)

would be more preferable for the purpose of capturing the vortical layer, since in a FDM both the wall and symmetry values are defined. A partially improved result for the vortical layer might be achieved by means of a finer grid in those regions.

6.4 Shock Locations for Elliptic Cones

Figure (6-3a) shows the shock locations for an elliptic cone (Type-*A* waverider generator) by the HSDT method and numerical calculation. It can be seen that the shock angle due to the approximate analytic method is greater than that obtained by the numerical integration of the Euler equations. Figure (6-3b) shows the shock locations obtained by the above two ways for another elliptic cone (Type-*B* waverider generator). For this case the HSDT shock is located inside of the numerical shock. These phenomena correspond to the results of Table (6-2). In the figures we can also see that the shock locations predicted by the HSDT and CFD methods are in reasonable agreement, the more so in the Type-*A* waverider generator.

Chapter VII

WAVERIDER FLOW SOLUTIONS

In this chapter we present and discuss the numerical Euler solutions for supersonic/hypersonic flows past elliptic-cone waveriders. The base on-design condition is for $M_\infty = 4$ and $\alpha = 0^\circ$. The chapter is divided into six parts. The first part discusses the on-design flows past the two *A* and *B* types of waveriders, and comparisons are made with the results of the HSDT. The second part considers off-design flows where $\alpha = 0^\circ$ is held fixed. The Mach numbers above the design condition are $M_\infty = 4.5, 5.0$, and 10.0 . The Mach number below the on-design condition is $M_\infty = 3$. The third part considers off-design conditions for which $M_\infty = 4$ is held fixed and both positive and negative angles of attack are considered. The fourth part considers the off-design conditions for which both the angle of attack and Mach number are different from those of the on-design condition. The fifth part discusses the constant entropy surfaces for the on-design flows. The sixth part deals with the inviscid lift and drag of the waveriders as functions of freestream Mach number and angle of attack.

7.1 On-Design Flows : $M_\infty = 4, \alpha = 0^\circ$

We consider separately the on-design flows for the Type-*A1, A2* waveriders in Figs.(7-1,2) and then the flows for the Type-*B1, B2* waveriders in Figs.(7-3,4). Next, we compare the computational solution to the flow past the Type-*A1* waverider with the analytic approximate solution based on the HSDT in Figs.(7-5) and to the flow past the Type-*B1* waverider in Figs.(7-6).

(1). Type-A1 Waverider ($K_\delta = 0.838$)

Figures (7-1) show various drawings for the numerical solution to the compressible flow past the Type-A1 waverider at its nominal on-design condition. Figure (7-1a) shows the *O*-type grid (83x41 mesh) that was used. The details of the typical *O*-type grids for the sharp tip region were presented in Figs.(5-2,3).

The disturbed velocity that is perpendicular to the x -axis is shown in Fig.(7-1b). Its magnified flow field near the leading edge is shown in Fig.(7-1c). A bow shock is captured under the waverider, and it ranges from the symmetry plane to the leading edge region. Below the shock there are dots which indicate that the flow is perpendicular to the $y - z$ plane and the freestream is not disturbed at all. In the region between the lower waverider wall and the dotted area we can see the velocity components in the $y - z$ plane, which indicate the freestream flow is deflected through the shock. In the upper region above the waverider we can observe that the freestream is disturbed. The right side of this disturbed region is the extension of the bow shock from under the waverider, and its strength is weakened as it goes upwards. This weakened shock finally becomes a Mach cone in the upper symmetry plane.

Figure (7-1d) shows a comparison of the bow shocks as calculated by means of the HSDT and as captured by the numerical integration. The computational shock position was defined by the locations where the largest pressure gradient along each constant η line occurs. The shock captured by the computation is found to stand off from the leading edge instead of being attached, which should be expected for the ideal on-design condition. The attached shock can be expected only if the waverider geometry is based on the exact solution to the corresponding elliptic-cone flow and the solution to the flow past such a waverider is also exact. Thus, if either or both of the two conditions are not met, we cannot expect an attached shock in general. The waverider configuration used in this investigation is generated by

means of an HSDT approximation. For the flow past the elliptic cone that generates the waverider, we could already see the difference between the two shocks by the HSDT and the computation in Fig.(6-3a) of the previous chapter. Through the gap between the leading edge and the shock, the flow appears to be spilling from the lower region to the upper region owing to the large pressure gradient in the circumferential direction. As a result, the flow in the upper region of the waverider is also disturbed.

The normalized azimuthal velocity component w/V_∞ along the waverider wall is shown in Fig.(7-1e). The horizontal axis denotes the η -coordinate along the wall. The azimuthal angle ϕ is measured from the lower symmetry plane anticlockwise. Obviously w goes to zero in the region at $\phi = 0$. As ϕ increases, its magnitude with negative sign increases. In the middle of the figure we can observe that w increases from negative values to large positive values. In other words, the flow near the tip accelerates from the lower compression part to the upper freestream part of the flow field.

Figure (7-1f) shows the normalized pressure distribution along the waverider surface p_w/p_∞ versus the horizontal axis z . For the computer computations, the z coordinate is measured at the location $x = 0.05$, where all the other numerical calculations are also carried out throughout this study. Since the flow and body are conical, the picture is similar in every vertical plane. The higher pressure line in the figure is for the waverider lower-compression surface, and the lower pressure line is for the upper-freestream surface. Strictly speaking, the pressure is for a half grid spacing above the wall. For the wall pressure the zero gradient assumption in the normal direction from the wall is used. As z increases, the pressure of the lower waverider surface also increases. This is mainly due to the larger deflection-angle effect from the minor axis to the major axis of the elliptic cone which is the waverider generator. For the same pressure line we can see the region where the

pressure decreases as z increases. This decrease is principally due to the pressure decreasing phenomenon of the elliptic-cone flow from the body to the shock as shown in Fig.(6-1e). Near the leading edge, the pressure of the under-compression area increases as z increases, and it has the peak value right before reaching the edge. On the other hand, according to the analytical calculation which will be presented in the subsection **Comparison with HSDT**, the pressure for the same region decreases as z approaches the tip. To check whether the numerical pressure has the trend of the analytical calculation or not, we calculated the flow by using a more clustered grid near the tip and also Fan-type grids shown in Figs.(5-4,5). But the pressure increasing trend remained almost the same. In other words, the behavior of the numerical solutions near the tip does not match that of the approximate solution, while the flow for the rest of the tip region remains nearly unchanged and shows good agreement with HSDT. This will be discussed in more detail subsequently. Figure (7-1g) shows the normalized pressure distribution near the lower symmetry plane $z \cong 0$. More precisely, it represents the pressure for the finite-volume elements whose left interfaces are located at the symmetry plane. The shock is found to be captured only with two internal grid points. It is a clean shock without any oscillations either after or before the shock.

Figure (7-1h) shows the pressure contours. A bow shock is clearly seen in the lower compression part, and it stands off from the tip as stated earlier. The right upper area of the waverider is disturbed by both the bleeding due to the pressure jump near the tip and the extended shock. This disturbed region is expected to be extend upwards further as the angle of attack is increased. Therefore, for the case of high angle of attack, care must be taken so that the outer boundary is sufficiently far from the waverider to cover this disturbed region. If not, numerical instability can occur. Figure (7-1i) shows the Mach number contours which are similar to the pressure contours.

(2). Type-A2 Waverider ($K_\delta = 0.838$)

In order to determine the effects of a change in shape of a waverider on the flow fields, calculations were made for the waverider with shape Type-A2. This shape has a tip angle of only 1.44 deg, compared with 10.45 deg for the Type-A1 waverider. The details for the tip angle are described in **Appendix C**. Figures (7-2a) through (7-2g) pertain to the Type-A2 waverider, and these are to be compared with the corresponding Figs.(7-1a) through (7-1g) for the Type-A1 waverider. Figures (7-2a,a') show the Fan-type grid that is used for the computation. In spite of the sharpness of the leading edge, a very smooth grid is generated. The Cross-Plane velocity distribution is shown in Fig.(7-2b) and its magnified portion for the tip region is in Fig.(7-2c). We can see that the flow disturbance above the tip region is very small compared with the corresponding flow in Figs.(7-1b,c). The shocks by the HSDT and the numerical solution are depicted in Fig.(7-2d) and show an amazingly good agreement between them, unlike the case of the Type-A1 waverider in Fig.(7-1d). From the comparison of the shock locations in Figs.(7-1,2d) we can assert that the reason for the large discrepancy for the shock locations in the Fig.(7-1d) near the tip region is from the error of the waverider configuration at the sharp leading edge. The azimuthal velocity component is shown in Fig.(7-2e), and the pressure distributions along the wall and near the lower symmetry plane are shown in Figs.(7-2f,g). The waverider wall pressure distribution in Fig.(7-2f) shows no pressure peak at the tip, unlike the case in Fig.(7-1f). The pressure distribution resembles the trend of the ideal on-design condition based on the HSDT.

(3). Type-B1 Waverider ($K_\delta = 1.30$)

Figures (7-3) show various drawings for the numerical solution to the compressible flow past the Type-B1 waverider at its nominal on-design condition. The O-type grid (83x41 mesh) used for the waverider is shown in Fig.(7-3a). Since the

Type-*B1* waverider has a larger deflection δ than the Type-*A1*, the flow of this type waverider has a larger hypersonic similarity parameter ($K_\delta \equiv M_\infty \delta$) and thus it has a more hypersonic feature. Figure (7-3b) shows the disturbed-velocity distribution, whose magnified portion for the tip region is shown in Fig.(7-3c). The disturbance region above the tip area can be found in the figure. This is located closer to the upper wall than that for the Type-*A1* shown in Fig.(7-1b). Thus, the possibility of interaction with the outer boundary is lessened. Due to this fact, for the case of high angle of attack this type waverider may give more stable results than the Type-*A1*. Since the Type-*B1* waverider is generated from the elliptic-cone flow whose numerical solution was presented in **Chapter 6**, ideally the flow pattern of the waverider lower compression portion should match that of the elliptic-cone flow pattern. We can see that the flow field in Fig.(7-3b) resembles the flow pattern in Fig.(6-1b).

Figure (7-3d) shows two shocks from the approximate and numerical solutions. As the case in Fig.(7-1d), the numerical shock for this type waverider is located outside of the HSDT shock. Figures (7 - 3e ~ i) show similar trends to those of the Type-*A1* waverider in Figs.(7 - 1e ~ i).

For the flow past the Type-*B1* waverider, there are other data available for the wall pressure coefficient. Figure (7-3j) shows the comparison of the pressure coefficients C_p by several researchers including the present study as functions of the azimuthal angle ϕ . The experimental data by Jischke et al.[7] are plotted in the figure. There is a noticeable discrepancy between the experimental and present numerical data. The similar discrepancy between the experimental and the Euler numerical data by Liao et al.[10] can be observed. In fact, a complete agreement cannot be expected, since the experimental data are related to the real viscous flow. However, except for this basic difference of the viscous and inviscid flows, it is difficult at the present time to explain very well the reason for the discrepancy

in C_p . In spite of this disagreement in magnitude between the experimental and computational data, the comparison shows very similar trends for the range of the given experimental data points. Furthermore, a very good agreement between the numerical results by Liao et al. and the present investigation can be found except for the very small region near the leading edge. The two results are obtained by completely different numerical integration methods. The above considerations on the trend and agreement lend confidence to the reliability of the present numerical results. In the figure the pressure coefficient by Jones[4] is also plotted. These data show better agreement with the experimental data for the lower values of ϕ , but for the higher values they do not. The trend shows somewhat irregular variation at $\phi \geq 30^\circ$.

For the purpose of further checking the reliability of the numerical result we calculated the flow by using two different mesh numbers. The coarse mesh is 45×21 and the fine mesh is 83×41 . The comparisons for the different mesh numbers are shown in Figs.(7-3k,l). Figure (7-3k) shows the normalized pressure near the lower symmetry plane versus the normalized vertical length $y/x \tan \delta$. The shock locations are almost identical. The wider shock structure denoted by the dotted line is due to the worse resolution by the coarse grid. Figure (7-3l) shows the normalized waverider wall pressure distributions p_w/p_∞ versus the normalized horizontal length $z/x \tan \delta$. As a whole, a good agreement except for the sharp leading edge region can be seen. The part of the reason for the discrepancy is from using the FVM, since the flow points for the grids of two different mesh sizes in the FVM cannot be identical. The other aspect is that the major numerical error occurs near the sharp leading edge.

(4). Type-B2 Waverider ($K_\delta = 1.30$)

Figures (7-4a) through (7-4g) pertain to the type *B2* waverider, and these are to be compared with the corresponding Figs.(7-3a) through (7-3g) for the type *B1* waverider. The Type-*B2* waverider has a tip angle of 4.12 deg., compared with 9.45 for the type *B1* waverider. Figure (7-4a) shows the Fan-type grid used for the computation. The cross-plane velocity distribution is shown in Fig.(7-4b), and the magnified region near the tip is shown in Fig.(7-4c). Although the shock is not attached at the tip, the stand-off distance is somewhat less than for waverider *B1*. A comparison of the shock locations by the HSDT and the numerical solution is shown in Fig.(7-4d). The numerically calculated position is always somewhat outside the HSDT. This can be partly associated with the fact that, for this case, the conical shock angle at the tip is about 25° , and when the angles get this large the small-angle approximations of HSDT lose their accuracy. The azimuthal velocity component w is shown in Fig.(7-4e), and the pressure distributions near the wall and near the lower symmetry plane are shown in Figs.(7-4f,g). The magnitude of the azimuthal velocity is much less for this case, and the peak in the pressure at the tip of the compression surface has been removed.

(5,6). Comparison with HSDT

One way to confirm numerical results is to check them at a special condition where we know analytic solutions. The basic waverider-generating flow field past an elliptic cone can be obtained by a perturbation method. The details for the solution procedure are described in Appendix A. Both approximate and numerical solutions for the Type-*A1* waverider are plotted in Figs.(7-5) and for the Type-*B1* waverider in Figs.(7-6). The *O*-type grids are used for each waverider. It should be kept in mind that the perturbation solution is an approximate solution, and the purpose of the comparison is to compare trends as well as magnitudes. As a

further reference, flow variables for unperturbed basic cones are also plotted; the polar angle θ within the circular-cone shock layer is given by the same relation as the waverider wall equation $\theta = \theta(\phi)$ in Eq.(2-12). All the dependent variables are nondimensionalized by their corresponding freestream values and represented in spherical coordinates (r, θ, ϕ) .

Figures (7-5) show the flow fields on the lower compression surface of the Type-A1 waverider as functions of azimuthal angle ϕ . The leading edge of the waverider is located at $\phi = 60^\circ$. At $\phi = 45^\circ$, the perturbed and unperturbed solutions are identical except for the azimuthal velocity component.

The radial (r) velocity components of both circular and elliptic cones are shown in Fig.(7-5a). They have a common value at $\phi = 45^\circ$ as mentioned before. This is due to the perturbation term $\cos 2\phi$ in Eq.(2-4a). At $\phi = 0^\circ$, the r -velocity component of the elliptic cone is larger than that of the circular cone, as can be expected from the fact that the elliptic cone has a smaller deflection angle there than the corresponding circular cone. This trend remains the same for the region of $0 < \phi < 45^\circ$. For the region $45^\circ < \phi < 60^\circ$ the opposite occurs by a similar reason. The trends of the analytic and numerical solutions are well matched. Even the magnitudes themselves are quite close to each other except for the tip region. For example, the numerical radial velocity component in Fig.(7-5a) near the symmetry line agrees with the analytic value within 0.15%.

The polar (θ) velocity components are shown in Fig.(7-5b). The difference between the components of the circular and elliptic cones is invisible on this scale. In other words, the θ -velocity component is insensitive to a slight disturbance on a circular cone.

In Fig.(7-5c) the azimuthal (ϕ) velocity components w are shown. The analytic value of w for the elliptic-cone flow has the term $\sin 2\phi$ (see Eq.(2-4c)) which is

different from the rest of the dependent variables. The maximum value of the ϕ -velocity component lies at $\phi \cong 45^\circ$ where the other perturbation variables vanish. Near the tip region, a relatively large discrepancy between the HSDT and the numerical calculation is detected. The much smaller numerical value of w from the computation is caused by the large pressure gradient in that region.

The pressure distributions along the waverider wall are shown in Fig.(7-5d). At $\phi = 0^\circ$, a larger pressure for the unperturbed cone is anticipated than for the corresponding elliptic cone.

As presented in **Appendix A**, the pressure and azimuthal velocity component obtained from the outer perturbation expansions are valid for the entire shock layer including the inner wall regime. On the other hand, the rest of the flow variables are not strictly valid near the wall. This lack of validity of the outer solution is because of the existence of a vortical layer and a vortical singularity in the vicinity of the elliptic cone minor axis, which will be discussed in a later section. For a uniformly-valid solution we need to also use the inner expansions so that these phenomena might be taken into account. In line with this, it is interesting to note that for the symmetry plane region where the vortical layer and vortical singularity are most significant, the agreement of the approximate analytic and numerical values for the pressure and azimuthal velocity component in Figs.(7-5c,d) is very good.

The density and temperature distributions according to the outer expansions are plotted in Figs.(7-5e,f). The agreement for those is not so good in comparison with the case of the pressure.

Corresponding comparisons for the Type-B1 waverider are made in Figs.(7-6). Figures (7-6a,b,c) show the normalized velocity components by the freestream velocity V_∞ in the r , θ , and ϕ directions. The comparisons for the radial and polar velocity components are very similar to those for the Type-A1 waverider in Figs.(7-5a,b). The comparison for w in Fig.(7-6c) shows much better overall agreement

between the numerical and analytical values than that in Fig.(7-5c). Figure (7-6d) compares the waverider wall pressure. As for Figs.(7-5c,d), we can see the very good agreement for the pressure and the azimuthal velocity component in Figs.(7-6c,d) near the lower symmetry plane. In Fig.(7-6e) the outer-expansion density variations are plotted. A relatively large discrepancy between the numerical and the analytic values is observed. It would be helpful to recall that for the outer expansion solutions the pressure and the azimuthal velocity component are valid throughout the entire shock layer, but the density in Fig.(7-6e) and the temperature in Fig.(7-6f) are not.

7.2 Off-Design Flow : $\alpha = 0^\circ$, $M_\infty \neq 4$

In the following three sections, the various off-design solutions for the Type-B1O waverider are discussed. The *O* means that an *O*-Type grid is used. Even for the off-design conditions, as well as the on-design condition, the flow is conical, since there is no characteristic length scale involved for inviscid supersonic flows. Therefore, for this problem it is enough to calculate the flow at a specific given position in the x -direction. In this study the waverider length is considered as unity and all the numerical calculations are carried out at $x = 0.05$. Thus, in the computation for conical flows savings in CPU time and storage are significant.

In this section the case for a lower Mach number than the on-design value is presented first and then the higher Mach number cases are presented. Finally their comparisons for the pressure distributions are made.

(7). For $M_\infty = 3$, $\alpha = 0^\circ$

Figures (7-7) show various plots for the waverider flow at $M_\infty = 3$ with no incidence. Figures (7-7a) shows the disturbance velocity parallel to the $y - z$ plane. The shock stands off from the leading edge somewhat further than for the on-design case. In Fig.(7-7b) the normalized waverider wall pressure is shown as a function

of the horizontal Cartesian coordinate z . Near the tip a large pressure gradient is seen. Because of this large pressure gradient and the sharp corner of the waverider geometry at the leading edge, the flow at the upper surface near the edge is disturbed significantly. For the flow at a Mach number below the on-design value, this kind of flow pattern near the tip area occurs quite typically. In Fig.(7-7c) the pressure across the shock layer at the lower symmetry plane is plotted. The normalized azimuthal velocity component w/V_∞ along the waverider wall is shown in Fig.(7-7d). The rapid change of w indicates the accelerated cross flow around the tip. In Fig.(7-7e,f) the pressure and Mach number contours are plotted and the shock stand off is clearly seen in those figures.

(8). For $M_\infty = 4.5, \alpha = 0^\circ$

Figures (7-8) show various plots for the waverider flow field at $M_\infty = 4.5$ with no incidence. At this condition the bow shock is attached at the leading edge in Figs.(7-8a,b). The disturbance region is confined by the shock, which ends at the tip, to the under portion of the body. Figure (7-8c) shows the waverider wall pressure; no pressure peak occurs at the leading edge and no significant flow disturbance occurs on the upper freestream surface. This has a similar pressure trend to the idealized case obtained by HSDT. In Fig.(7-8d) the pressure near the lower symmetry plane is plotted, and the azimuthal velocity component along the waverider wall is shown in Fig.(7-8e). For the waverider shape *B1*, this flow condition appears to be what should be called the on-design flow.

(9). For $M_\infty = 5, \alpha = 0^\circ$

Figures (7-9) show various plots for the waverider flow field at $M_\infty = 5$ with no incidence. In Fig.(7-9a) a bow shock is located inside of the tip. No flow disturbance is caught except for the lower portion of the waverider. The magnified flow for the leading edge is shown in Fig.(7-9b). In the figure we can see some other type of

flow disturbance from the bow shock to the tip. The main bow shock appears to terminate normal to the undersurface a short distance from the tip, and a very weak secondary shock emanates from the main shock, a short distance below the body surface, to the tip of the body. This shock interaction near the tip can be interpreted alternatively: For Mach numbers greater than for the on-design condition, the main conical bow shock will lie closer to the body. Except near the tip, the undersurface of the waverider is nearly the same as the originating elliptic cone, and the under portion of the bow shock corresponds to that for the elliptic cone. The flow near the tip, however, is governed by component of the freestream Mach number that is not parallel to the shock. At the tip $\theta = \theta_s(\phi_s)$, this component is $M_{\perp} = M_{\infty} \sin \theta_s$, and is parallel to the freestream surface. This component of the flow is termed the crossflow. The crossflow undergoes a deflection angle Δ at the tip, and this generates a weak oblique shock. The concave curvature near the tip causes a slight concave curvature in the oblique lip shock. The weak oblique lip shock and the strong conical bow shock intersect a short distance away from the lip. A strong Mach stem emanates from the line of intersection to a perpendicular location on the waverider body. The shock structure near the intersecting component has three legs which appear to have the shape of a "lambda". We thus refer to the interacting shock as the lambda shock. We shall consider this further after examining the case for $M_{\infty} = 10$. A schematic diagram is shown in Fig.(7-10c). Figure (7-9c) shows the total pressure distribution for the tip region. Since the total pressure loss is also directly related to the entropy, this figure also indicates the entropy variation in the area. In Fig. (7-9d) the waverider wall pressure is plotted. There are two rapid pressure drops in the tip area. The larger pressure gradient is caused by the main bow shock and the smaller pressure gradient is caused by the very weak shock located in the region from the main shock to the tip. The upper surface shows the undisturbed freestream pressure. In Fig.(7-9e) the pressure distribution across

the shock layer near the lower symmetry plane is drawn. The shock strength is stronger than that of the on-design condition as can be seen in Fig.(7-3g). Figure (7-9f) shows the azimuthal velocity component near the wall. Figures (7-9g,h) show the pressure and Mach number contours. The contours appearing to pass through the body surface near the tip in Fig.(7-9h) are due to the interpolation for the contour plots in the graphic package SURFACEII which is used for this figure. These also represent the lambda shock inside of the tip.

(10). For $M_\infty = 10, \alpha = 0^\circ$

Figures (7-10) show various plots for the waverider flow field at $M_\infty = 10$ with no incidence. Figure (7-10a) shows the disturbed-velocity distribution on the plane perpendicular to the x -axis. The disturbance is limited to a small region below the waverider, and a bow shock is captured very close to the waverider compression surface. Near the tip region, a lambda shock pattern is established, and it is more pronounced than for the $M_\infty = 5$ case. It is shown more dramatically by the stagnation pressure contours which are shown in Fig.(7-10b) and which correspond to the $M_\infty = 5$ case shown in Fig.(7-9c). A schematic diagram of the lambda shock pattern is shown in Fig.(7-10c). The oblique shock from the tip is stronger for the $M_\infty = 10$ case since the cross flow Mach number is larger and the cross flow undergoes the same deflection angle. Figure (7-10d) shows the wall pressure distribution. The rapid pressure jump on the lower surface occurs across the Mach-stem portion of the lambda shock that is normal to the surface. The upper surface has the undisturbed freestream value. Figure (7-10e) shows the pressure distribution across the shock layer near the lower symmetry plane. Even though the shock is quite strong, it is a very clean shock with only one internal grid point and no wiggles around it. In Fig.(7-10f) the azimuthal velocity component is depicted.

(11). Comparisons for Flows at $M_\infty \neq 4, \alpha = 0^\circ$

Figures (7-11) show the comparisons of the pressure distributions at various freestream Mach numbers $M_\infty = 3, 4, 4.5$, and 5 with the fixed angle of attack $\alpha = 0^\circ$. Figure (7-11a) compares the the pressure distribution across the shock layer near the lower symmetry plane. It can be seen that as M_∞ increases, the shock strength increases and the shock location moves toward the body. Figure (7-11b) compares the wall pressure distributions. The wall pressure for the upper waverider surface does not change so much except for the case of the Mach number below the on-design value. This implies that the upper freestream surface remains undisturbed for the higher Mach numbers above the on-design value. Especially at $M_\infty = 4.5$ the pressure variation near the tip resembles that of the HSDT prediction and the waverider upper surface has the freestream pressure. The wall pressure for the lower compression surface increases as the Mach number increases except for the leading edge region.

7.3 Off-Design Flow : $M_\infty = 4, \alpha \neq 0^\circ$

In this section the cases for positive angle of attack are presented first and then the cases for negative angle of attack are presented. Finally their comparisons for the pressure distributions are made.

(12). For $M_\infty = 4, \alpha = +3^\circ$

Figures (7-12) show various plots for the waverider flow field at $M_\infty = 4$ and $\alpha = +3^\circ$. Figure (7-12a) shows the disturbance velocity in the $y - z$ plane. Its magnified portion for the tip area is shown in Fig.(7-12b). In Fig.(7-12a) it can be seen that the flow region below the bow shock has uniform upward velocity which represents the freestream component due to the positive angle of attack. The bow shock stands off outside of the tip. The movement of the shock outwards from the on-design condition is caused by the increased effective deflection through

the positive angle of attack. Figure (7-12c) shows the pressure distribution along the waverider wall. The upper part of the figure represents the lower compression surface of the waverider, and the lower part represents the upper surface. We see that the pressure for the upper surface near the tip is smaller than the freestream value. The pressure drop is produced by an expansion wave around the sharp leading edge. We can detect a pressure rise near the symmetry plane for the upper waverider surface. This is produced by the formation of an imbedded weak conical shock that is needed to turn the flow that has expanded around the leading edge back to a direction parallel to the symmetry plane. This pressure rise was also observed by Jischke et al.[7] in their experiment for waveriders. The similar phenomenon can be seen by a supersonic flow past a delta wing at a positive angle of attack with a supersonic leading edge. Figure (7-12d) shows the pressure distribution near the lower symmetry plane. The shock is stronger than that of the on-design condition as in Fig.(7-3g). Figure (7-12e) shows the pressure distribution in the ζ direction at the waverider top surface for the first grid cells whose left faces are at the upper symmetry plane. We can see the expansion that occurs from the freestream to the waverider upper wall. Fig.(7-12f) shows the azimuthal velocity component with the η coordinate.

(13). For $M_\infty = 4, \alpha = +10^\circ$

Figures (7-13) show various plots for the waverider flow field at $M_\infty = 4$ and $\alpha = +10^\circ$. As a whole, these figures present the characteristics of Figs.(7-12) more distinctly. Figure (7-13a) shows the disturbance velocity. The bow shock is located more outwards. The disturbance region extends more outwards than its counterpart in Fig.(7-12a), and the undisturbed freestream exhibits now the uniform velocity components upwards clearly. The magnified disturbance velocity is plotted in Fig.(7-13b). The wall pressure is shown in Fig.(7-13c). We can see that

the cross flow around the leading edge affects the upper part of the waverider more forcibly. The pressure-rise region for the waverider upper surface is smaller than its counterpart in Fig.(7-12c). The shock near the lower symmetry plane and the expansion near the upper symmetry plane are shown in Figs.(7-13d,e). Both the expansion and shock become stronger than those in Figs.(7-12d,e). In Fig.(7-13f) the azimuthal velocity shows a positive peak value which indicates the accelerated cross flow at the leading edge. The azimuthal velocity w should be zero on the waverider upper surface. The w depicted in Fig.(7-13f) shows the values for the half grid spacing off from the wall. A small discontinuity is detected at $\eta \cong 75$. This corresponds to the pressure-rise point near the upper waverider surface at $z/x \tan \delta \cong 0.4$ in Fig.(7-13c).

(14). For $M_\infty = 4, \alpha = -2^\circ$

Figures (7-14) show various plots for the waverider flow field at $M_\infty = 4$ and $\alpha = -2^\circ$. At this condition the shock appears to be nearly attached at the tip as can be seen in Figs.(7-14a,b). In Fig.(7-14c) the pressure distribution along the lower wall does not show any peak value near the tip. In this respect the pressure trend for the lower compression surface resembles that of the HSDT result which represents the idealized on-design condition. It is interesting to note that at about this condition the maximum lift/drag ratio occurs, as will be presented in Section 7.6. Figures (7-14d,e) show the pressure distributions near the lower and upper symmetry planes respectively. In Fig.(7-14e) we can see the gradual compression from the freestream to the wall. Figure (7-14f) shows the azimuthal velocity component versus the η coordinate.

(15). For $M_\infty = 4, \alpha = -4^\circ$

Figures (7-15) show various plots for the waverider flow field at $M_\infty = 4$ and $\alpha = -4^\circ$. Figures (7-15a,b) show quite different flow patterns compared to their

counterparts in Figs.(7-12a,b) and Figs.(7-13a,b). First of all, the bow shock is located inside of the tip, which is caused by the reduced effective deflection angle through the negative angle of attack. Next, the upper disturbed region has the opposite flow direction to its counterpart in Figs.(7-12,11a). That is, the upper disturbed velocity is in the direction of the leading edge. The gas near the leading edge flows downwards instead of upwards and the freestream has downward velocity components. In Fig.(7-15c) we can observe that, near the leading edge, the pressure on the upper surface is higher than the pressure on the lower surface. Thus, near the leading edge a negative lift is produced. The shock for the lower surface in Fig.(7-15d) becomes weaker than the corresponding situation with positive angles of attack in Figs.(7-12,11d). Unlike the cases with positive angles of attack, the upper surface along the symmetry plane experiences a compression from the freestream to the wall of the waverider instead of an expansion as can be seen in Fig.(7-15e). In Fig.(7-15f) the azimuthal velocity component shows negative values including the negative peak value near the leading edge.

(16). For $M_\infty = 4, \alpha = -8^\circ$

Figures (7-16) show various plots for the waverider flow field at $M_\infty = 4$ and $\alpha = -8^\circ$. These represent the characteristics of the previous Figures (7-15) more dramatically. The bow shock in Fig.(7-16a) moves more inwards than that of Fig.(7-15a). Figure (7-16b) shows the downward flow more clearly. Figure (7-16c) shows the stagnation pressure contours where we can see the development of the upper and lower shocks. The shock below the waverider has a stronger strength near the tip area, and it becomes weaker as it approaches the lower symmetry plane. The shock above the waverider is nearly attached at the tip and weakens as it approaches the upper symmetry plane. In Fig.(7-16d) we can see the two areas delineated by the difference between the upper and lower wall pressures have approximately the same

size. This implies that the lift is almost zero. The situation of zero lift will be seen again in Section 7.6. The compression by the shock in Fig.(7-16e) becomes weaker than its counterpart in Fig.(7-15d), and the compression in Fig.(7-16f) becomes stronger than its counterpart in Figs.(7-15e). In Fig.(7-16g) the azimuthal velocity is shown. The azimuthal velocity component is always negative on the lower surface.

(17). For $M_\infty = 4, \alpha = -12^\circ$

Figures (7-17) show various plots for the waverider flow field at $M_\infty = 4$ and $\alpha = -12^\circ$. Figures (7-17a,b) show somewhat irregular flow patterns for the waverider lower portion near the tip area. In Fig.(7-17c) we can observe that the lower surface pressure is smaller than that of the upper surface. As a result, a negative lift is generated, which will be presented again in Section 7.6. Figure (7-17d) shows the pressure distribution in the shock layer under the body near the symmetry plane; the flow downstream of the bow shock undergoes a gradual compression. Figure (7-17e) shows the pressure in the shock layer above the body near the symmetry plane. Figure (7-17f) shows the azimuthal velocity component which has a somewhat irregular variation.

(18). Comparisons for Flows at $M_\infty = 4, \alpha \neq 0^\circ$

Figures (7-18) show the comparisons of the pressure distributions at various angles of attack $\alpha = -8^\circ, -4^\circ, 0^\circ, +3^\circ, +10^\circ$ with freestream Mach number fixed at $M_\infty = 4$. Figure (7-18a) compares the pressure distribution and shock locations near the lower symmetry plane. It can be seen that as α increases, the shock strength increases and the shock moves toward the body. In this respect the effect of the increasing α is similar to that of the increasing M_∞ as can be seen in Fig.(7-11a). Figure (7-18b) compares the wall pressure distributions. For the negative angles of attack the pressure lines for the lower waverider surface intersect those for the upper waverider surface. The areas of the left hand side of the intersection

denote positive lift, but the areas of the right hand side denote negative lift. This is the reason for the decreasing lift at negative angles of attack. At the positive angles of attack the pressure near the upper symmetry plane becomes higher than that near the tip region, because a weak imbedded shock develops on the upper surface. We can also see the pressure near the lower symmetry plane increases in comparison with the tip region, as α increases. This is because the flow deflection near the symmetry plane due to the high angle of attack is greater than the flow deflection due to the perturbed elliptic cone near the major axis, as α increases.

7.4 Off-Design Flow : $M_\infty \neq 0, \alpha \neq 0^\circ$

In this section the cases of different Mach number and angle of attack from the on-design values are presented and then their comparisons for the pressure distributions are made.

(19). For $M_\infty = 5, \alpha = +4^\circ$

Figures (7-19) show various plots for the waverider flow field at $M_\infty = 5$ and $\alpha = +4^\circ$. Figures (7-19a,b) indicate that the bow shock is slightly detached from the tip. The larger freestream Mach number than the on-design value causes the shock to move inwards. On the other hand, the positive angle of attack causes the shock to move outwards. These two opposite effects work together to result in moving the shock nearer to the tip. In Fig.(7-19a) the freestream flow shows the upward velocity component. Figure (7-19c) shows the wall pressure distribution. As shown in the cases of other positive angle of attack with the fixed Mach number $M_\infty = 4$, we can see a small pressure increase near the upper symmetry plane. Figure (7-19d) shows the pressure distribution and the shock near the lower symmetry plane. Due to the larger M_∞ than the on-design value and the positive angle of attack the shock becomes very strong. The pressure distribution near the upper symmetry plane is

shown in Fig.(7-19e), which shows an expansion from the shock to the body. The azimuthal velocity component near the body surface is shown in Fig.(7-19f).

(20). For $M_\infty = 5, \alpha = -4^\circ$

Figures (7-20) show various plots for the waverider flow field at $M_\infty = 5$ and $\alpha = -4^\circ$. In Figs.(7-20a,b) we can see that the shock is located inside of the tip. Both the larger Mach number and negative angle of attack cause the shock to move inward. The freestream portion shows the downward velocity component. For the region near the top ridge of the waverider we can observe that there is no velocity component in the $y - z$ plane as in the case in Fig.(7-19a). Whereas the vertical flow is directed toward the ridge, the flow parallel to the waverider upper surface is directed outward from the ridge. The cross flow near the leading edge shows a smooth variation. The wall pressure line shown in Fig.(7-20c) intersects itself at the lower right side of the figure. From this we can see that the upper surface pressure near the leading edge is larger than that of its corresponding lower surface with the small pressure gradient. Therefore, the flow near the tip is downward with a smooth variation as seen in Fig.(7-20a,b). If we compare the pressure distribution in the lower symmetry plane in Fig.(7-20d) with that in Fig.(7-2g), it can be seen that there is no big change in the shock strength. That is because the larger Mach number causes an increase of the shock strength, whereas the negative angle of attack causes a decrease. The pressure distribution near the upper symmetry plane is shown in Fig.(7-20e), and the azimuthal velocity around the body surface is shown in Fig.(7-20f).

(21). For $M_\infty = 3, \alpha = +4^\circ$

Figures (7-21) show various plots for the waverider flow field at $M_\infty = 3$ and $\alpha = +4^\circ$. As can be seen in Fig.(7-21a) the disturbance area of the upper flow region extends far away. Both the larger angle of attack and smaller Mach number

than the on-design values cause the disturbance area to move more outwards. At this condition numerical instability can often occur due to the extended disturbance and the irregular flow pattern near the upper tip region as shown in Fig.(7-21b). In Fig.(7-21c) we can see a large pressure gradient near the tip. In the figure we see that the pressure change of the upper surface is significant, but the pressure variation for the lower surface is mild. In Fig.(7-21d) the pressure distribution for the lower symmetry plane is illustrated. For the pressure distribution near the upper symmetry plane, shown in Fig.(7-21e), the flow expansion field is fairly large. From the right upper portion of the figure, we can see that the pressure near the outer boundary seems to be influenced by the boundary which is not taken large enough to embrace the disturbance region. The azimuthal velocity component near the body surface is shown in Fig.(7-21f). A small discontinuity can be detected at $\eta \cong 65$, as happens usually for the cases with $\alpha > 0^\circ$ so far.

(22). For $M_\infty = 3, \alpha = -4^\circ$

Figures (7-22) show various plots for the waverider flow field at $M_\infty = 3$ and $\alpha = -4^\circ$. Figure (7-22a) shows the flow field perpendicular to the x -axis. For the upper part the weakened extended shock and the compression due to the negative angle of attack are combined together. In the figure we can see that the outer boundary near both the lower and upper symmetry planes does not embrace the whole disturbance region. In order to get more desirable solution we need to extend the outer boundary more outwards. In Fig.(7-22b) the magnified flow field for the sharp leading edge area is shown. The flow above the upper waverider surface, which is somewhat parallel to the wall, is directed toward the leading edge. Before reaching the tip the flow is deflected upwards a little bit due to the pressure gradient in the region. Figure (7-22c) shows the wall pressure distribution. We can see the pressure rising near the leading edge for the upper wall. In Figs.(7-22d,e) we see that both

the lower and upper surfaces near the symmetry planes undergo compressions. The compression for the upper surface is due to the negative angle of attack and possibly due to the extended bow shock. The other compression for the lower surface is due to the flow deflection caused by the waverider geometry, as is usual for the cases so far. Figure (7-22f) shows the azimuthal velocity component near the body wall.

(23). Comparisons for Flows at $M_\infty \neq 4, \alpha \neq 0^\circ$

Figures (7-23) show the comparisons of the pressure distributions at the two angles of attack $\alpha = \pm 4^\circ$ and the two freestream Mach numbers $M_\infty = 3, 5$. Figure (7-23a) compares the pressure distributions and the shock locations near the lower symmetry plane. As far as the shock strength and location are concerned, increasing the angle of attack and increasing the Mach number exert similar effects. Thus, at the condition of $M_\infty = 5$ and $\alpha = +4^\circ$ the shock strength is strongest and the shock is located nearest to the waverider body wall. For the case of $M_\infty = 3$ and $\alpha = -4^\circ$ the opposite phenomenon happens. Figure (7-23b) compares the wall pressure distributions. The closed area in the figure by a pressure line is a measure for the lift. We can see that the lift at $M_\infty = 5, \alpha = +4$ is very large but at $M_\infty = 3, \alpha = -4$ it is very small.

7.5 Entropy Distribution

Figures (7-24) show the constant entropy contours for the flows past the Type-*B1* waverider with the two different types of grids. Figure (7-24a) is for the Type-*B1* waverider with a Fan-type grid (denoted by *B1F*) and Fig.(7-24b) for the same waverider with an *O*-type grid (denoted by *B1O*). The comparison of the three plots of Figs.(6-2b) and (7-24a,b) provides us one feature of entropy increase. The entropy for the waverider flow in Fig.(7-24a) with a Fan-type grid is increased in comparison with its corresponding elliptic-cone flow in Fig.(6-2a). This is mainly due to the sharp leading edge which makes the flow change very rapidly. Further

entropy increase can be seen in Fig.(7-24b) which is for the same waverider with an *O*-Type grid. The major difference between Figures (7-24a,b) is the grid structure near the tip. The *O*-Type grid is more skewed than the Fan-Type grid near the tip. The entropy production caused by the skewed grid may be explained in terms of a numerical viscosity. For viscous flow the shock location moves outwards compared with that of the corresponding inviscid flow due to the increased deflection by the momentum displacement. Accordingly this numerical viscosity may cause the shock to move outwards more or less. Recall that for both the Type-*A* and *B* the shocks are located outside of the leading edges as shown in Figs.(7-1d,2d). On the other hand, the entropy production by an *O*-Type grid is concentrated mainly on the small upper region near the tip. Because of this localized high entropy distribution the overall flow is not affected so much in comparison with the Fan-Type case except for the region of high entropy. And its effect on the shock location seems to be very little.

Again from the comparisons of entropy contours in Figs.(6-2b) and (7-24a,b), it can be now seen that the constant entropy lines in Fig.(6-2b) have similar shapes to the lower compression parts in Figs.(7-24a,b). This can be expected from the fact that the waverider is generated from the elliptic-cone flow. As in Figs.(6-2b), in Figs.(7-24a,b) we can observe the vortical layer near the waverider wall where the entropy gradient is large. A large entropy gradient can be also seen near the sharp tip. The large variation of the entropy there would be a source of error and difficulty in the numerical calculation. Above the upper surface we can see the entropy change. This is from the shock stand-off at the leading edge. At the idealized on-design condition the entropy of the upper region should be the freestream value. Recall that any conical stream surface for an elliptic cone in the shock layer is composed of stream lines which originate from the same ray on the shock surface coming out of an elliptic-cone apex. We know each conical stream

surface has a constant entropy. Thus, the waverider surface should be a constant entropy surface at an idealized on-design condition. But we cannot confirm the constant entropy for the waverider surface. The partial reason for this is due to the utilization of the finite-volume method (FVM) with its pertinent boundary-condition imposition. In the FVM the flow data are not defined at the wall and the boundary condition for the pressure is imposed by means of the linear extrapolation from the value at the center points of the first grid cells from the wall. A partially improved result would be obtained by using a finer grid near the waverider surface.

7.6 Aerodynamic Forces

The aerodynamic force coefficients at off-design Mach numbers are shown in Figs.(7-25a,b,c) at zero angle of attack for the Type-*B* waverider. Both C_L and C_D decrease monotonically with increasing M_∞ . The lift-to-drag ratio L/D decreases from 3.52 to 3.27, as M_∞ increases from 3 to 5. For this Mach number range, the variation of aerodynamic forces with respect to freestream Mach number is significant.

Also shown in these figures are the on-design results ($M_\infty = 4$) according to experiment [6], the full-potential equation [3], and the HSDT approximation for the idealized cone-derived waverider (Eq.7-1). At the on-design condition, C_L from the Euler equations is about 3.6% lower than the result for the full-potential equations, and about 9.6% lower than the result from experiment. The on-design value of C_D from the Euler equations is about 13.7% lower than the result for the full potential equations, and about 19.5% lower than the result from experiment. The experimental result, it should be noted, includes a contribution from viscous effects. The L/D ratio according to the Euler calculations are 13.4% greater than for the full-potential equations and 7.3% greater than the experimental result.

The normal-force coefficient in the y -direction C_N and the axial-force coefficient in the x -direction C_A are shown in Figs.(7-25d,e), as a function of α for $M_\infty = 4$. The comparison of C_N in Fig.(7-25d) of numerical and experimental data[6] shows very good agreement, and C_N varies almost linearly. Figure (7-25e) illustrates C_A vs. α . As expected the numerical data are lower than the experimental data, since the C_A of viscous flow has an additional contribution due to the skin friction.

Figures (7-25f,g,h) show aerodynamic quantities C_L , C_D , and L/D for the elliptic-cone waverider Type-*B* as functions of angle of attack α at the design Mach number of 4. It is known[22] that the lift/drag ratio of viscous flow for an idealized cone waverider, for example, which has infinitesimally thin winglets, approaches the value of its corresponding inviscid flow as the cone deflection angle δ increases. The waverider investigated here has $\delta = 18.62^\circ$ for which the difference of lift/drag ratio between inviscid and viscous flows is small, that is, the viscous drag is much smaller than the wave drag. This indicates that the comparison of the numerical inviscid solutions with the experimental viscous results can be justified accordingly.

Figure (7-25f) shows the lift coefficients C_L as a function of angle of attack at the on-design Mach number 4. The agreement of the numerical results obtained by solving the complete Euler equations with experimental data is quite good for the range of α from -12° and 10° . Approximately, C_L increases linearly with α . As α decreases, C_L also decreases and becomes zero at $\alpha \cong -8.5^\circ$. For negative α , the full-potential result is very close to the experimental data, but the accuracy declines as α increases in the positive region. These phenomena can be expected from the theoretical restrictions on the potential theory. As α has larger positive value, the effective flow deflection angle becomes much larger. This causes the flow to be more nonlinear and to increase the rotationality. Accordingly, the homentropic approximation which is assumed in the full potential theory becomes worse, as α increases. On the other hand, negative angles of attack do not increase the effective

flow deflection angle for the range of α used here, considering that at the on-design condition the centerline of the waverider ($\cong \delta/2$) has already positive deflection to the freestream direction and the negative angle of attack is compensated by this deflection more or less. This is the reason why the agreement is good for negative angles of attack.

The drag coefficients C_D are plotted in Fig.(7-25g) with the same conditions as in Fig.(7-25f). The variation resembles a parabolic shape about the α of zero lift value. The numerical values are lower than the experimental data, as expected. For the positive angles of attack, there is considerable discrepancy between the full-potential result and the experimental data, again as for C_L .

The L/D ratios are depicted in Fig.(7-25h). The maximum value of L/D for both the Euler and full-potential calculations occurs at $\alpha \cong -2^\circ$, whereas the maximum value for the experimental results occurs at $\alpha \cong 0^\circ$ (the on-design condition). In principle, the L/D for inviscid flow should be greater than that for viscous flow, since viscosity increases the drag while affecting the lift only a small amount. The Euler results are in accord with this whereas the full-potential results are not, at least for $\alpha > -2^\circ$. Systematic errors in the calculation of C_L and C_D tend to compensate when the ratio is taken to obtain L/D . This is especially true for the calculation of the reference area since it cancels out entirely for the L/D ratio.

So far only the Type-B waverider has been discussed. To anticipate the L/D ratio for another type waverider it would be useful to consider an idealized cone waverider which has infinitesimally thin winglets. The L/D for such a waverider can be obtained from reference[34] as

$$L/D = \frac{\sin \phi_s}{\delta \phi_s} \frac{4\sigma^2/(\sigma + 1)}{1 + \frac{\sigma^2}{\sigma^2 - 1} \ln \sigma^2} \quad (7-1)$$

The Type-A waverider has smaller δ and ϕ_s than Type-B. According to Eq.(7-1) these smaller values provide a larger L/D ratio for Type-A. Actually the on-design

numerical value of L/D for Type-*A* is 6.52, which is much greater than 3.38 for Type-*B* waverider. Those values of L/D due to Eq.(7-1) are slightly less than the above numerical results for elliptic-cone waveriders .

Chapter VIII

CONCLUDING REMARKS

A comprehensive study has been carried out for the numerical calculation of the inviscid hypersonic flow past a class of elliptic-cone derived waveriders. The on-design conditions were $M_\infty = 4$ and $\alpha = 0^\circ$. A variety of off-design conditions ($M_\infty \neq 4$, $\alpha \neq 0^\circ$) was studied, all for zero yaw. Thus all the flows were symmetric about a central vertical plane. Both the body of the waverider and the associated flow fields were conical. An extensive background analysis of the underlying hypersonic small-disturbance theory was given, and comparative results for the on-design flows were presented. The basic flow past the elliptic cone that generates the waveriders was also studied as a means for evaluating the flow past the waveriders themselves.

The numerical results for the waverider flow fields for the on-design conditions compared well with the HSDT and the numerical elliptic-cone flow fields except near the sharp leading edge of the waverider. Here it was found that the bow shock stand off from the leading edge rather than being attached as it should according to the underlying waverider concept. This was found to be true both for an *O*-type grid and a fan-type grid near the leading edge. The approximate formula use to generate the waverider compression surfaces for the *A1* and *B1* models was the same as was used in previous investigations to study the same waverider shape. This approximate formula produces a leading-edge tip angle that is considerably larger than it should be to reproduce the proper elliptic-cone flow field. When a better approximate formula is used to determine the waverider compression surfaces,

giving models *A2* and *B2*, the correct tip angle is obtained. For model *A2*, the CFD results show that the shock becomes attached at the leading edge, as it should be. For model *B2*, the shock does not become attached, but the stand-off distance is less. For models *B1* and *B2*, the conical shock angle at the tip is about 25° . When the angles become this large, the small-angle approximations associated with HSDT becomes less accurate. This explains in part some of the remaining differences between the HSDT and CFD results. Overall, the agreement of the CFD results with what was expected at the on-design conditions was deemed to be good.

The great importance for the CFD calculations is associated with the off-design results. At $\alpha = 0^\circ$ and for $M_\infty > 4$, the bow shock fits more tightly under the waverider body. Near the leading-edge of the waverider, a lambda-type shock configuration appears to develop. This becomes more pronounced as M_∞ increases, the largest value being $M_\infty = 10$ in this study. This is a new effect that was not known from previous experimental studies. The lambda-shock configuration occurs for other off-design conditions also as part of the adjustment of the main conical bow shock to the local leading-edge conditions.

For $M_\infty < 4$ and $\alpha = 0^\circ$, the bow shock stands off from the body, the more so as M_∞ decreases. There is then a flow in the gap between the shock and the leading edge as the flow adjusts to the higher pressure under the body to the lower pressure on top.

When the angle of attack is positive, $\alpha > 0^\circ$, the shock tends to fit tighter to the lower compression surface, and there is an expansion region over the upper surface. A very weak shock develops on the upper surface. This is needed to deflect the flow that has expanded over the leading edge back parallel to the vertical symmetry plane. For negative angles of attack, the shock below the body weakens and a bow shock develops over the upper surface of the body.

The forces on the waveriders could be calculated from the pressure distributions on the surfaces. Of course, the viscous contributions could not be calculated from the Euler-code results. The results were thus not directly comparable with those of experiments, but the trends in variation with angle of attack were very similar. The orientation for zero-lift agreed with experiment, and the interpretation in terms of the flow-field properties is a unique capability of the CFD analysis.

For the conical waverider under investigation the Lawrence Code was found to be an effective means of producing the numerical results. Care must be taken to produce an effective grid structure especially near the sharp leading edges. Unlike some other researches for supersonic flows with a sharp leading edge, which appeared recently, we adopted steady equations instead of unsteady equations for the computation. This can save the computer storage and CPU time evidently. Due to this saving we could solve waverider flows for a wide range of off-design conditions.

There is a substantial amount of research that remains for the future. It would be useful to calculate the effects of yaw, or sideslip. More important would be the calculation of viscous and heat-transfer effects. Attempts associated with the present investigation were not successful. In addition, it would also be desirable to incorporate real-gas effects. There are other classes of waverider shapes that are also of interest. Comprehensive studies relating to their on-design and off-design flow fields would be very desirable.

REFERENCES

- [1] D. Küchemann, The Aerodynamic Design of Aircraft, Pergamon, 1978.
- [2] K. M. Jones, N. A. Talcott Jr., and V. Shankar, "Application of a Full Potential Method for Computation of Three-Dimensional Supersonic Flows," AIAA Paper 84-0139, 22nd Aerospace Sciences Meeting, Jan. 9-12, 1984/Reno, Nevada.
- [3] K. M. Jones, "Application of a Full Potential Method for Predicting Supersonic Flowfields and Aerodynamic Characteristics," J. of Spacecraft and Rockets, Vol.23, No.1, Jan.-Feb., pp.63-69, 1986.
- [4] K. M. Jones, "Application of a Supersonic Full Potential Method for Analysis of Waverider Configurations," NASA Technical Paper 2608, September 1986.
- [5] M. L. Rasmussen, "Waverider Configurations Derived from Inclined Circular and Elliptic Cones," J. of Spacecraft and Rockets, Vol.17, No.6, Nov.-Dec., pp.537-545, 1980.
- [6] M. L. Rasmussen, M. C. Jischke, and D. C. Daniel, "Experimental Forces and Moments on Cone-Derived Waveriders for $M_\infty = 3$ to 5," J. of Spacecraft and Rockets, Vol.19, No.6, Nov.-Dec., pp.592-598, 1982.
- [7] M. C. Jischke, M. L. Rasmussen, and D. C. Daniel, "Experimental Surface Pressures on Cone-Derived Waveriders for $M_\infty = 3 - 5$," J. of Spacecraft and Rockets, Vol.20, No.6, Nov.-Dec., pp.539-545, 1983.
- [8] L. N. Long, "Off-Design Performance of Hypersonic Waveriders," J. of Aircraft, Vol.27, No.7, July, 1990.

- [9] K. D. Jones and F. C. Dougherty, "Computational Simulation of Flows about Hypersonic Geometries with Sharp Leading Edges," AIAA Paper 90-3065-CP, 8th Applied Aerodynamics Conference, Aug. 20-22, 1990/Portland, Oregon.
- [10] J. R. Liao, K. M. Isaac, and J. B. Miles, "Navier-Stokes Simulation of Waverider Flowfields," AIAA Paper 90-3066-CP, 8th Applied Aerodynamics Conference, Aug. 20-22, 1990/Portland, Oregon.
- [11] D. A. Anderson, J. C. Tannehill, and R. H. Pletcher,
Computational Fluid Mechanics and Heat Transfer, McGraw-Hill, 1984.
- [12] R. L. Sorenson, "A Computer Program to Generate Two-Dimensional Grids About Airfoils and Other Shapes by the Use of Poisson's Equation," NASA TM-81198, May 1980.
- [13] D. A. Anderson, "Equidistribution Schemes, Poisson Generators, and Adaptive Grids," Applied Mathematics and Computation, Vol.24, pp.211-227, 1987
- [14] P. L. Roe, "Approximate Riemann Solvers, Parameter Vectors, and Difference Schemes," J. of Computational Physics, Vol.43, pp.357-372, 1981.
- [15] B. van Leer, "Flux-Vector Splitting for the Euler Equations,"
Lecture Notes in Physics, Vol.170, pp.507-512, 1982.
- [16] S. L. Lawrence, J. C. Tannehill, and D. S. Chaussee, "An Upwind Algorithm for the Parabolized Navier-Stokes Equations," AIAA Paper 86-1117, May 1986.
- [17] H. C. Yee and A. Harten, "Implicit TVD Schemes for Hyperbolic Conservation Laws in Curvilinear Coordinates," AIAA J., Vol.25, No.2, pp.266-274, 1987.
- [18] A. Harten, "High Resolution Schemes for Hyperbolic Conservation Laws,"
J. of Computational Physics, Vol.49, pp.357-393, 1983.
- [19] S. R. Chakravarthy and S. Osher, "A New Class of High Accuracy TVD Schemes for Hyperbolic Conservation Laws," AIAA Paper 85-0363, Jan. 1985.

- [20] S. R. Chakravarthy, K-Y. Szema, U. C. Goldberg, and J. J. Gorski, and S. Osher, "Application of a New Class of High Accuracy TVD Schemes to the Navier-Stokes Equations," AIAA Paper 85-0165, Jan. 1985.
- [21] M. L. Rasmussen, "Aerodynamics of Cone-Derived Waveriders and Related Lifting Bodies," Air Force Armament Laboratory Report AFATL-TR-84-70, Eglin AFB, Florida.
- [22] M. L. Rasmussen, A Course in Hypersonic Flow, Textbook in preparation for John Wiley & Sons.
- [23] M. L. Rasmussen and H. M. Lee, "Approximation for Hypersonic Flow Past a Slender Elliptic Cone," AIAA Paper 79-0364, 17th Aerospace Sciences Meeting, Jan. 15-17, 1979/New Orleans, La.
- [24] A. Ferri, "Supersonic Flow around Circular Cones at Angles of Attack," NACA Report 1045, Langley Aeronautical Laboratory, 1951.
- [25] A. G. Munson, "The Vortical Layer on an Inclined Cone," J. Fluid Mech. Vol.20, Part 4, pp.625-643, 1964.
- [26] M. L. Rasmussen, "Experiments on a Slender Waverider Configuration with and without an Inlet," Air Force Armament Laboratory Report AFATL-TR-86-07, Eglin AFB, FL, 1986.
- [27] V. Shankar, "Conservative Full Potential, Implicit Marching Scheme for Supersonic Flows," AIAA J., Vol.20, No.11, pp.1508-1514, Nov., 1982.
- [28] S. L. Lawrence, Application of an Upwind Algorithm to the Parabolized Navier-Stokes Equations, Ph.D. Dissertation, Iowa State University, 1987.
- [29] J. F. Thompson, L. E. Lijewski, and B. Gatlin, "Efficient Application Techniques of the EAGLE Grid Code to Complex Missile Configurations," AIAA Paper 89-0361, 27th Aerospace Sciences Meeting Jan. 9-12, 1989/Reno, Nevada.

- [30] J. F. Thompson, F. C. Thames, and C. W. Mastin, "Boundary-Fitted Curvilinear Coordinate Systems for Solution of Partial Differential Equations on Fields Containing Any Number of Arbitrary Two-Dimensional Bodies," NASA CR-2729 July 1977.
- [31] P. D. Thomas and J. F. Middlecoff, "Direct Control of the Grid Point Distribution in Meshes Generated by Elliptic Equations," AIAA J., Vol.18, No.6, pp.652-656, June, 1980.
- [32] M. Vinokur, "An Analysis of Finite-Difference and Finite-Volume Formulations of Conservation Laws," NASA CR 177416, June 1986.
- [33] J. L. Sims, Tables for Supersonic Flow around Right Circular Cones at Zero Angle of Attack, NAS 1.21 NASA SP-3004, 1964.
- [34] B. S. Kim, M. L. Rasmussen, M. C. Jischke, "Optimization of Waverider Configurations Generated from Axisymmetric Conical Flows," J. of Spacecraft and Rockets, Vol.20, No.5, pp.461-469, Sept.-Oct., 1983.
- [35] R. T. Doty and M. L. Rasmussen, "Approximation for Hypersonic Flow Past an Inclined Cone," AIAA J., Vol.11, No.9, pp.1310-1315, Sept. 1973.
- [36] L. Pottsepp, "Inviscid Hypersonic Flow over Unyawed Circular Cones," J. of the Aero/Space Sciences, pp.558-559, July, 1960.
- [37] M. L. Rasmussen, "On Hypersonic Flow Past an Unyawed Cone," AIAA J., Vol.5, No.8, pp.1495-1497, August, 1967.
- [38] C. G. Chernyi, Introduction to Hypersonic Flow, Academic press, 1961.
- [39] R. M. Beam and R. F. Warming, "An Implicit Finite-Difference Algorithm for Hypersonic System in Conservation-Law Form," J. of Computational Physics, Vol.22, pp.87-110, 1976.

- [40] P. G. Buning and J. L. Steger, "Solution of the Two-Dimensional Euler Equations with Generalized Coordinate Transformation Using Flux Vector Splitting," AIAA Paper 82-097, AIAA/ASME 3rd Joint Conference, June 7-11, St. Louis, Missouri, 1982.
- [41] P. G. Buning, "Computaton of Inviscid Transonic Flow Using Flux Vector Splitting in Generalized Coordinates," Ph.D. Dissertation, Stanford University, Oct. 1983.
- [42] Y. C. Vigneron, J. V. Rakich, and J. C. Tannehill, "Calculation of Supersonic Viscous Flow over Delta Wings with Sharp Subsonic Leading Edges," AIAA Paper 78-1137, 11th Fluid and Plasma Dynamics Conference, Seattle, Wash. /July 10-12, 1978.
- [43] J. L. Steger and R. F. Warming, "Flux Vector Splitting of the Inviscid Gas-dynamics Equations with Application to Finite-Difference Method," J. of Computational Physics, Vol.40, pp.263-293, 1981.
- [44] P. Colella and P. R. Woodward, "The Piecewise Parabolic Method (PPM) for Gas-Dynamical Simulations," J. of Computational Physics, Vol.54, pp.174-201, 1984.
- [45] C. A. J. Fletcher, Computational Techniques for Fluid Dynamics, Vol.I & II, Springer-Verlag, 1988.
- [46] W. H. Press, B. P. Flannery, S. A. Teukolsky, and W. T. Vetterling, Numerical Recipes, Cambridge University Press, 1987.
- [47] R. F. Warming, R. M. Beam, and B. J. Hyett, "Diagonalization and Simultaneous Symmetrization of the Gas-Dynamic Matrices," Mathematics of Computation, Vol.29, No.132, Oct. 1975. pp.1037-1045.

Appendix A

APPROXIMATE ANALYTICAL SOLUTIONS

The waverider investigated in this study is derived based on the inviscid flow field over an elliptic cone. To check the validity of the numerical results of the flow over the waverider, it may be necessary to calculate approximate analytical solutions to the inviscid flow around an elliptic cone. The elliptic cone can be considered as a perturbed circular cone. Rasmussen et al.[21,22,35] obtained approximate solutions to the flows around circular and elliptic cones with a small angle of attack by means of perturbation theory. They are expressed by linear combination of the small perturbed terms of the eccentricity and angle of attack in the framework of the Hypersonic Small Disturbance Theory (HSDT). Since the purpose of this introduction of the approximate solution is to check the validity of the numerical solutions as mentioned before, presented are only the elliptic cone solutions without incidence that are corresponding to the flow at the on-design condition of an elliptic cone waverider. It will be also useful for understanding the physics of the waverider flow to study analytical solutions of an elliptic cone flow.

The first section of this chapter presents the assumed solutions by outer expansion forms. Then unperturbed and perturbed solutions are sought separately and they are combined to get the desired analytical approximate solutions. From the consideration of streamlines the lower compression part of the waverider configuration is determined.

A.1 Perturbation Series Expansions

For slightly perturbed elliptic cone without incidence, the solutions can be approximated by outer expansions as

$$\begin{aligned}
 u(\theta, \phi) &= u_0(\theta_0) + \epsilon_2 u_2(\theta_0) \cos 2\phi + O(\epsilon_2^2), \\
 v(\theta, \phi) &= v_0(\theta_0) + \epsilon_2 v_2(\theta_0) \cos 2\phi + O(\epsilon_2^2), \\
 w(\theta, \phi) &= \epsilon_2 w_2(\theta_0) \sin 2\phi + O(\epsilon_2^2), \\
 p(\theta, \phi) &= p_0(\theta_0) [1 + \epsilon_2 P_2(\theta_0) \cos 2\phi] + O(\epsilon_2^2), \\
 \rho(\theta, \phi) &= \rho_0(\theta_0) [1 + \epsilon_2 R_2(\theta_0) \cos 2\phi] + O(\epsilon_2^2), \\
 s(\theta, \phi) &= s_0 + c_v \epsilon_2 S_2(\theta_0) \cos 2\phi + O(\epsilon_2^2),
 \end{aligned} \tag{A-1a, b, c, d, e, f}$$

where the subscript $_0$ denotes an unperturbed basic cone quantity and the subscript $_2$ denotes a perturbed quantity. The independent variable θ_0 is defined in terms of θ and ϕ in a later section. Here P_2 , R_2 , and S_2 are dimensionless but all the rest flow variables are dimensional.

A.2 Unperturbed Basic Circular Cone Solution

The gas dynamics equation of inviscid axisymmetric cone flow is called Taylor-Maccoll equation which can be written as

$$\left(1 - \frac{v_0^2}{a^2}\right) \frac{d^2 u_0}{d\theta^2} + \cot \theta \frac{du_0}{d\theta} + \left(2 - \frac{v_0^2}{a^2}\right) u_0 = 0. \tag{A-2}$$

The Eq.(A-2) is a highly nonlinear ODE of second order, since both v_0^2 and a^2 are functions of u_0 . The irrotational condition which is obtained from the r -momentum equation is given by $v_0 = du_0/d\theta$, and the homenergetic condition determines the $a - u_0$ relation, that is

$$a^2 = (\gamma - 1) \left[h_t - \frac{1}{2}(u_0^2 + v_0^2) \right]. \tag{A-3}$$

This flow is homentropic for the region between the shock and the cone wall, since the entropy jump at the points on the shock is the same.

Pottsepp[36] made an approximate relation to Eq.(A-2) which results in a linear equation without v_0^2/a^2 terms. Rasmussen[37] also obtained approximate solutions by means of the HSDT. This theory is to assume the limit that $\delta \rightarrow 0, M_\infty \rightarrow \infty$, while $K_\delta \equiv M_\infty \sin \delta$ is held constant. The brief procedure will be introduced in the following. First we can see that $\cos \theta$ is a solution to the linearized equation. This suggests an idea about the Taylor-Maccoll's solution in the form of $U(\theta) \cos \theta$ where $U(\theta)$ is an unknown function of θ . After substitution of the assumed solution and neglecting the higher order terms than θ^2 , the desired solutions are obtained as

$$\begin{aligned} \frac{u_0(\theta)}{V_\infty} &= 1 - \frac{\theta^2}{2} - \frac{1-\epsilon}{2} \beta^2 \ln\left(\frac{\beta^2}{\theta^2}\right), \\ \frac{v_0(\theta)}{V_\infty} &= -\theta[1 - (1-\epsilon)\frac{\beta^2}{\theta^2}], \end{aligned} \quad (A-4a, b)$$

where $\epsilon \equiv \rho_\infty/\rho(\beta)$ is the density ratio across the shock. The gas dynamics equation is the second order, but there are three boundary conditions; two at the shock and one at the wall. The second order differential equation needs the first two conditions. The third one is from the impermeable condition at the wall. This is necessary for the determination of shock location which is another unknown variable. If we apply the last restriction to the v -equation, it gives

$$\frac{\beta}{\delta} = \frac{1}{\sqrt{1-\epsilon}}, \quad (A-5)$$

where

$$\epsilon = \frac{(\gamma-1)K_\beta^2 + 2}{(\gamma+1)K_\beta^2} = \frac{(\gamma-1)K_\delta^2 + 2}{(\gamma+1)K_\delta^2}, \quad K_\beta \equiv M_\infty \beta, \quad K_\delta \equiv M_\infty \delta. \quad (A-6, b, c)$$

After combining the above three relations, the hypersonic similarity shock formula can be obtained as

$$\sigma \equiv \frac{\beta}{\delta} = \sqrt{\frac{\gamma+1}{2} + \frac{1}{K_\delta^2}}. \quad (A-7)$$

Eq.(A-2) was derived by Chernyi[38] and also by Rasmussen by means of the HSDT. This represents a very good agreement with the exact formula especially in the hypersonic limit. The velocity components u_0, v_0 can be obtained as

$$\begin{aligned}\frac{u_0(\theta)}{V_\infty} &= 1 - \frac{\delta^2}{2} \left[\frac{\theta^2}{\delta^2} + \ln\left(\frac{\beta^2}{\theta^2}\right) \right], \\ \frac{v_0(\theta)}{V_\infty} &= -\theta \left(1 - \frac{\delta^2}{\theta^2} \right).\end{aligned}\tag{A-8a, b}$$

For temperature, we use the homenergetic relation like

$$\frac{T_0(\theta)}{T_\infty} = \frac{h(\theta)}{h_\infty} = 1 + \frac{\gamma-1}{2} M_\infty^2 \left(1 - \frac{V^2(\theta)}{V_\infty^2} \right).\tag{A-9}$$

With the aid of Eq.(A-3) the Eq.(A-9) becomes

$$\frac{T_0(\theta)}{T_\infty} = 1 + \frac{\gamma-1}{2} K_\delta^2 \left[2 - \frac{\delta^2}{\theta^2} + \ln\left(\frac{\beta^2}{\theta^2}\right) \right].\tag{A-10}$$

For pressure, homentropic condition can be used to relate the pressure to enthalpy which is a linear function of temperature. That is

$$\frac{p_0(\theta)}{p_\infty} = \frac{p_0(\beta)}{p_\infty} + \frac{\gamma}{\gamma-1} \frac{1}{\epsilon} \left[\frac{T_0(\theta)}{T_\infty} - \frac{T_0(\beta)}{T_\infty} \right].\tag{A-11}$$

The first term on the right hand side can be obtained through the oblique shock relation and the temperature ratio is given by Eq.(A-10). Thus, we can have

$$\frac{p_0(\theta)}{p_\infty} = 1 + \frac{\gamma}{2} K_\delta^2 \left\{ 1 + \frac{1}{\epsilon} \left[1 - \frac{\delta^2}{\theta^2} + \ln\left(\frac{\beta^2}{\theta^2}\right) \right] \right\}.\tag{A-12}$$

A.3 Perturbed Solutions

The approximate solutions for slightly perturbed cone flows by Rasmussen[22] deal with the inclined circular, elliptic, ternary, and quartic cones parametrically. A perturbed body can be obtained by identifying a single term out of a Fourier-series expansion terms. Here we consider an elliptic cone flows without angle of attack. It is well known that the curved shock is a source of rotationality. The elliptic

cone has a nonuniform transverse shock curvature and thus the flow is no longer irrotational even in the inviscid region unlike the axisymmetric cone flow. The analytical solutions about slightly perturbed body can play an important role in the studying the physics of the waverider flow where we don't know exact solutions.

Ellitic Cone Body and Shock Shape

A conical body can be expressed by $F(\theta, \phi) = 0$ as well as its corresponding bow shock in spherical coordinate system. For a specific body geometry there must be a constraint between θ and ϕ such as $\theta = \theta_c(\phi)$. A conical body may be expressed by

$$F = \theta - \theta_c(\phi). \quad (A - 13)$$

An elliptic cone cross section is given by

$$\theta_c(\phi) = \delta[1 - \epsilon_2 \cos 2\phi + O(\epsilon_2^2)], \quad (A - 14)$$

where $|\epsilon_2| \ll 1$. In the same line with the body shape, the shock shape may be assumed to have the form $\theta = \theta_s(\phi)$

$$\theta_s(\phi) = \delta[\sigma - \epsilon_2 g_2 \cos 2\phi + O(\epsilon_2^2)], \quad (A - 15)$$

where g_2 is a shock eccentricity factor which must be determined as a part of solutions.

Boundary Conditions for Body and Shock

The wall boundary has only tangential velocity with its normal component vanishing

$$\vec{V} \cdot \hat{n} = 0, \quad (A-16)$$

where \hat{n} is an outward unit normal vector. The shock jump conditions can be imposed by identifying \hat{n} at the shock surface. That is,

$$\hat{n}_s = \hat{e}_\theta - \epsilon_2 \frac{2\delta g_2}{\sin \beta} \sin 2\phi \hat{e}_\phi + O(\epsilon_2^2). \quad (A-17)$$

The mass conservation and tangential momentum conservation become the two shock boundary conditions.

$$\vec{V}_s \cdot \hat{n}_s = \frac{\rho_\infty}{\rho_s} (\vec{V}_\infty \cdot \hat{n}_s), \quad (A-18)$$

$$\vec{V}_s \times \hat{n}_s = \vec{V}_\infty \times \hat{n}_s. \quad (A-19)$$

Stretched Independent Variable

Considering that θ is smaller than δ for some ϕ a stretched independent variable θ_0 is defined by

$$\eta_0 \equiv \frac{\theta_0 - \delta}{\beta - \delta} \equiv \frac{z - 1}{\sigma - 1} \equiv \frac{\theta - \theta_c(\phi)}{\theta_s(\phi) - \theta_c(\phi)}, \quad (A-20)$$

where $z \equiv \theta_0/\delta$. The three independent variables have the ranges of

$$\delta \leq \theta_0 \leq \beta, \quad 1 \leq z \leq \sigma, \quad 0 \leq \eta_0 \leq 1. \quad (A-21a, b, c)$$

On the basis of these independent variables, the following dependent variables are introduced as

$$U(\theta_0) = U^*(z) = U^{**}(\eta_0). \quad (A-22)$$

Solution

After some algebra and approximation based on the HSDT, the mass conservation equation can be expressed as

$$\dot{\theta}_0^2 U''(\theta_0) + \theta_0 U'(\theta_0) - 4U(\theta_0) = -2H_2(\theta_0), \quad (A - 23a)$$

where

$$H_2(\theta_0) \equiv -\frac{2S_2(\beta)}{\gamma(\gamma-1)} \frac{a_0^2(\delta)}{V_\infty} \left[1 - \sqrt{\frac{\theta_0^2 - \delta}{\beta^2 - \delta^2}} \right]. \quad (A - 23b)$$

Note that the differential equation is equidimensional and thus the homogeneous solution can be obtained. The particular solution can also be obtained by means of the method of variation of parameters. The solution in terms of z can be obtained as

$$U^*(z) = U_H^*(z) + U_P^*(z), \quad (A - 24)$$

where its homogeneous and particular solutions are given by

$$\frac{U_H^*(z)}{\delta^2 V_\infty} = \frac{g_2}{2\sigma} \left[\left(\frac{z}{\sigma} \right)^2 + \left(\frac{\sigma}{z} \right)^2 \right] - \frac{\sigma g_2}{\gamma + 1} \left[\left(\frac{z}{\sigma} \right)^2 - \left(\frac{\sigma}{z} \right)^2 \right], \quad (A - 25)$$

and

$$\begin{aligned} \frac{U_P^*(z)}{\delta^2 V_\infty} = \frac{J g_2}{2\sigma^3} \left\{ 2 - \frac{\sigma^2}{z^2} - \sqrt{\frac{z^2 - 1}{\sigma^2 - 1}} + \frac{2}{3} \frac{\sigma^2 - 1}{z^2} \left[1 - \left(\frac{z^2 - 1}{\sigma^2 - 1} \right)^{3/2} \right] \right. \\ \left. + \frac{z^2 (\cos^{-1} \frac{1}{z} - \cos^{-1} \frac{1}{\sigma})}{\sqrt{\sigma^2 - 1}} \right\}, \end{aligned} \quad (A - 26)$$

where

$$J \equiv \frac{a_0^2(\delta)}{a_0^2(\beta)} = \frac{1 + \frac{\gamma-1}{2} K_\delta^2 (1 + \ln \sigma^2)}{1 + \frac{\gamma-1}{2} K_\delta^2 (2 - 1/\sigma^2)}. \quad (A - 27)$$

The eccentricity factor g_2 will be determined at the end of this subsection. Thus the perturbed solutions can be obtained as

$$\begin{aligned} u_2(\theta_0) &= U(\theta_0) + v_0(\theta_0) \Theta_2(\theta_0), \\ v_2(\theta_0) &= U'(\theta_0) + v_0'(\theta_0) \Theta_2(\theta_0), \\ w_2(\theta_0) &= \frac{1}{\sin \theta_0} [2v_0(\theta_0) \Theta_2(\theta_0) + H_2(\theta_0) - 2u_2(\theta_0)], \\ P_2(\theta_0) &= -\gamma [u_0(\theta_0) u_2(\theta_0) + v_0(\theta_0) v_2(\theta_0)] / a_0^2 - S_2(\beta) / (\gamma - 1), \\ R_2(\theta_0) &= -[u_0(\theta_0) u_2(\theta_0) + v_0(\theta_0) v_2(\theta_0)] / a_0^2 - S_2(\beta) / (\gamma - 1), \end{aligned} \quad (A - 28a, b, c, d, e)$$

where

$$\Theta_2(\theta_0) \equiv \frac{(\theta_0 - \delta)(1 - g_2)}{\sigma - 1} - \delta, \quad S_2(\beta) \equiv -\frac{\gamma(\gamma - 1)K_\delta^2}{a_0^2(\beta)/a_\infty^2} \frac{g_2}{\sigma^3}, \quad a_0^2 \equiv \gamma \frac{p_0}{\rho_0}. \quad (A - 29a, b, c)$$

From the boundary condition, we have

$$v_2(\delta) = 0. \quad (A - 30)$$

If Eq.(A-30) is combined with v_1 equation in Eq.(A-28), then g can be obtained as

$$\frac{1}{g_2} = \frac{\sigma^4 - 1}{2\sigma^3} + \frac{\sigma^4 + 1}{\sigma(\gamma + 1)} + \frac{J}{6\sigma^3} \left[\frac{3 \cos^{-1} \frac{1}{\sigma}}{\sqrt{\sigma^2 - 1}} - \sigma^2 - 2 \right]. \quad (A - 31)$$

A.4 Streamline and Waverider Configuration

The compression undersurface of the waverider is obtained from the differential equation for streamlines expressed by

$$\vec{V} \times d\vec{r} = 0. \quad (A - 32)$$

The streamline equation to the first order becomes

$$\frac{dr}{u_0(\theta_0)} = \frac{r d\theta_0}{v_0(\theta_0)} = \frac{r \theta_0 d\phi}{\epsilon_2 w_2(\theta_0) \sin 2\phi}. \quad (A - 33)$$

Within the framework of the HSDT with the assumption, $\theta_0 \rightarrow \delta$, the right side equation can be integrated to obtain

$$\frac{\theta_0 - \delta}{\beta - \delta} = \left(\frac{\tan \phi}{\tan \phi_s} \right)^{1/e}, \quad (A - 34)$$

where

$$e \equiv -\epsilon_2 \frac{w_2(\delta)}{\delta V_\infty}, \quad \frac{w_2(\delta)}{\delta V_\infty} = \frac{2Jg_2}{\sigma^3} - \frac{2U(\delta)}{\delta^2 V_\infty}. \quad (A - 35a, b)$$

In the physical variable, Eq.(A-35) become

$$\left(\frac{\theta}{\delta} \right) = \left[\frac{\theta_c(\phi)}{\delta} \right] + \left\{ \left[\frac{\theta_s(\phi)}{\delta} \right] - \left[\frac{\theta_c(\phi)}{\delta} \right] \right\} \left(\frac{\tan \phi}{\tan \phi_s} \right)^{1/e}. \quad (A - 36)$$

This is another relation describing the compression undersurface of a waverider which has a slightly different form from the Eq.(2-13).

A.5 Approximate Solution for Shock Layer

To get the outer solutions of the flow for the compression lower portion of the waverider we need to combine Eqs.(A-1), (A-8), (A-10), and (A-12) with Eq.(A-28). If we use the constraint on θ and ϕ , Eq.(A-36), the flow variables on the lower waverider wall can be obtained. It should be noted that all the approximate analytic solutions are not valid across the entire flow field. Nonetheless, the pressure and azimuthal velocity component are valid uniformly including the vortical layer which exists very near the elliptic-cone body surface.

Appendix B

NUMERICAL ALGORITHM

The first section introduces a numerical algorithm along with discretization, linearization, and operator splitting procedure. The following two sections provide the elements of the algorithm; flux Jacobian matrices with the first order expression for flux and flux differences with the second order expression for flux. Finally, the construction of a block tridiagonal matrix is explained.

B.1 Algorithm

To numerically integrate the PNS equations we need to express them in discretized forms. In this study Lawrence's algorithm[28] based on Chakravarthy's [19,20] TVD[17,18] scheme is adapted.

Finite Difference and Finite Volume Methods

The discretization is accomplished in the frame work of Finite Volume Method (FVM) [32]. This utilizes the conservation equations in the integral form and replaces the surface integrals with the sum of the flux multiplied by its corresponding surface element of a finite volume. There is another discretizing method; Finite Difference Method (FDM)[39] which has been widely used. Both of them are in the category of local methods. The main differences lie in the treatment of boundary conditions and the definition of metrics. The first control points of FDM are located on the boundary, while those of FVM are off the boundary and thus better to handle irregular boundary problems than the former. Considering the waverider

geometry has sharp corners, the FVM would be more appropriate than the FDM for the study of waveriders. The FVM defines metrics at cell interfaces and the conservative variables at primary grid points, but the FDM does not separate them and use the same points for both metrics and flow variables.

Discretized Equation in Finite Volume Framework

Considering that the concept of the physical conservation laws which govern the gas dynamics is based on a finite region, let's express governing equations in an integral form for a finite volume V enclosed by a surface S .

$$\int_V \frac{\partial \bar{U}}{\partial t} dV + \oint_S \bar{\mathbf{H}} \cdot \hat{n} dS = \int_V \bar{P} dV, \quad (B-1)$$

where \bar{U} is a conservative variable column matrix and \bar{P} is the rate of production of \bar{U} . For a steady flow without any source term, it becomes

$$\oint_S \bar{\mathbf{H}} \cdot \hat{n} dS = 0, \quad (B-2)$$

where the dyadic $\bar{\mathbf{H}}$ is defined as

$$\bar{\mathbf{H}} \equiv \bar{E}\hat{i} + \bar{F}\hat{j} + \bar{G}\hat{k}, \quad (B-3)$$

and \hat{n} = outward unit normal vector. Here it is noticeable that for a freestream where the fluxes are constant, the integral equation agrees with the geometric conservation, that is,

$$\oint_S \hat{n} dS = \oint_S d\vec{S} = 0. \quad (B-4)$$

This means that the integral form of the governing equations satisfies the freestream conservation automatically. However, that is not the case for some earlier upwind algorithms like that of Buning et al.[40] and Buning[41], and thus various efforts have been exerted to remove this drawback. The discretized form of the integral

equation for a finite volume which is bounded by six surfaces as in Fig.(5-8) is given by

$$\sum_{\alpha=1}^6 \vec{H} \cdot \Delta \vec{S}_\alpha = 0, \quad (B-5)$$

where

$$\begin{aligned} \Delta \vec{S}_1 &\equiv \Delta \vec{S}_{k,l}^{n+1}, & \Delta \vec{S}_2 &\equiv \Delta \vec{S}_{k+\frac{1}{2},l}^{n+\frac{1}{2}}, & \Delta \vec{S}_3 &\equiv \Delta \vec{S}_{k,l+\frac{1}{2}}^{n+\frac{1}{2}}, \\ \Delta \vec{S}_4 &\equiv \Delta \vec{S}_{k,l}^n, & \Delta \vec{S}_5 &\equiv \Delta \vec{S}_{k-\frac{1}{2},l}^{n+\frac{1}{2}}, & \Delta \vec{S}_6 &\equiv \Delta \vec{S}_{k,l-\frac{1}{2}}^{n+\frac{1}{2}}, \end{aligned} \quad (B-6a, b, c, d, e, f)$$

and

$$\Delta \vec{S}_\alpha \equiv l_\alpha \hat{i} + m_\alpha \hat{j} + n_\alpha \hat{k}, \quad \alpha = 1, 2, \dots, 6. \quad (B-7)$$

Note that the subscripts k and l denote primary grids according to Vinokur's terminology[32]. Two kinds of grid points such as primary and secondary grids are shown in Fig.(5-8). The Eq.(B-5) can be now expressed as

$$\left\{ \tilde{E}^{n+1} - \tilde{E}^n \right\}_{k,l} + \left\{ \tilde{F}_{k+\frac{1}{2}} - \tilde{F}_{k-\frac{1}{2}} \right\}_l^{n+\frac{1}{2}} + \left\{ \tilde{G}_{l+\frac{1}{2}} - \tilde{G}_{l-\frac{1}{2}} \right\}_k^{n+\frac{1}{2}} = 0, \quad (B-8)$$

with the definition of each element

$$\begin{aligned} \tilde{E}_{k,l}^{n+1} &\equiv \vec{H} \cdot \Delta \vec{S}_1, & \tilde{F}_{k+\frac{1}{2},l}^{n+\frac{1}{2}} &\equiv \vec{H} \cdot \Delta \vec{S}_2, & \tilde{G}_{k,l+\frac{1}{2}}^{n+\frac{1}{2}} &\equiv \vec{H} \cdot \Delta \vec{S}_3, \\ \tilde{E}_{k,l}^n &\equiv -\vec{H} \cdot \Delta \vec{S}_4, & \tilde{F}_{k-\frac{1}{2},l}^{n+\frac{1}{2}} &\equiv -\vec{H} \cdot \Delta \vec{S}_5, & \tilde{G}_{k,l-\frac{1}{2}}^{n+\frac{1}{2}} &\equiv -\vec{H} \cdot \Delta \vec{S}_6, \end{aligned} \quad (B-9a, b, c, d, e, f)$$

and

$$\vec{H} \cdot \Delta \vec{S}_\alpha = l_\alpha \bar{E} + m_\alpha \bar{F} + n_\alpha \bar{G}, \quad \alpha = 1, 2, \dots, 6. \quad (B-10)$$

Eq.(B-8) is a discrete form of Eq.(3-5) for steady flow. At this stage, the above expression discretized based on a finite volume frame work is the same as that for the finite difference approach. One important difference lies in that l_α, m_α , and n_α are calculated at cell interfaces instead of primary grid points. In chapter V it will be explained that $\Delta \vec{S}_\alpha$ are related to the metrics. As in the previous chapter we can

obtain a discretized expression for the PNS equations by dropping the streamwise viscous derivative terms as

$$\left\{ \hat{E}^{n+1} - \hat{E}^n \right\}_{k,l} + \left\{ \hat{F}_{k+\frac{1}{2}} - \hat{F}_{k-\frac{1}{2}} \right\}_l^{n+\frac{1}{2}} + \left\{ \hat{G}_{l+\frac{1}{2}} - \hat{G}_{l-\frac{1}{2}} \right\}_k^{n+\frac{1}{2}} = 0, \quad (B-11)$$

where \hat{E} , \hat{F} , and \hat{G} are given in Eq.(3-7).

Streamwise Flow (Space Marching)

We define a streamwise flux Jacobian matrix \hat{A}^* and an operator δ^{n+1} as

$$\hat{A}_{k,l}^{*n} \equiv \left[\frac{\partial \hat{E}^*(\Delta \vec{S}^{n+1}, \bar{U}^n)}{\partial \bar{U}} \right]_{k,l}, \quad (B-12a, b)$$

$$\delta^{n+1}() \equiv ()^{n+1} - ()^n,$$

To implement the space-marching we introduce Vigneron's[42] technique as

$$\hat{E}^n \equiv \hat{E}^*(\Delta \vec{S}^n, \bar{U}^n) + \hat{E}^p(\Delta \vec{S}^n, \bar{U}^{n-1}) \quad (B-13)$$

where

$$\hat{E}^* \equiv [\rho \hat{U}, \rho u \hat{U} + \left(\frac{\xi_x}{J}\right) \omega p, \rho v \hat{U} + \left(\frac{\xi_y}{J}\right) \omega p, \rho w \hat{U} + \left(\frac{\xi_z}{J}\right) \omega p, (E_t + p) \hat{U}]^T,$$

$$\hat{E}^p \equiv (1 - \omega) p [0, \left(\frac{\xi_x}{J}\right), \left(\frac{\xi_y}{J}\right), \left(\frac{\xi_z}{J}\right), 0]^T, \quad (B-14a, b)$$

with

$$\omega = \min \left[1, \frac{\sigma \gamma M_\xi^2}{1 + (\gamma - 1) M_\xi^2} \right], \quad \hat{U} \equiv \frac{1}{J} \nabla \xi \cdot \vec{V}, \quad (B-15a, b)$$

where σ is a safe factor for nonlinear effect and \hat{U} is a contravariant velocity component in the ξ -direction. Now the streamwise flux difference can be expressed by

$$\delta^{n+1} \{ \hat{E} \}_{k,l} = [\hat{A}^*]_{k,l}^n \delta^{n+1} \bar{U}_{k,l} + [\delta^n \hat{A}_{k,l}^*] \bar{U}_{k,l}^n + \delta^n \hat{E}_{k,l}^p, \quad (B-16)$$

where the marching steps of \hat{A}^* and \hat{E}^p are lagged by one for the conservative vector \bar{U} only. Thus, the operator $\delta^{\bar{n}}$ in Eq.(B-16) is defined by

$$\begin{aligned}\delta^{\bar{n}} \hat{A}_{k,l}^* &\equiv \hat{A}^*(\Delta \bar{S}_{k,l}^{n+1}, \bar{U}_{k,l}^n) - \hat{A}^*(\Delta \bar{S}_{k,l}^n, \bar{U}_{k,l}^{n-1}), \\ \delta^{\bar{n}} \hat{E}_{k,l}^p &\equiv \hat{E}^p(\Delta \bar{S}_{k,l}^{n+1}, \bar{U}_{k,l}^n) - \hat{E}^p(\Delta \bar{S}_{k,l}^n, \bar{U}_{k,l}^{n-1}).\end{aligned}\tag{B-17a,b}$$

From now on, the \hat{E}^* replaces the role of \hat{E} and the \hat{E}^p is neglected or treated like a source term in the space marching scheme.

Crosswise Flows (Linearization)

To avoid confusion and make the linearization procedure of cross flows clear, some notations as in Table 3 are introduced.

Table 3				
κ	m	\hat{H}	\hat{H}_i	\hat{H}_v
η	k, l^*	\hat{F}	\hat{F}_i	\hat{F}_v
ζ	k^*, l	\hat{G}	\hat{G}_i	\hat{G}_v

where $\hat{H} \equiv \hat{H}_i + \hat{H}_v$ and the superscript $*$ is for an inert index by an operator, which means that the index with $*$ does not vary. The \hat{H} denotes a difference expression of an inviscid and/or a viscous flux. But \hat{H} is strictly reserved for the flux itself such as either \hat{F} or \hat{G} . The subscripts i, v stand for the inviscid and viscous respectively. The general flux difference is defined by a difference operator δ_κ as

$$\delta_\kappa \hat{H}_m^{n+1} \equiv \hat{H}_{m+1/2}^{n+1} - \hat{H}_{m-1/2}^{n+1},\tag{B-18}$$

where we raised the marching level $(n + 1/2)$ to $(n + 1)$ for the purpose of both simplicity and stability. In the above equation the subscript m denotes the cell center point and the subscripts $m \pm 1/2$ denote the cell interface points. Before starting linearization it is to be noted that

$$\hat{H}_{m \pm 1/2} = f_n(\bar{U}_m, \bar{U}_{m \pm 1}, \Delta \bar{S}_{m \pm 1/2}).\tag{B-19}$$

This means that the flow quantities are defined at the cell centers, while the metrics are defined at the cell interfaces where the fluxes are calculated also. Considering the elements of $\hat{H}_{m\pm 1/2}^{n+1}$ in Eq.(B-19) we can linearize it as

$$\hat{H}_{m\pm 1/2}^{n+1} \equiv \hat{H}_{m\pm 1/2}^n + \frac{\partial \hat{H}_{m\pm 1/2}^n}{\partial \bar{U}_m} \delta^{n+1} \bar{U}_m + \frac{\partial \hat{H}_{m\pm 1/2}^n}{\partial \bar{U}_{m\pm 1}} \delta^{n+1} \bar{U}_{m\pm 1}, \quad (B-20)$$

where

$$\delta^{n+1} \bar{U} \equiv \bar{U}^{n+1} - \bar{U}^n. \quad (B-21)$$

Depending on the above linearization the general flux difference at the marching level $(n+1)$ can be now obtained in terms of n marching level values

$$\delta_\kappa \hat{H}_m^{n+1} = \delta_\kappa \hat{H}_m^n + \left[\frac{\partial}{\partial \bar{U}_m} (\delta_\kappa \hat{H}_m^n) + \bar{\delta}_\kappa \left(\frac{\partial \hat{H}_m^n}{\partial \bar{U}_m} \right) \right] \delta^{n+1} \bar{U}_m, \quad (B-22)$$

where

$$\delta_\kappa \hat{H}_m^n \equiv \hat{H}_{m+1/2}^n - \hat{H}_{m-1/2}^n, \quad (B-23)$$

$$\frac{\partial}{\partial \bar{U}_m} (\delta_\kappa \hat{H}_m^n) \delta^{n+1} \bar{U}_m \equiv \frac{\partial \hat{H}_{m+1/2}^n}{\partial \bar{U}_m} \delta^{n+1} \bar{U}_m - \frac{\partial \hat{H}_{m-1/2}^n}{\partial \bar{U}_m} \delta^{n+1} \bar{U}_m, \quad (B-24)$$

$$\bar{\delta}_\kappa \left(\frac{\partial \hat{H}_m^n}{\partial \bar{U}_m} \right) \delta^{n+1} \bar{U}_m \equiv \frac{\partial \hat{H}_{m+1/2}^n}{\partial \bar{U}_{m+1}} \delta^{n+1} \bar{U}_{m+1} - \frac{\partial \hat{H}_{m-1/2}^n}{\partial \bar{U}_{m-1}} \delta^{n+1} \bar{U}_{m-1}. \quad (B-25)$$

It is to be noted that the $\bar{\delta}_\kappa$ in the Eq.(B-25) operates on the whole portion which follows the operator.

First Form of Algorithm

To have a desired discretized algorithm all the terms containing $\delta^{n+1} \bar{U}$ are moved to the left hand side and the other terms to the right hand side of the equation after substituting the appropriate expressions for $\delta_\kappa \hat{H}_m^{n+1}$ into Eq.(B-11)

with the help of the Table 3. Then the following algorithm in the so called δ -form can be obtained,

$$\begin{aligned} & \left[\hat{A}^* + \frac{\partial}{\partial \bar{U}} (\delta_\eta \hat{F}^I + \delta_\zeta \hat{G}^I) + \bar{\delta}_\eta \frac{\partial \hat{F}^I}{\partial \bar{U}} + \bar{\delta}_\zeta \frac{\partial \hat{G}^I}{\partial \bar{U}} \right]_{k,l}^n \delta^{n+1} \bar{U}_{k,l} \\ & = - \left\{ (\delta^{\bar{n}} \hat{A}^*) \bar{U} + \delta^{\bar{n}} \hat{E}^p + \delta_\eta \hat{F}^{II} + \delta_\zeta \hat{G}^{II} \right\}_{k,l}^n, \end{aligned} \quad (B-26)$$

where $[\]_{k,l}^n$ and $\{ \}_{k,l}^n$ are for a Jacobian matrix and a flux respectively and

$$\begin{aligned} \hat{F}^I &\equiv \hat{F}_i^I + \hat{F}_v, \hat{G}^I \equiv \hat{G}_i^I + \hat{G}_v, \\ \hat{F}^{II} &\equiv \hat{F}_i^{II} + \hat{F}_v, \hat{G}^{II} \equiv \hat{G}_i^{II} + \hat{G}_v. \end{aligned} \quad (B-27a, b)$$

The superscripts I and II denote the first and the second order expressions for the inviscid fluxes respectively. More generally, we introduce the notations, \hat{H}^I and \hat{H}^{II} , like

$$\begin{aligned} \hat{H}^I &= \text{either } \hat{F}^I \text{ or } \hat{G}^I, \\ \hat{H}^{II} &= \text{either } \hat{F}^{II} \text{ or } \hat{G}^{II}. \end{aligned} \quad (B-28a, b)$$

It must be noted that these notations are not the general fluxes, but they are the expressions for the first and the second order difference representation of them. They will be specified in the following sections. If the first order accurate discretization is used on the *LHS*, then block tridiagonal matrices are obtained. If we choose the second order expression, then it will become pentadiagonal matrices which will require much more efforts to inverse them than the tridiagonal matrices. In view of the above fact it would be adequate to use the first order differencing the *LHS*. On the other hand, the *RHS* must be handled with much care and a lot of efforts are to be exerted to improve the accuracy. For the *RHS* the second order differencings are usually used.

Final Form of Algorithm (Approximate Operator Factorization)

The Eq.(B-26) cannot be used directly. To numerically integrate this it is rewritten by approximate operator factorization[43] as

$$[\alpha][\hat{A}_{k,l}^{*n}]^{-1}[\beta]\delta^{n+1}\bar{U}_{k,l}^n = \{RHS\}^n, \quad (B-29)$$

where

$$[\alpha] \equiv \left[\hat{A}^* + \frac{\partial}{\partial \bar{U}} \delta_\eta (\hat{F}_i^I + \hat{F}_v) + \bar{\delta}_\eta \frac{\partial}{\partial \bar{U}} (\hat{F}_i^I + \hat{F}_v) \right]_{k,l}^n, \quad (B-30a)$$

$$[\beta] \equiv \left[\hat{A}^* + \frac{\partial}{\partial \bar{U}} \delta_\zeta (\hat{G}_i^I + \hat{G}_v) + \bar{\delta}_\zeta \frac{\partial}{\partial \bar{U}} (\hat{G}_i^I + \hat{G}_v) \right]_{k,l}^n, \quad (B-30b)$$

$$\begin{aligned} \{RHS\}^n \equiv & - \left[\hat{A}^*(\Delta \bar{S}_{k,l}^{n+1}, \bar{U}_{k,l}^n) - \hat{A}^*(\Delta \bar{S}_{k,l}^n, \bar{U}_{k,l}^{n-1}) \right] \bar{U}_{k,l}^n \\ & - \left\{ \hat{E}^p(\Delta \bar{S}_{k,l}^{n+1}, \bar{U}_{k,l}^n) - \hat{E}^p(\Delta \bar{S}_{k,l}^n, \bar{U}_{k,l}^{n-1}) \right\} \\ & - \delta_\eta \left\{ \hat{F}_i^{II} + \hat{F}_v \right\}_{k,l}^n \\ & - \delta_\zeta \left\{ \hat{G}_i^{II} + \hat{G}_v \right\}_{k,l}^n. \end{aligned} \quad (B-30c)$$

At this stage any reasonable finite difference expression can be chosen for \hat{H}^I or \hat{H}^{II} . The special form used for this study will be presented later. The solving procedure of the Eq.(B-29) can be taken as the following four steps.

1. $[\alpha]\bar{X} = \{RHS\}^n,$
 2. $\bar{Y} = \left[\hat{A}_{k,l}^{*n} \right] \bar{X},$
 3. $[\beta]\delta^{n+1}\bar{U}_{k,l} = \bar{Y},$
 4. $\bar{U}_{k,l}^{n+1} = \bar{U}_{k,l}^n + \delta^{n+1}\bar{U}_{k,l},$
- (B-31a, b, c, d)

Both of $[\alpha]$ and $[\beta]$ is a block tridiagonal matrices which will be explained in the last section.

B.2 Flux Jacobian Matrices

The *LHS* of the previous algorithm Eq.(B-29) contains some Jacobian matrices in $[\alpha]$ and $[\beta]$. Their calculating procedure is described in the following subsections.

Inviscid Flux Jacobian (First Order Upwind Scheme)

Before introducing inviscid flux Jacobian a Jacobian matrix $\tilde{C}_{m+1/2}$ is defined first as

$$\tilde{C}_{m+1/2}(\Delta\tilde{S}_{m+1/2}, \tilde{U}_{m+1/2}) \equiv \frac{\partial(\hat{H}_i)_{m+1/2}}{\partial\hat{E}_{m+1/2}^*}, \quad (B-32)$$

where $\text{sgn}\tilde{C}$ is given by

$$\text{sgn}\tilde{C} = \tilde{R}(\text{sgn}\tilde{\Lambda})\tilde{R}^{-1}, \quad \text{sgn}\tilde{\Lambda} \equiv |\tilde{\Lambda}|\tilde{\Lambda}^{-1} = \tilde{\Lambda}|\tilde{\Lambda}^{-1}|, \quad (B-33a, b)$$

where \tilde{R}^{-1} and \tilde{R} are the left and right eigen vector matrices of the Jacobian matrix \tilde{C} respectively. To evaluate \tilde{R}^{-1} , \tilde{R} , and $\tilde{\Lambda}$ Roe-averaged values are used. The notation “ \sim ” is introduced to denote the Roe average values. The first order expression of the general inviscid flux can be now expressed in terms of $\text{sgn}\tilde{C}$ by

$$(\hat{H}_i^I)_{m+1/2} = \frac{1}{2} \left\{ (\hat{H}_i)_{m+1} + (\hat{H}_i)_m \right\} - \frac{1}{2} (\text{sgn}\tilde{C})_{m+1/2} \Delta\hat{H}_i, \quad (B-34)$$

where

$$\Delta() \equiv ()_{m+1} - ()_m, \quad |\tilde{C}| \equiv \tilde{R}(\tilde{\Lambda}^+ - \tilde{\Lambda}^-)\tilde{R}^{-1}, \quad \text{sgn}\tilde{C}\Delta\hat{H}_i = |\tilde{C}|\Delta\hat{E}^*. \quad (B-35a, b, c)$$

Based on the Eq.(B-34), the inviscid Jacobian matrices are calculated as

$$\begin{aligned} \frac{\partial(\hat{H}_i^I)_{m+1/2}}{\partial\tilde{U}_{m+1}} &= \frac{1}{2} [I - (\text{sgn}\tilde{C})_{m+1/2}] B_i(\Delta\tilde{S}_{m+1/2}, \tilde{U}_{m+1}), \\ \frac{\partial(\hat{H}_i^I)_{m+1/2}}{\partial\tilde{U}_m} &= \frac{1}{2} [I + (\text{sgn}\tilde{C})_{m+1/2}] B_i(\Delta\tilde{S}_{m+1/2}, \tilde{U}_m), \end{aligned} \quad (B-36a, b)$$

with the definition of B_i as

$$\begin{aligned} B_i(\Delta \vec{S}_{m+1/2}, \bar{U}_{m+1}) &\equiv \frac{\partial(\hat{H}_i)_{m+1/2}}{\partial \bar{U}_{m+1}}, \\ B_i(\Delta \vec{S}_{m+1/2}, \bar{U}_m) &\equiv \frac{\partial(\hat{H}_i)_{m+1/2}}{\partial \bar{U}_m}. \end{aligned} \quad (B-37a, b)$$

For the case of $(\hat{H}_i^I)_{m-1/2}$ m in Eqs(B-36,37) is to be changed into $m-1$.

Viscous Flux Jacobian

For viscous flux Jacobian matrices they are simply defined as

$$\begin{aligned} B_v(\Delta \vec{S}_{m+1/2}, \bar{U}_{m+1}) &\equiv \frac{\partial(\hat{H}_v)_{m+1/2}}{\partial \bar{U}_{m+1}}, \\ B_v(\Delta \vec{S}_{m+1/2}, \bar{U}_m) &\equiv -\frac{\partial(\hat{H}_v)_{m+1/2}}{\partial \bar{U}_m}. \end{aligned} \quad (B-38a, b)$$

Inviscid and Viscous Flux Jacobian

Considering the definition of \hat{H}

$$\hat{H}^I \equiv \hat{H}_i^I + \hat{H}_v. \quad (B-39)$$

Jacobian matrices for both the inviscid and viscous terms are obtained from the previous two subsections as

$$\begin{aligned} \frac{\partial(\hat{H}^I)_{m\pm 1/2}}{\partial \bar{U}_{m\pm 1}} &= \frac{1}{2}[I \mp (\text{sgn} \tilde{C})_{m\pm 1/2}]B_i(\Delta \vec{S}_{m\pm 1/2}, \bar{U}_{m\pm 1}) \pm B_v(\Delta \vec{S}_{m\pm 1/2}, \bar{U}_{m\pm 1}), \\ \frac{\partial(\hat{H}^I)_{m\pm 1/2}}{\partial \bar{U}_m} &= \frac{1}{2}[I \pm (\text{sgn} \tilde{C})_{m\pm 1/2}]B_i(\Delta \vec{S}_{m\pm 1/2}, \bar{U}_m) \mp B_v(\Delta \vec{S}_{m\pm 1/2}, \bar{U}_m), \end{aligned} \quad (B-40a, b)$$

where the matrices \tilde{C} , B_i , and B_v are given in reference[28]. The above two equations can determine all the terms on the *LHS* of Eq.(B-29) except for \hat{A}^* which is given already in Eq.(B-12).

B.3 Flux Differences

The *RHS* of the final algorithm of Eq.(B-29) contains the flux differences of the second order in \hat{F} and \hat{G} as can be seen in Eq.(B-30c). The general flux difference is divided into the inviscid and viscous portions as

$$\delta_{\kappa}(\hat{H}^{II})_m \equiv \delta_{\kappa}(\hat{H}_i^{II})_m + \delta_{\kappa}(\hat{H}_v)_m. \quad (B - 41)$$

The inviscid flux difference is defined as

$$\delta_{\kappa}(\hat{H}_i^{II})_m \equiv (\hat{H}_i^{II})_{m+1/2} - (\hat{H}_i^{II})_{m-1/2}. \quad (B - 42)$$

The second order expression for \hat{H}_i , [28] is obtained by adding higher order correction terms to the first order expression in Eq.(B-34) like

$$\begin{aligned} (\hat{H}_i^{II})_{m\pm 1/2} \equiv & (\hat{H}_i^I)_{m\pm 1/2} + \left(\frac{1-\phi}{4}\right)\{\Delta\tilde{\tilde{F}}_1^+ - \Delta\tilde{\tilde{F}}_3^-\}_{m\pm 1/2} \\ & + \left(\frac{1+\phi}{4}\right)\{\Delta\tilde{\tilde{F}}_2^+ - \Delta\tilde{\tilde{F}}_2^-\}_{m\pm 1/2}. \end{aligned} \quad (B - 43)$$

Depending on the value of the accuracy parameter ϕ various schemes can be obtained. For example, if $\phi = 1$, it becomes an upwind scheme. The notations $\tilde{\tilde{\cdot}}$ and $\tilde{\cdot}$ denote the limited flux differences through the MINMOD limiter which is defined by

$$MINMOD(x, y) \equiv sgn(x) \cdot \max\{0, \min(|x|, \beta sgn(x)y)\}, \quad (B - 44)$$

where β is a compression parameter. The *MINMOD* picks up a minimum absolute value (modulus), if the two arguments are of the same sign. On the other hand, it assigns zero, if they are of opposite sign. Therefore, it plays a role of limiting the fluxes, whenever it meets very steep variations. But for mild variation it returns un-limited fluxes, since β is large compared with 1 in most case. At maximum, minimum, or inflection points where the sign of the neighboring fluxes are changed, the limiter returns zero. As a result, if we use *MINMOD* based on the Total Variation Diminishing (TVD) condition. it will not introduce new maxima or minima and

thus it removes glitches and expansion shocks. This is somewhat parallel with the Piecewise Parabolic Method (PPM) by Collela and Woodward[44]. As β becomes larger, we can get a sharper distribution near discontinuity. However, to satisfy the TVD condition, its value is restricted. For instance, in one-dimensional scalar nonlinear equation or systems of linear equations,

$$1 < \beta \leq \frac{3 - \phi}{1 - \phi}. \quad (B - 45)$$

Even though the equations used here are multi-dimensional non-linear systems of equations, it is known that this can provide quite good guideline for them also.

The viscous flux difference which can be simply determined by

$$\delta_{\kappa}(\hat{H}_v)_m \equiv (\hat{H}_v)_{m+1/2} - (\hat{H}_v)_{m-1/2}. \quad (B - 46)$$

B.4 Block Tridiagonal Matrix

Matrix Construction

In order to integrate the PNS equations by the algorithm given by Eq.(B-29) the Eqs.(B-40) and (B-38) must be inserted in Eq.(B-30). In doing so the first step of Eq.(B-31) is important, since it contains a block tridiagonal matrix[45] on the left hand side. The third step is the same as the first in the point of numerical calculation. The rest two steps are not difficult. Thus, the solving procedure of block tridiagonal matrix will be presented in the following. The Eq.(B-31a) can be rewritten as

$$[\alpha_1]_{k,l}\{X\}_{k-1,l} + [\alpha_2]_{k,l}\{X\}_{k,l} + [\alpha_3]_{k,l}\{X\}_{k+1,l} = \{RHS\}_{k,l}, \quad (B - 47)$$

where

$$\begin{aligned}
[\alpha_1]_{k,l} &\equiv -\frac{\partial(\hat{F}^I)_{k-1/2,l}}{\partial\bar{U}_{k-1,l}}, \\
[\alpha_2]_{k,l} &\equiv \frac{\partial(\hat{F}^I)_{k+1/2,l}}{\partial\bar{U}_{k,l}} - \frac{\partial(\hat{F}^I)_{k-1/2,l}}{\partial\bar{U}_{k,l}} + [\hat{A}_{k,l}^*], \\
[\alpha_3]_{k,l} &\equiv \frac{\partial(\hat{F}^I)_{k+1/2,l}}{\partial\bar{U}_{k+1,l}}.
\end{aligned} \tag{B-48a,b,c}$$

Here the $[\alpha_1]_{k,l}$, $[\alpha_2]_{k,l}$, and $[\alpha_3]_{k,l}$ are 5x5 square matrices. $\{X\}_{k-1,l}$, $\{X\}_k$, $\{X\}_{k+1,l}$, and $\{RHS\}_{k,l}$ are 1x5 column matrices. Thus the coefficient matrices, $[\alpha_i]$, compose a block tridiagonal matrix. Eq.(B-47) is solved along the η -direction ($l = \text{const}$), while Eq.(B-31c) is solved along the ζ -direction ($k = \text{const}$). Thus the calculating procedure changes the directions. For this reason it is called Alternating Directional Implicit (ADI) method.

Matrix Solver

A system of equations composed of a scalar tridiagonal matrix can be solved by means of Thomas algorithm. For a block tridiagonal matrix, we can also apply the same algorithm combined with the inverse matrix solver. The solution procedure of a system of equation with tridiagonal matrix is described in brief. First, we eliminate the sub-diagonal matrices below the diagonal matrices by using the upper row matrices and then the present row matrices are multiplied by the inversed diagonal matrix element. Thus we can construct upper triangular matrix whose elements are 5x5 block matrices. To obtain the inverse matrix we use Crout's algorithm[46] which decompose any matrix into lower and upper triangular matrices. The final step is to take the backward sweep to get the desired block column matrices which contain the dependent (conservative) variables.

Appendix C

GEOMETRY OF LEADING EDGE

It is desired to determine the angle Δ between the upper planar surface and the lower compression surface. The outward pointing unit normal of compression surface is determined by $\hat{n} = -\nabla F/|\nabla F|$, where $F(\theta, \phi) = \theta - \theta(\phi)$, where $\theta(\phi)$ is determined by Eq.(2-6). For small polar angles, we have

$$\hat{n} = \frac{\hat{e}_\theta - \frac{1}{\theta} \frac{d\theta}{d\phi} \hat{e}_\phi}{\left[1 + \left(\frac{1}{\theta} \frac{d\theta}{d\phi}\right)^2\right]^{1/2}}. \quad (C-1)$$

Since the outward normal to the freestream planar surface is \hat{e}_ϕ , we can determine the leading edge tip angle Δ (where $\theta = \beta$) by $\cos(\pi - \Delta) = \hat{n} \cdot \hat{e}_\phi$. It can then be determined that

$$\tan \Delta = \beta \left(\frac{d\phi}{d\theta} \right)_{\theta=\beta} = -\frac{\epsilon_2 w_2(\beta) \sin 2\phi_s}{V_\infty \delta \sigma (1 - \frac{1}{\sigma^2})}. \quad (C-2)$$

The azimuthal velocity at the shock can be determined from the shock boundary conditions [21,22] :

$$\frac{w_2(\beta)}{\delta V_\infty} = -\frac{2g_2}{\sigma^2}. \quad (C-3)$$

Thus the leading-edge tip angle is determined by

$$\tan \Delta = \frac{2\epsilon_2 g_2 \sin 2\phi_s}{\sigma(\sigma^2 - 1)}. \quad (C-4)$$

The tip angle according to the approximate formula (2-9) is determined by a different result. It is

$$(\tan \Delta)_{\text{approx}} = \frac{e\sigma}{2(\sigma - 1)} \sin 2\phi_s. \quad (C-5)$$

The tip angles for models *A1* and *B1* are determined by the approximate formula (C-5), whereas the tip angles for models for *A2* and *B2* are determined by the correct formula (C-4). The numerical values are shown in the following table:

Table (C-1)

Model	Δ
<i>A1</i>	10.45°
<i>A2</i>	1.44°
<i>B1</i>	9.45°
<i>B2</i>	4.12°

The models *A1* and *B1* with the compression surface described by the approximate formula (2-9) have considerably thicker angles than the corresponding correct waveriders would have.

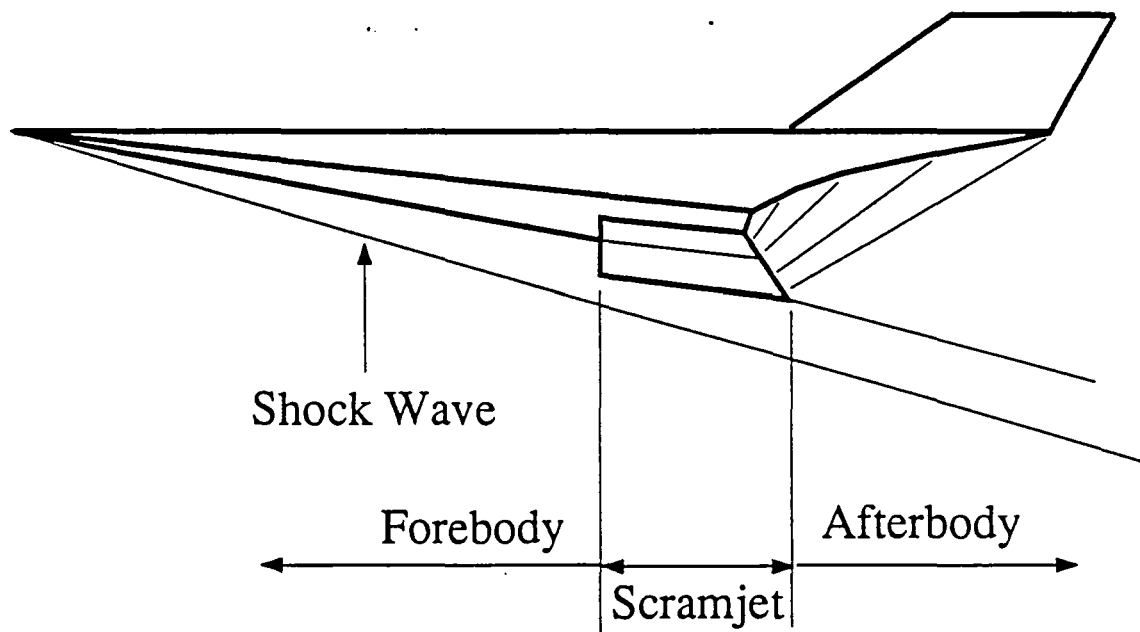


Fig.(1-1) Model of Aero-space Plane

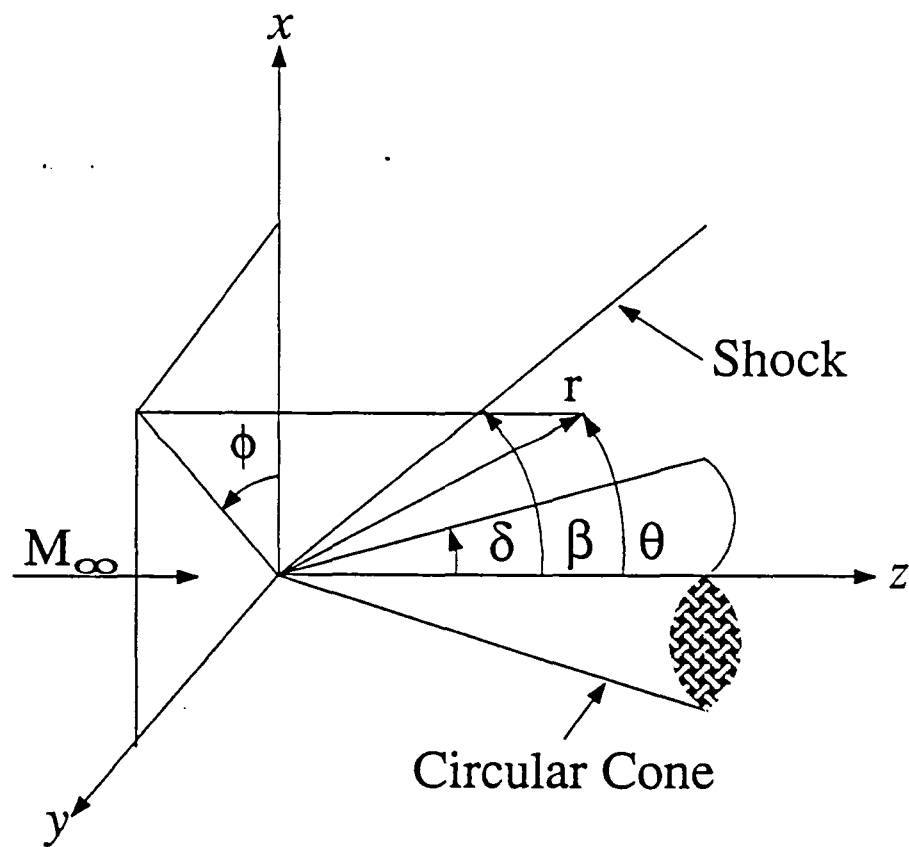


Fig.(2-1) Spherical Polar Coordinates

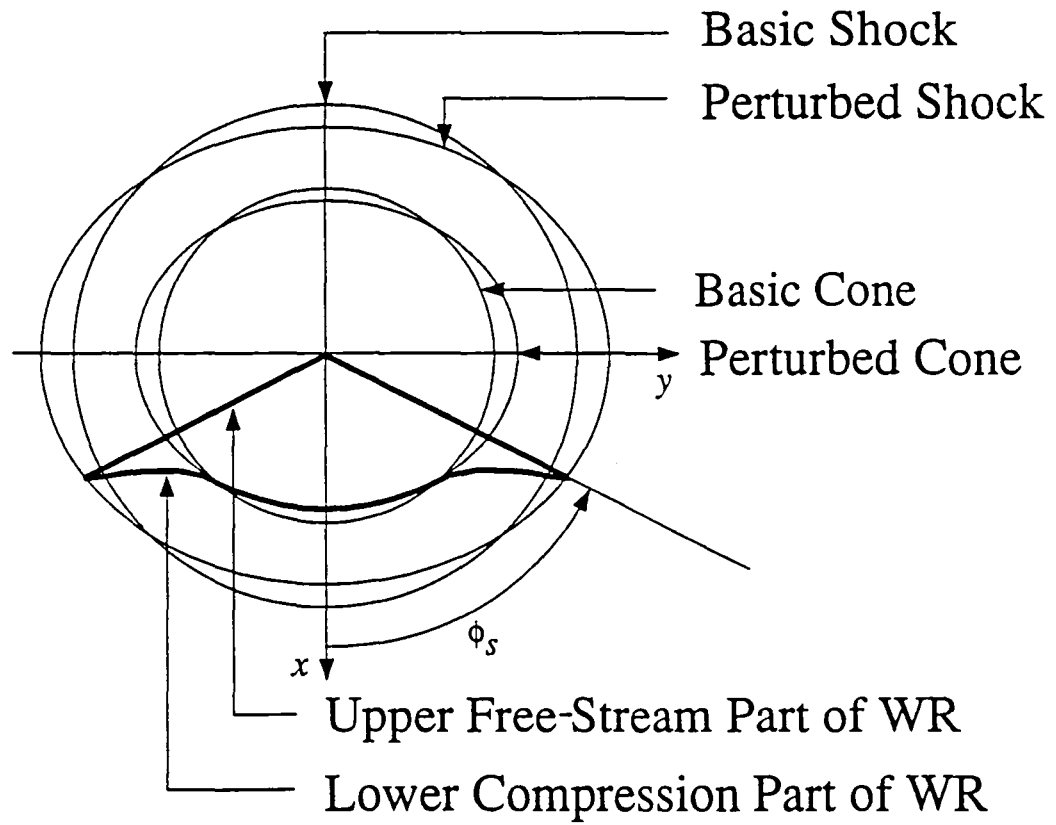


Fig.(2-2) Construction of Elliptic-Cone Waverider

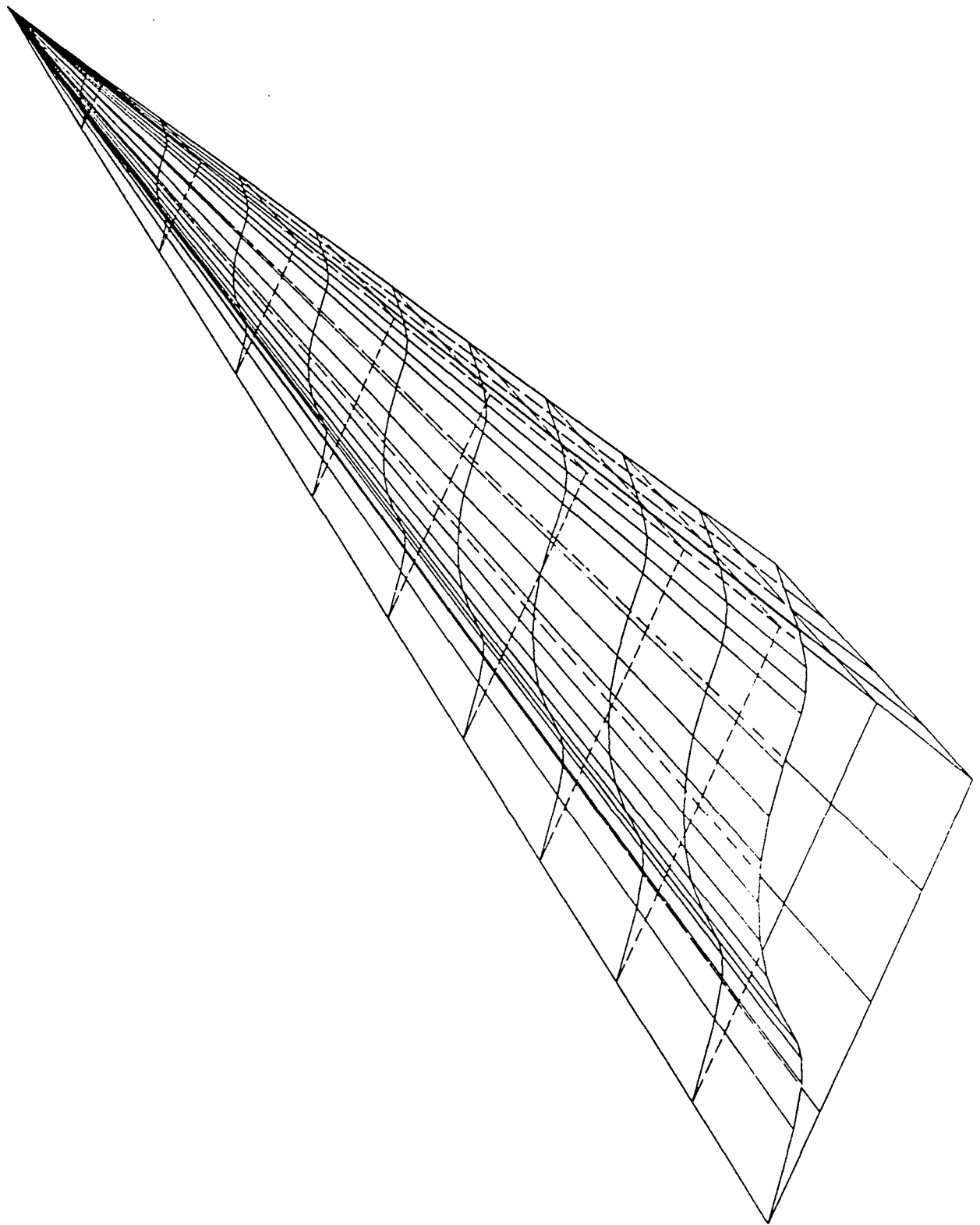


Fig. (2-3) Waverider Configuration

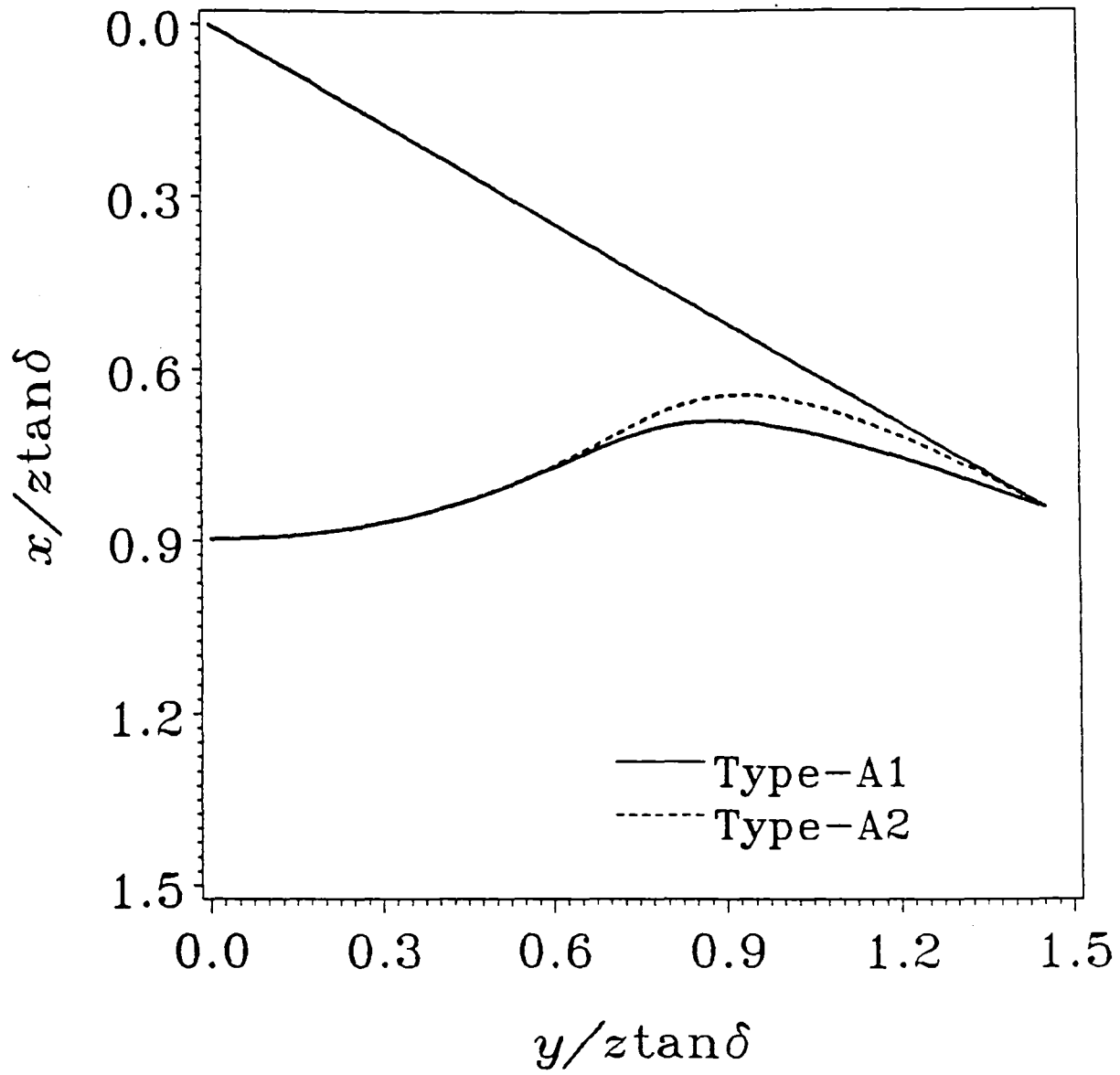


Fig.(2-4) Waverider Type-A

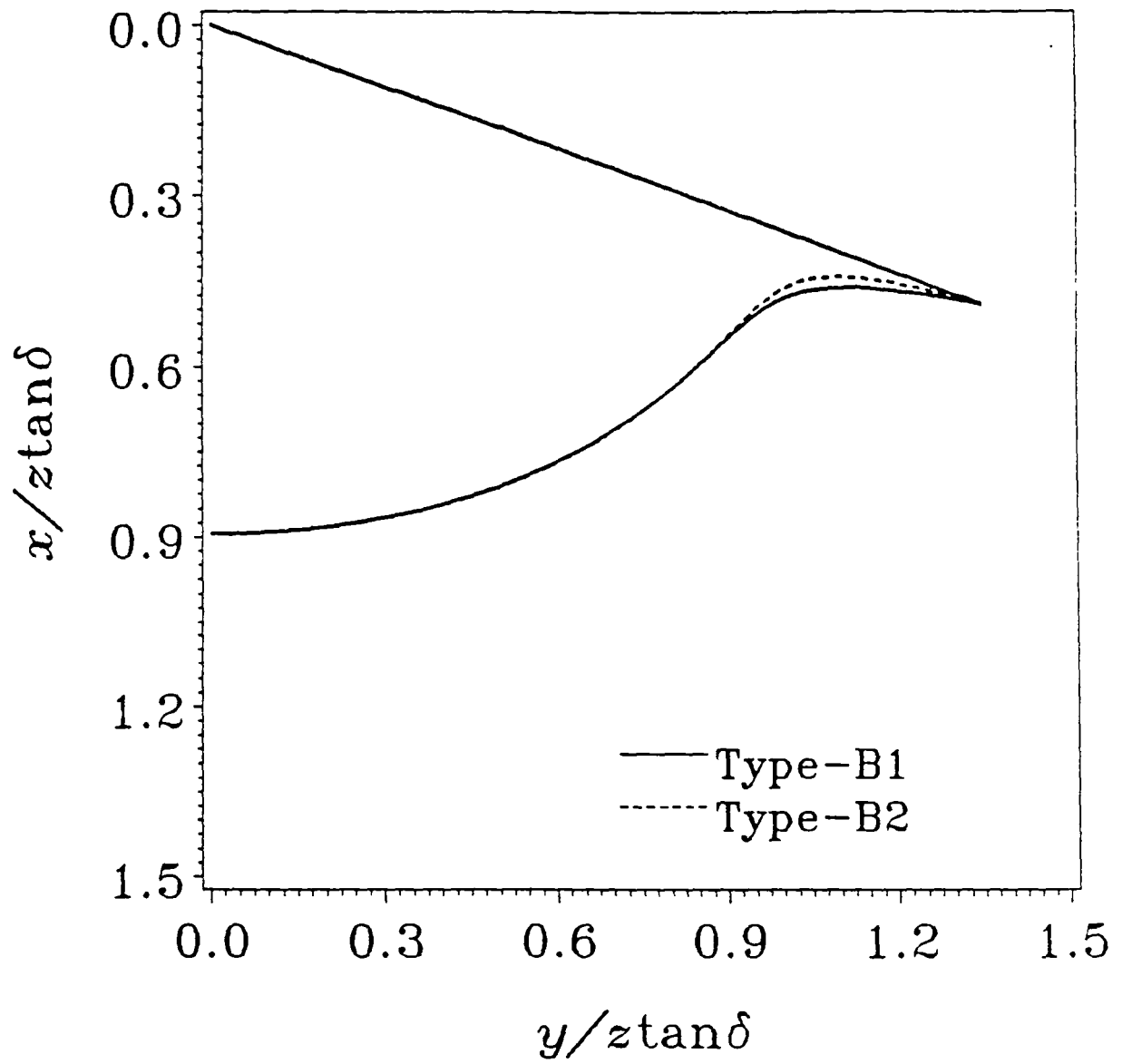
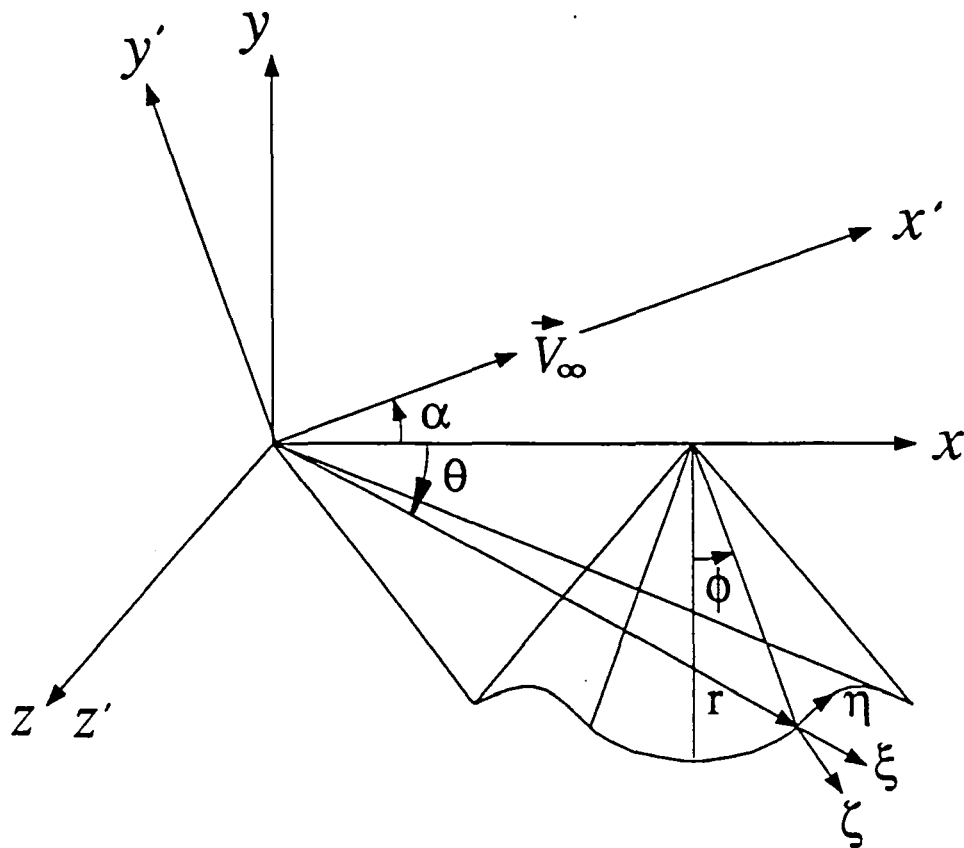


Fig.(2-5) Waverider Type-B

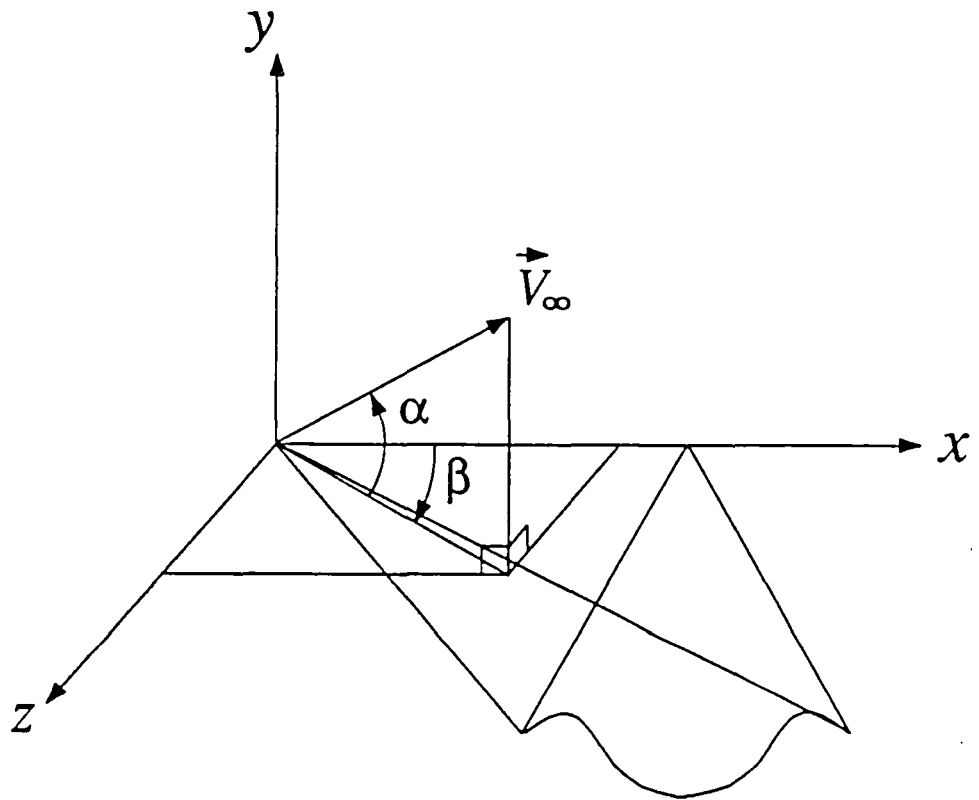


$(x, y, z) = \text{Cartesian}$

$(r, \theta, \phi) = \text{Spherical}$

$(\xi, \eta, \zeta) = \text{Body-fitted}$

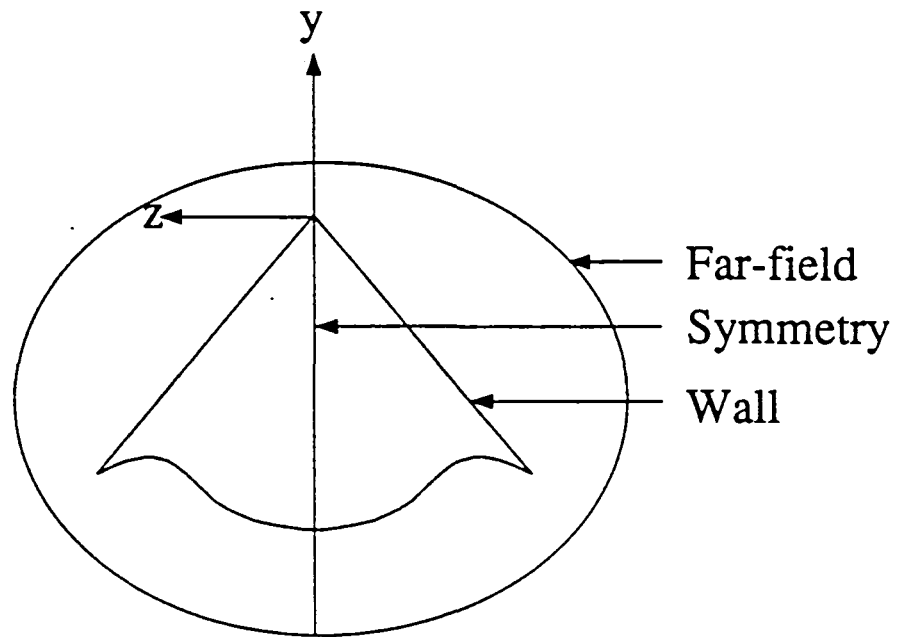
Fig.(3-1) Coordinate Systems



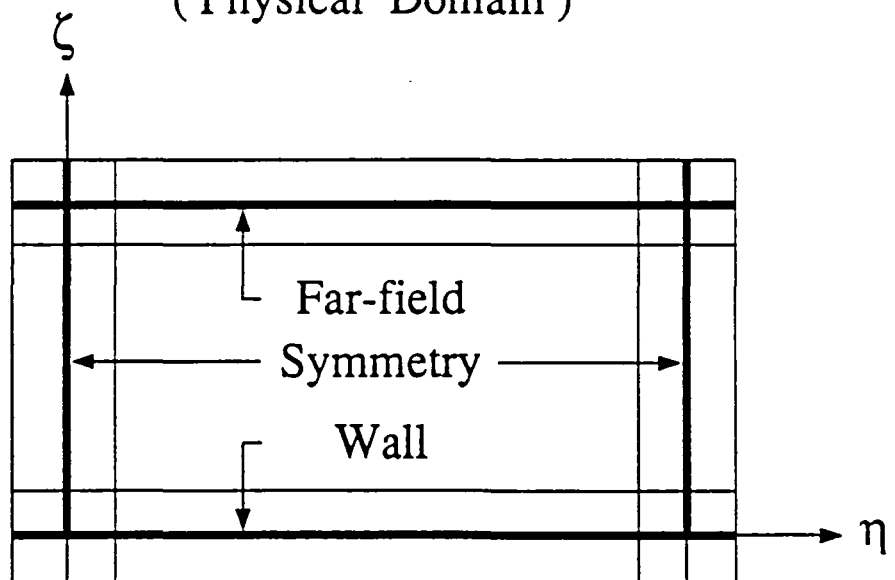
$\alpha =$ angle of attack

$\beta =$ angle of yaw

Fig.(3-2) Initial Conditions

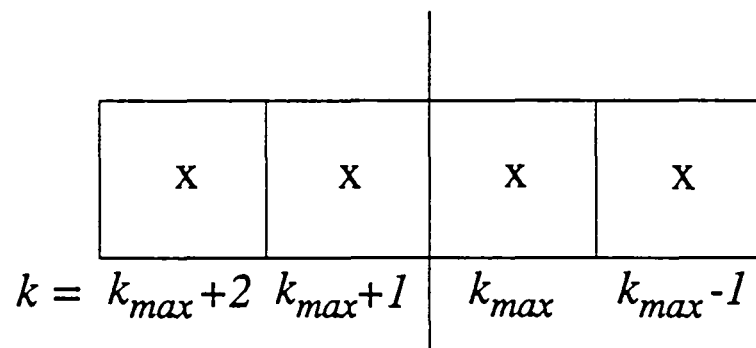


(Physical Domain)

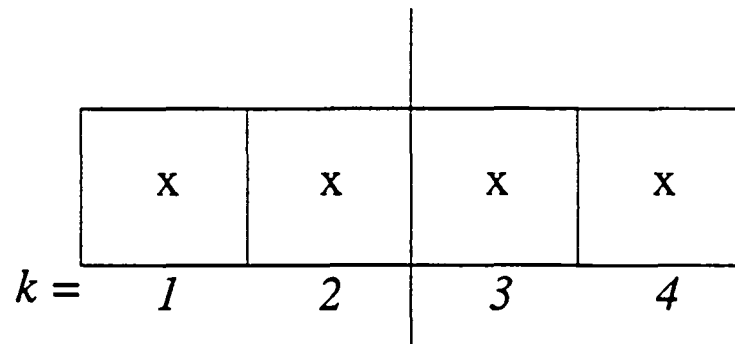


(Computational Domain)

Fig.(3-3) Boundary Conditions

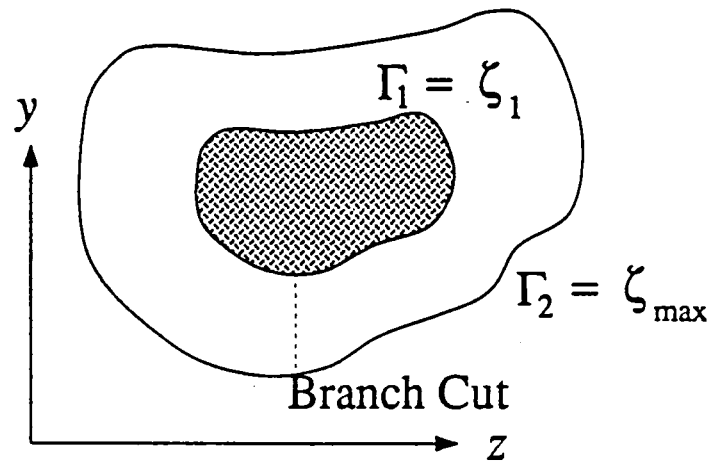


Upper Symmetry Plane

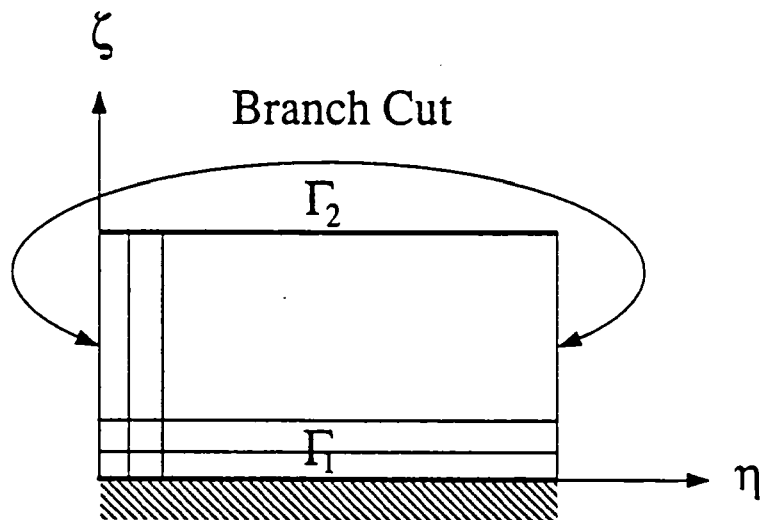


Lower Symmetry Plane

Fig.(3-4) Reflection Condition



(Physical Domain)



(Computational Domain)

Fig.(5-1) Elliptic Grid Generation

Fig. (5-2) O-Type Grid

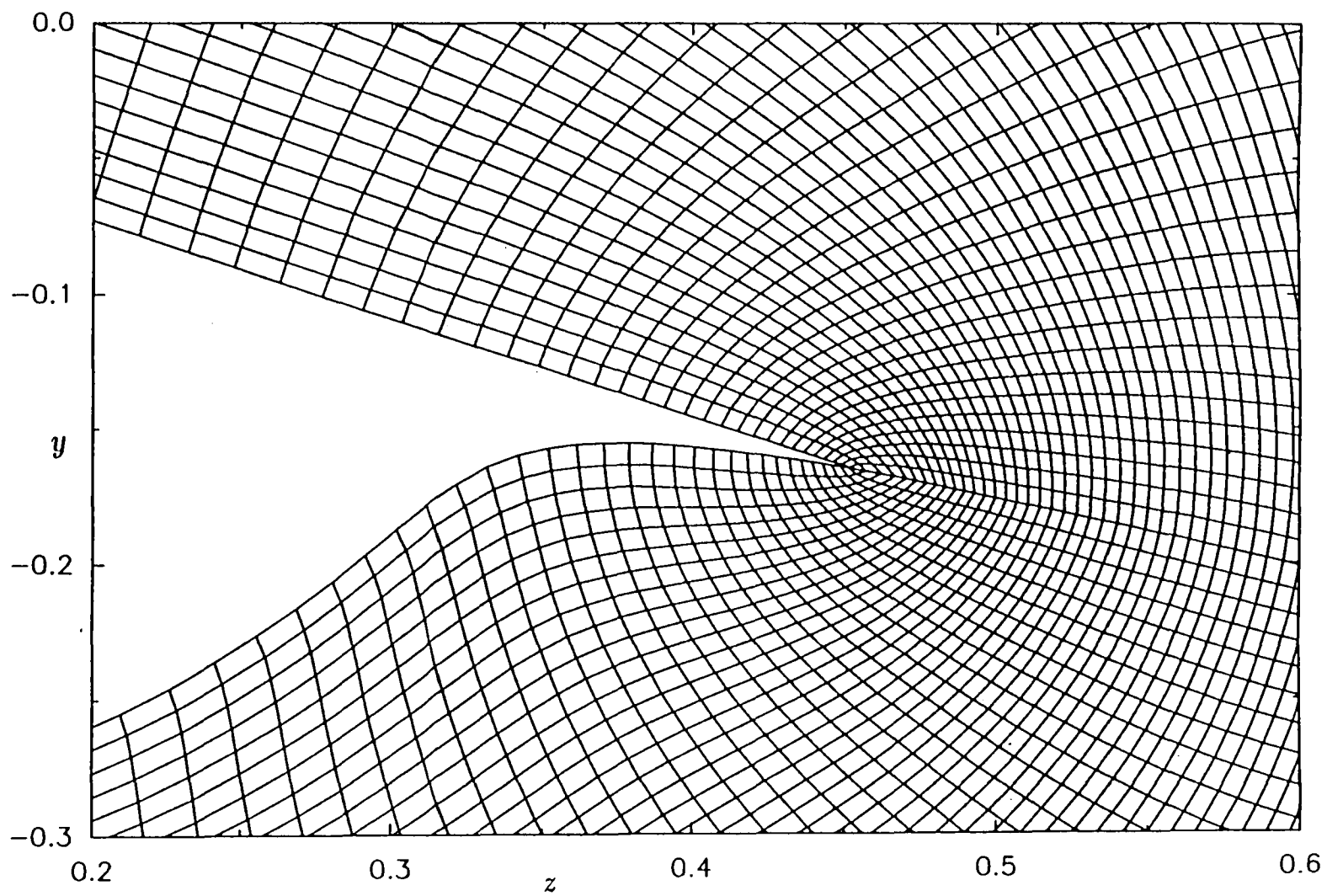


Fig. (5-3) Magnified O-Type Grid

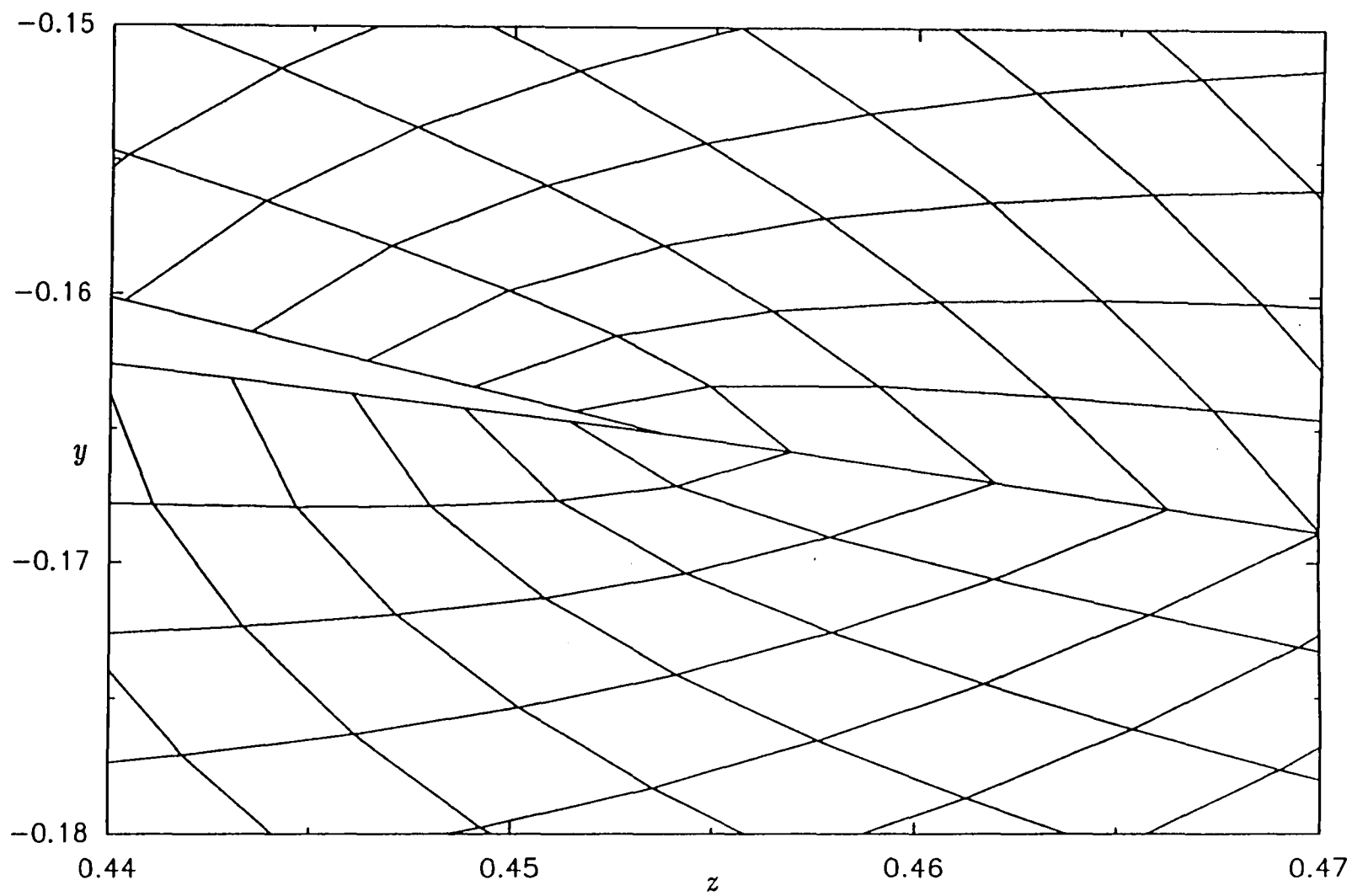


Fig. (5-4) Fan-Type Grid

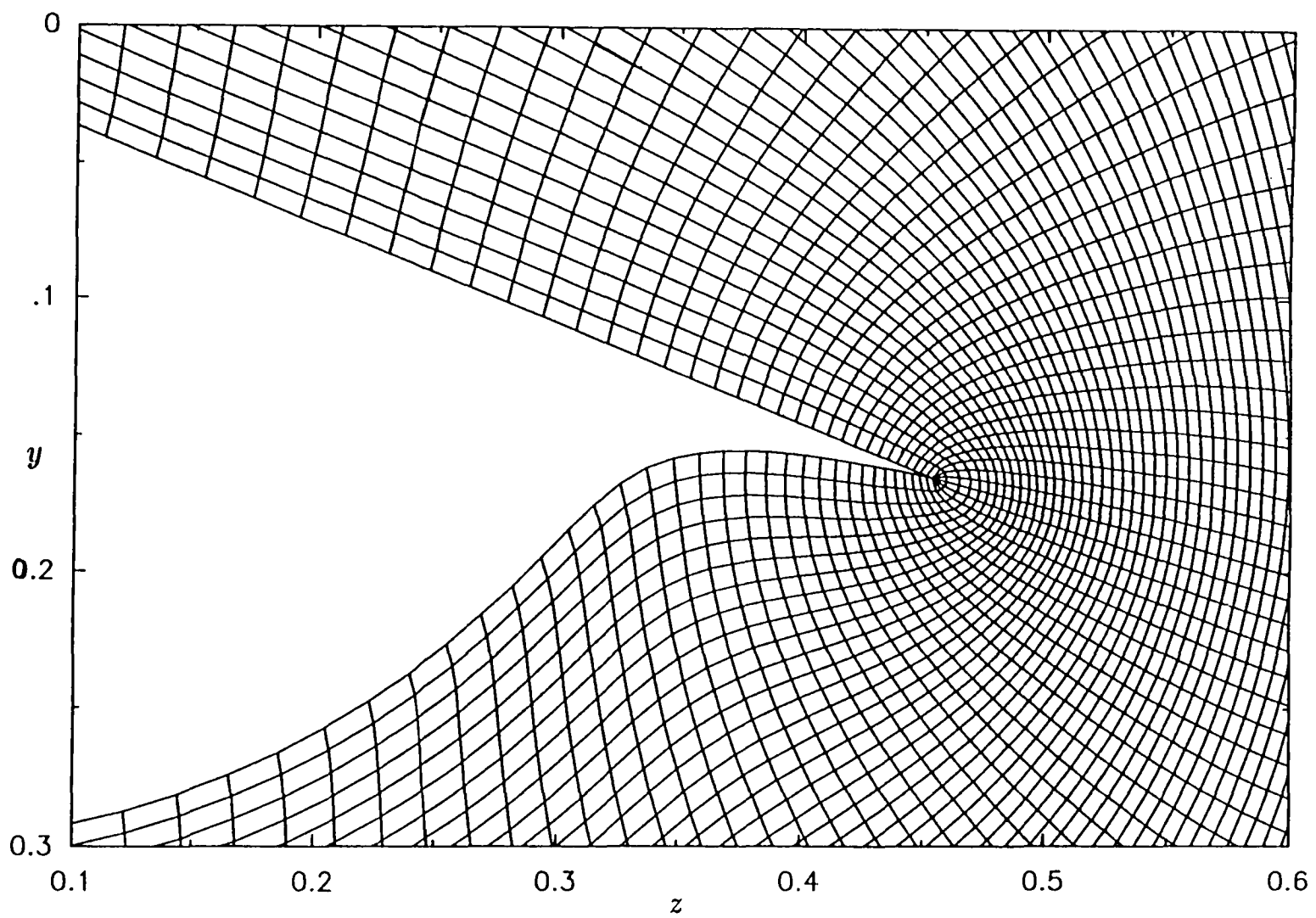


Fig. (5-5) Magnified Fan-Type Grid

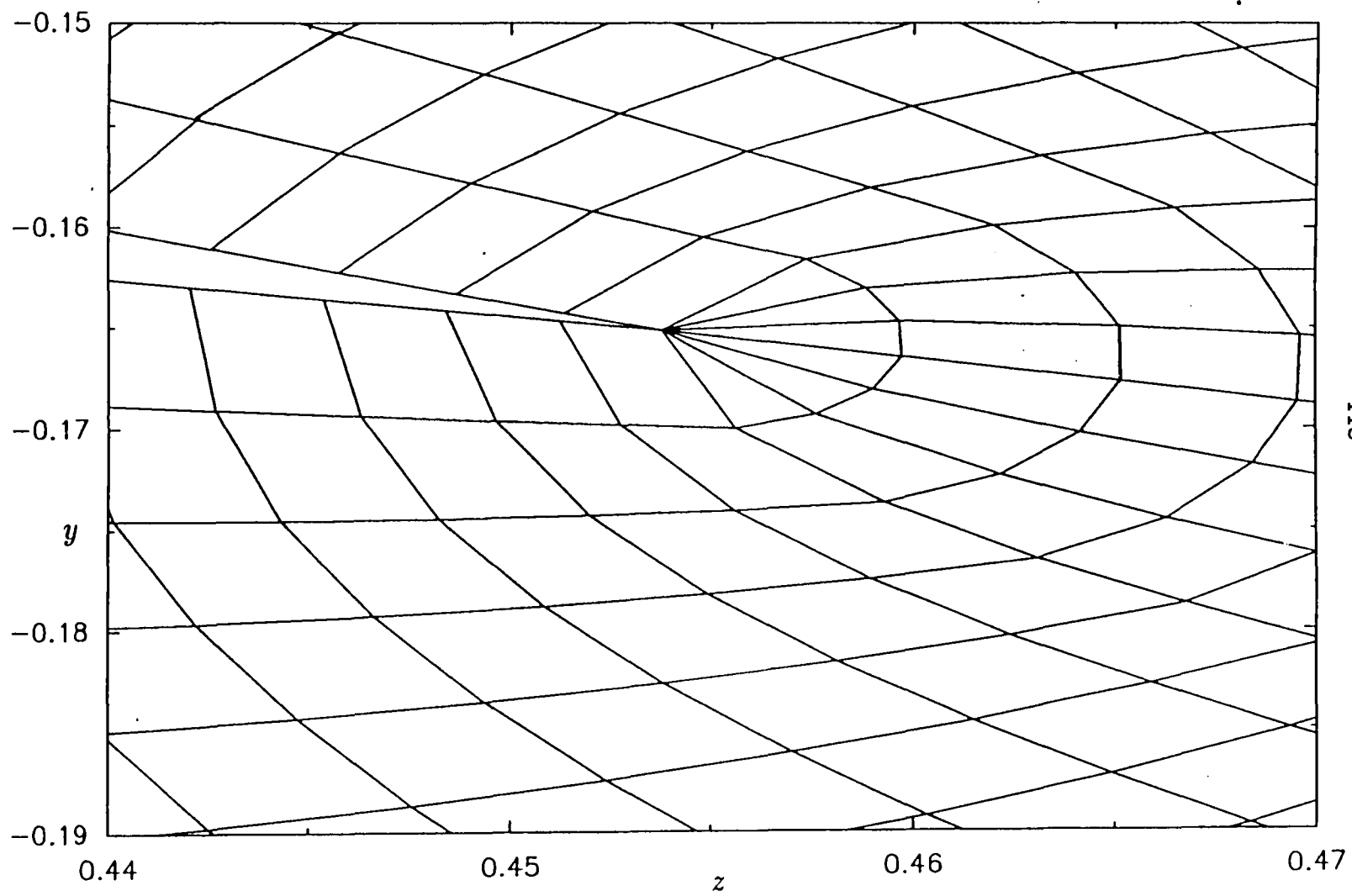


Fig. (5-6) Adaptive Grid

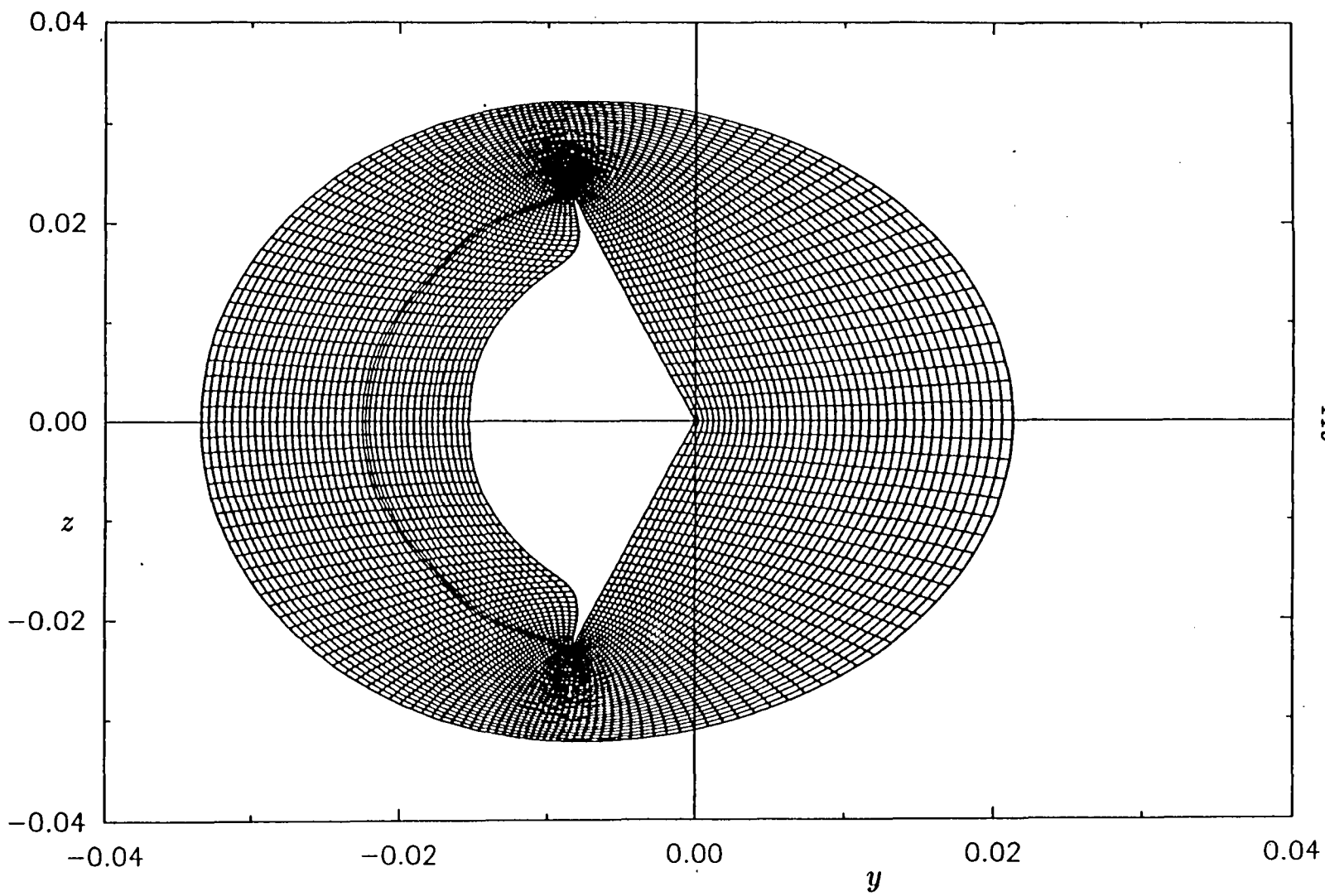
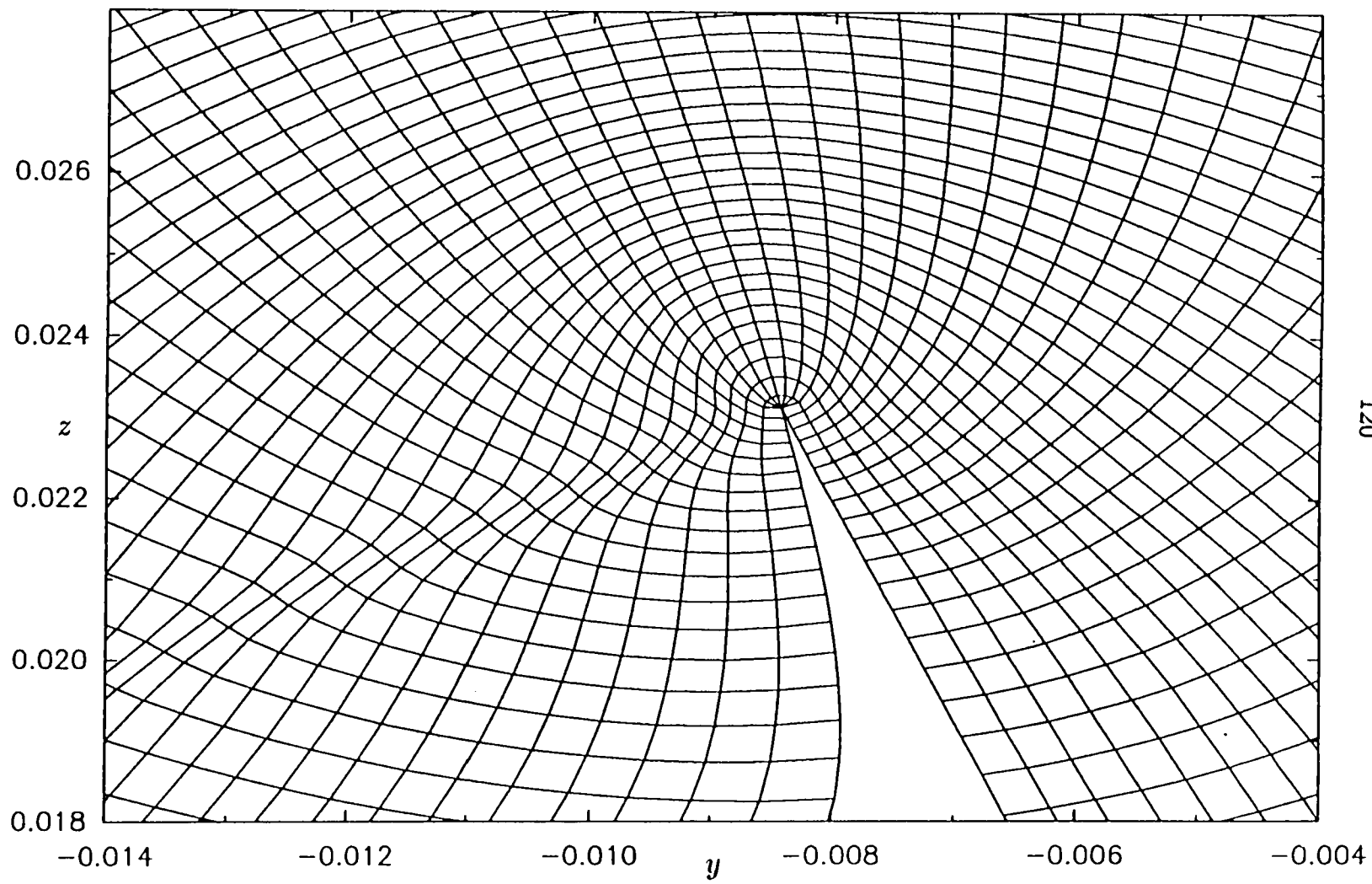
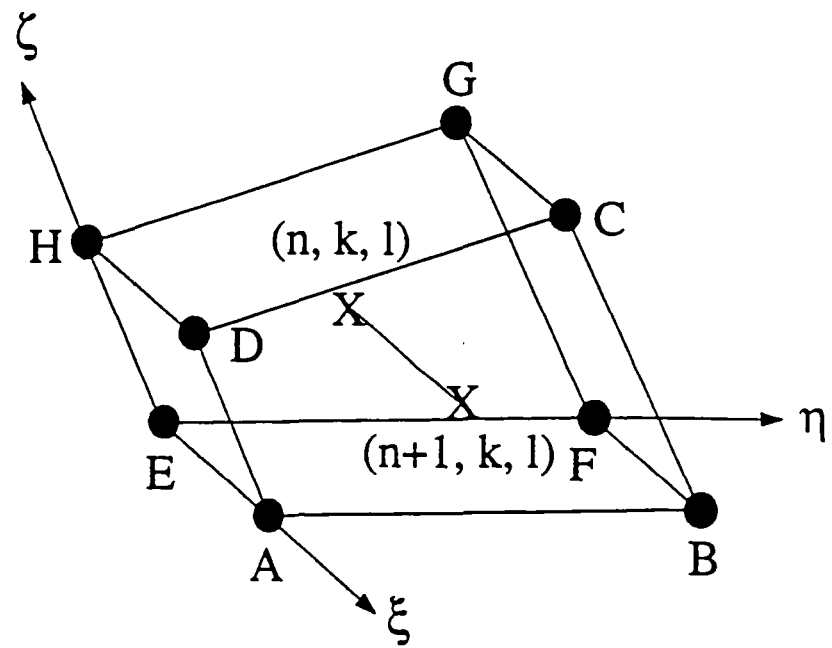


Fig. (5-7) Magnified Adaptive Grid





● = Primary Grid Points
 X = Secondary Grid Points

Fig.(5-8) Finite-Volume Element

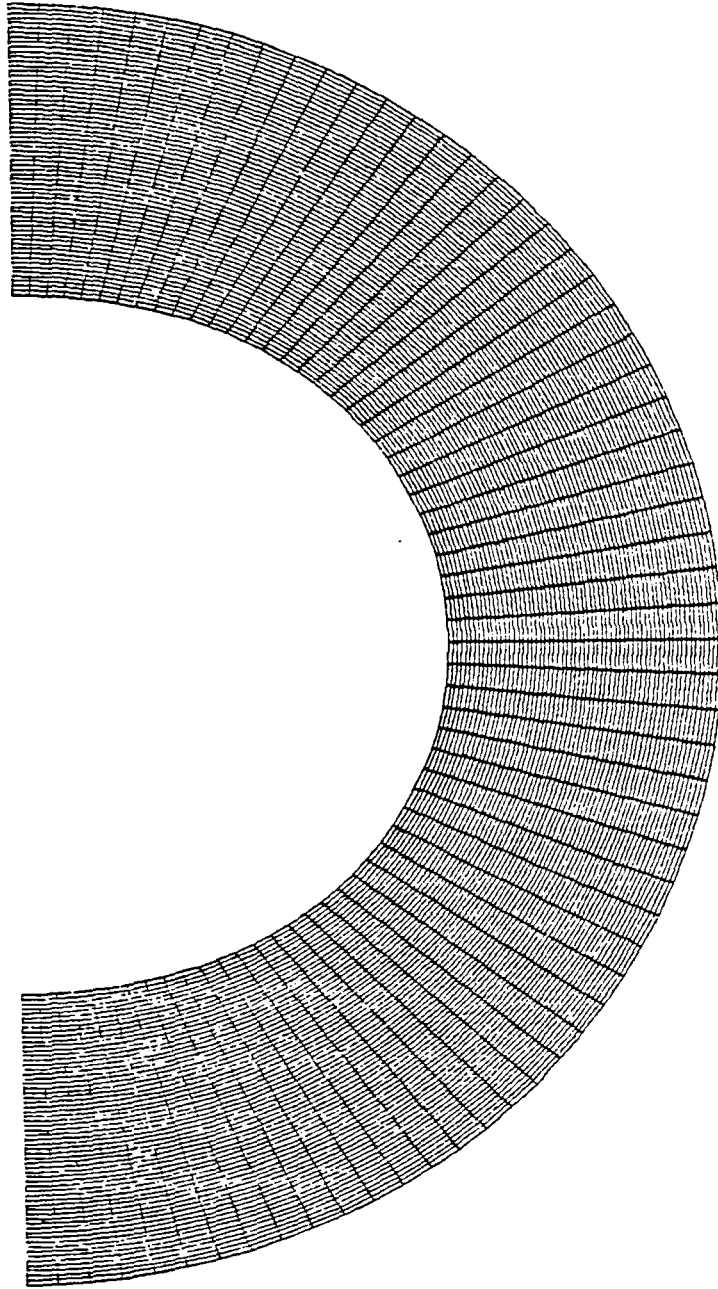


Fig. (6-1a) Grid for Elliptic-Cone Flow (for WR Type-*B*)

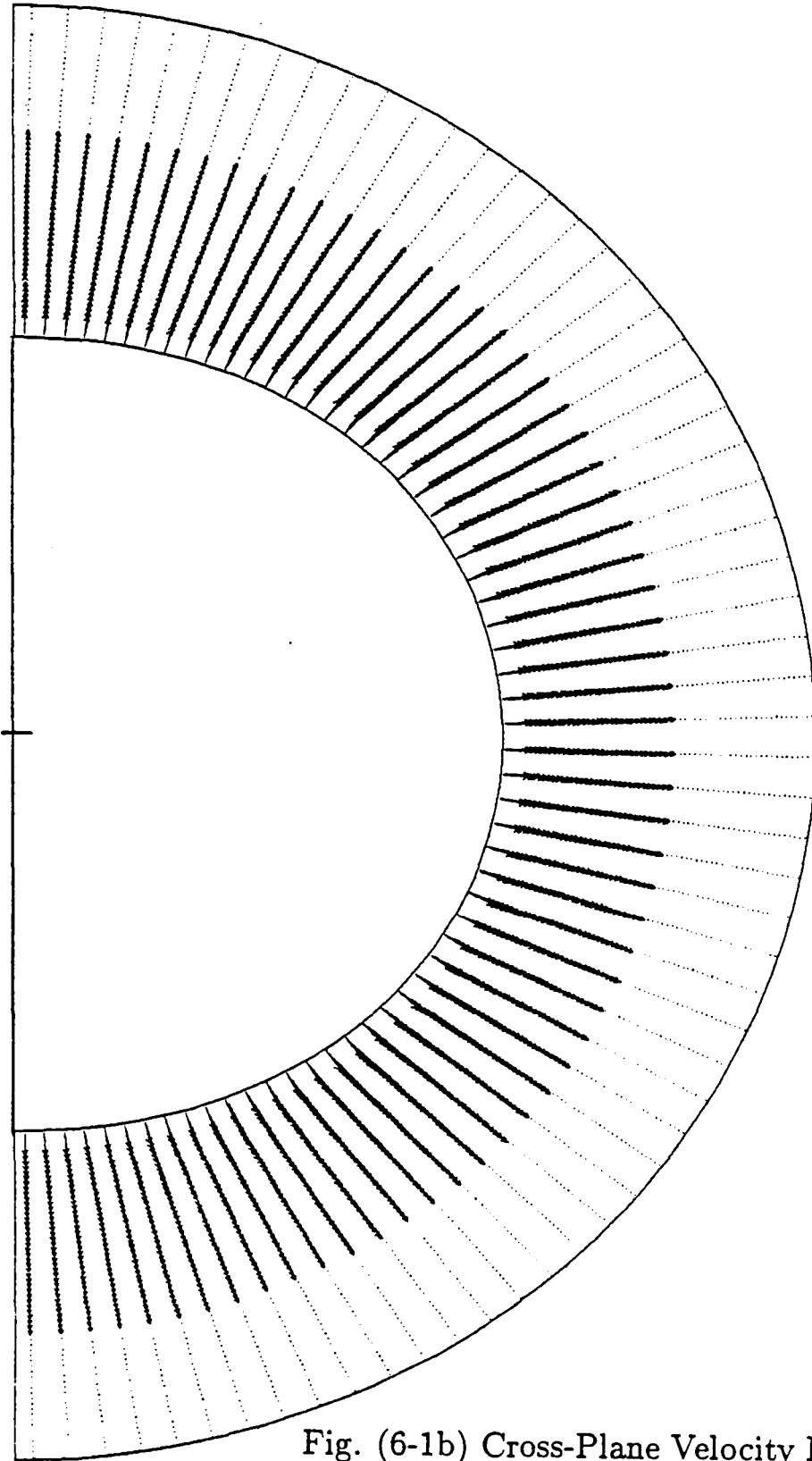


Fig. (6-1b) Cross-Plane Velocity Distribution

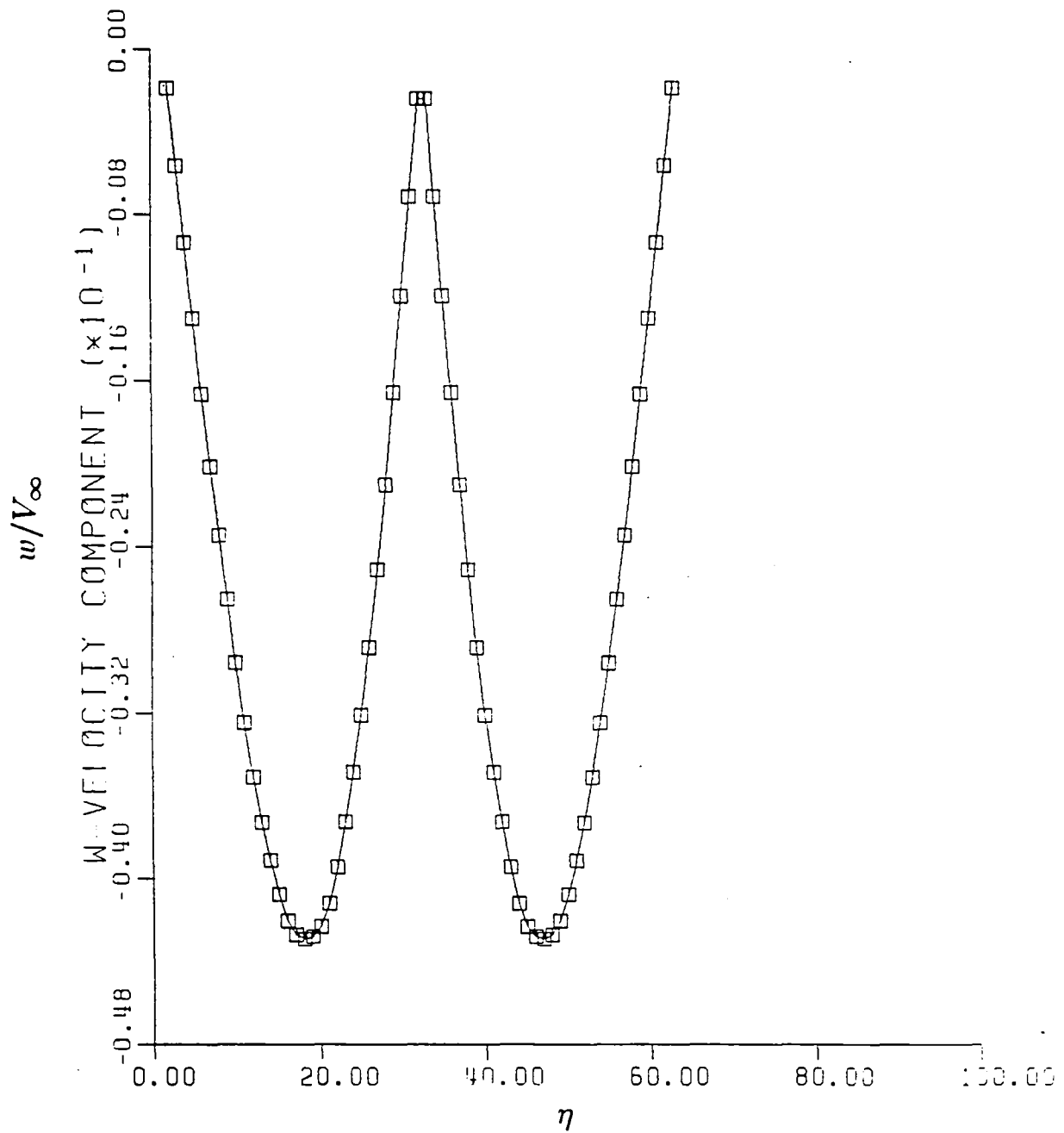


Fig. (6-1c) Azimuthal Velocity Component

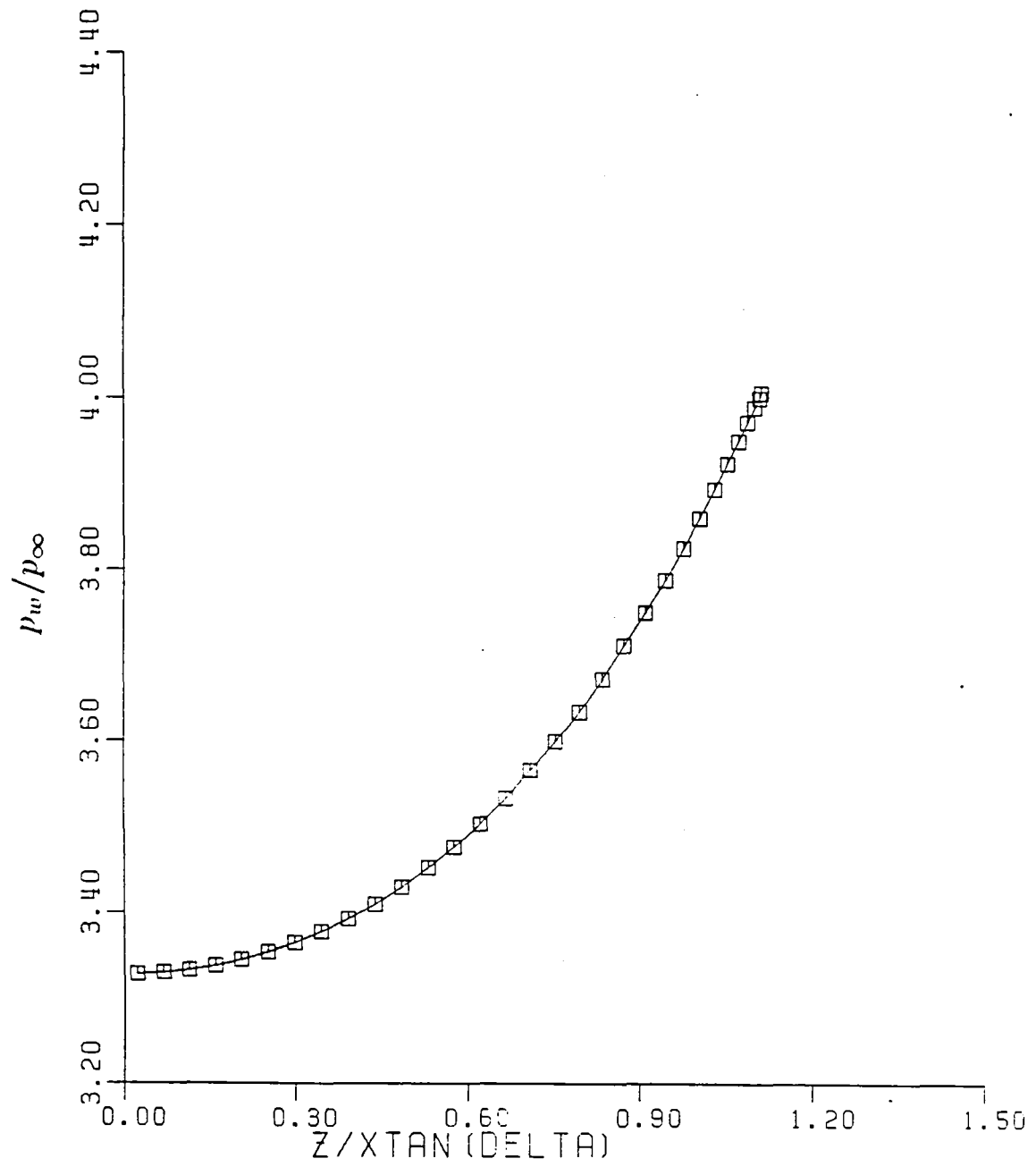


Fig. (6-1d) Wall Pressure Distribution

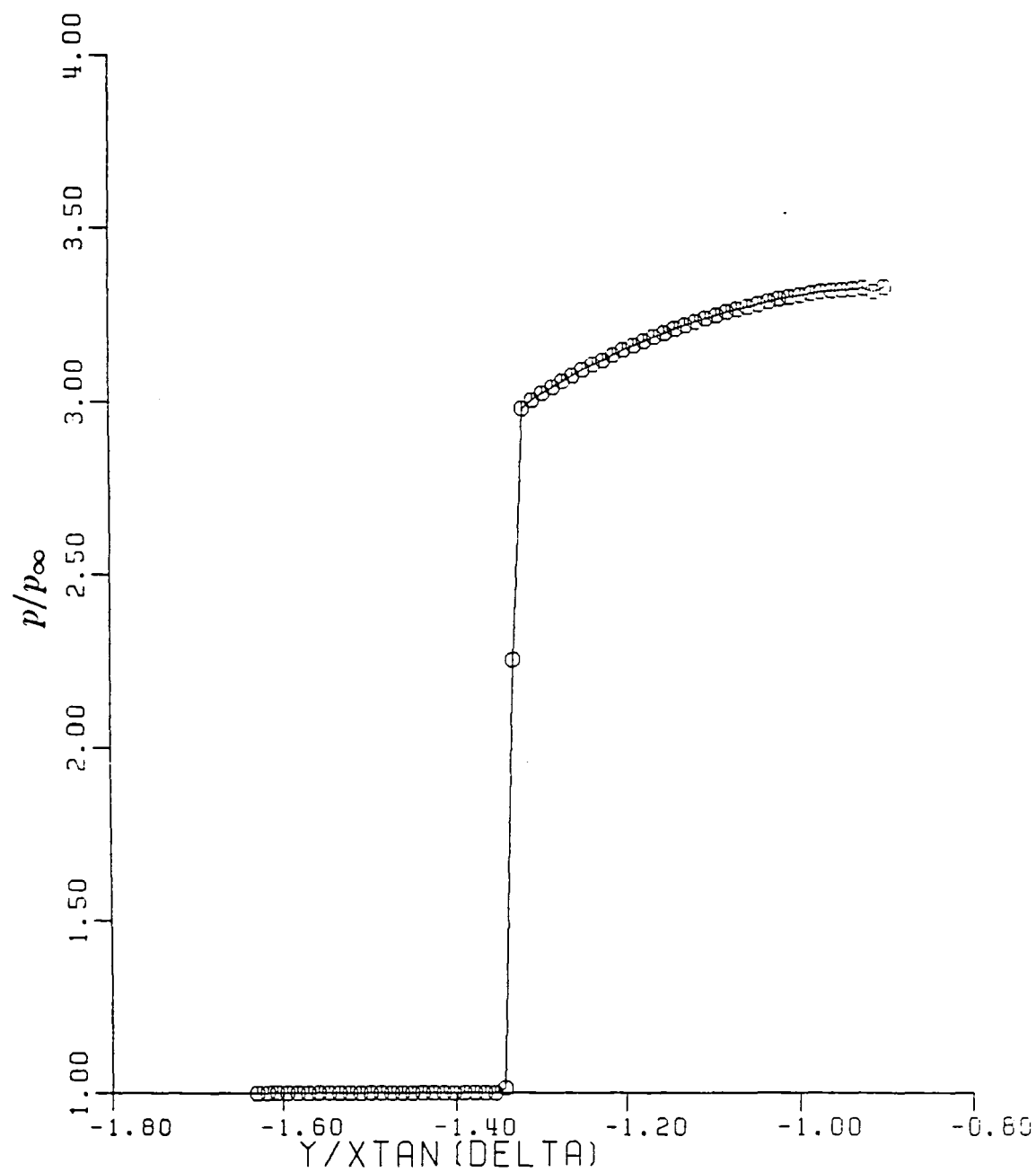


Fig. (6-1e) Pressure near Lower Symmetry Plane

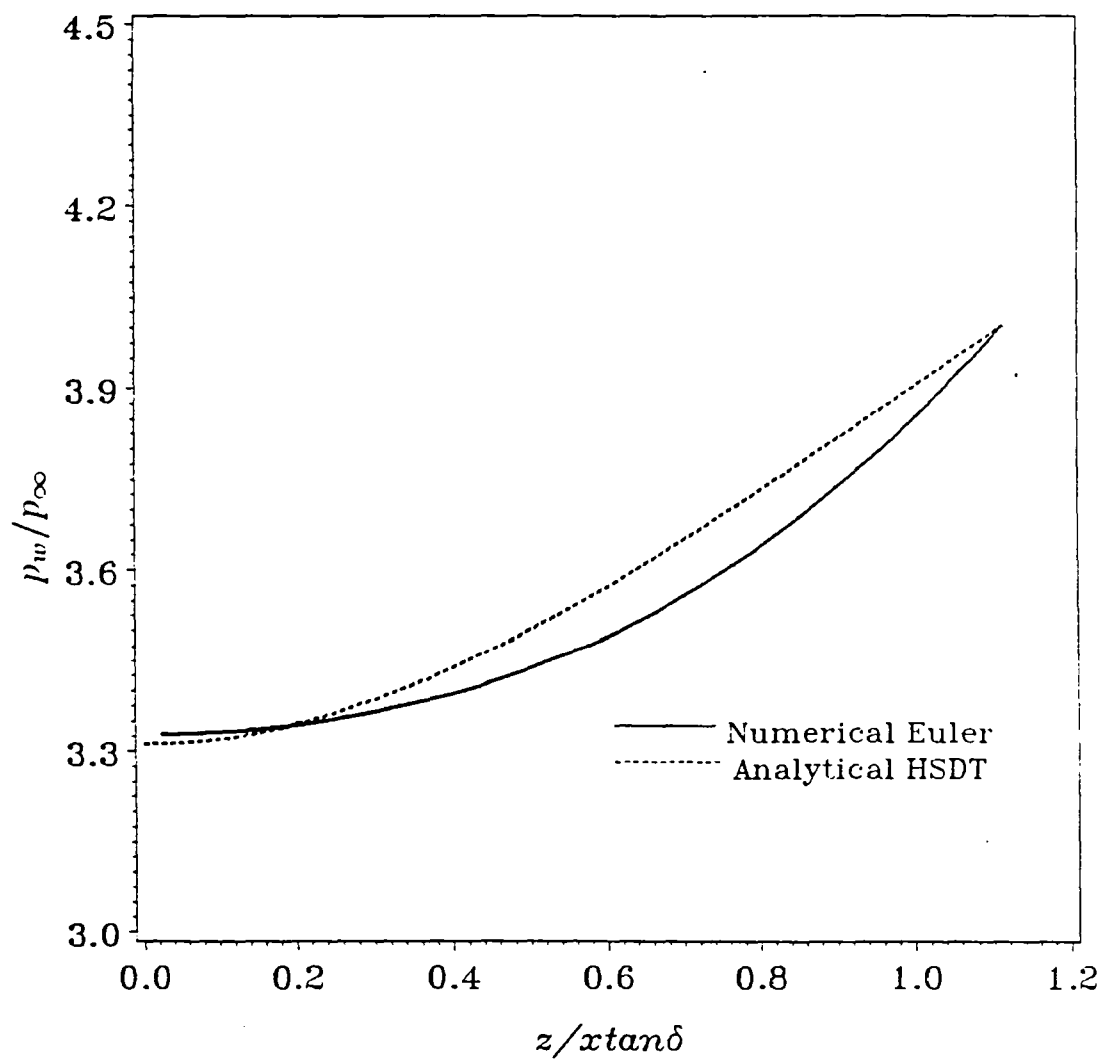


Fig. (6-1f) Wall Pressure Comparison

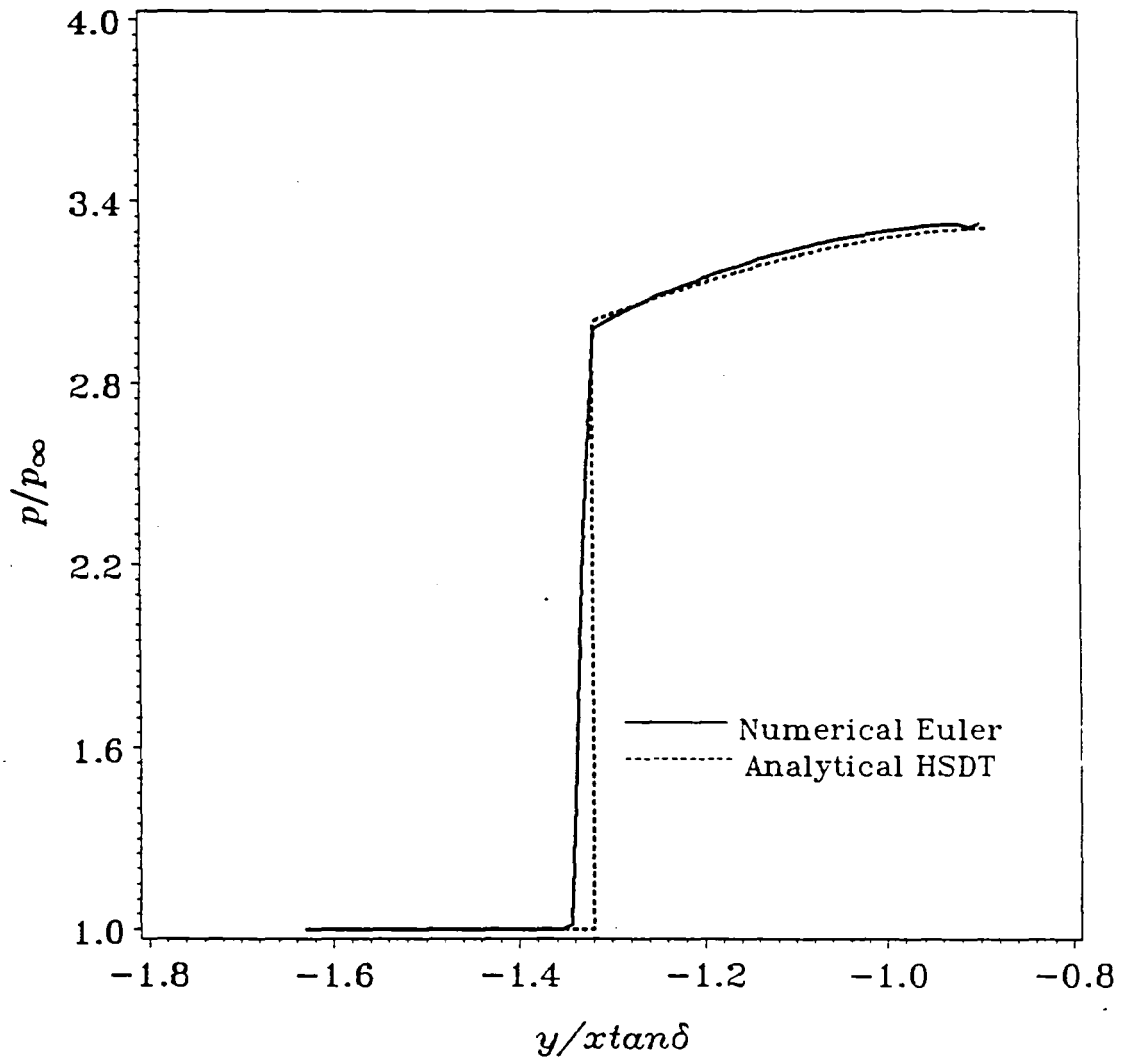


Fig. (6-1g) Comparison of Pressure near Lower Symmetry Plane

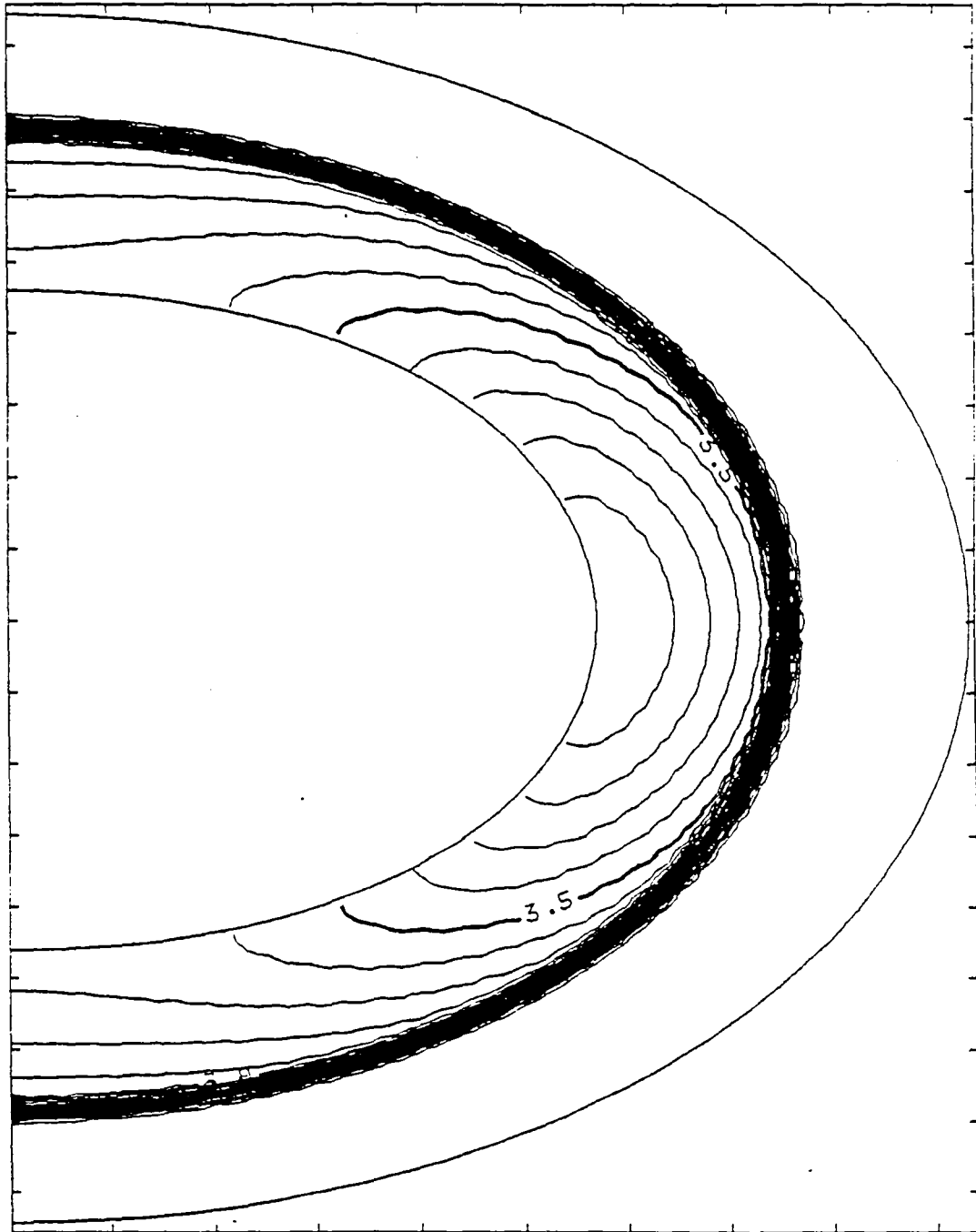


Fig. (6-1h) Pressure Contours

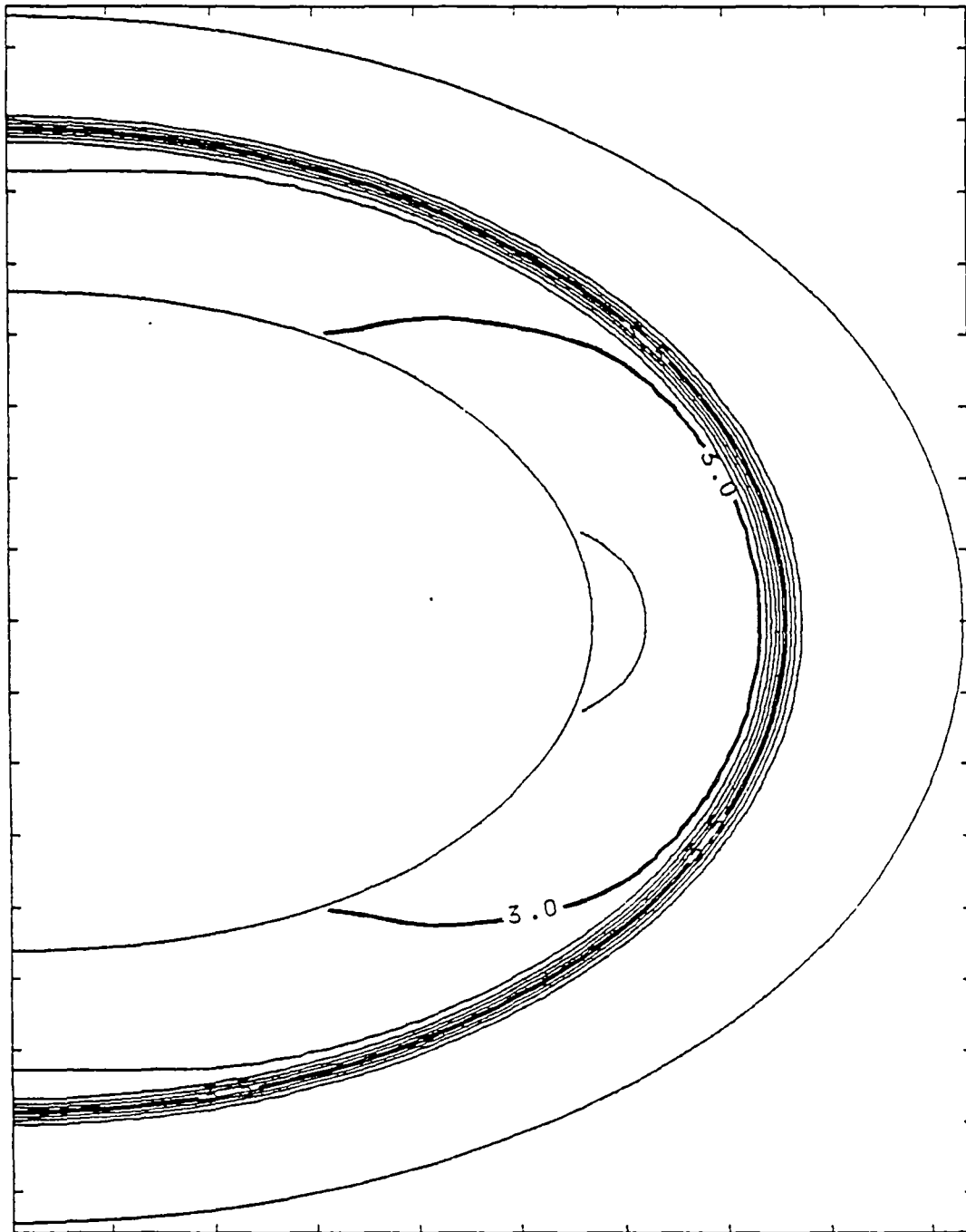


Fig. (6-1i) Mach Number Contours

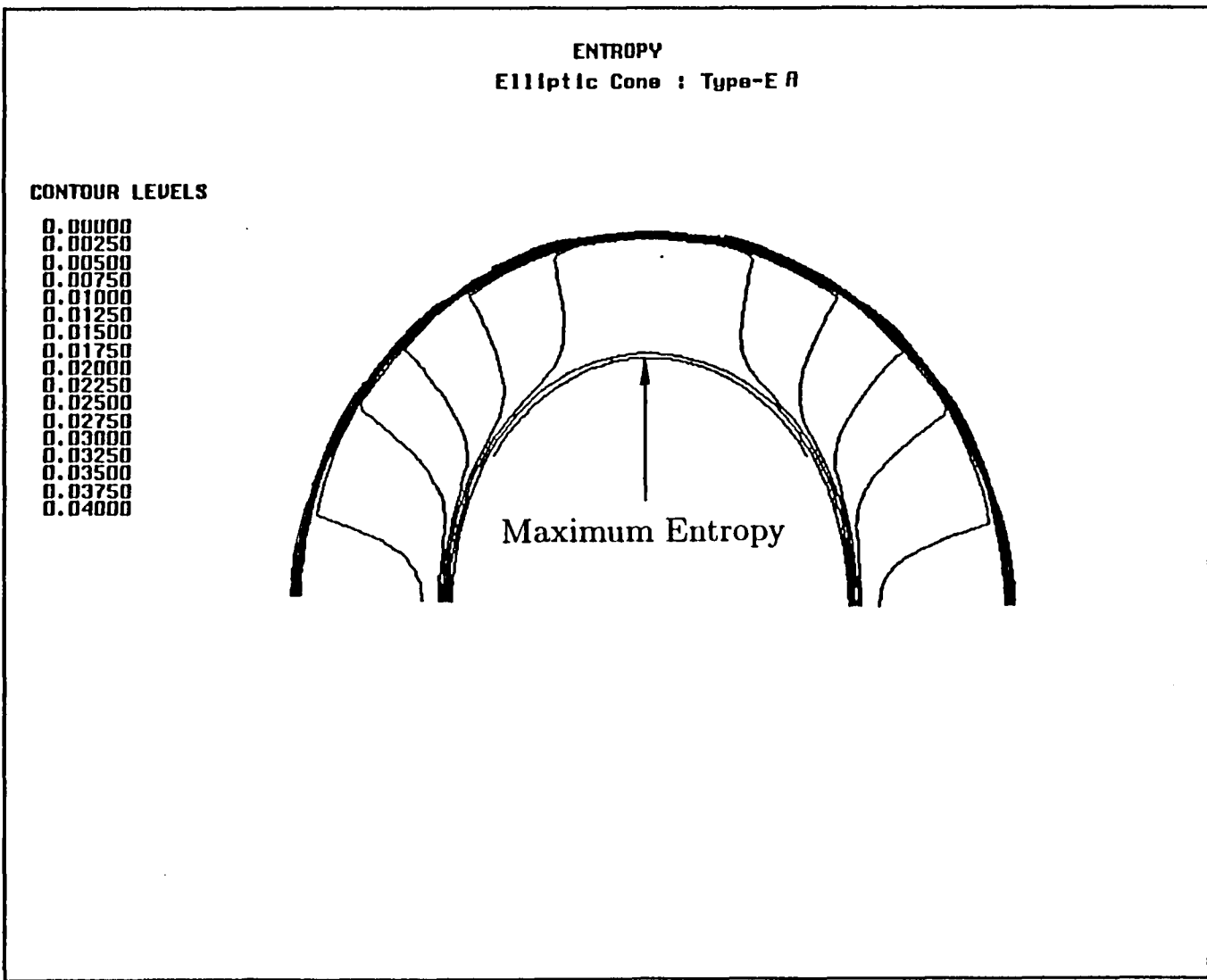


Fig. (6-2a) Entropy Contours ($\delta = 12^\circ$ Elliptic Cone)

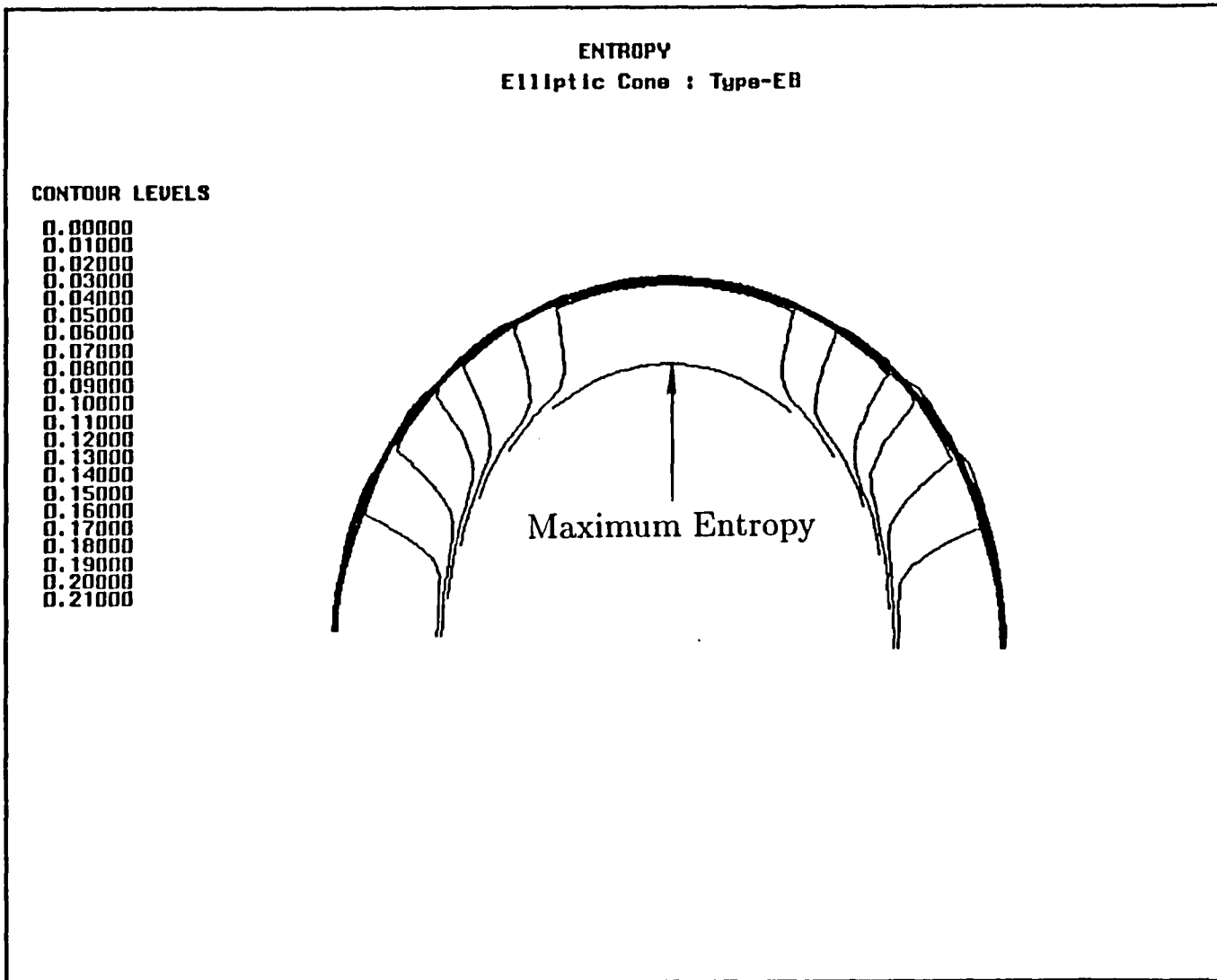


Fig. (6-2b) Entropy Contours ($\delta = 18.62^\circ$ Elliptic Cone)

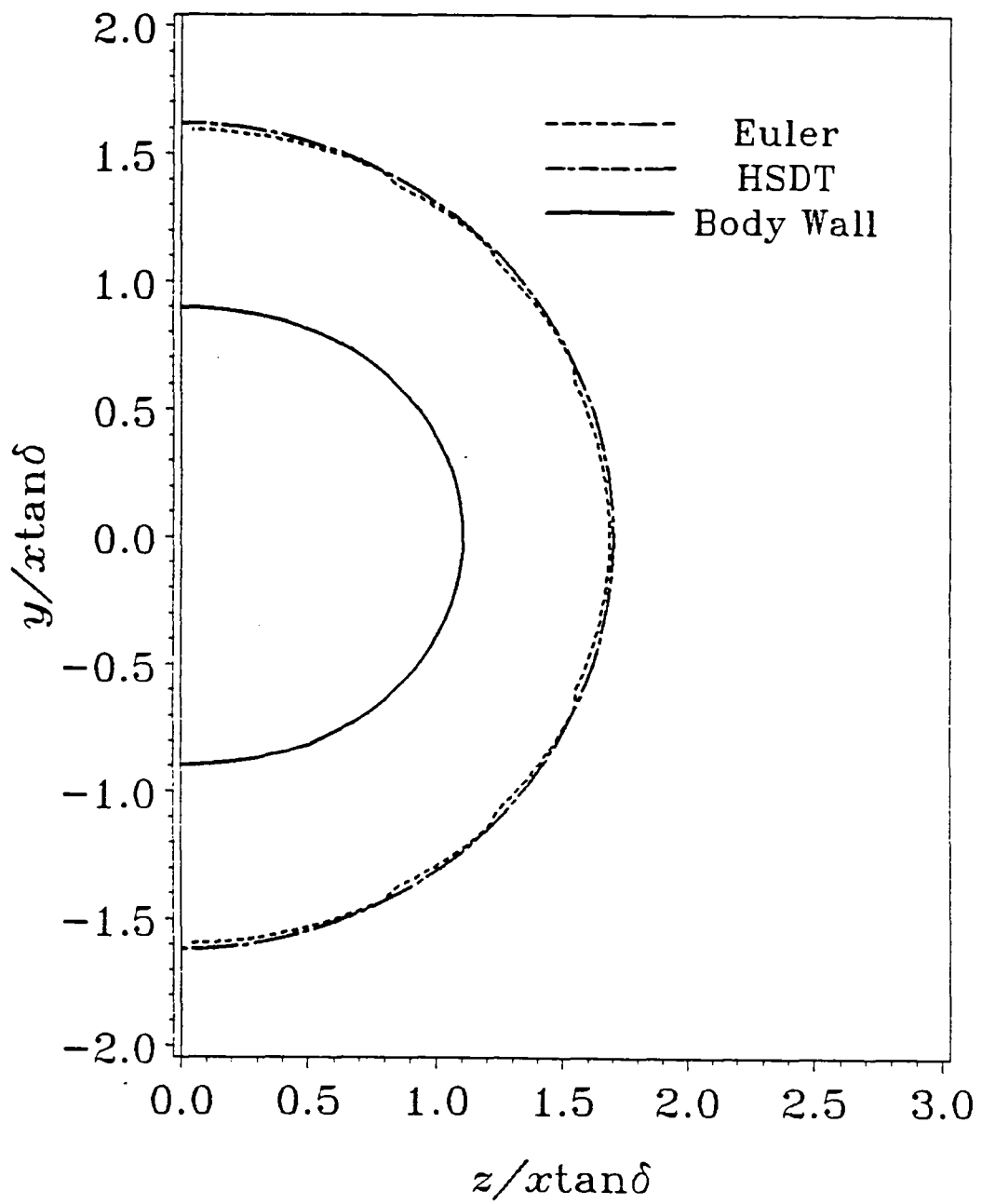


Fig. (6-3a) Shock Comparison ($\delta = 12^\circ$ Elliptic Cone)

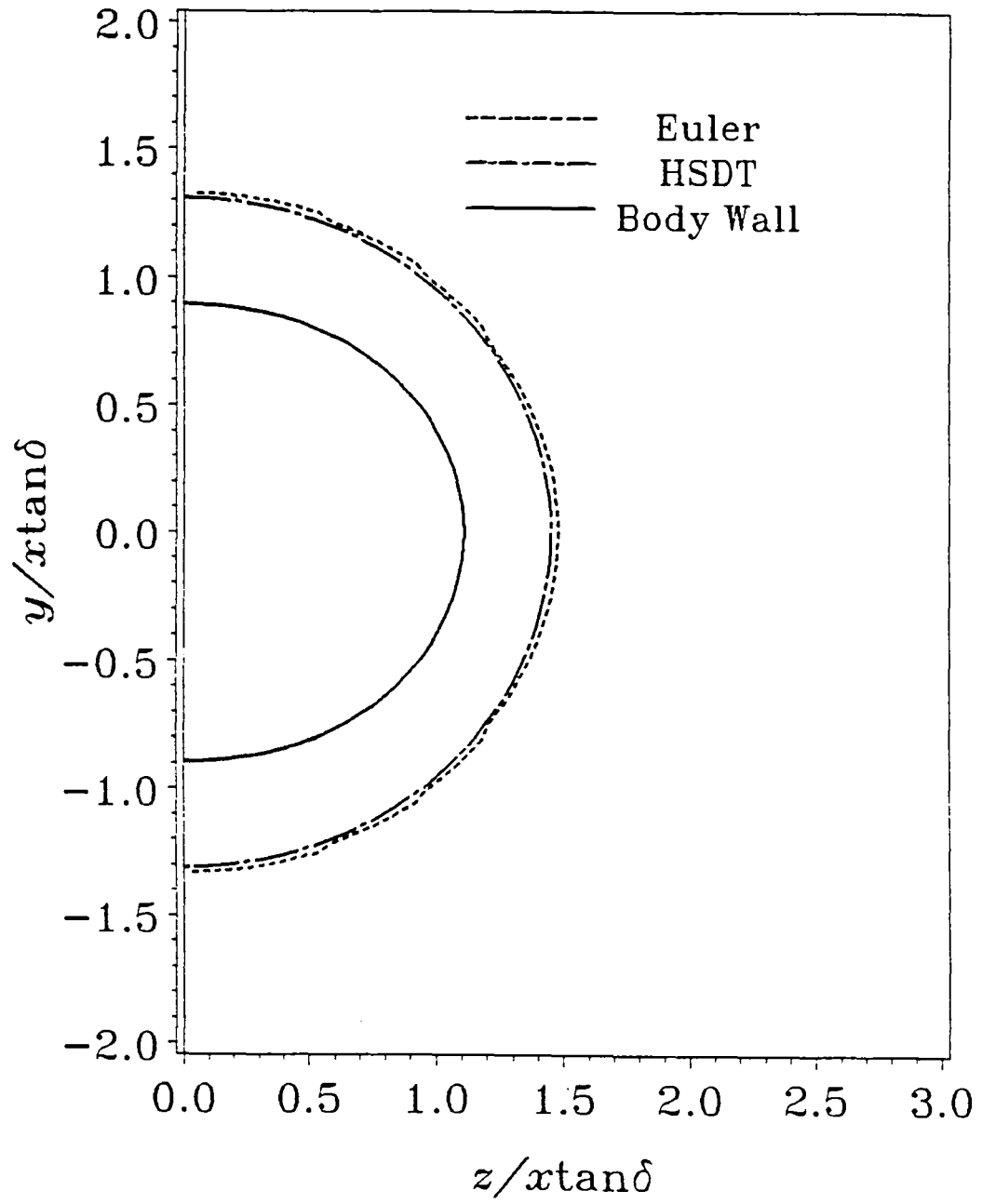


Fig. (6-3b) Shock Comparison ($\delta = 18$) 62° Elliptic Cone)

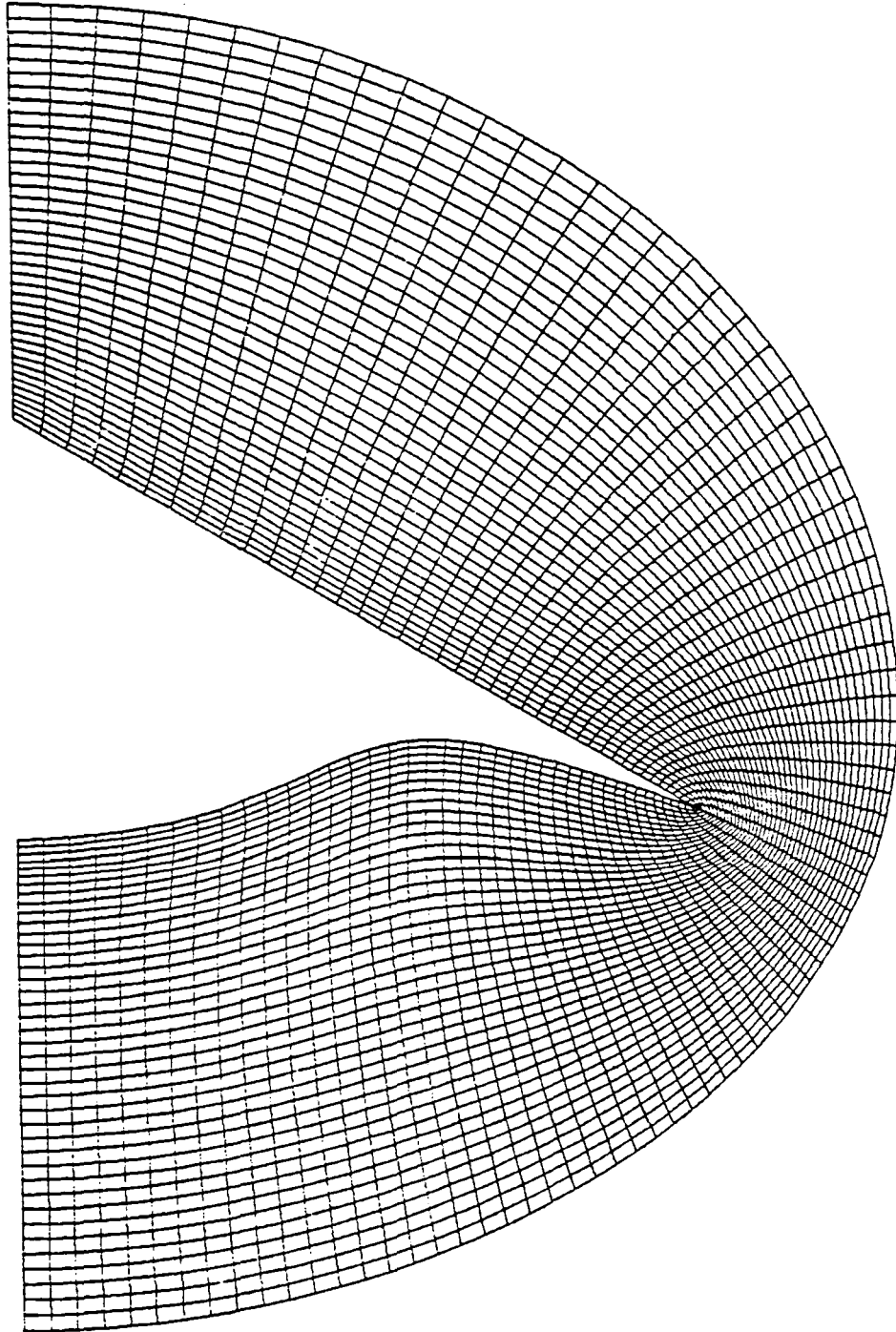


Fig. (7-1a) Grid for Type-A1O Waverider

(On-Design, WR Type-A1O)

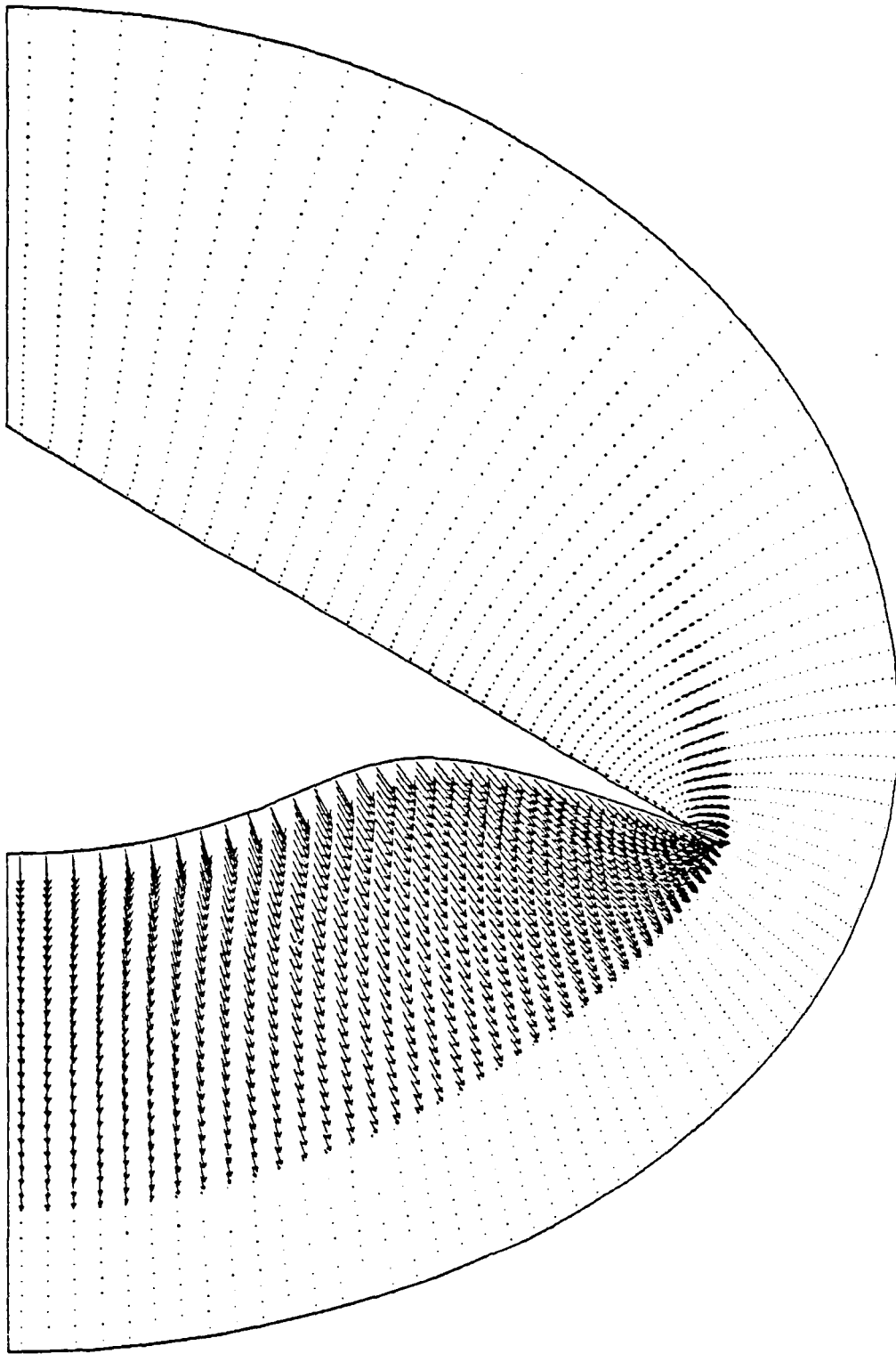


Fig. (7-1b) Cross-Plane Velocity Distribution

(On-Design, WR Type-A10)

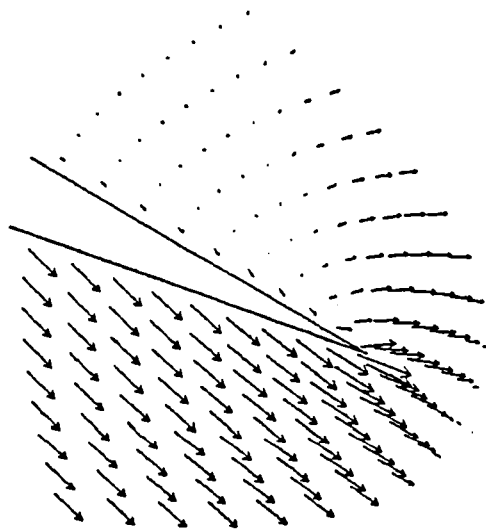


Fig. (7-1c) Magnified Cross-Plane Velocity near Tip

(On-Design, WR Type-A1O)

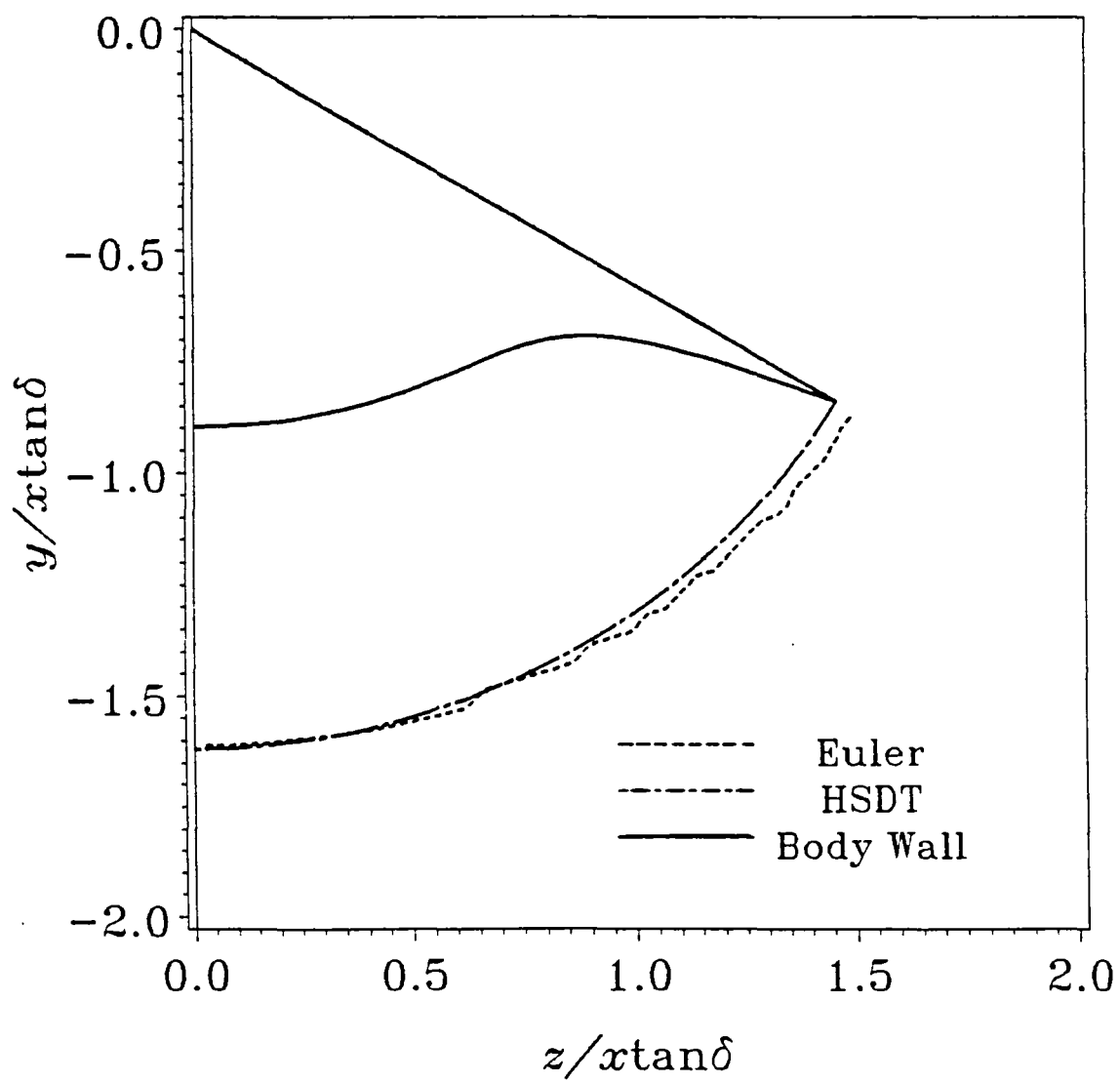


Fig. (7-1d) Shock Location Comparison

(On-Design, WR Type-A1O)

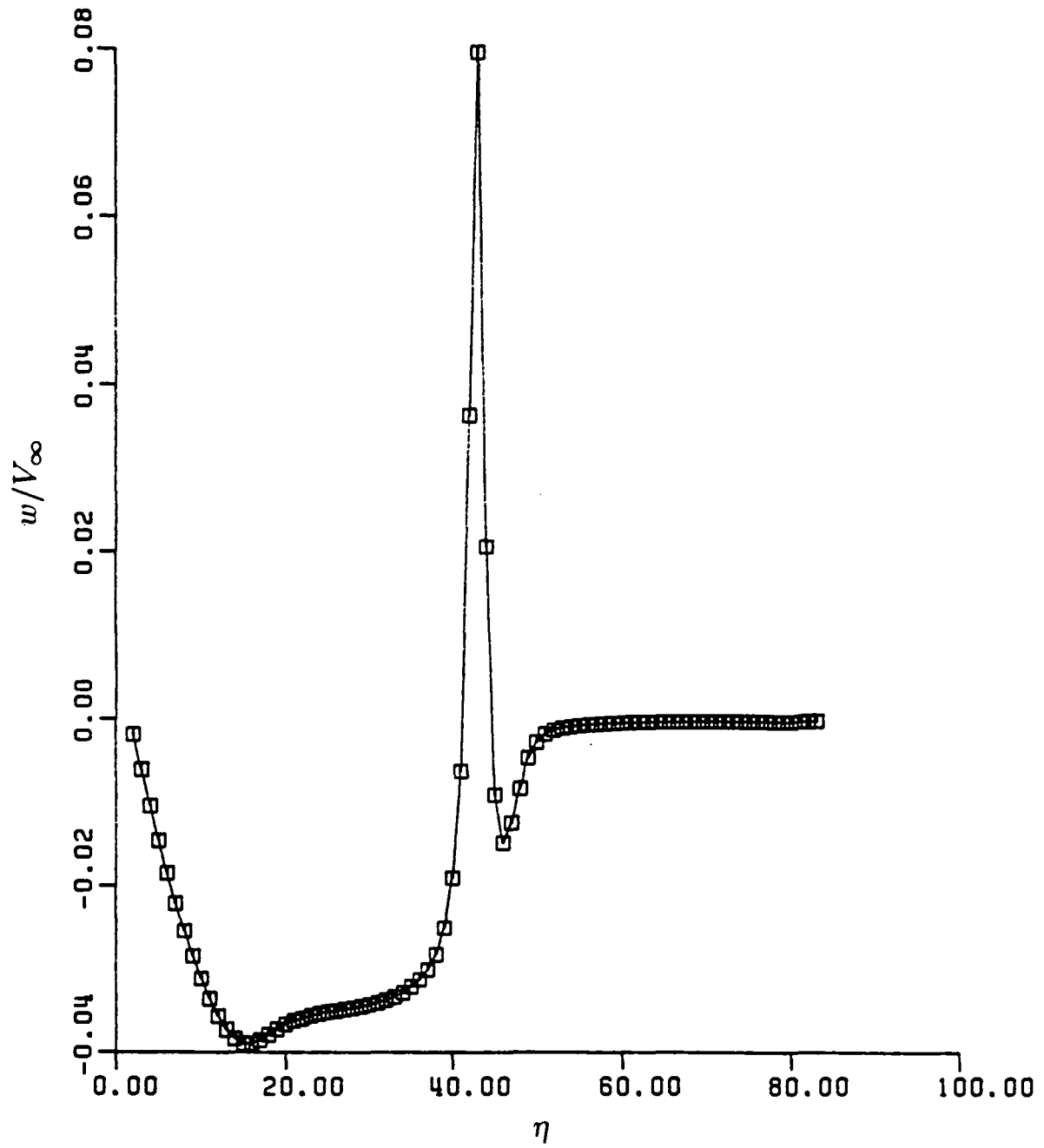


Fig. (7-1e) Azimuthal Velocity Component

(On-Design, WR Type-A1O)

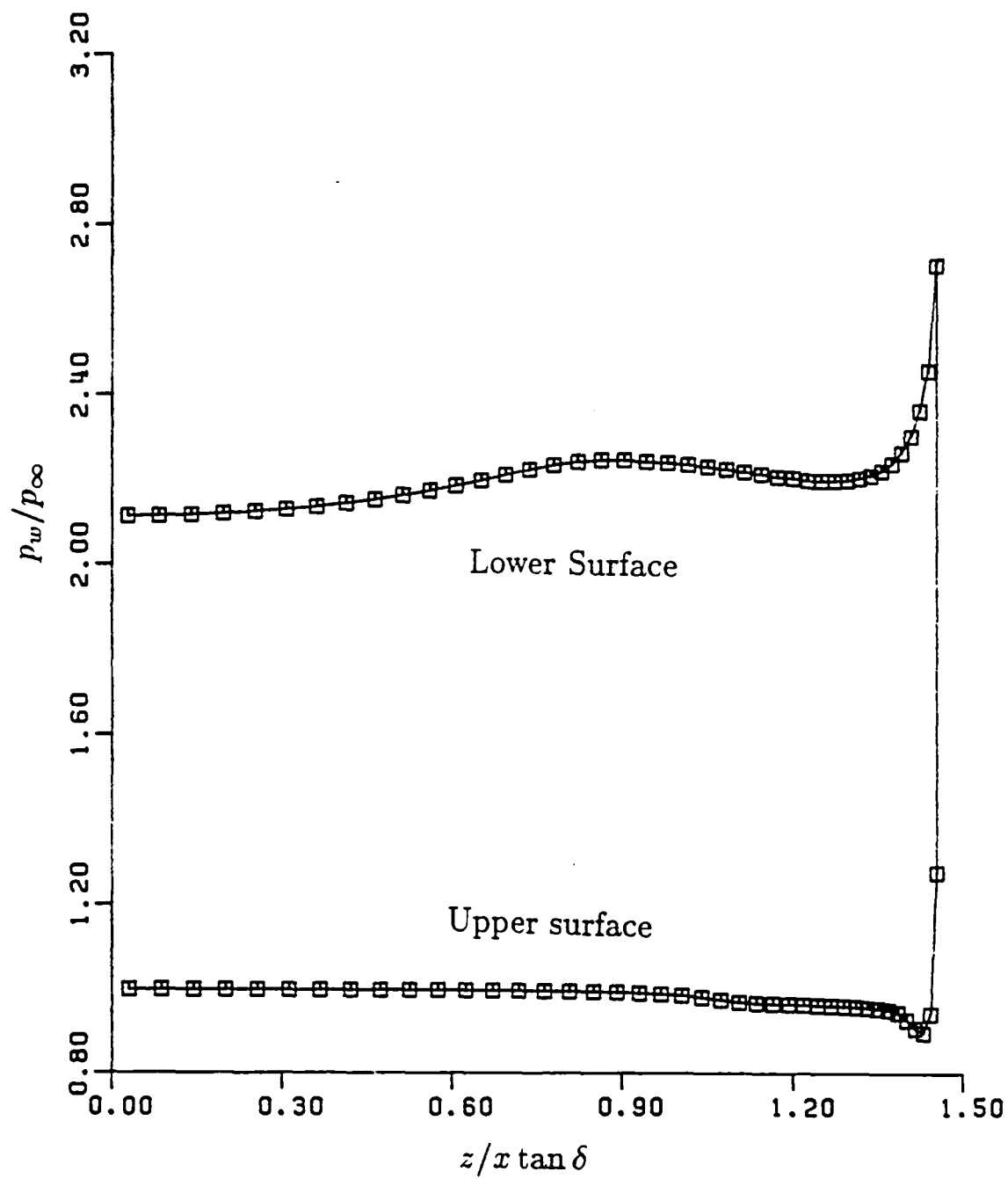


Fig. (7-1f) Wall Pressure Distribution

(On-Design, WR Type-A10)

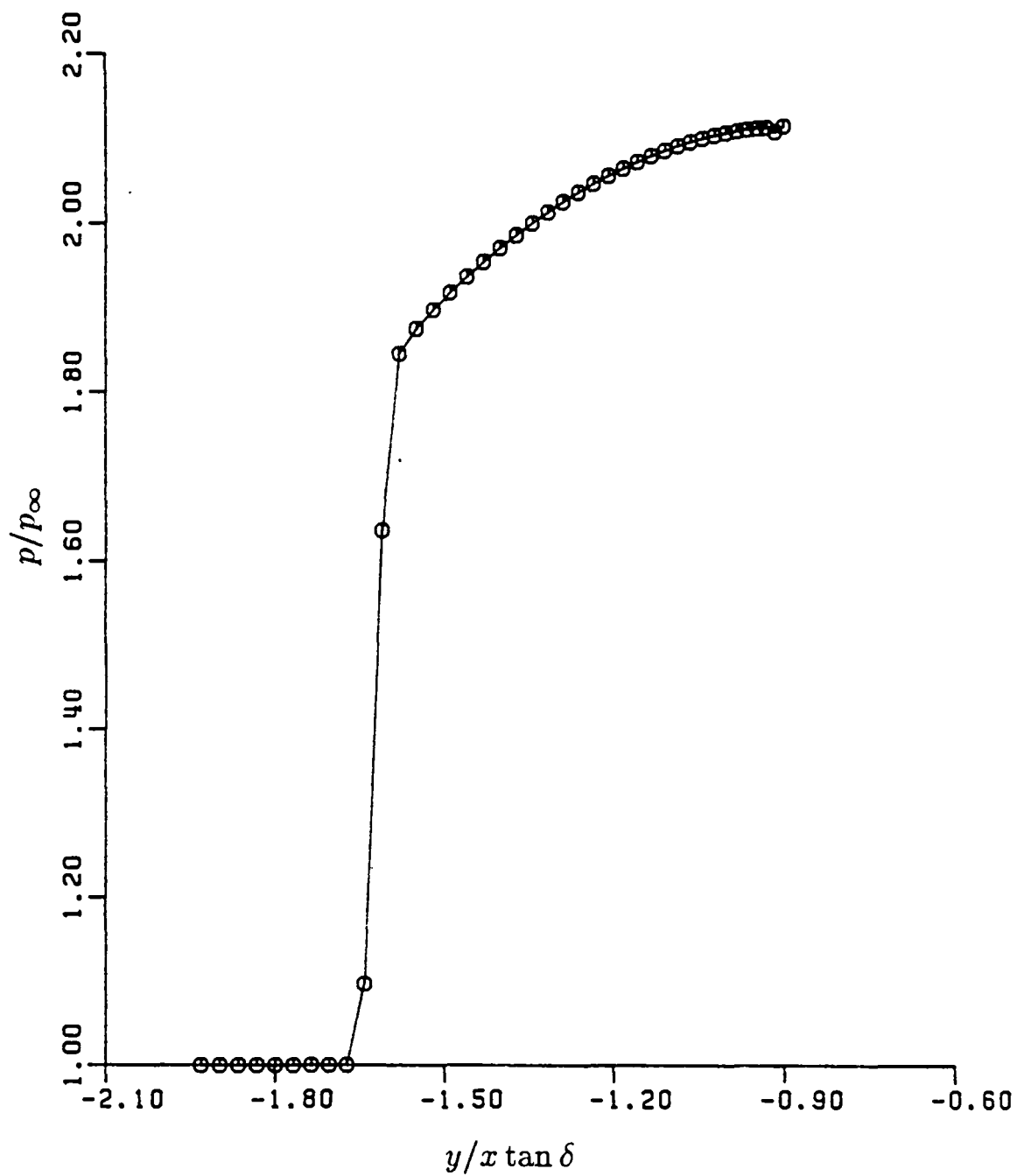


Fig. (7-1g) Pressure near Lower Symmetry Plane

(On-Design, WR Type-A10)

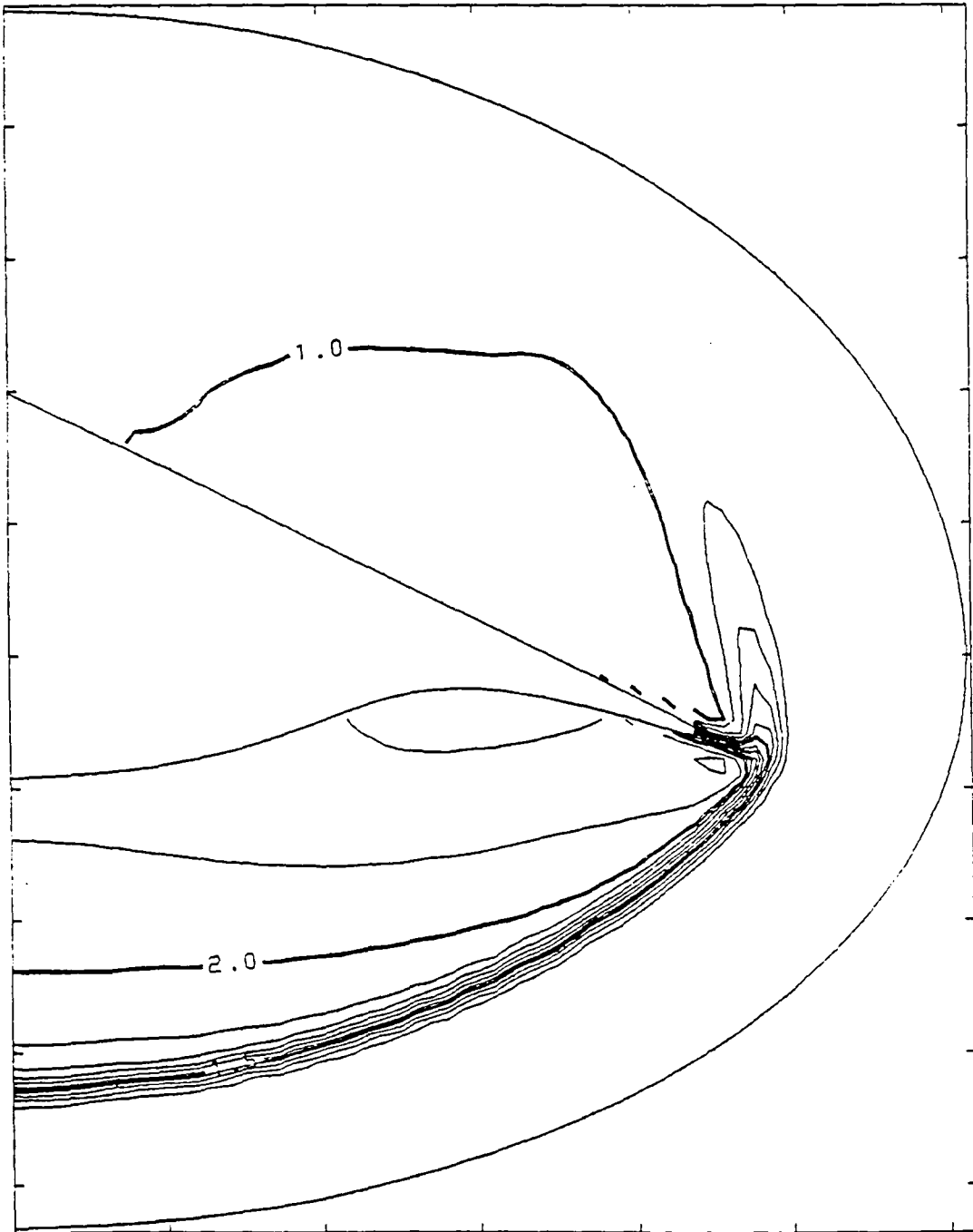


Fig. (7-1h) Pressure Contours

(On-Design, WR Type-A10)

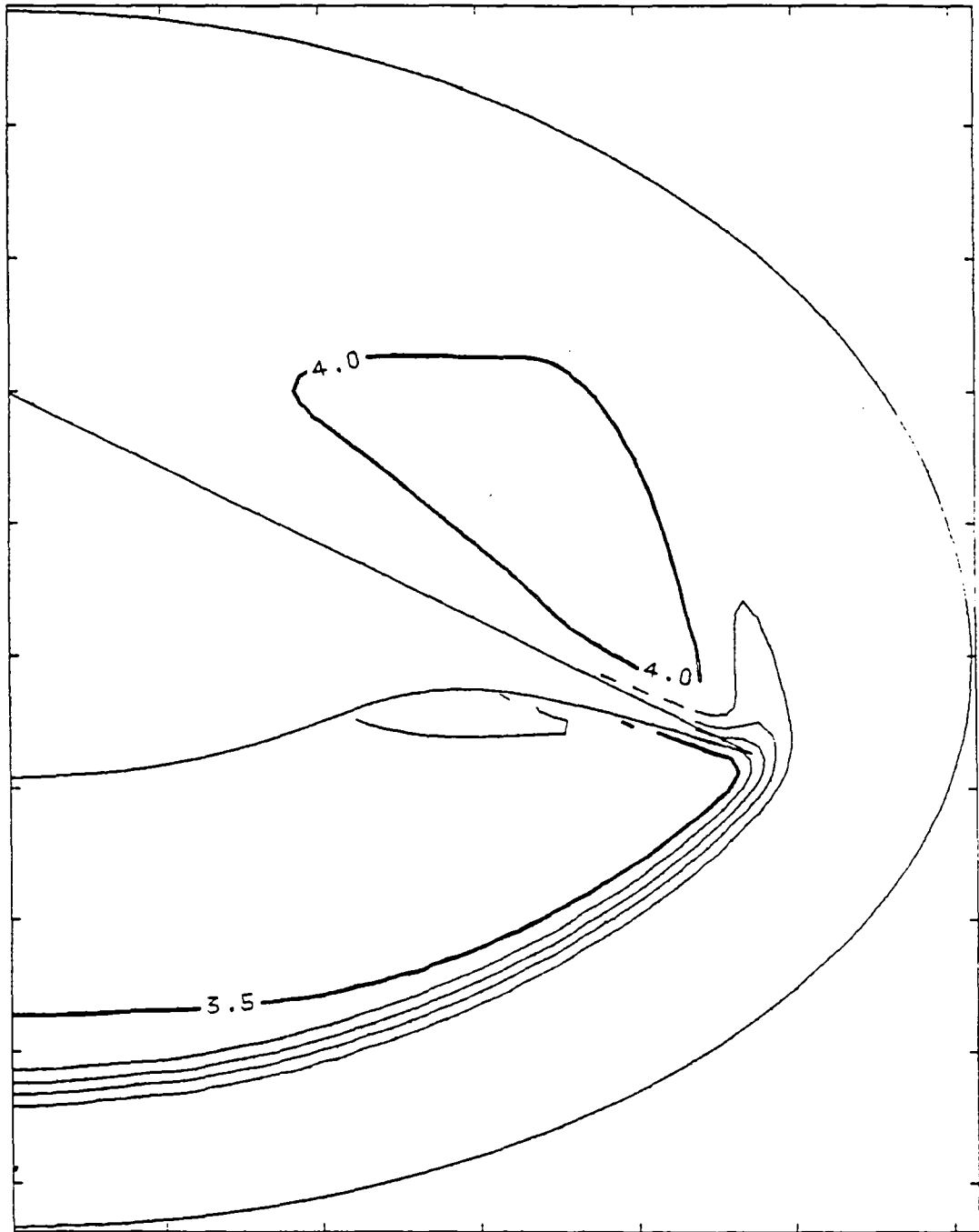


Fig. (7-1i) Mach Number Contours

(On-Design, WR Type-A10)

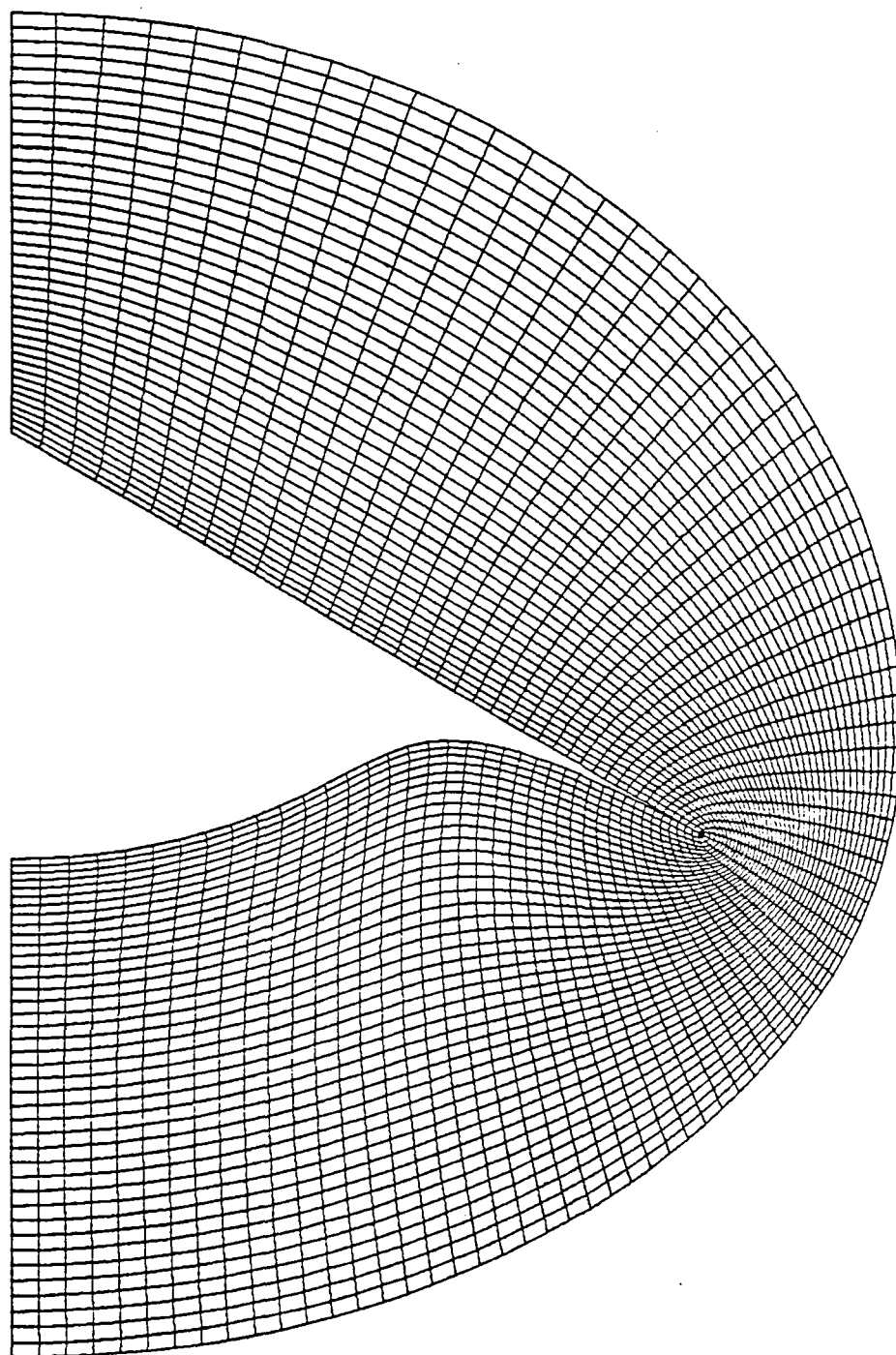


Fig. (7-2a) Grid for Type-A2F Waverider

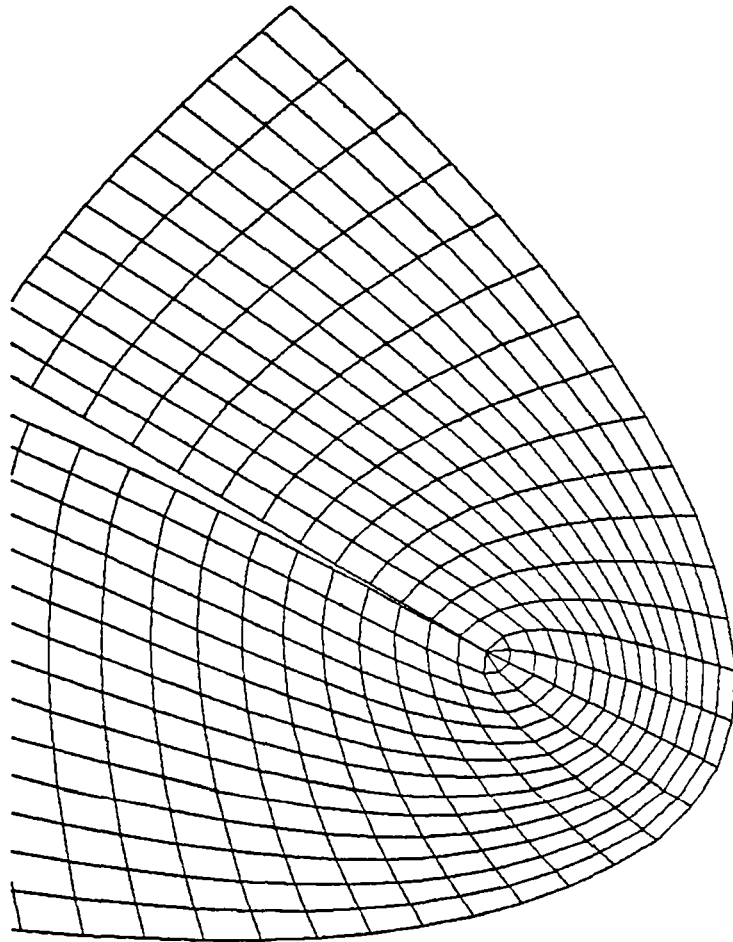


Fig. (7-2a') Magnified Fan-grid for Tip Region

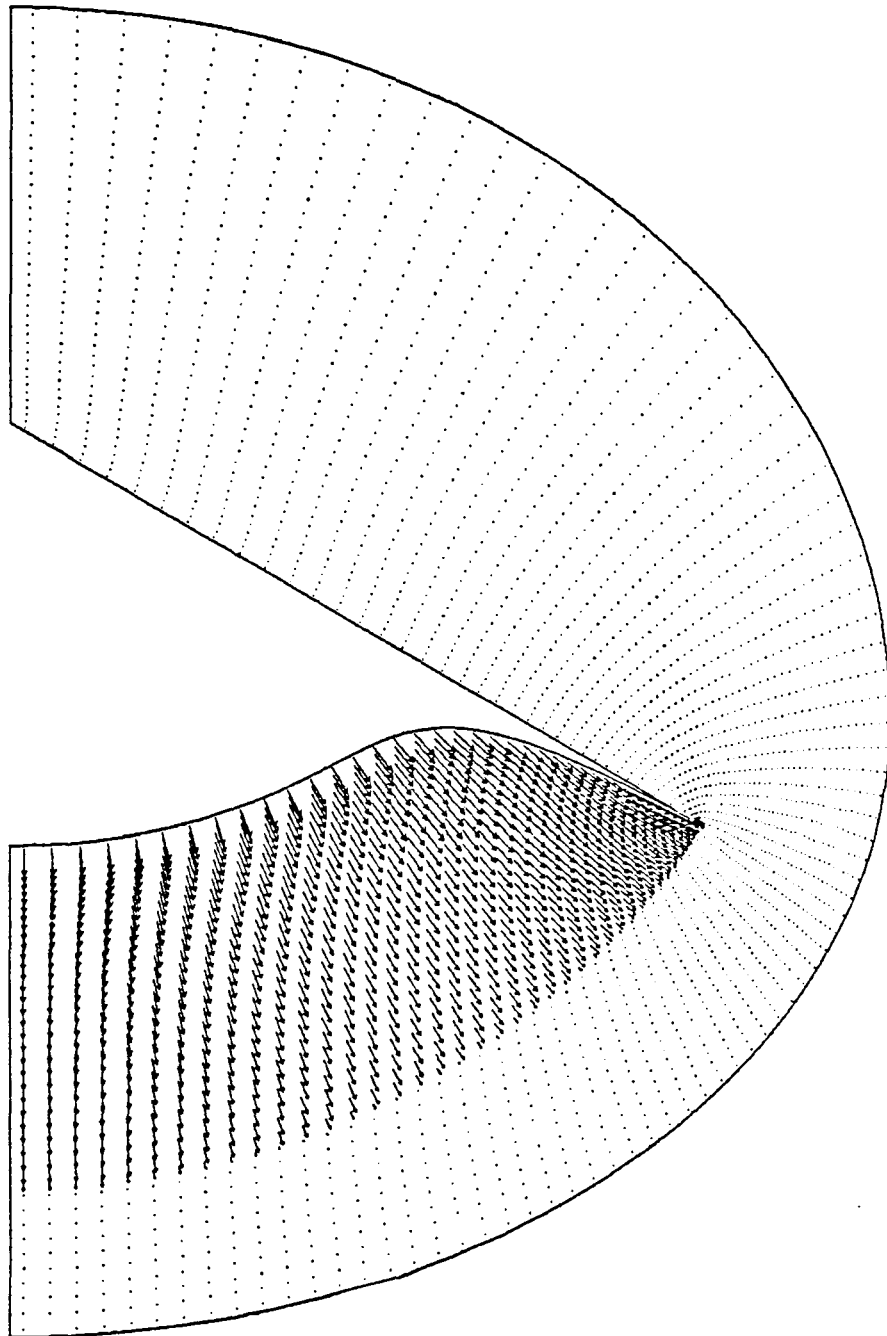


Fig. (7-2b) Cross-Plane Velocity Distribution

(On-Design, WR Type-A2F)

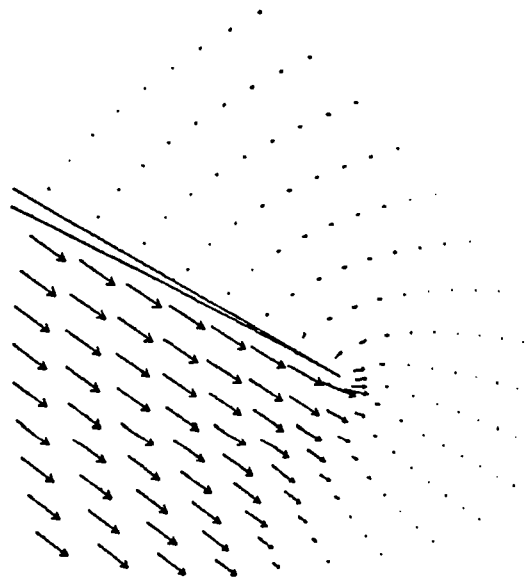


Fig. (7-2c) Magnified Cross-Plane Velocity near Tip

(On-Design, WR Type-A2F)

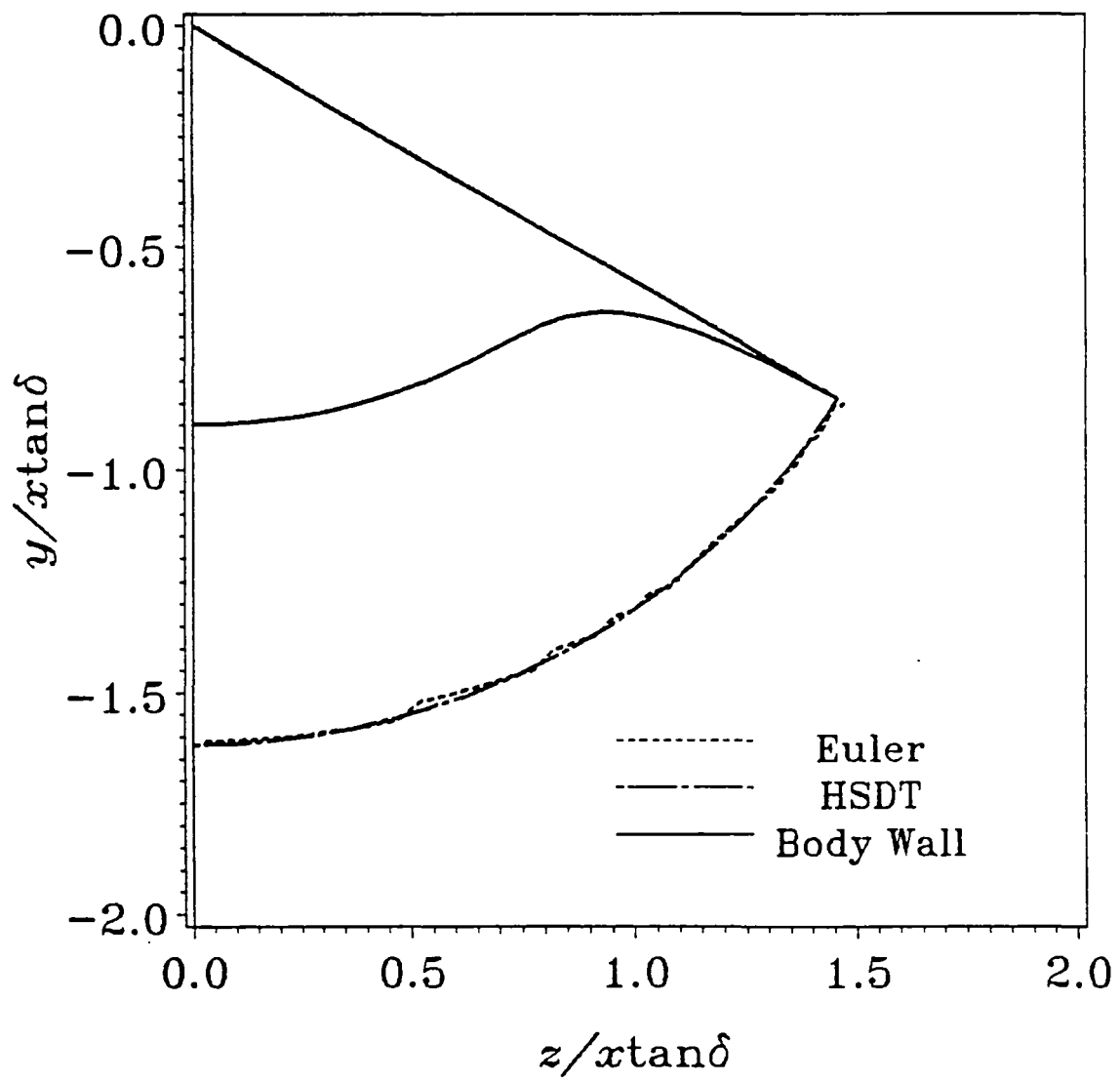


Fig. (7-2d) Shock Location Comparison

(On-Design, WR Type-A2F)

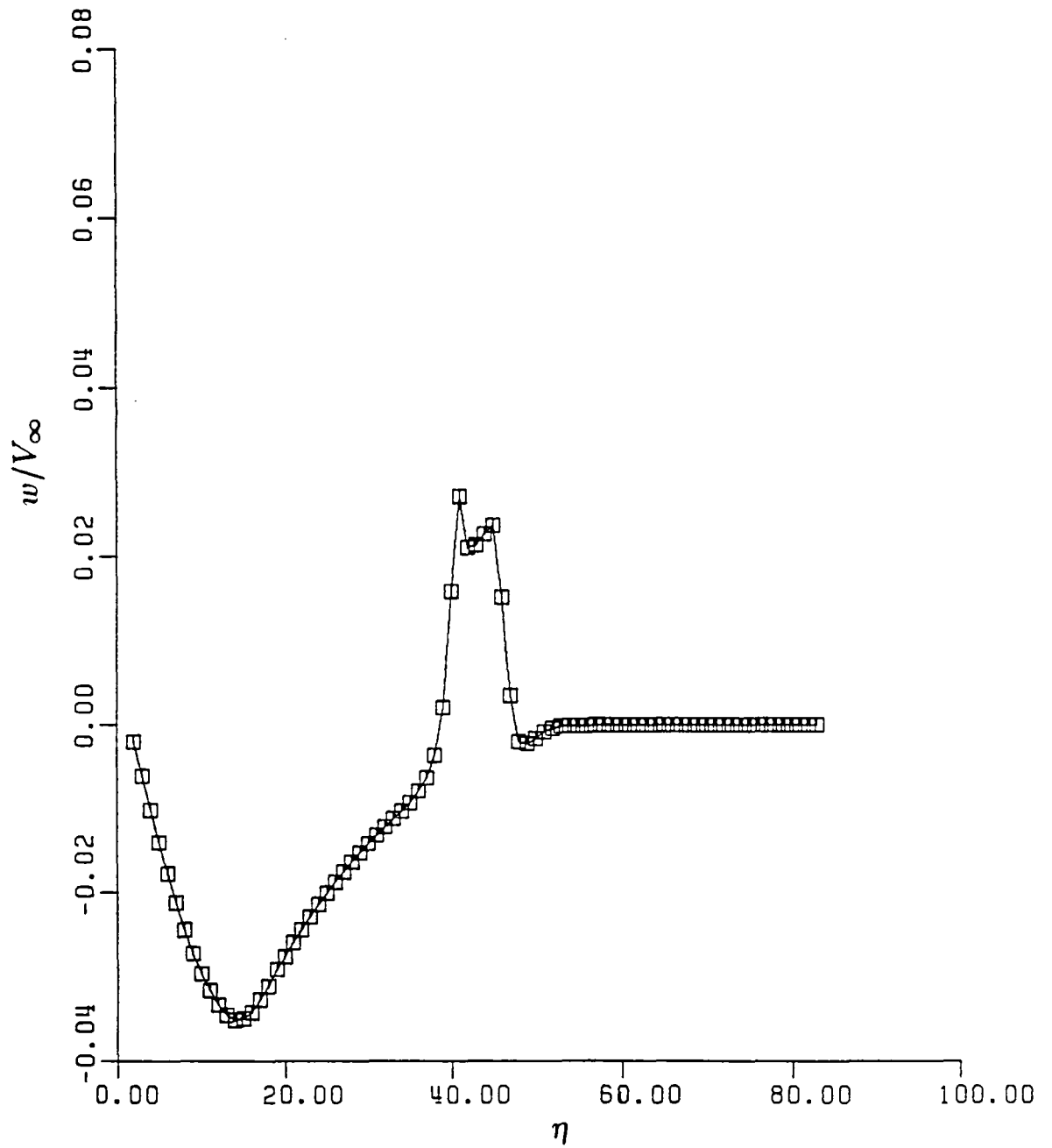


Fig. (7-2e) Azimuthal Velocity Component

(On-Design, WR Type-A2F)

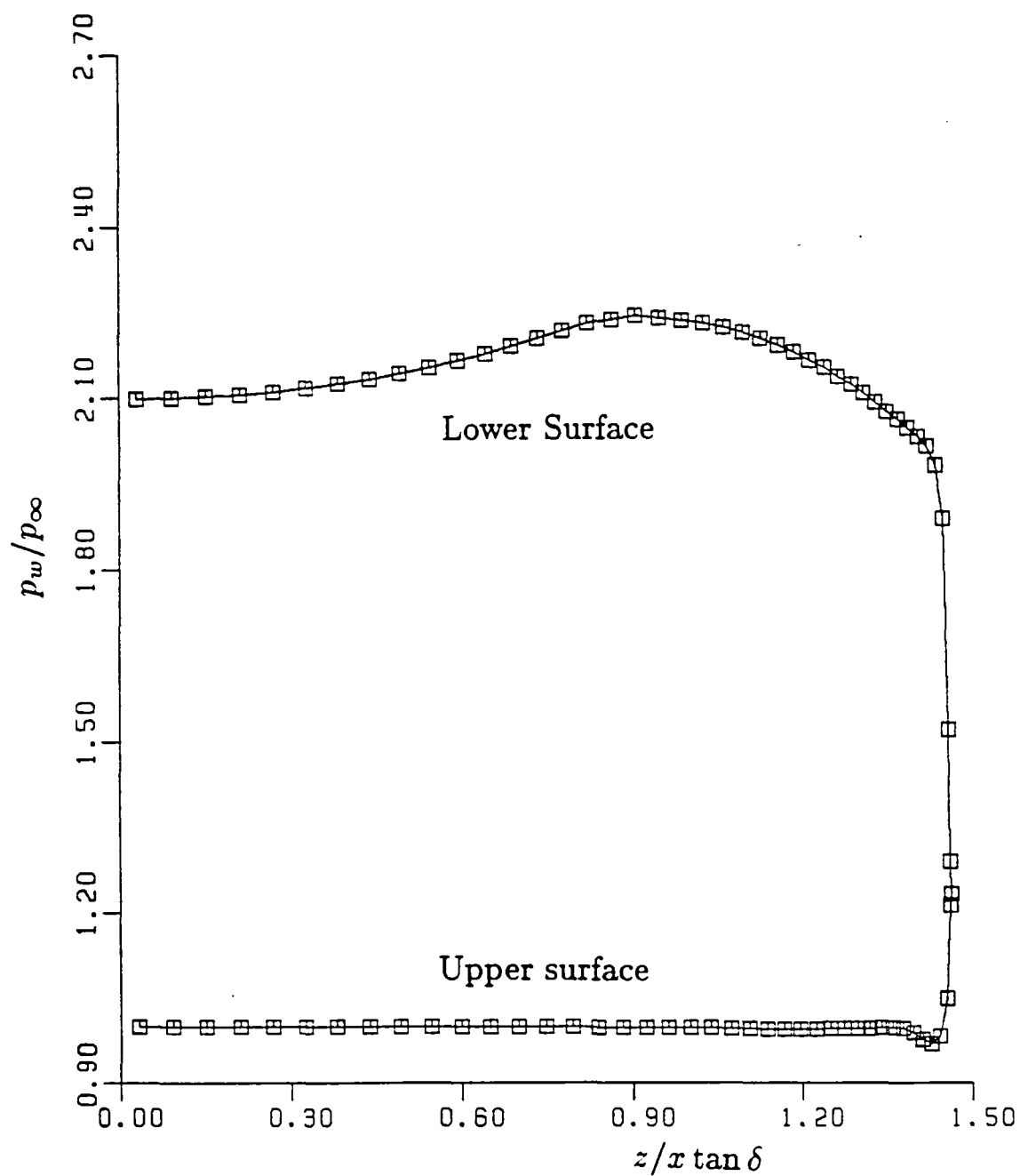


Fig. (7-2f) Wall Pressure Distribution

(On-Design, WR Type-A2F)

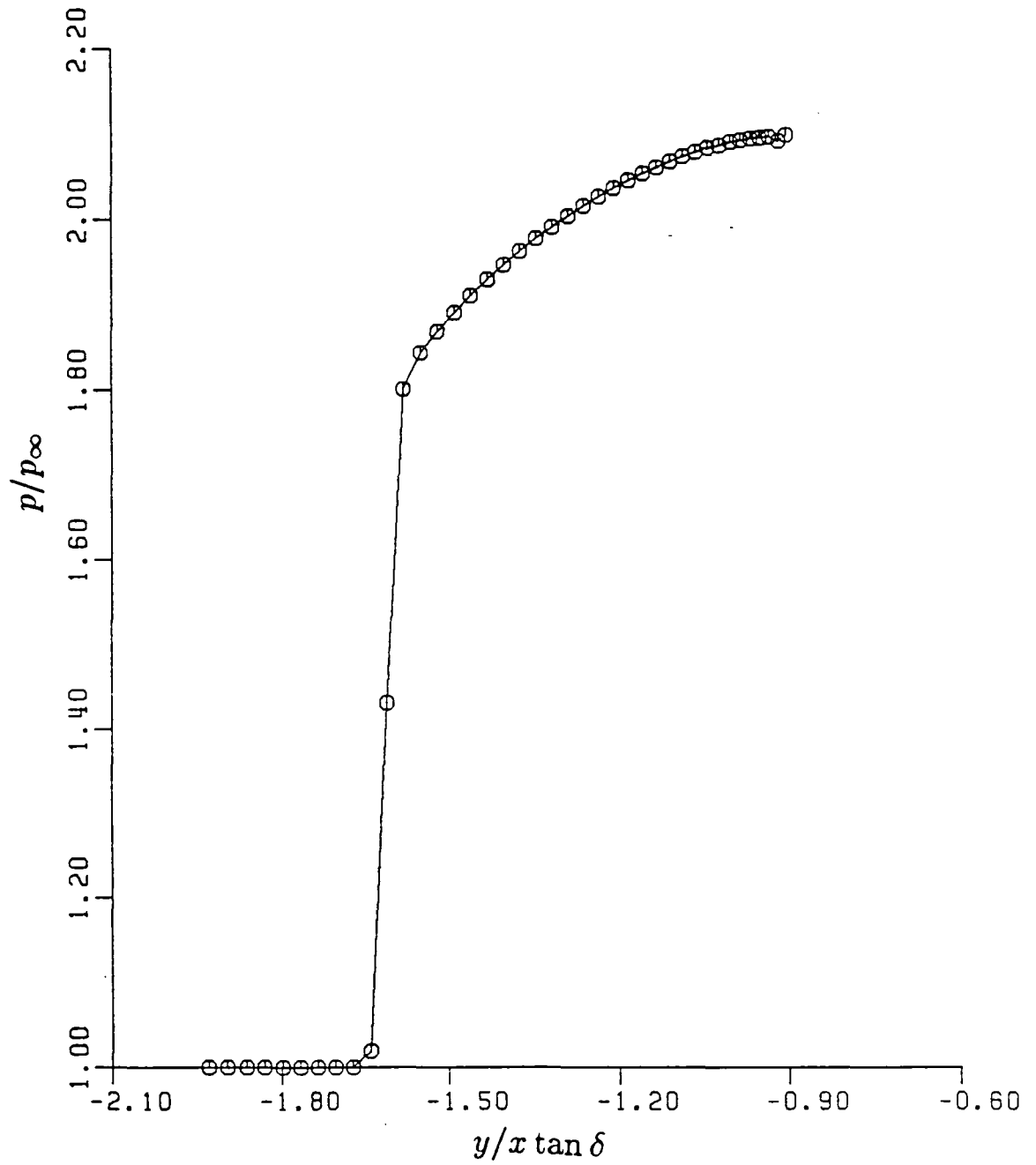


Fig. (7-2g) Pressure near Lower Symmetry Plane

(On-Design, WR Type-A2F)

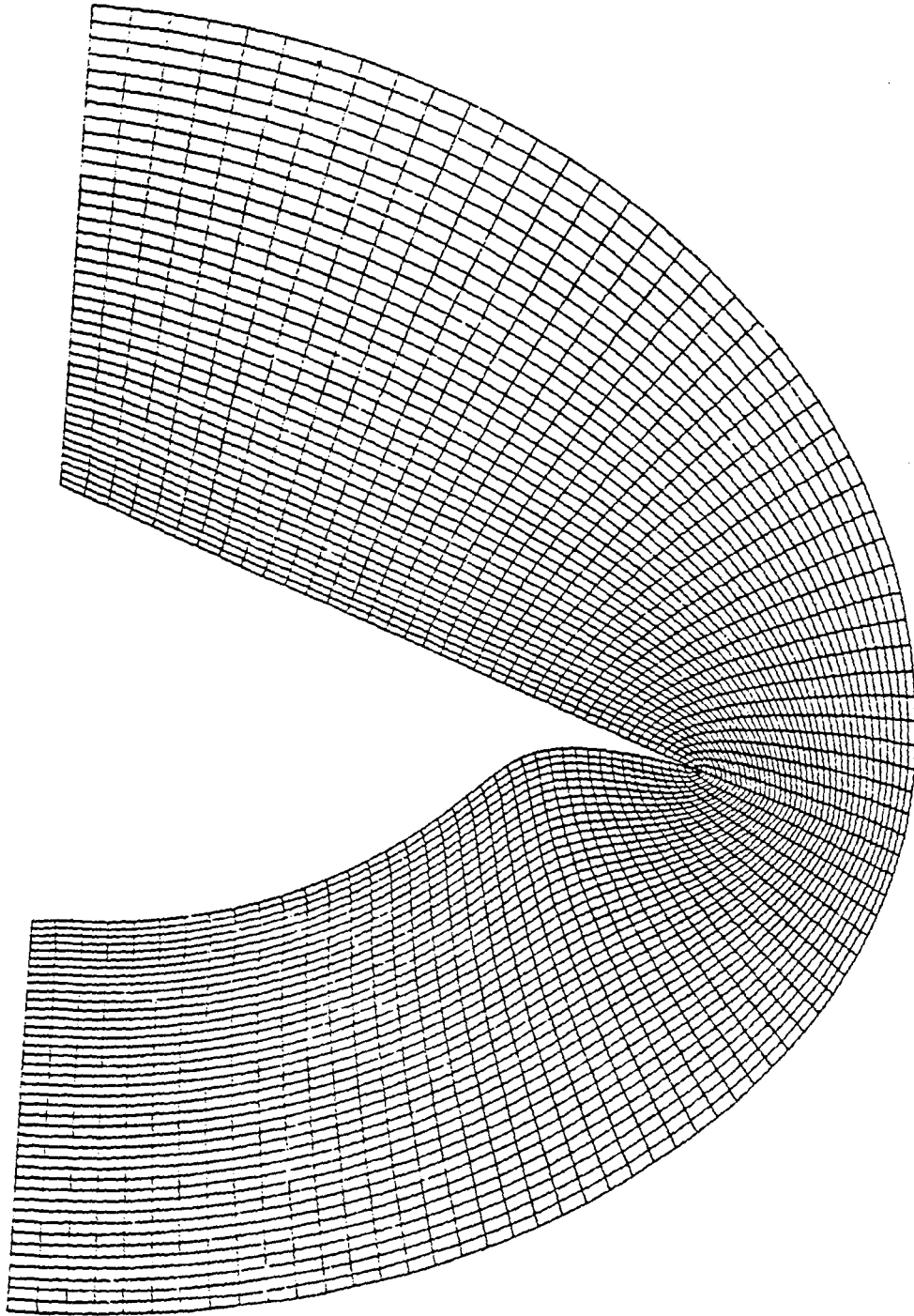


Fig. (7-3a) Grid for Type-*B10* Waverider

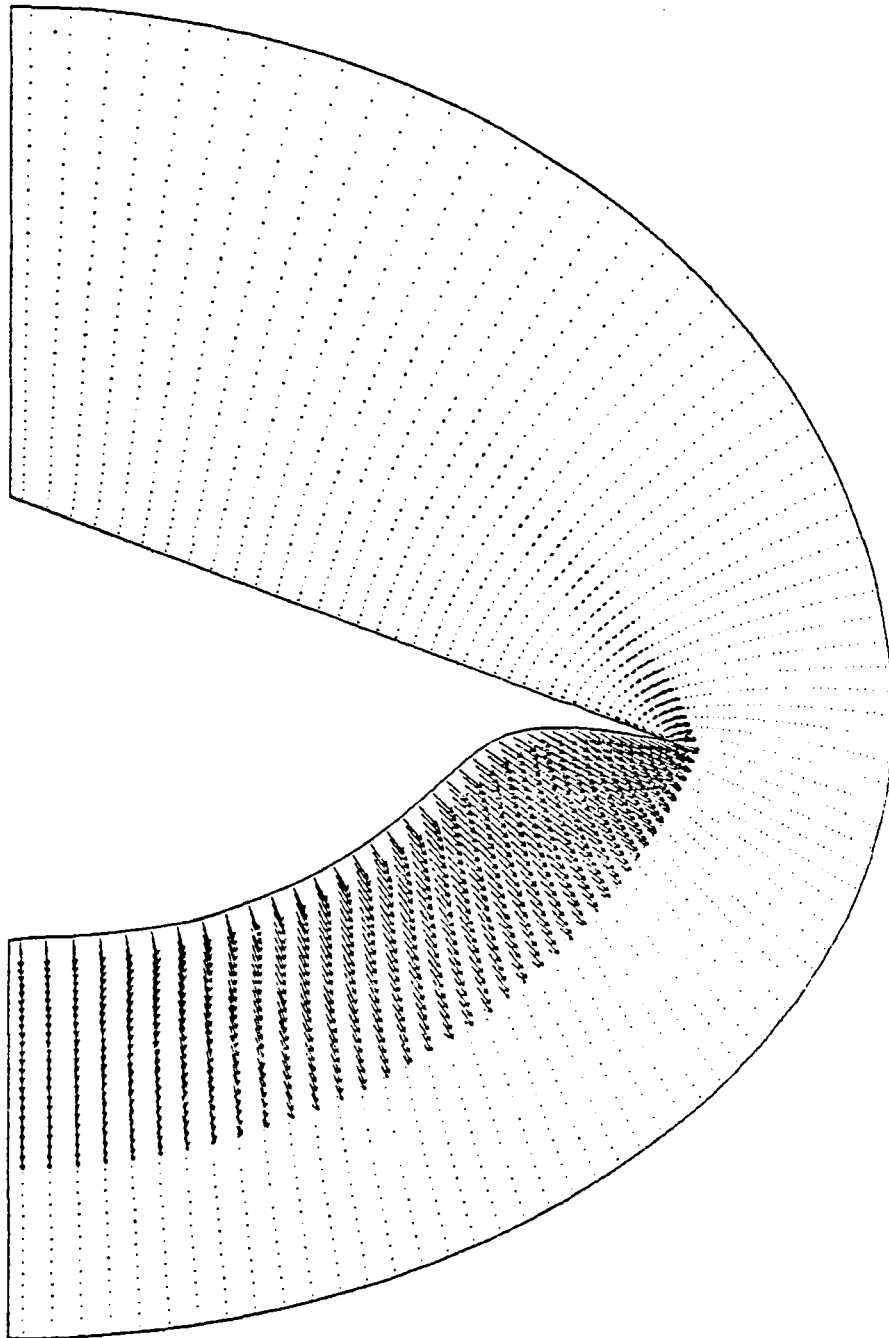


Fig. (7-3b) Cross-Plane Velocity Distribution

(On-Design, WR Type-B10)

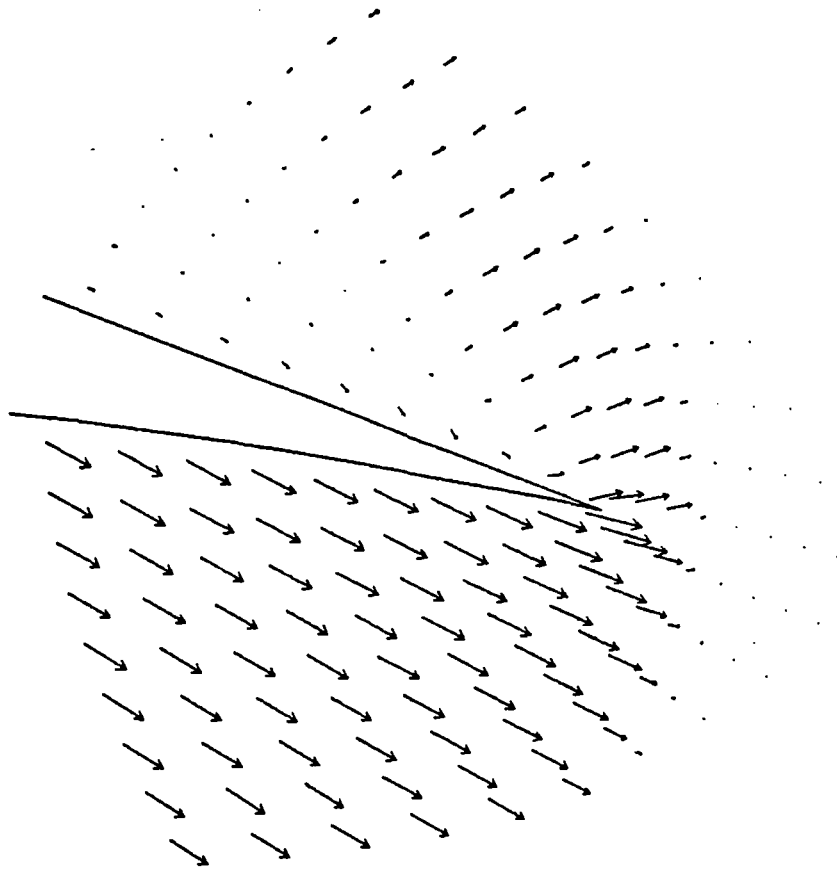


Fig. (7-3c) Magnified Cross-Plane Velocity near Tip

(On-Design, WR Type-B10)

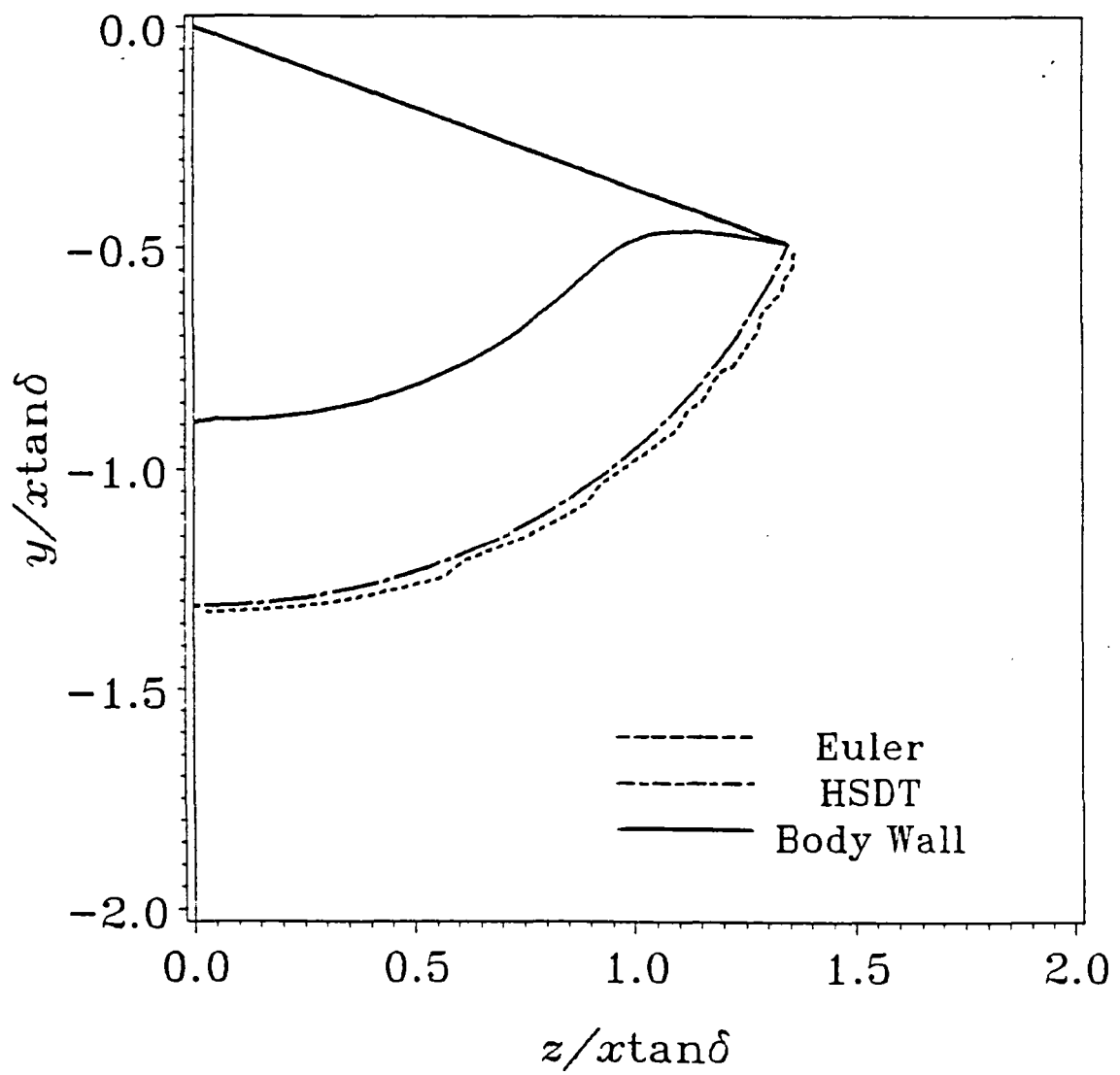


Fig. (7-3d) Shock Location Comparison

(On-Design, WR Type-B10)

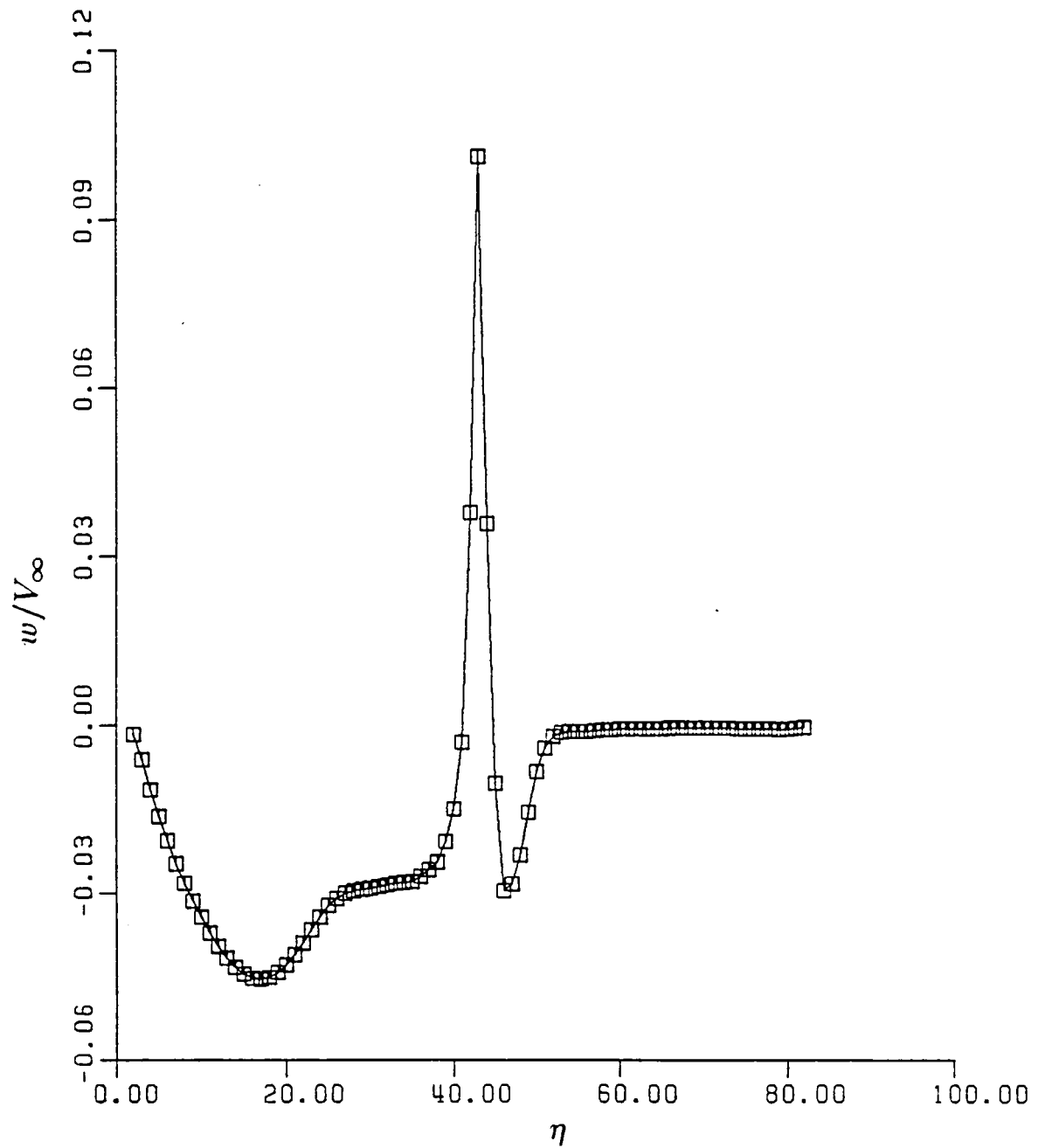


Fig. (7-3e) Azimuthal Velocity Component

(On-Design, WR Type-B1O)

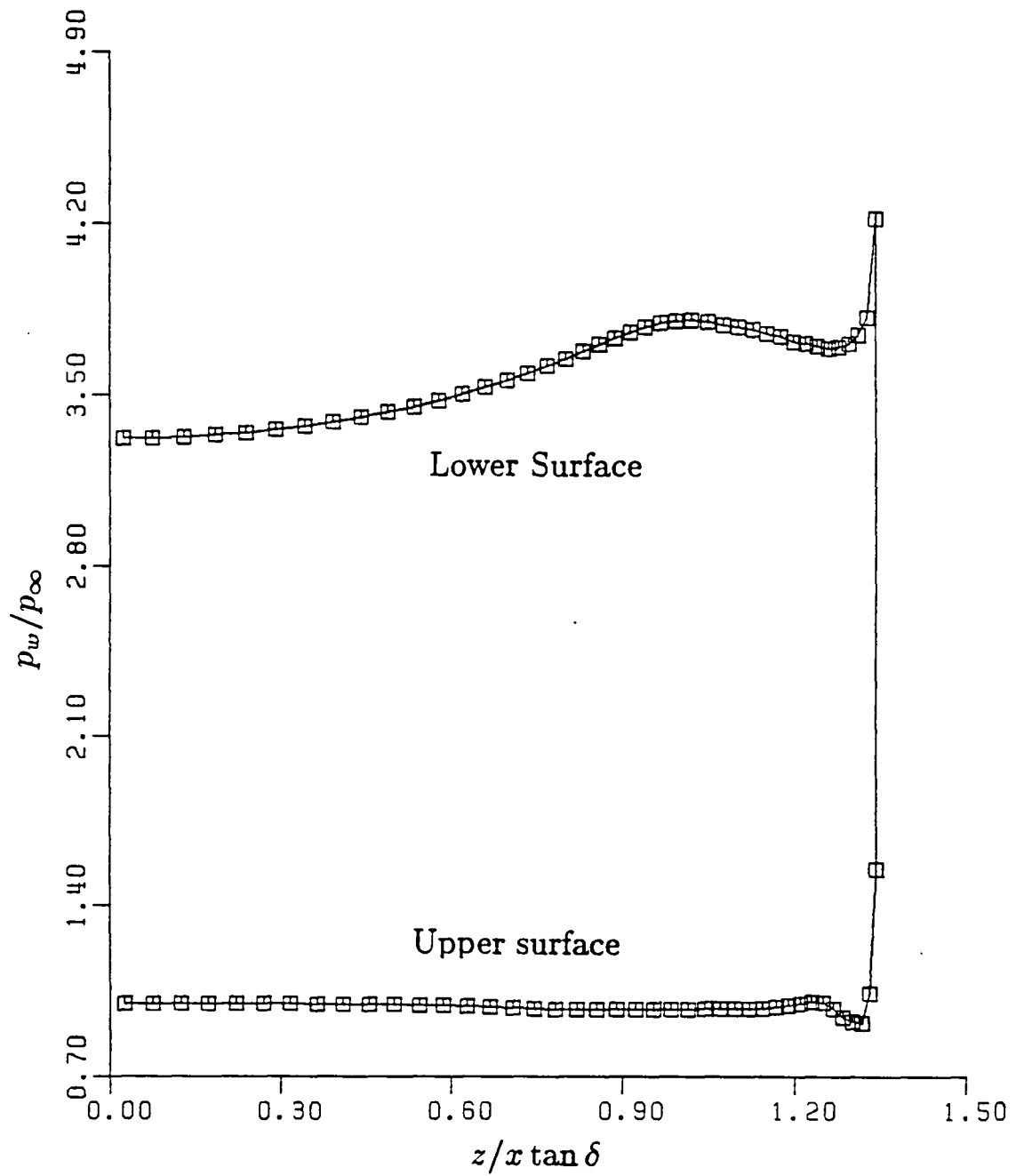


Fig. (7-3f) Wall Pressure Distribution
(On-Design, WR Type-B1O)

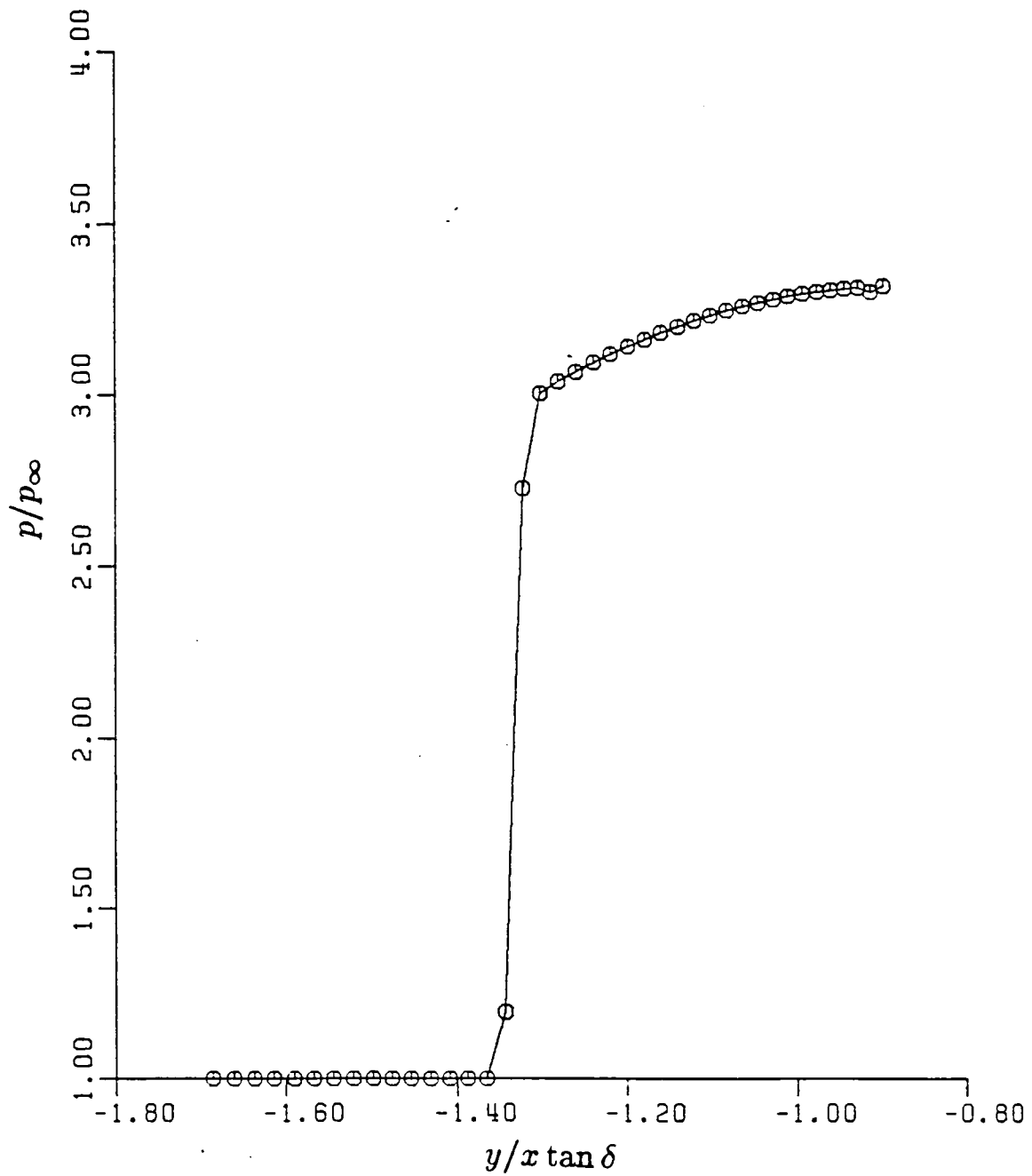


Fig. (7-3g) Pressure near Lower Symmetry Plane

(On-Design, WR Type-B1O)

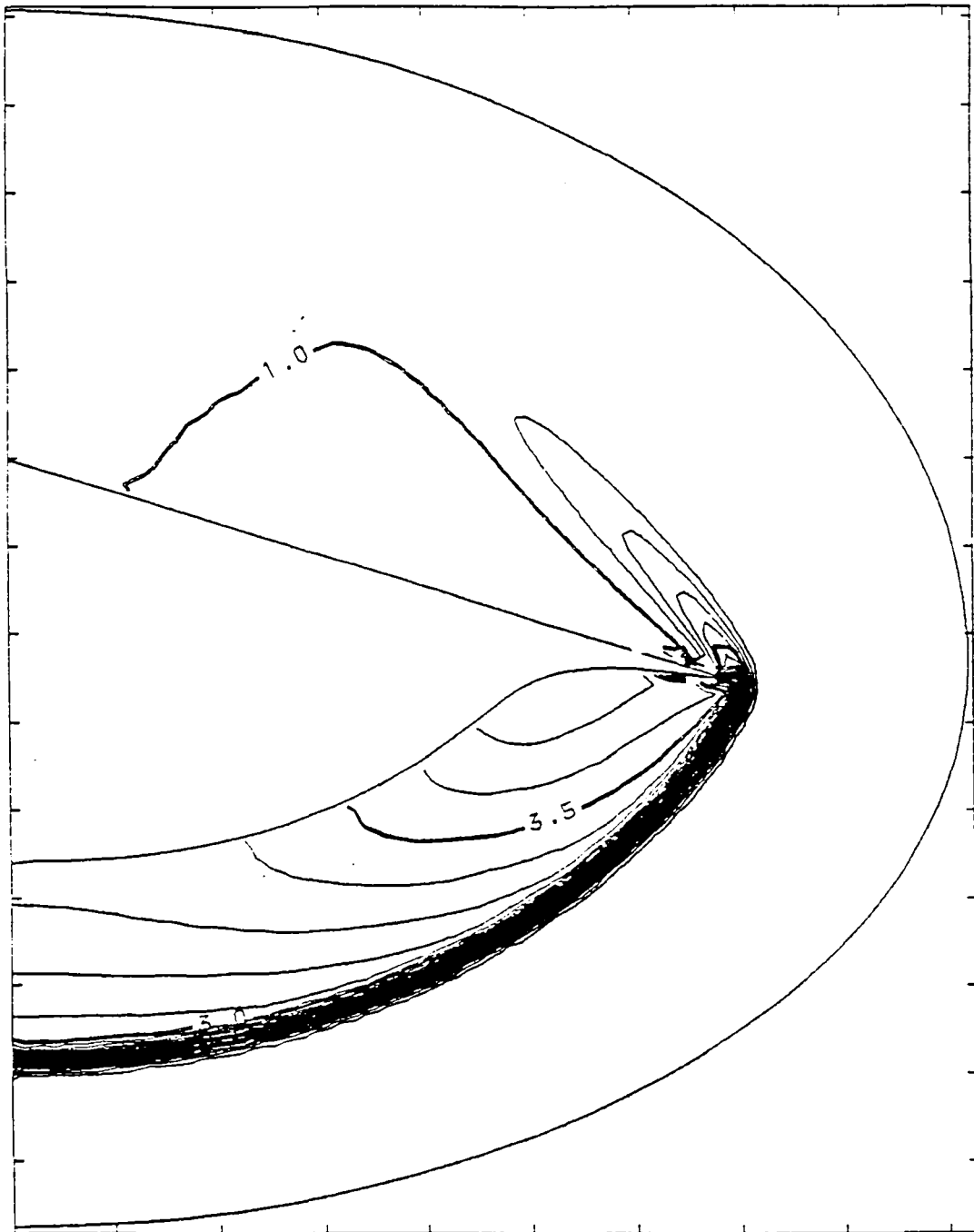


Fig. (7-3h) Pressure Contours
(On-Design, WR Type-B10)

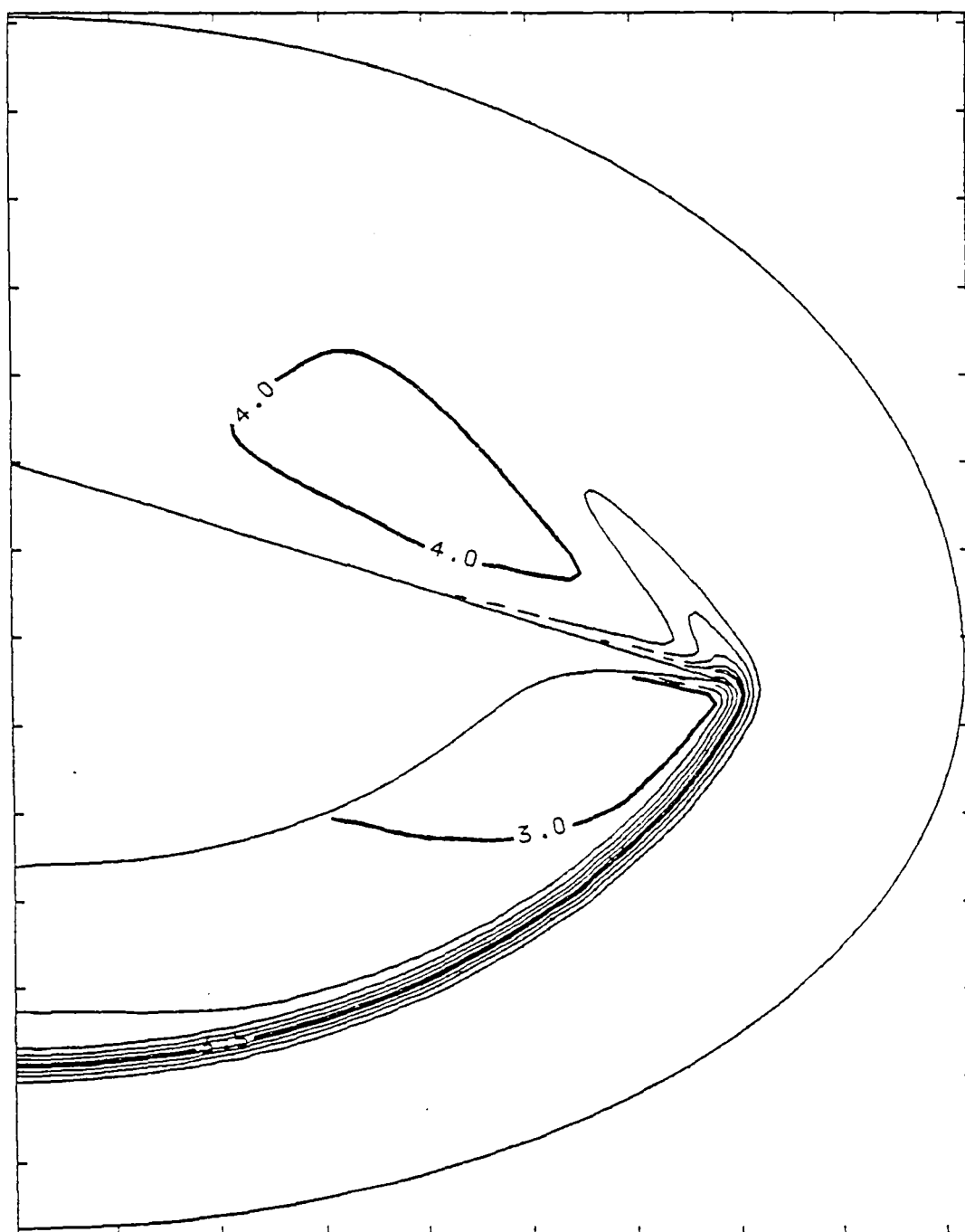


Fig. (7-3i) Mach Number Contours

(On-Design, WR Type-B10)

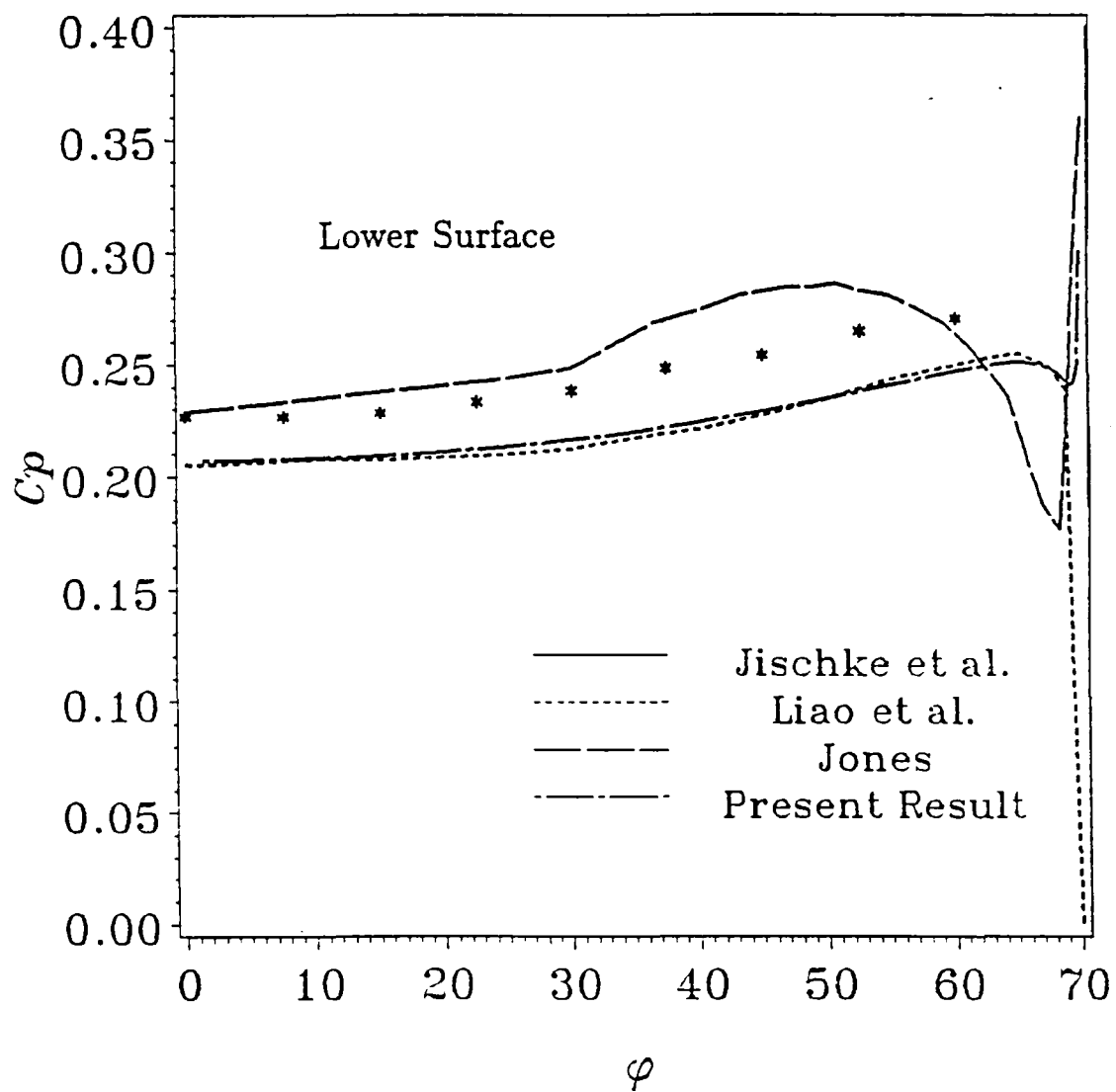


Fig. (7-3j) Wall Pressure Coefficients

(On-Design, WR Type-B1O)

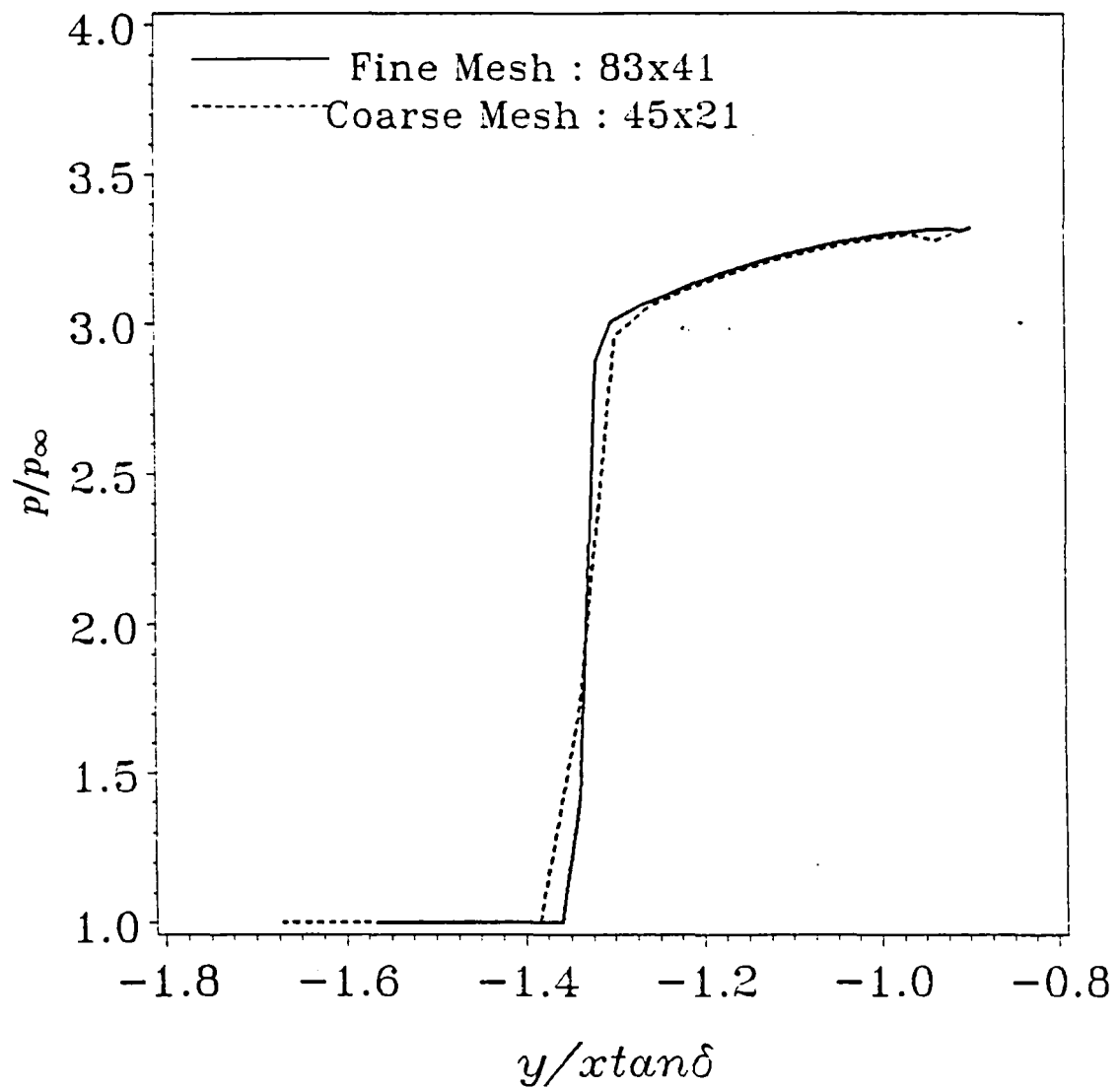


Fig. (7-3k) Mesh Size Effect (Shock)
(On-Design, WR Type-B1O)

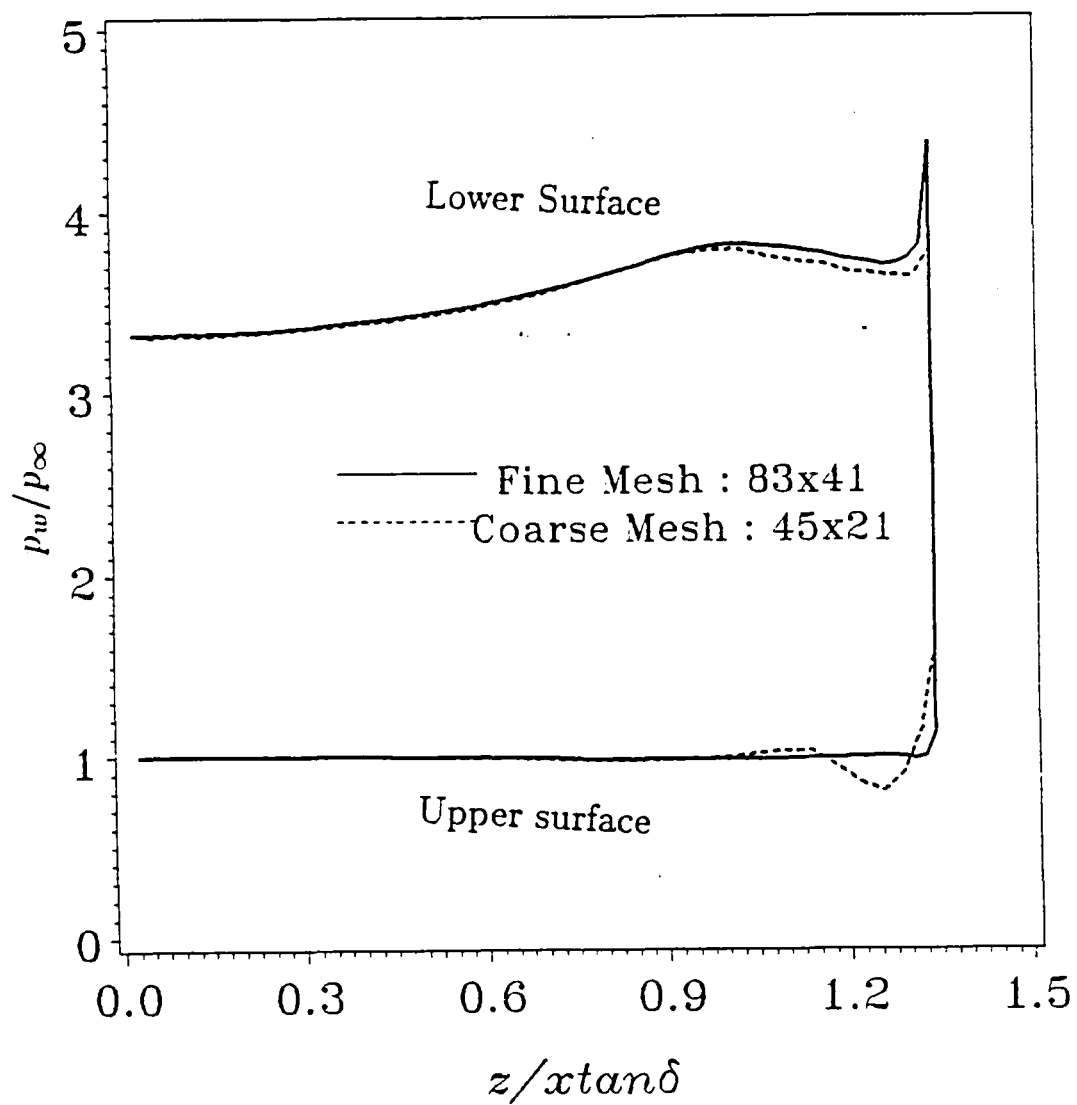


Fig. (7-31) Mesh Size Effect (Leading Edge)

(On-Design, WR Type-B10)

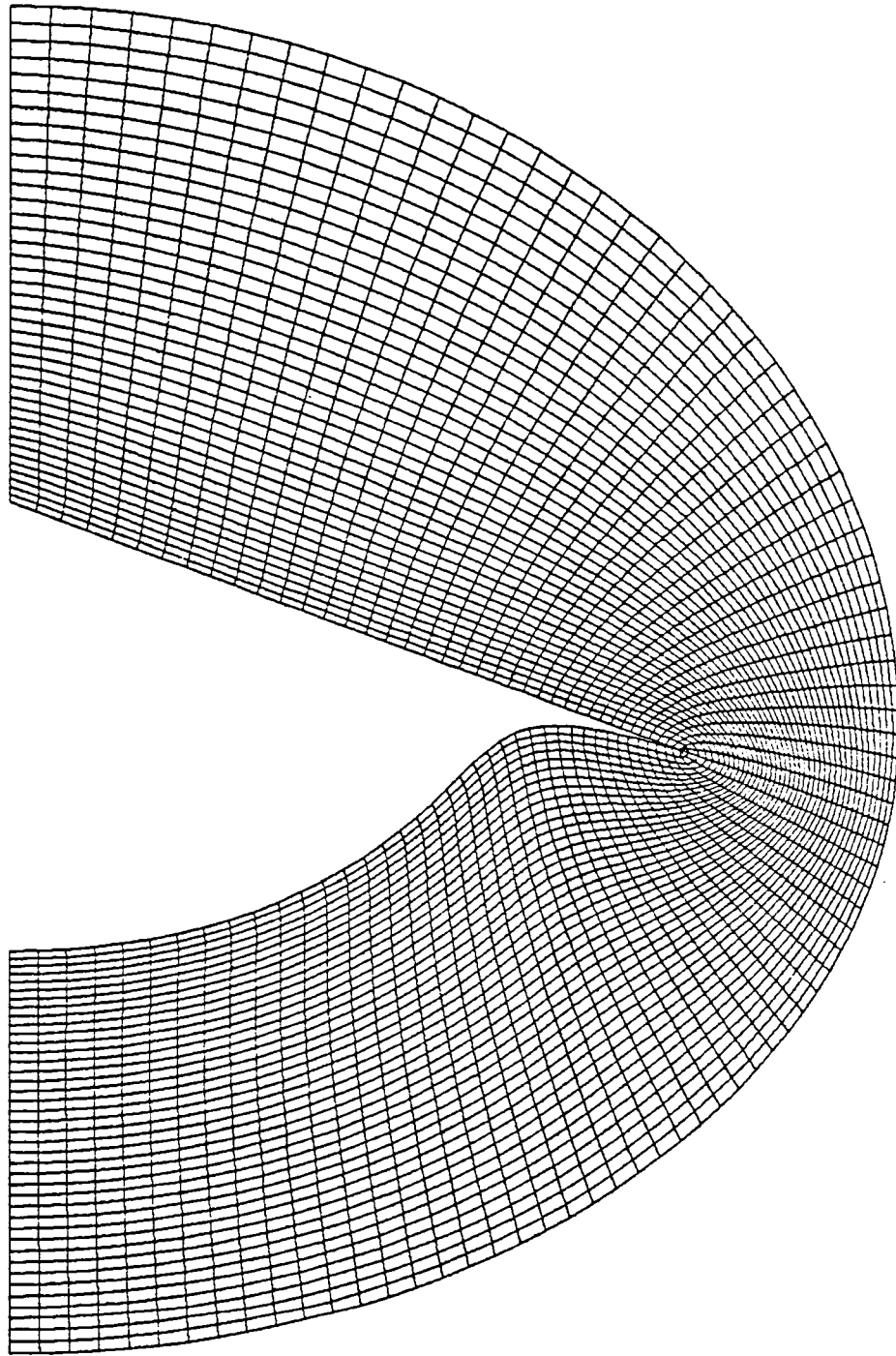


Fig. (7-4a) Grid for Type-*B2F* Waverider

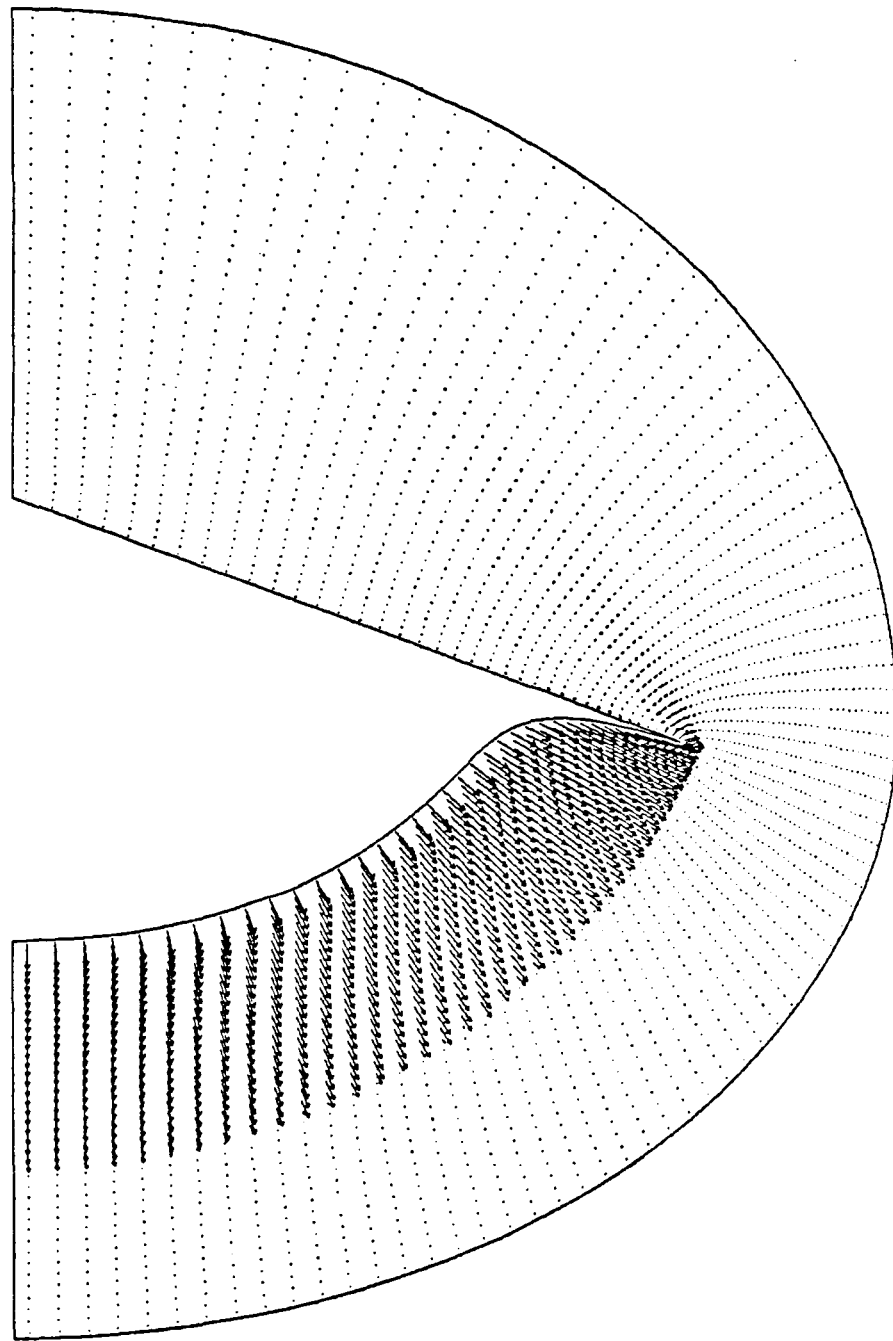


Fig. (7-4b) Cross-Plane Velocity Distribution
(On-Design, WR Type-B2F)

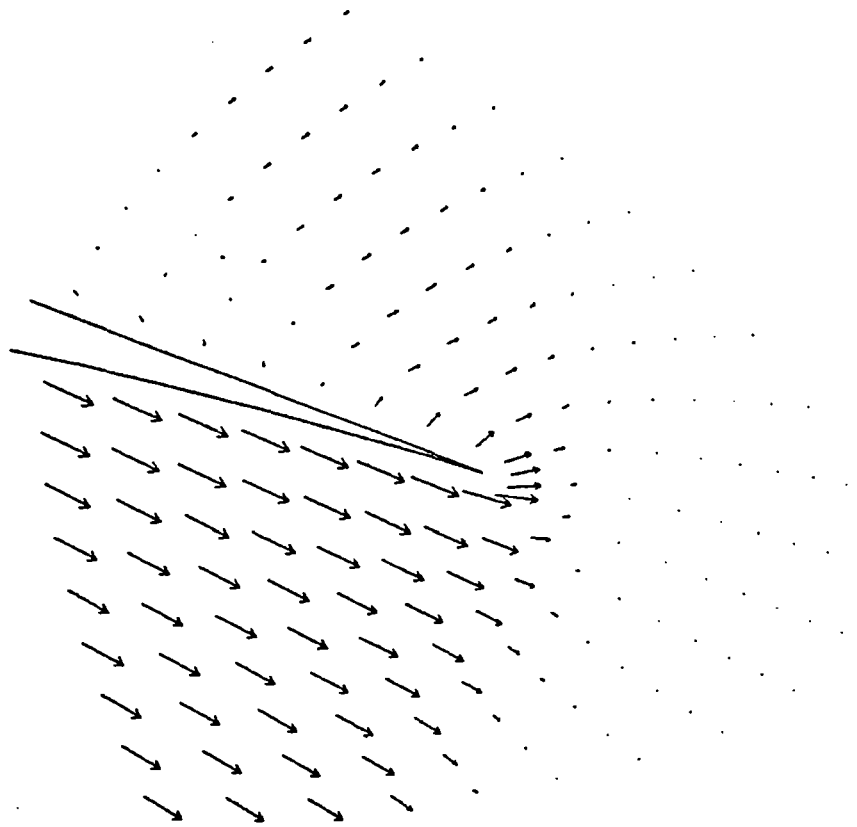


Fig. (7-4c) Magnified Cross-Plane Velocity near Tip
(On-Design, WR Type-B2F)

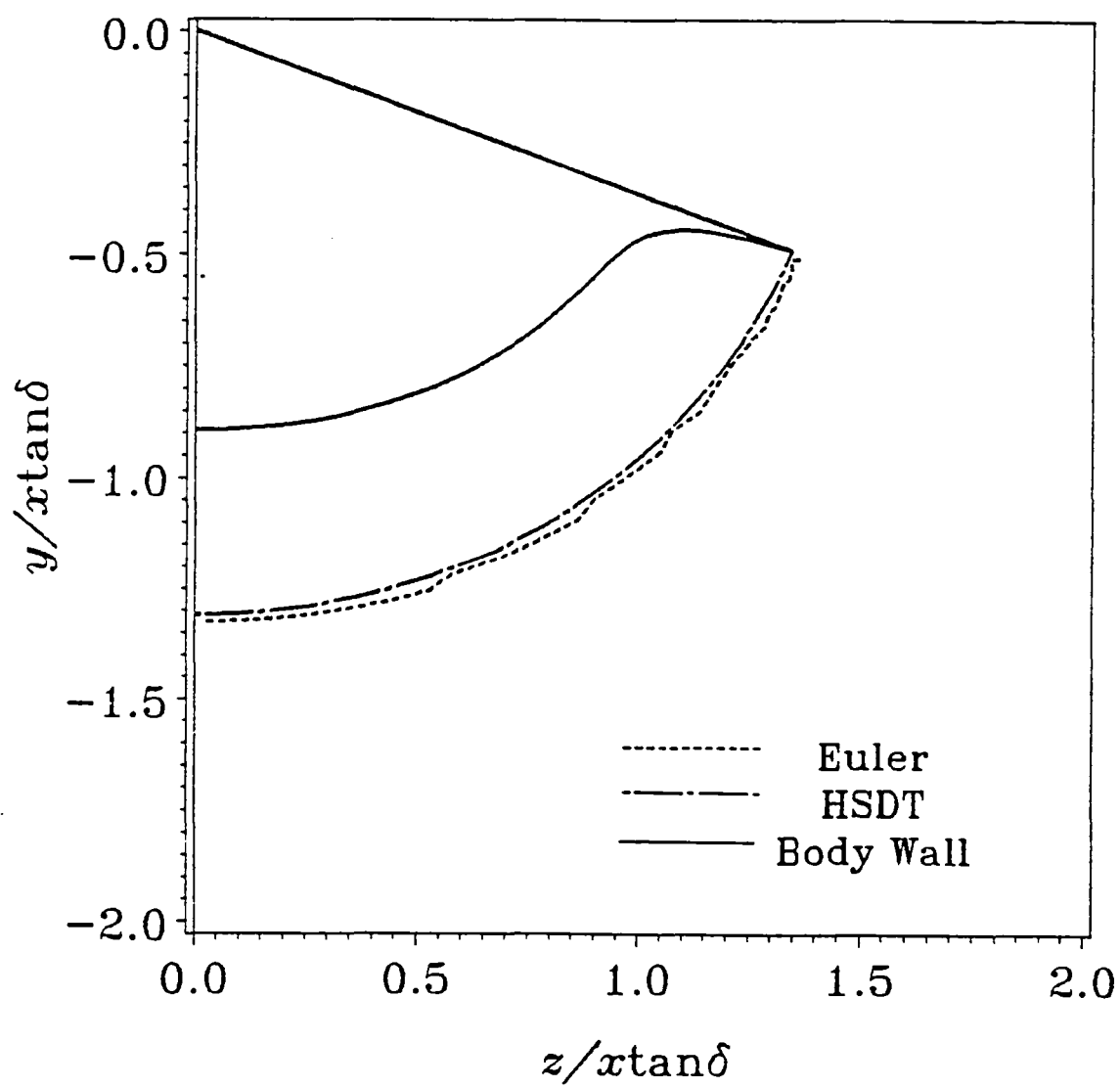


Fig. (7-4d) Shock Location Comparison
(On-Design, WR Type-B2F)

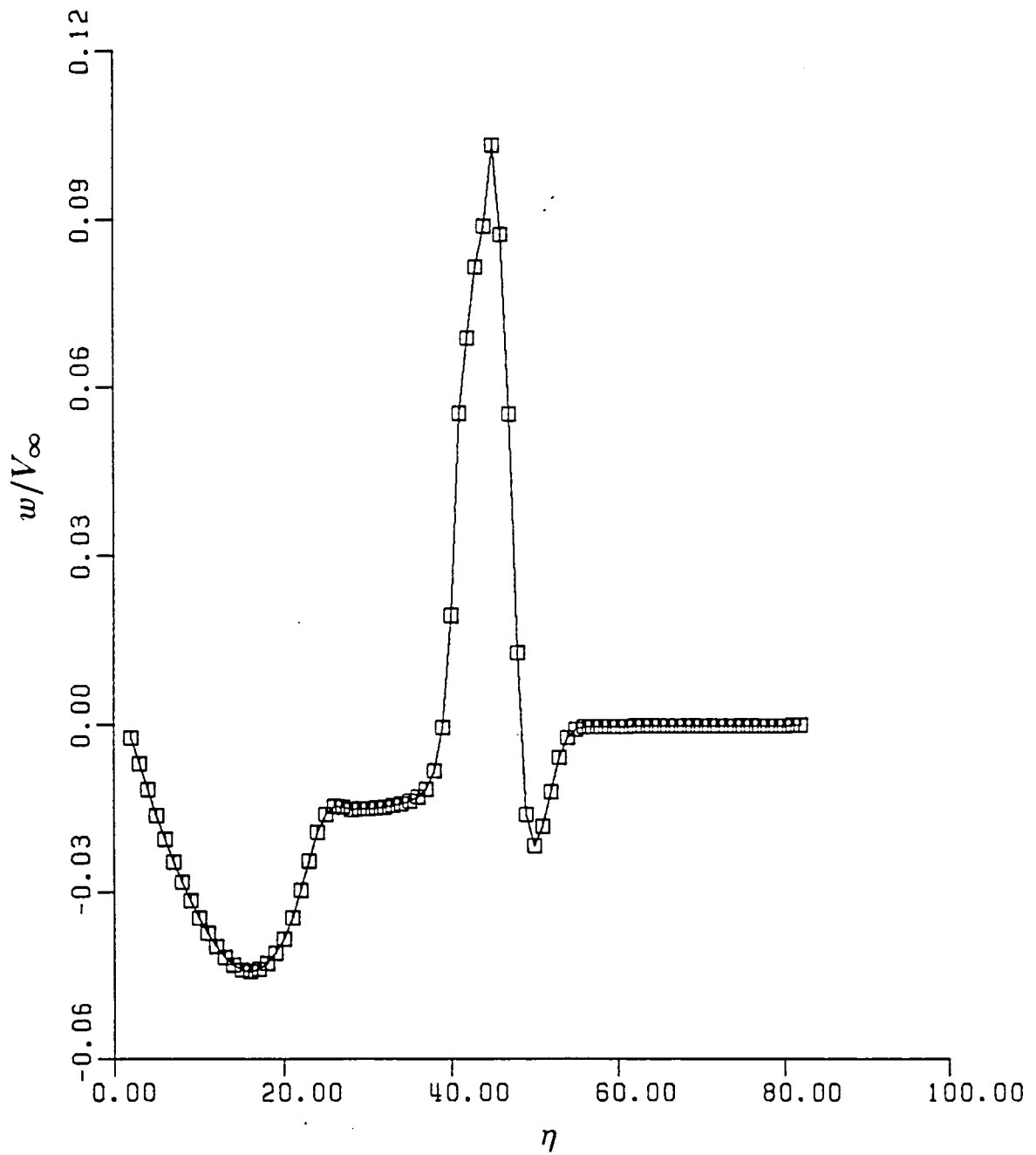


Fig. (7-4e) Azimuthal Velocity Component
(On-Design, WR Type-B2F)

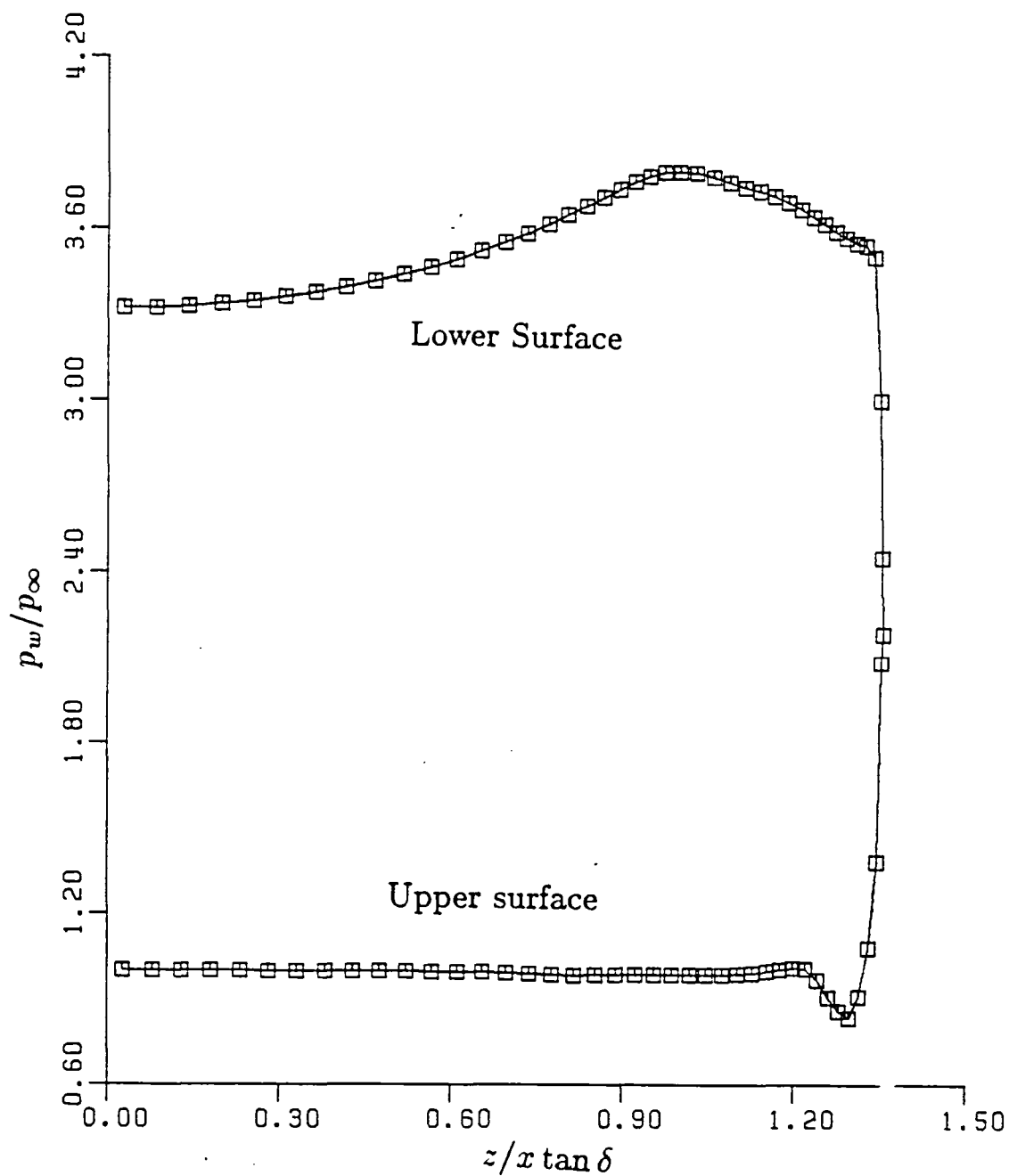


Fig. (7-4f) Wall Pressure Distribution
(On-Design, WR Type-B2F)

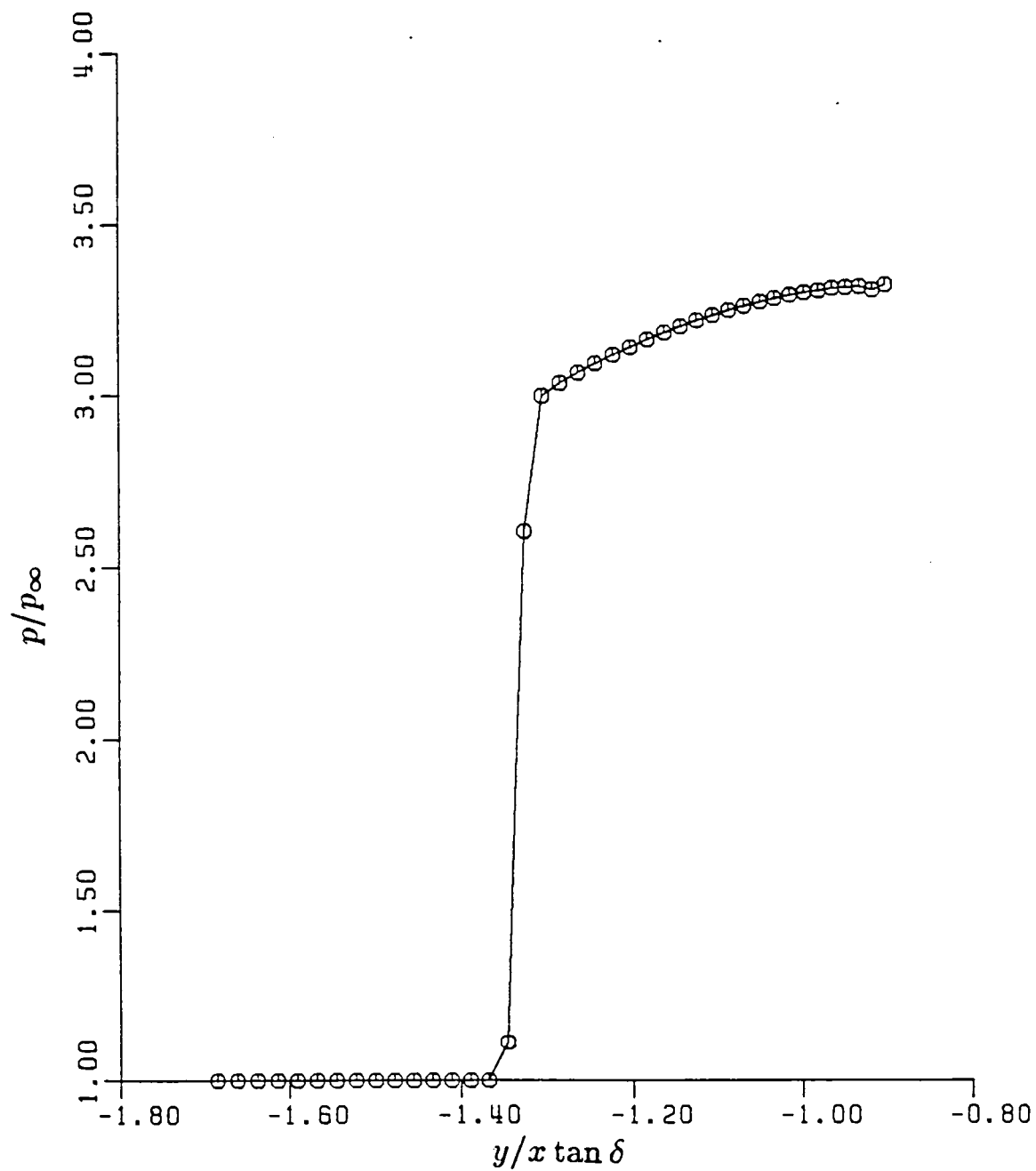
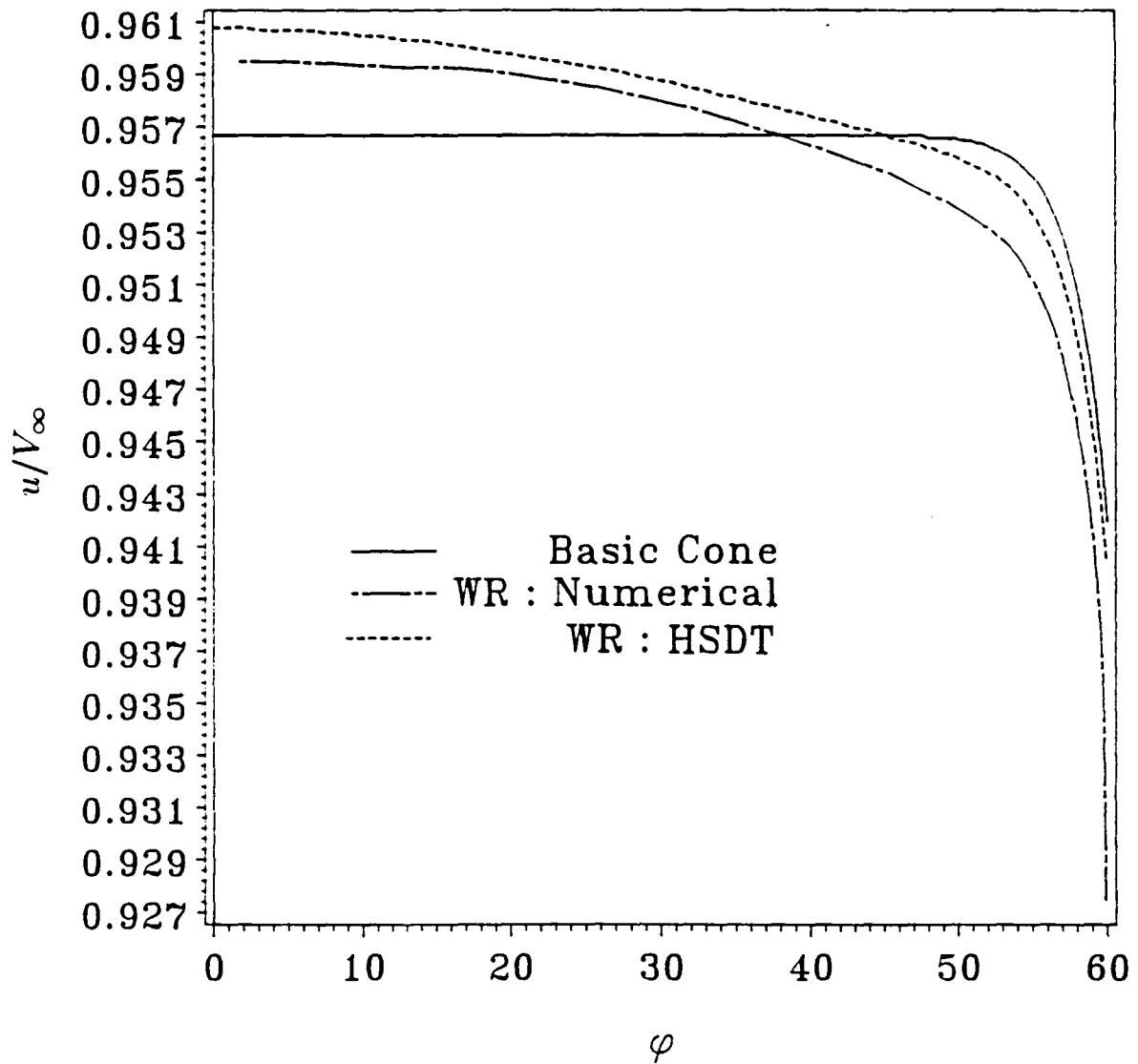


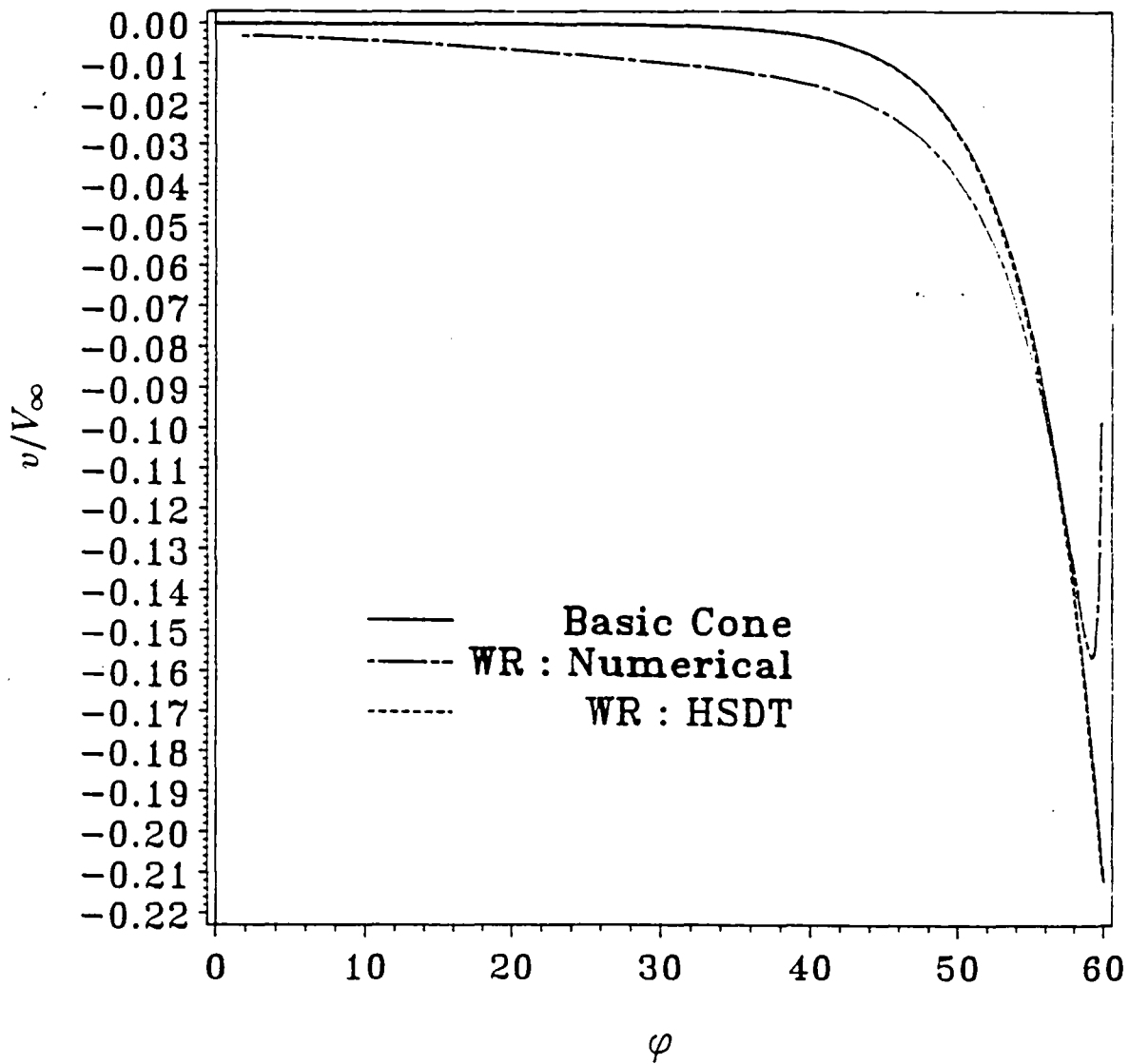
Fig. (7-4g) Pressure near Lower Symmetry Plane

(On-Design, WR Type-B2F)

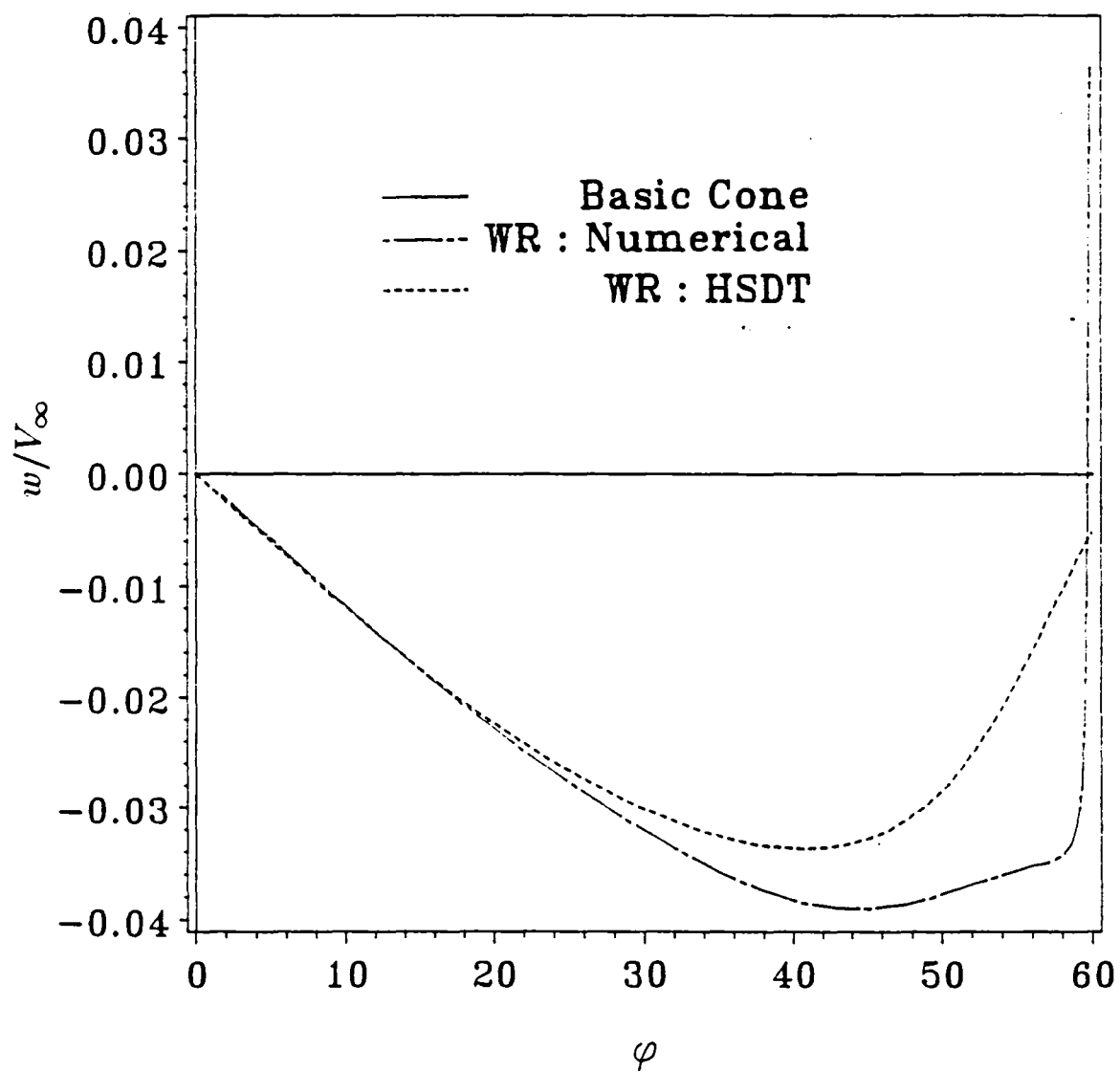
Waverider Type-A10

Fig. (7-5a) u : Radial Velocity Component

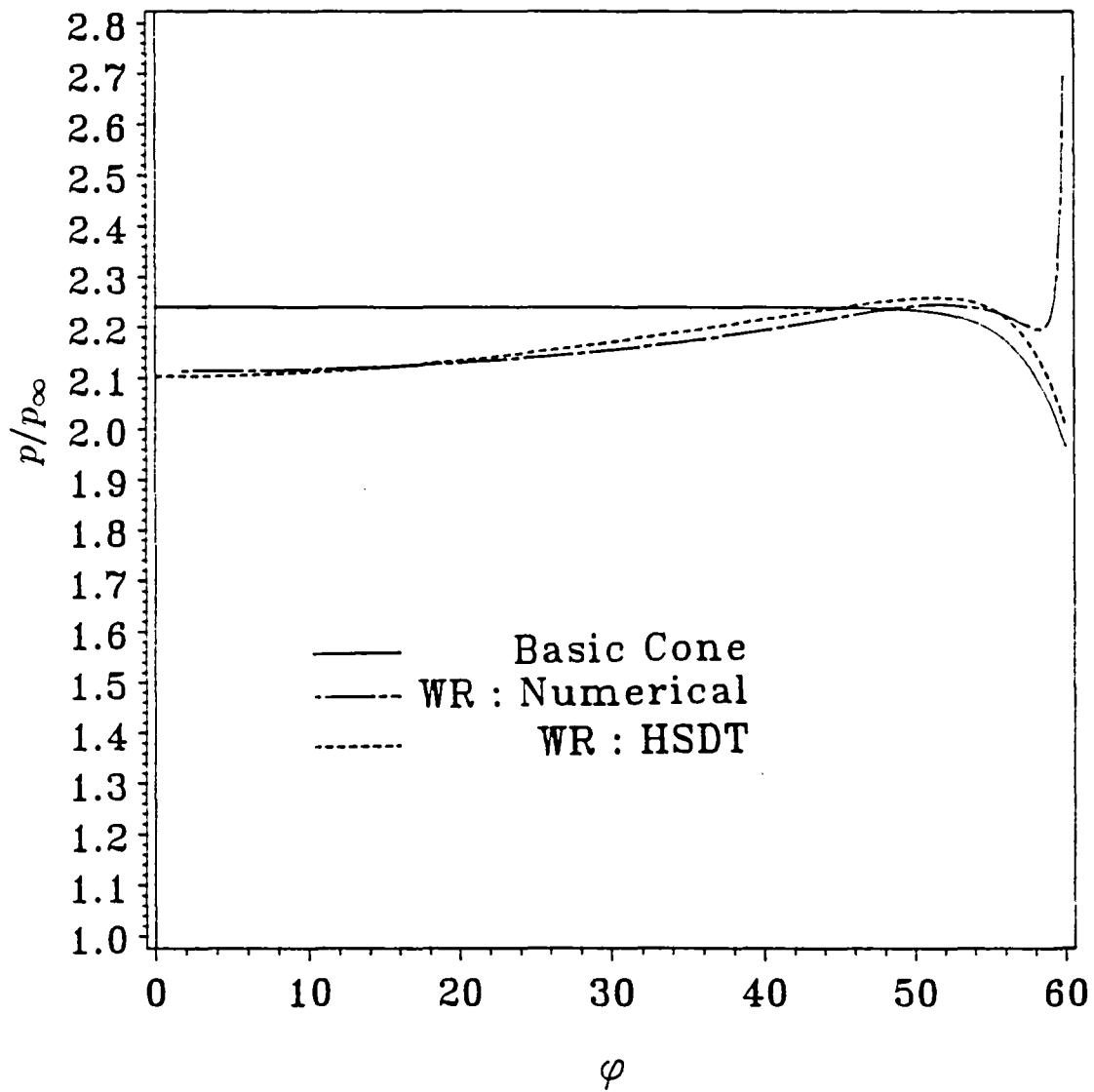
Waverider Type-A10

Fig. (7-5b) v : Polar Velocity Component

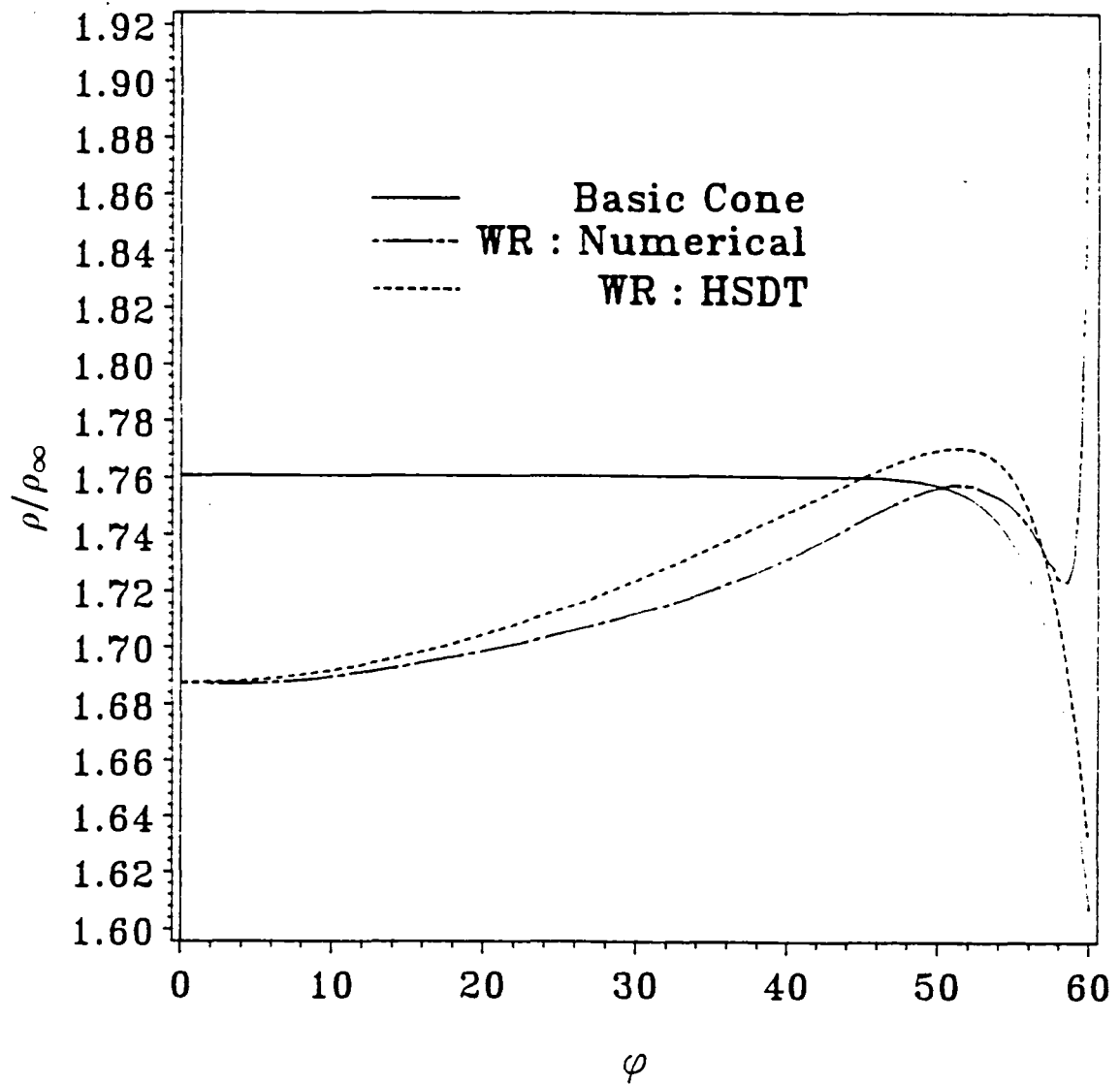
Waverider Type-A10

Fig. (7-5c) w : Azimuthal Velocity Component

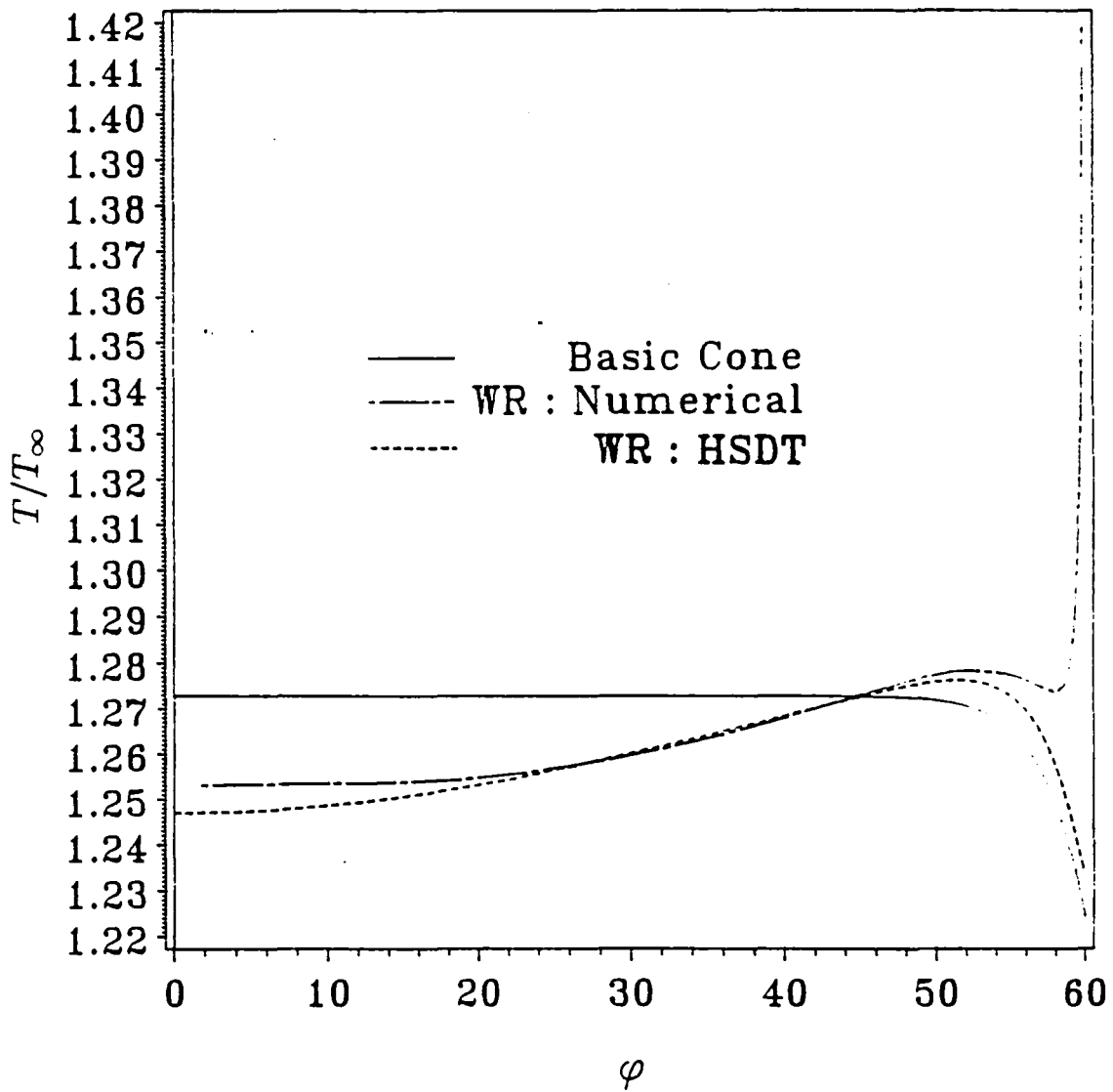
Waverider Type-A10

Fig. (7-5d) p : Pressure Distribution

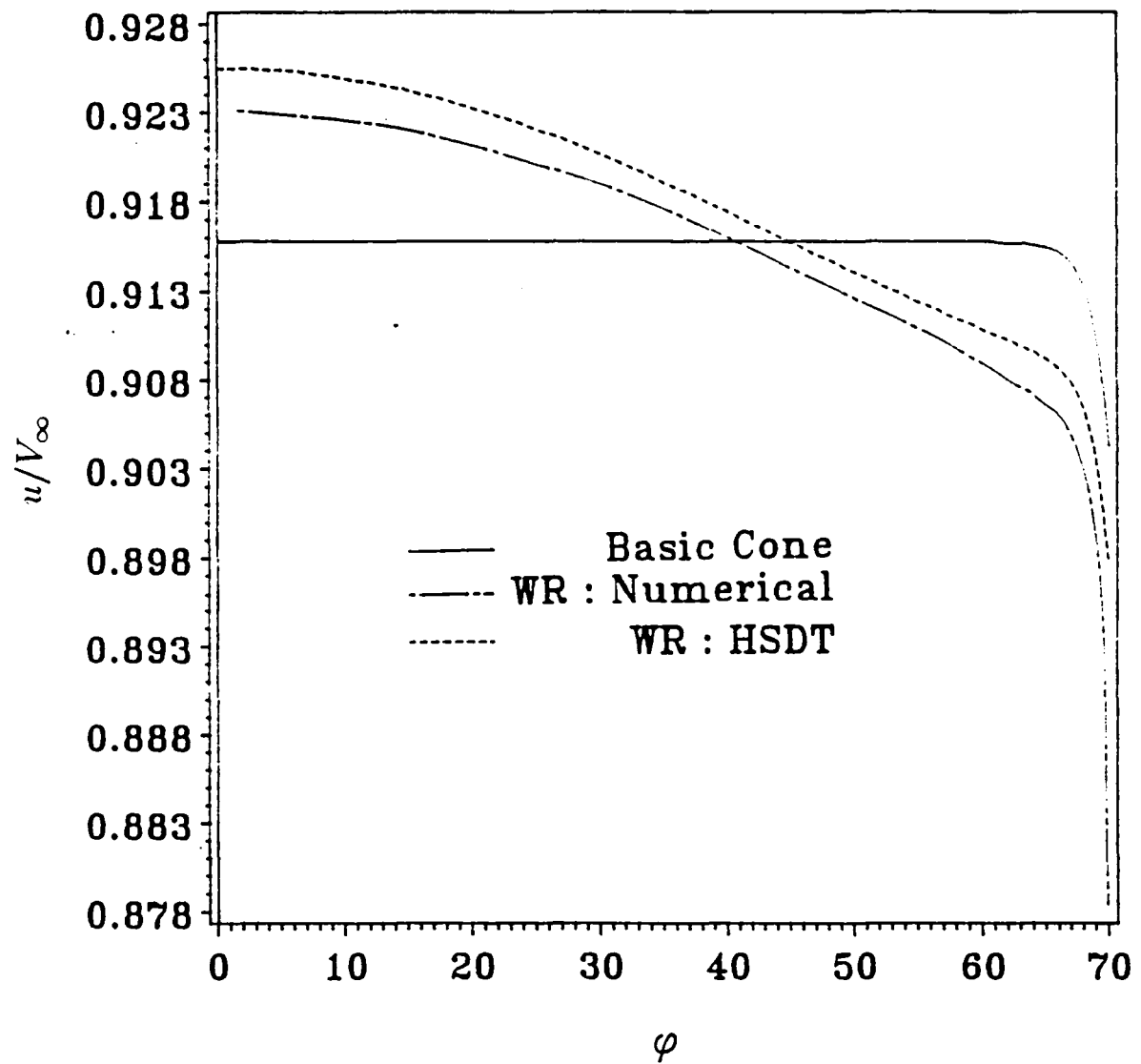
Waverider Type-A10

Fig. (7-5e) ρ : Density Distribution

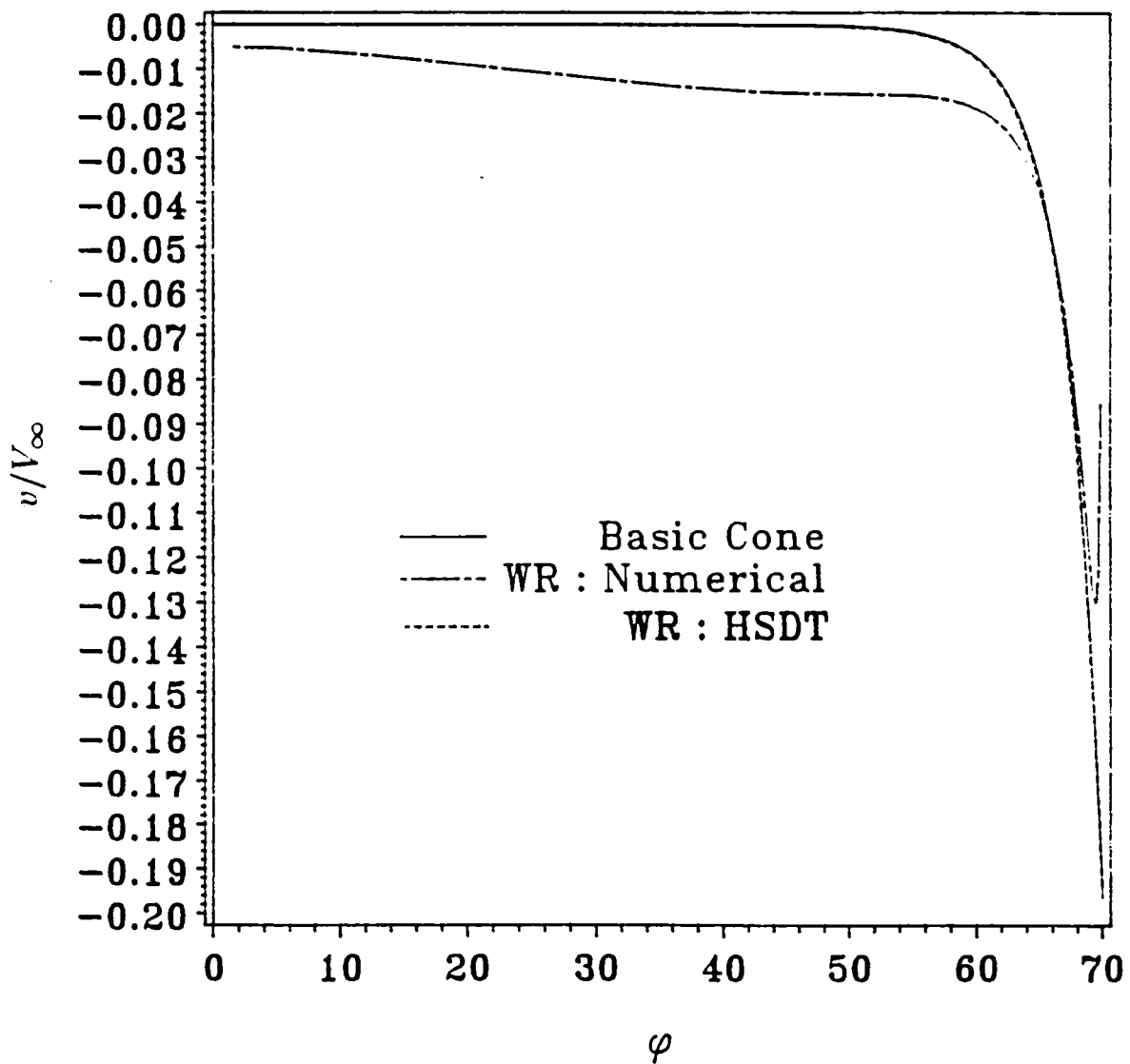
Waverider Type-A10

Fig. (7-5f) T : Temperature Distribution

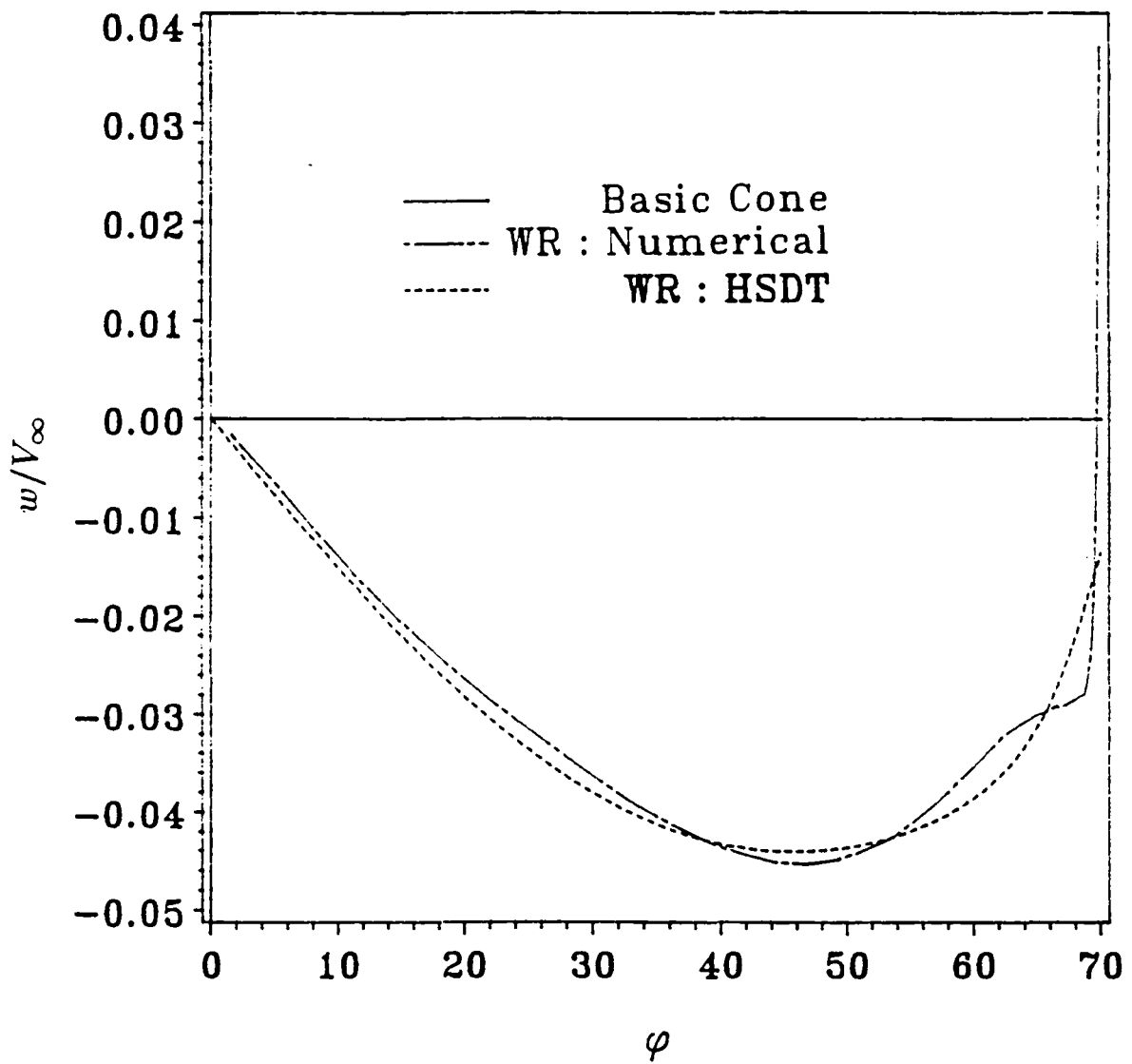
Waverider Type-B10

Fig. (7-6a) u : Radial Velocity Component

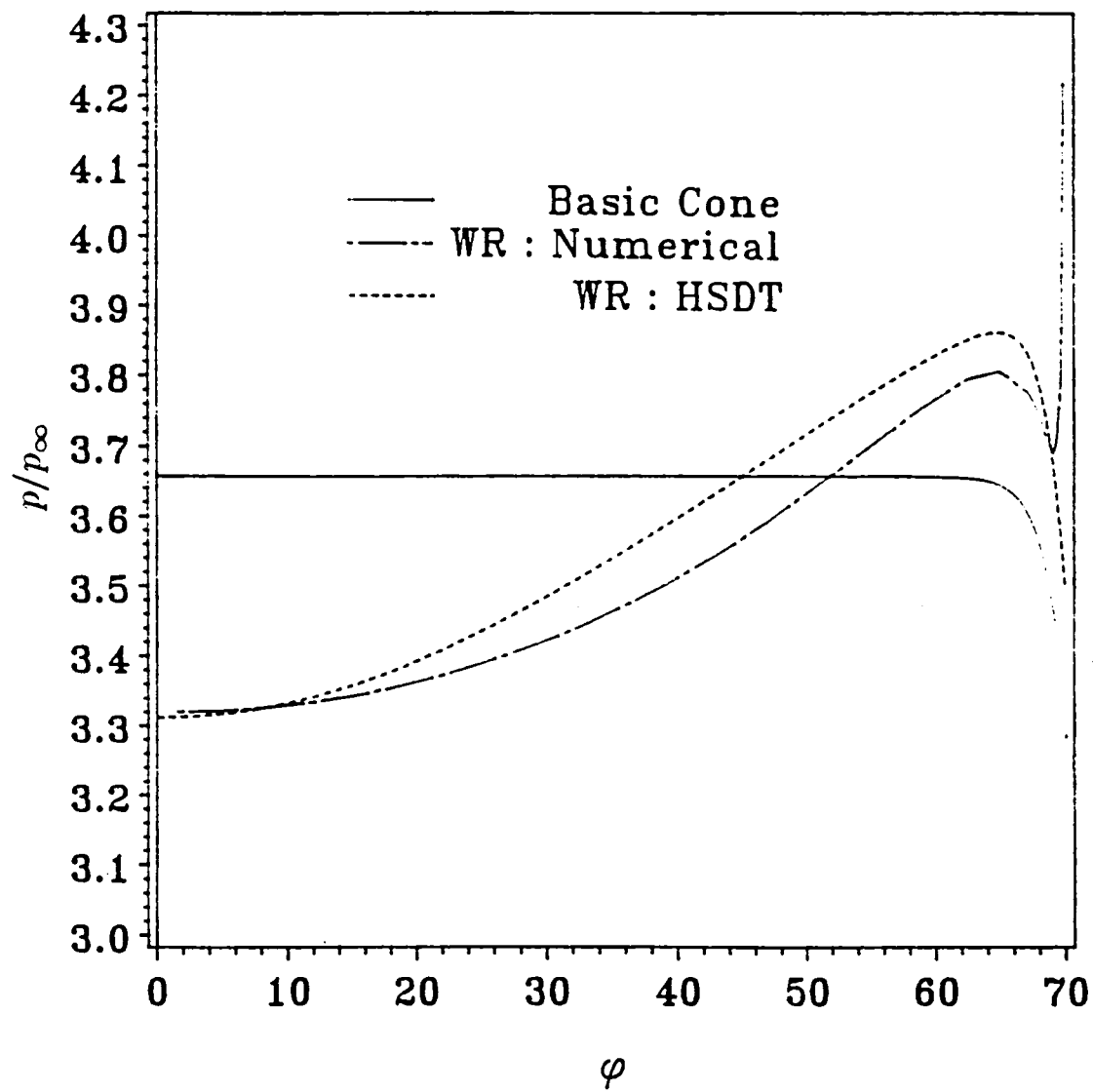
Waverider Type-B10

Fig. (7-6b) v : Polar Velocity Component

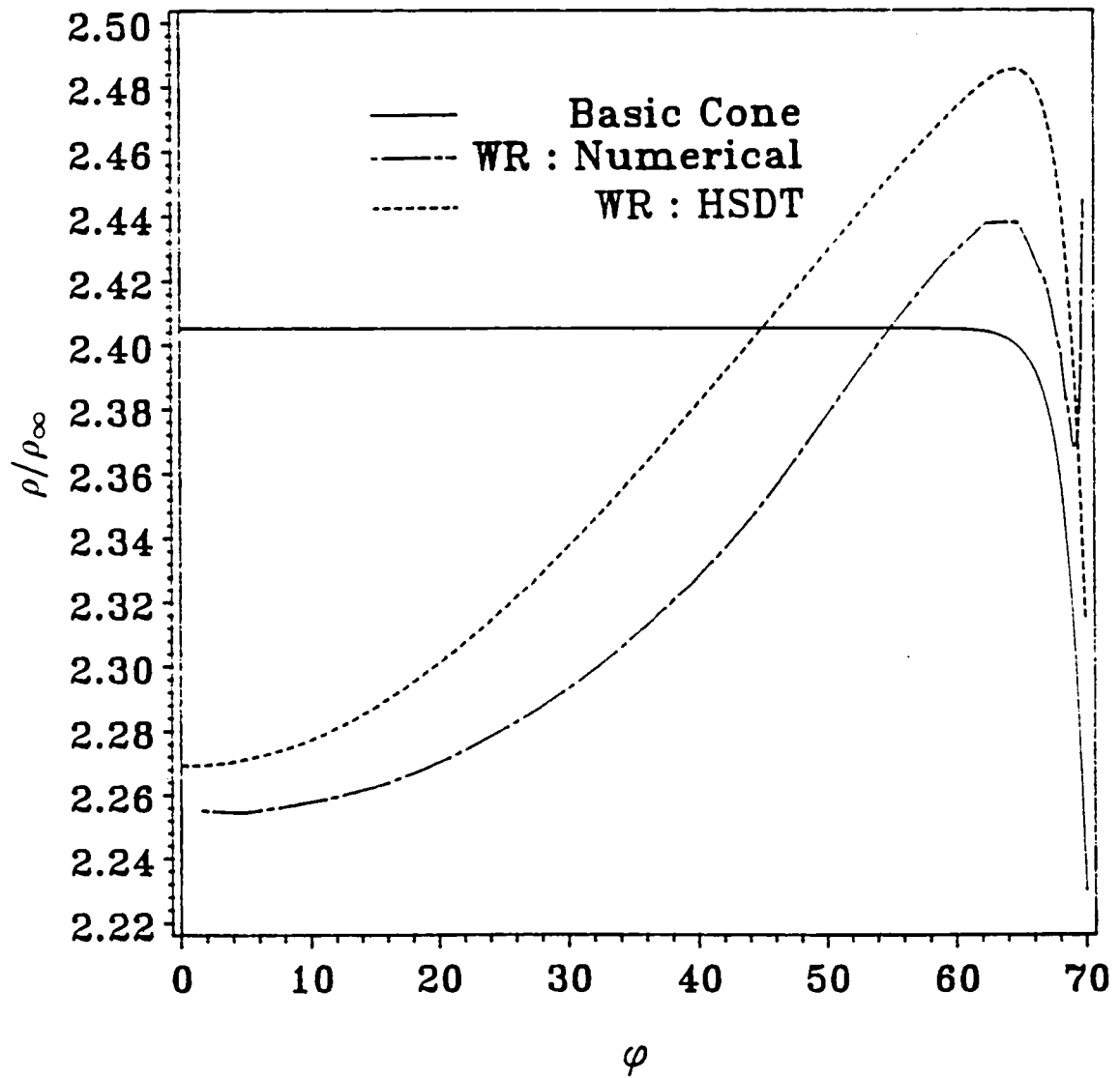
Waverider Type-B10

Fig. (7-6c) w : Azimuthal Velocity Component

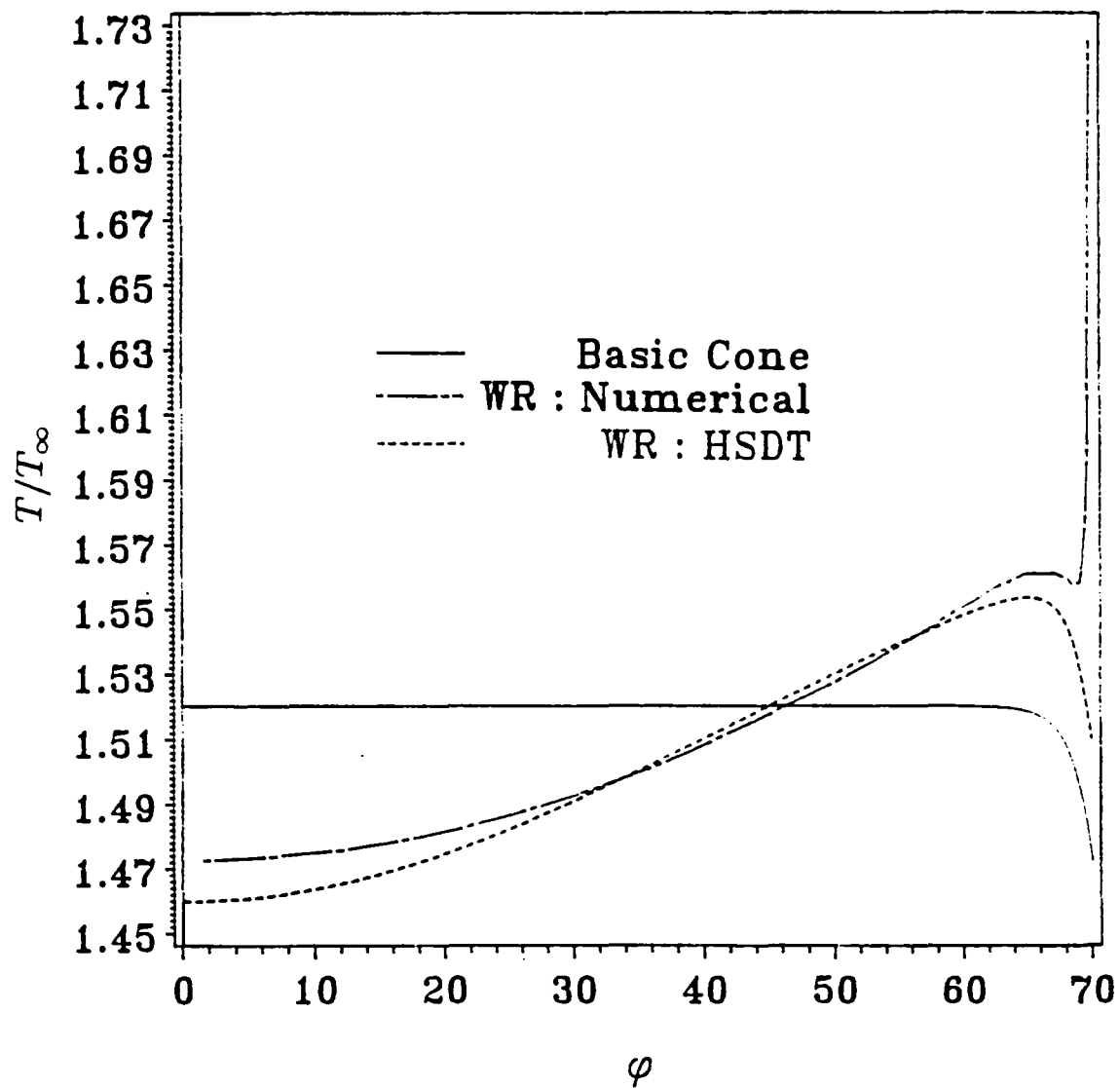
Waverider Type-B10

Fig. (7-6d) p : Pressure Distribution

Waverider Type-B10

Fig. (7-6e) ρ : Density Distribution

Waverider Type-B10

Fig. (7-6f) T : Temperature Distribution

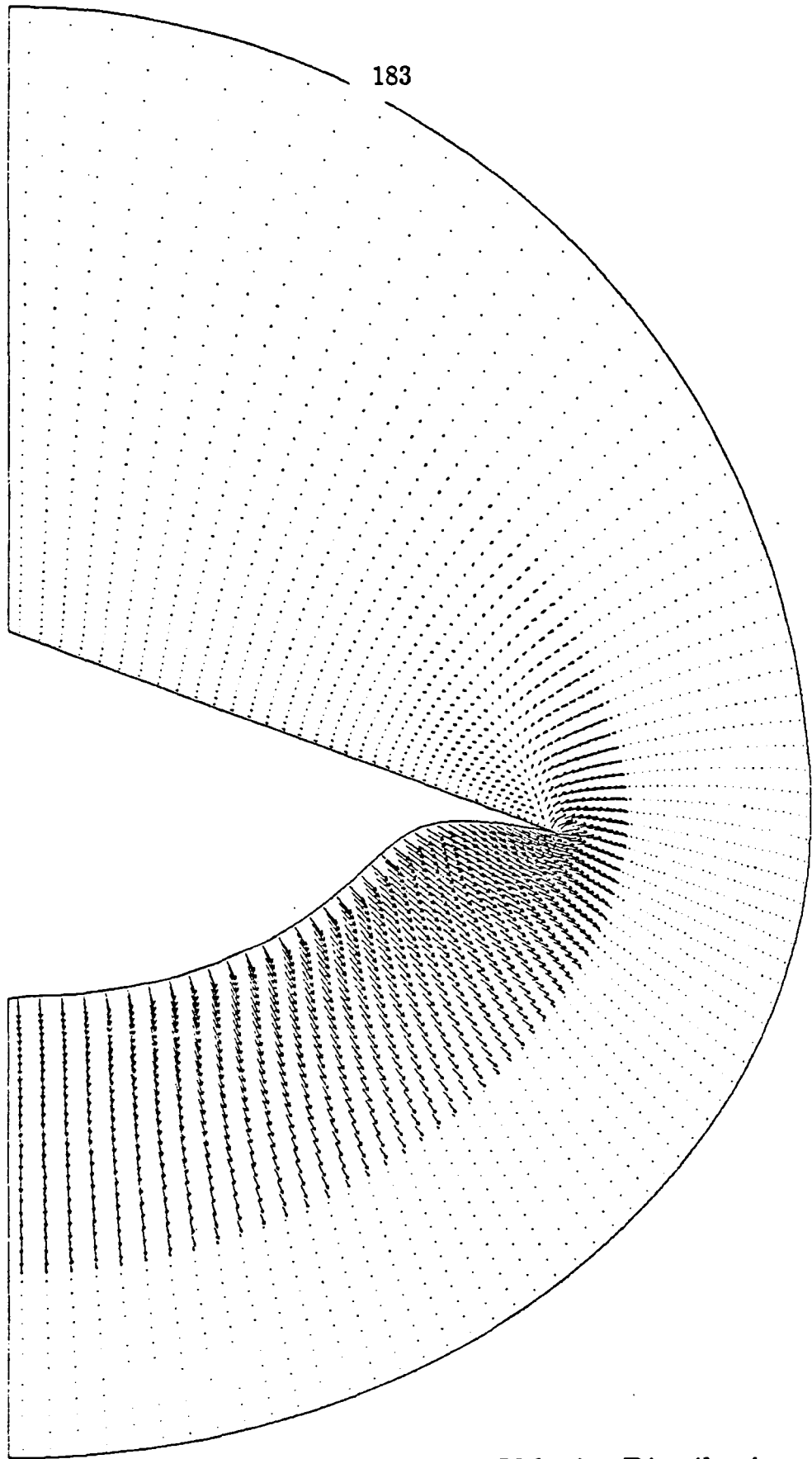


Fig. (7-7a) Cross-Plane Velocity Distribution

$$(M_{\infty} = 3, \quad \alpha = 0^{\circ})$$

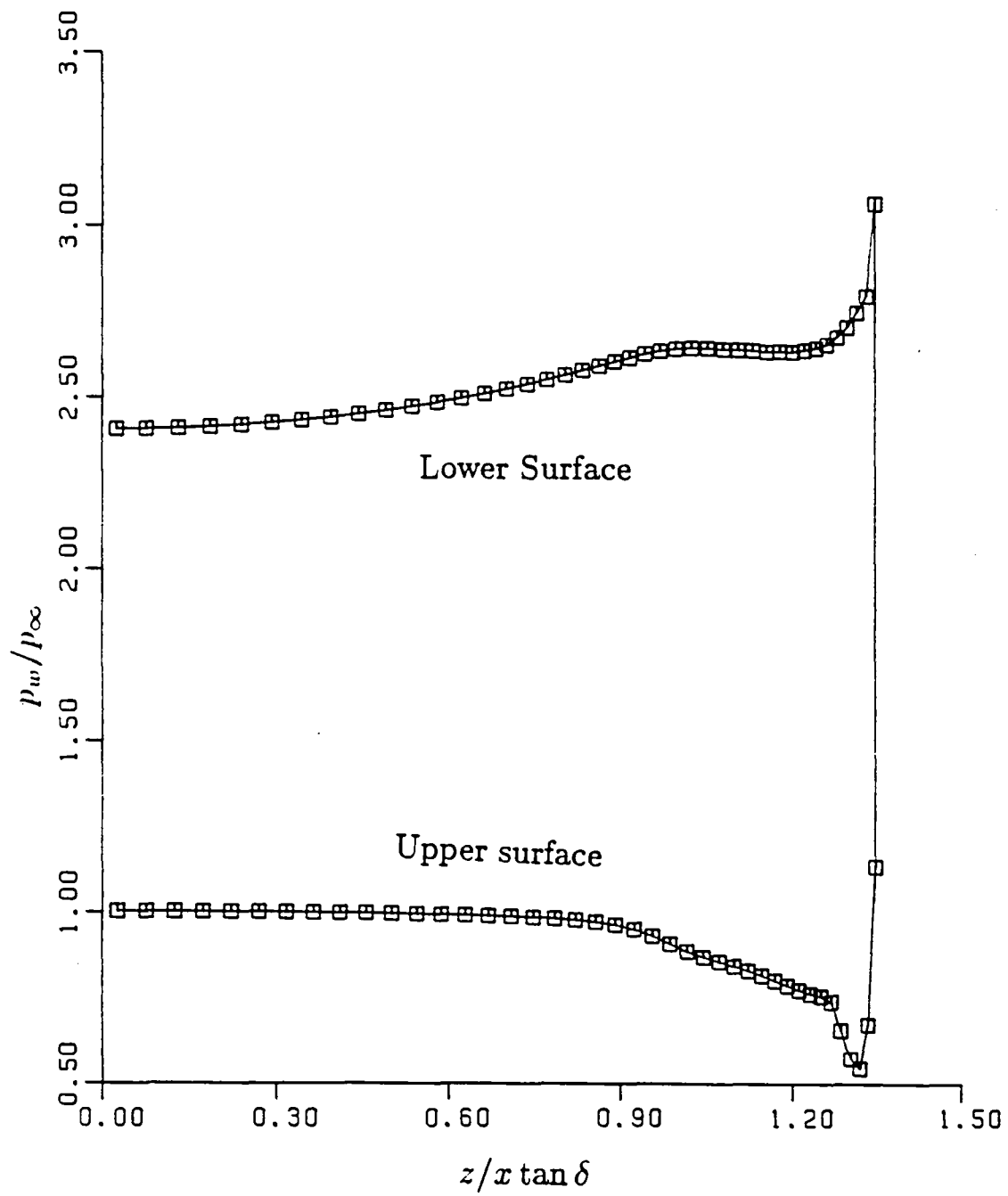


Fig. (7-7b) Wall Pressure Distribution

$$(M_\infty = 3, \quad \alpha = 0^\circ)$$

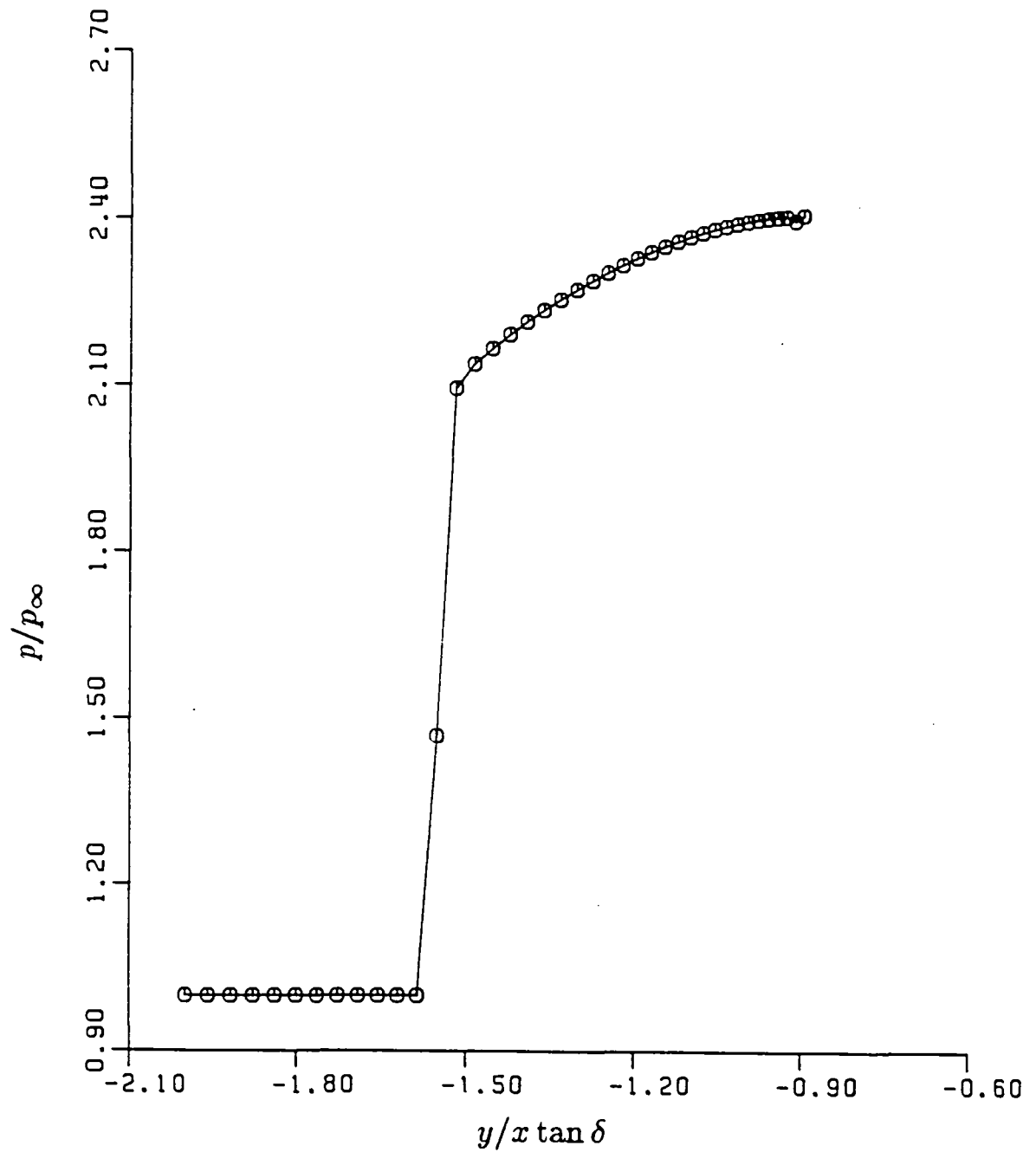


Fig. (7-7c) Pressure near Lower Symmetry Plane

$$(M_\infty = 3, \quad \alpha = 0^\circ)$$

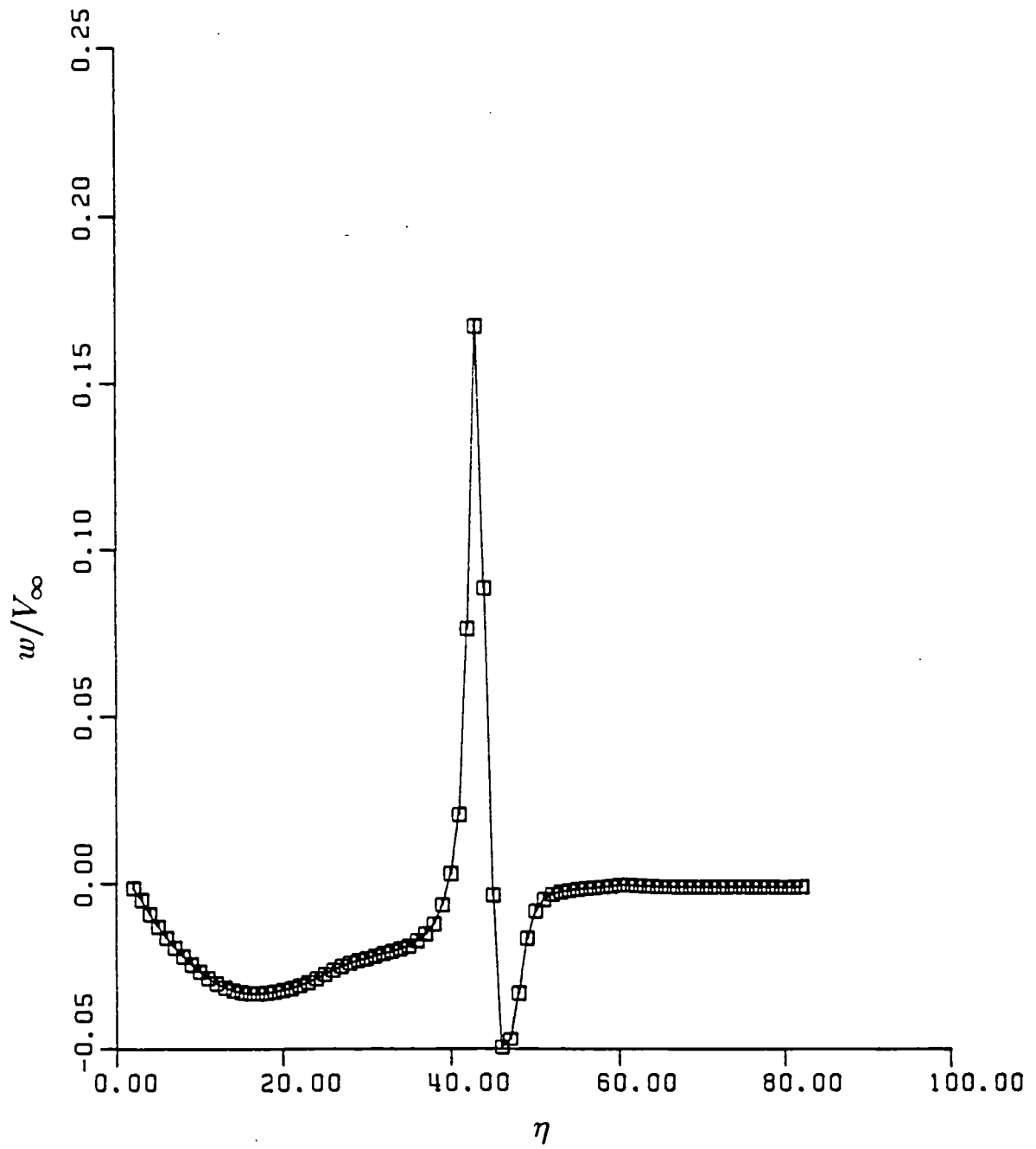


Fig. (7-7d) Azimuthal Velocity Component

$$(M_\infty = 3, \quad \alpha = 0^\circ)$$

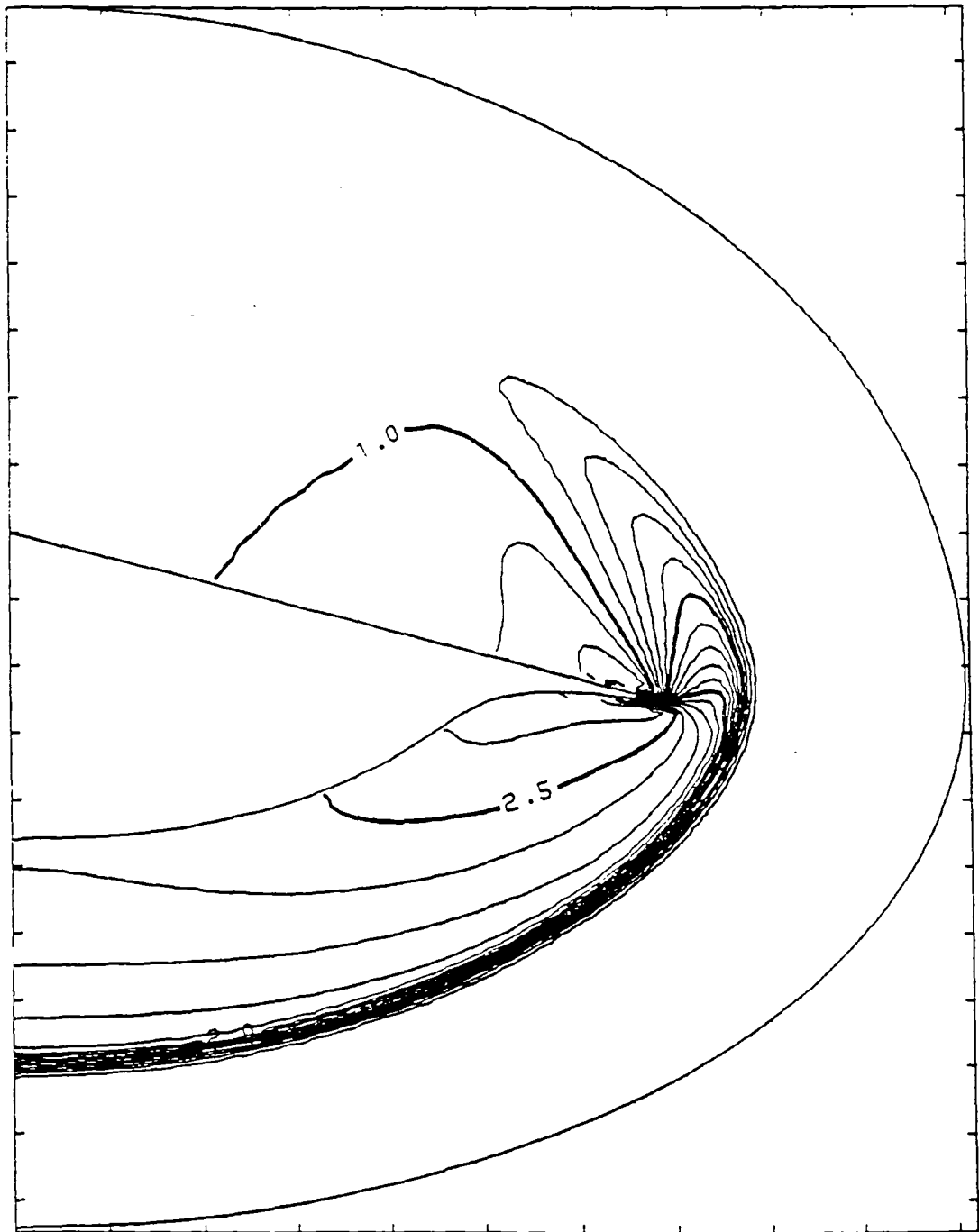


Fig. (7-7e) Pressure Contours

($M_\infty = 3$, $\alpha = 0^\circ$)

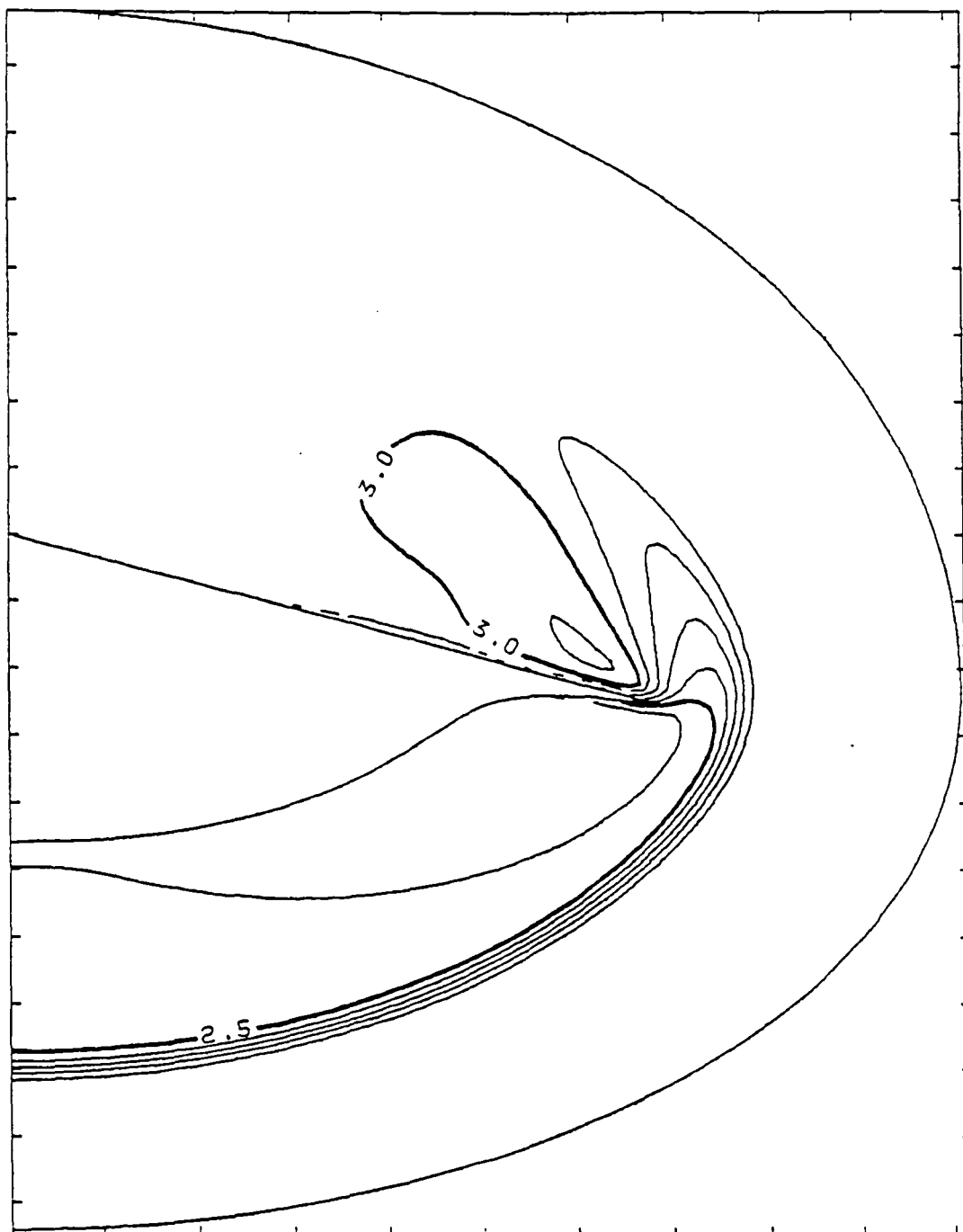


Fig. (7-7f) Mach Number Contours

($M_{\infty} = 3$, $\alpha = 0^{\circ}$)

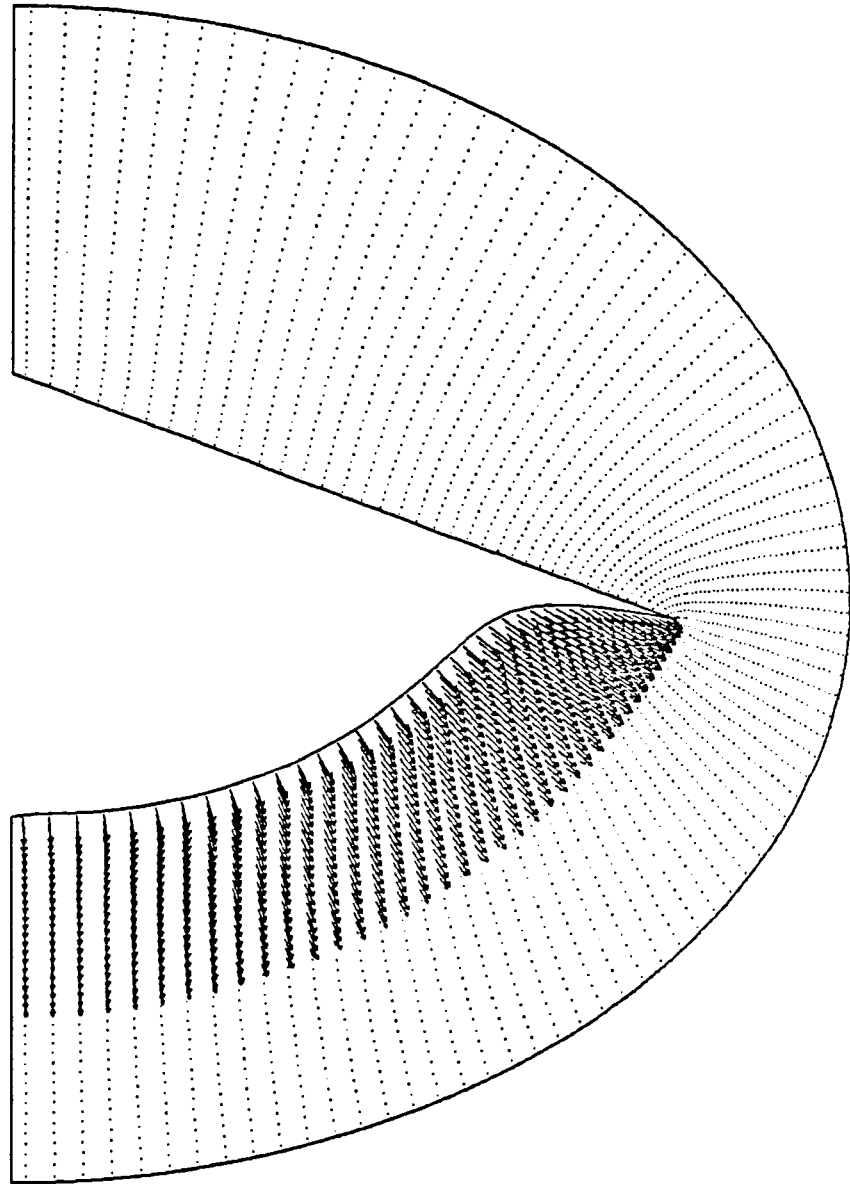


Fig. (7-8a) Cross-Plane Velocity Distribution

$$(M_{\infty} = 4.5, \quad \alpha = 0^{\circ})$$

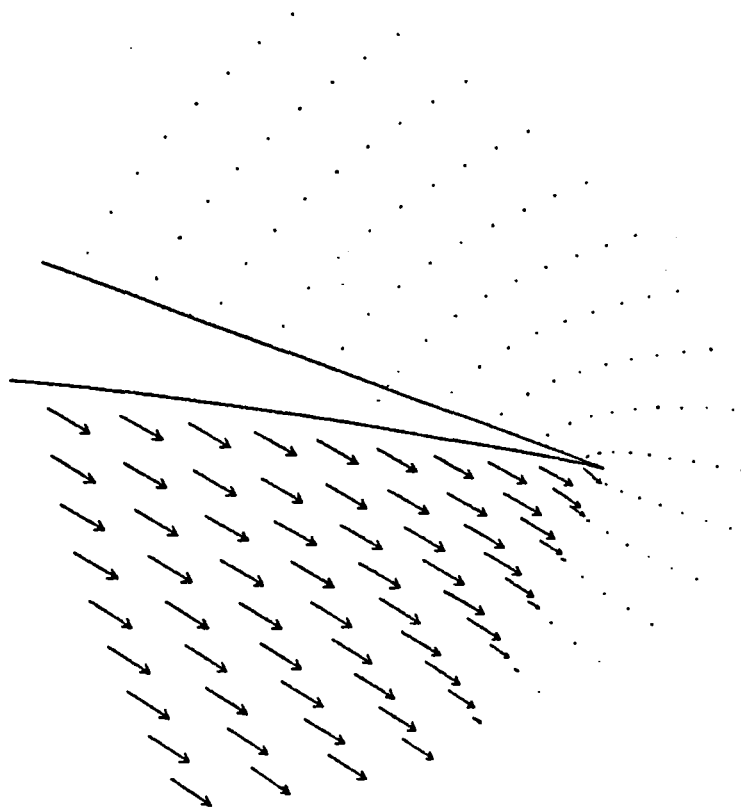


Fig. (7-8b) Magnified Cross-Plane Velocity near Tip

$$(M_{\infty} = 4.5, \quad \alpha = 0^{\circ})$$

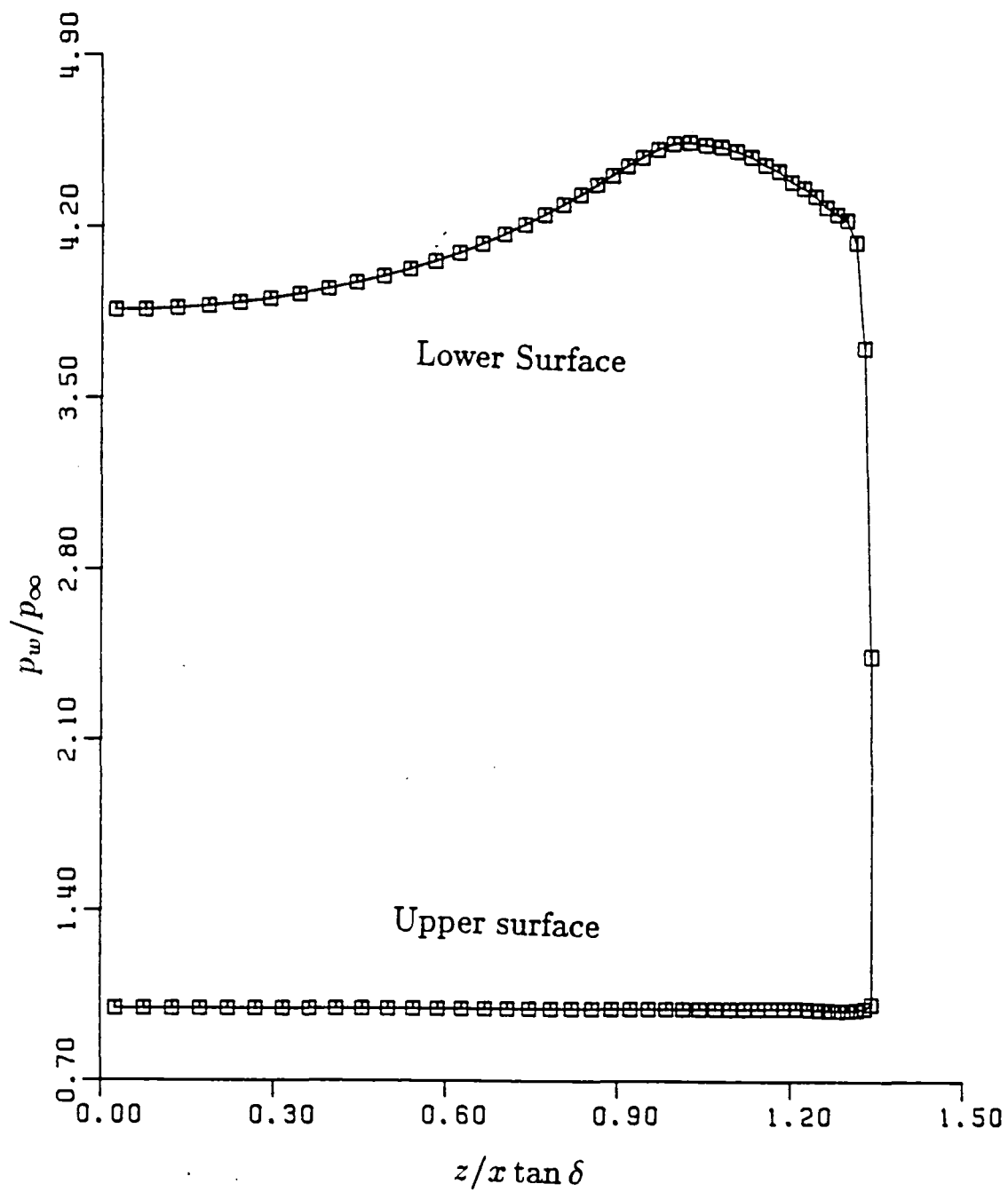


Fig. (7-8c) Wall Pressure Distribution
($M_\infty = 4.5$, $\alpha = 0^\circ$)

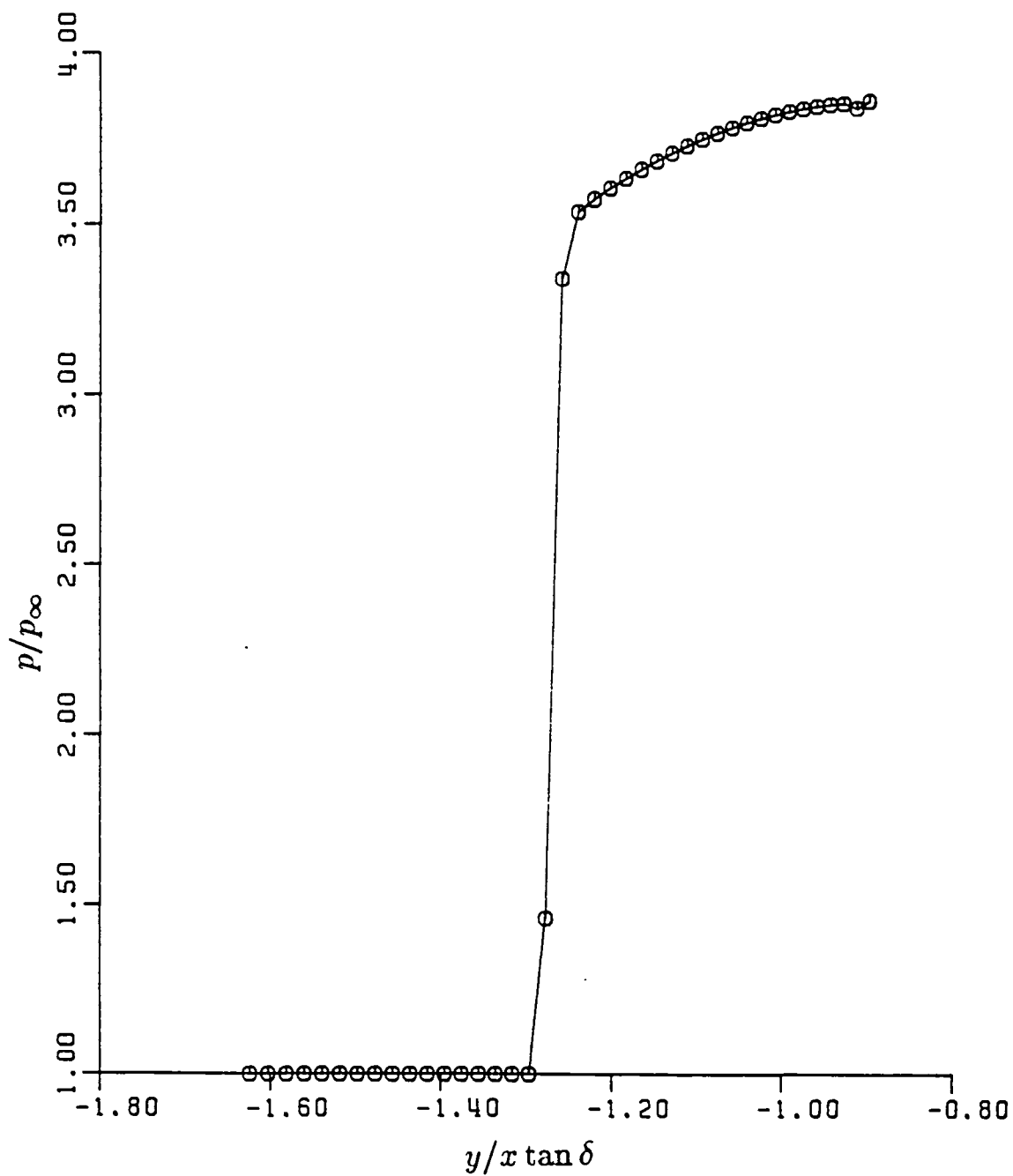


Fig. (7-8d) Pressure near Lower Symmetry Plane

$$(M_\infty = 4.5, \quad \alpha = 0^\circ)$$

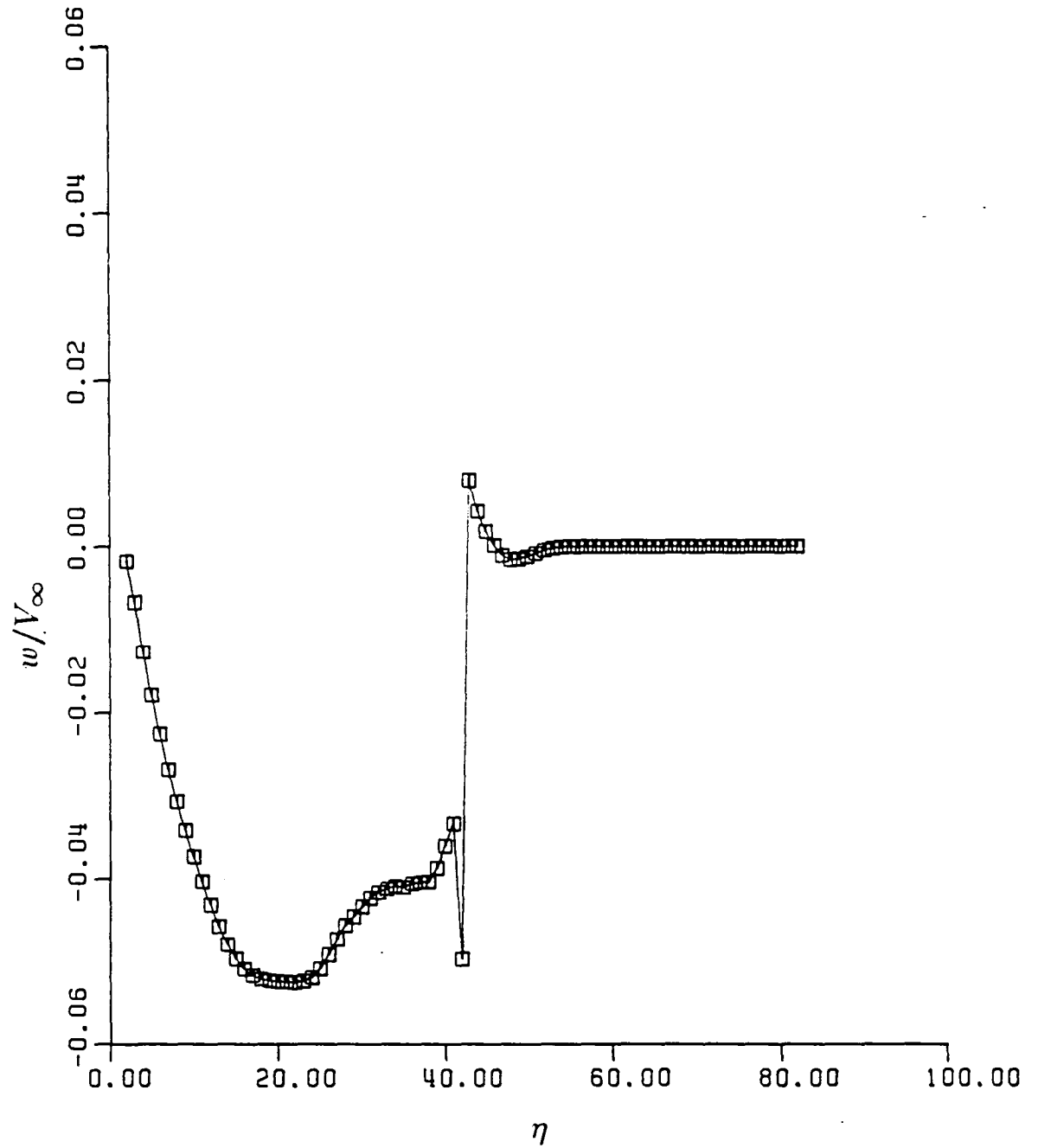


Fig. (7-8e) Azimuthal Velocity Component

$$(M_\infty = 4.5, \quad \alpha = 0^\circ)$$

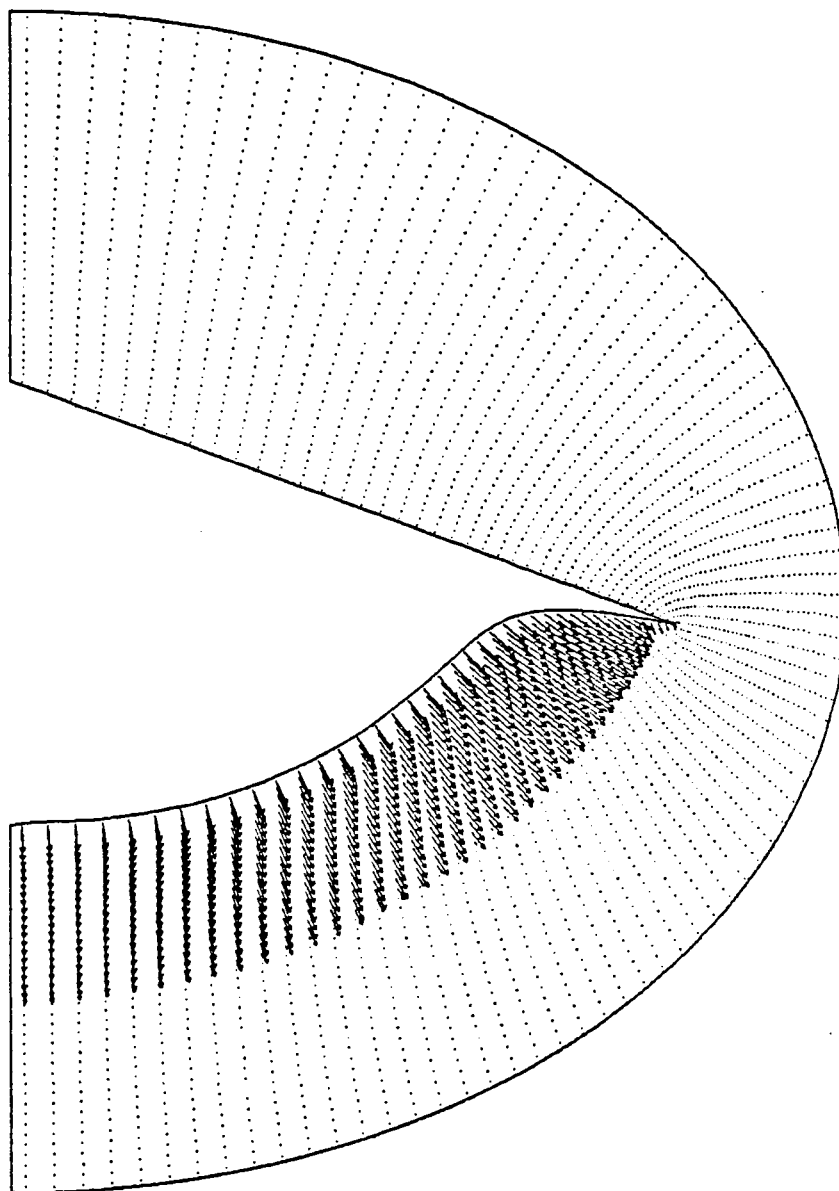


Fig. (7-9a) Cross-Plane Velocity Distribution

$$(M_{\infty} = 5, \quad \alpha = 0^{\circ})$$

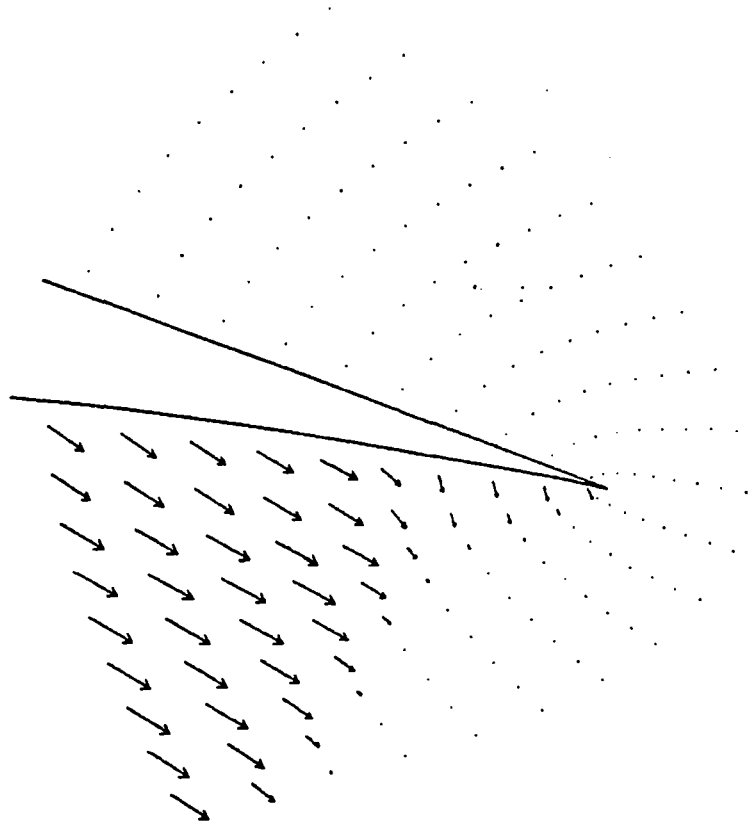


Fig. (7-9b) Magnified Cross-Plane Velocity near Tip

$$(M_{\infty} = 5, \quad \alpha = 0^{\circ})$$

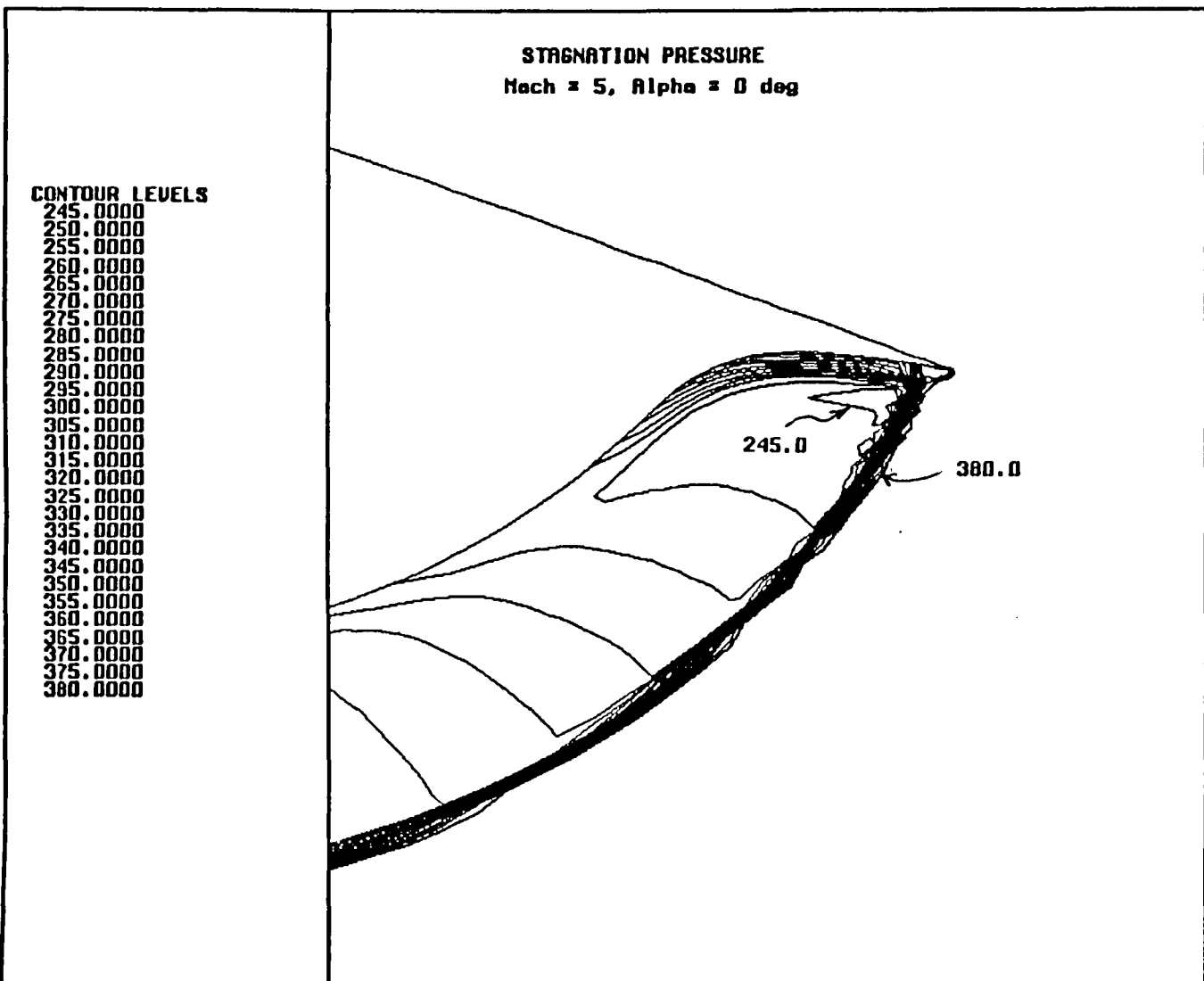


Fig. (7-9c) Total Pressure Contours

 $(M_\infty = 5, \alpha = 0^\circ)$

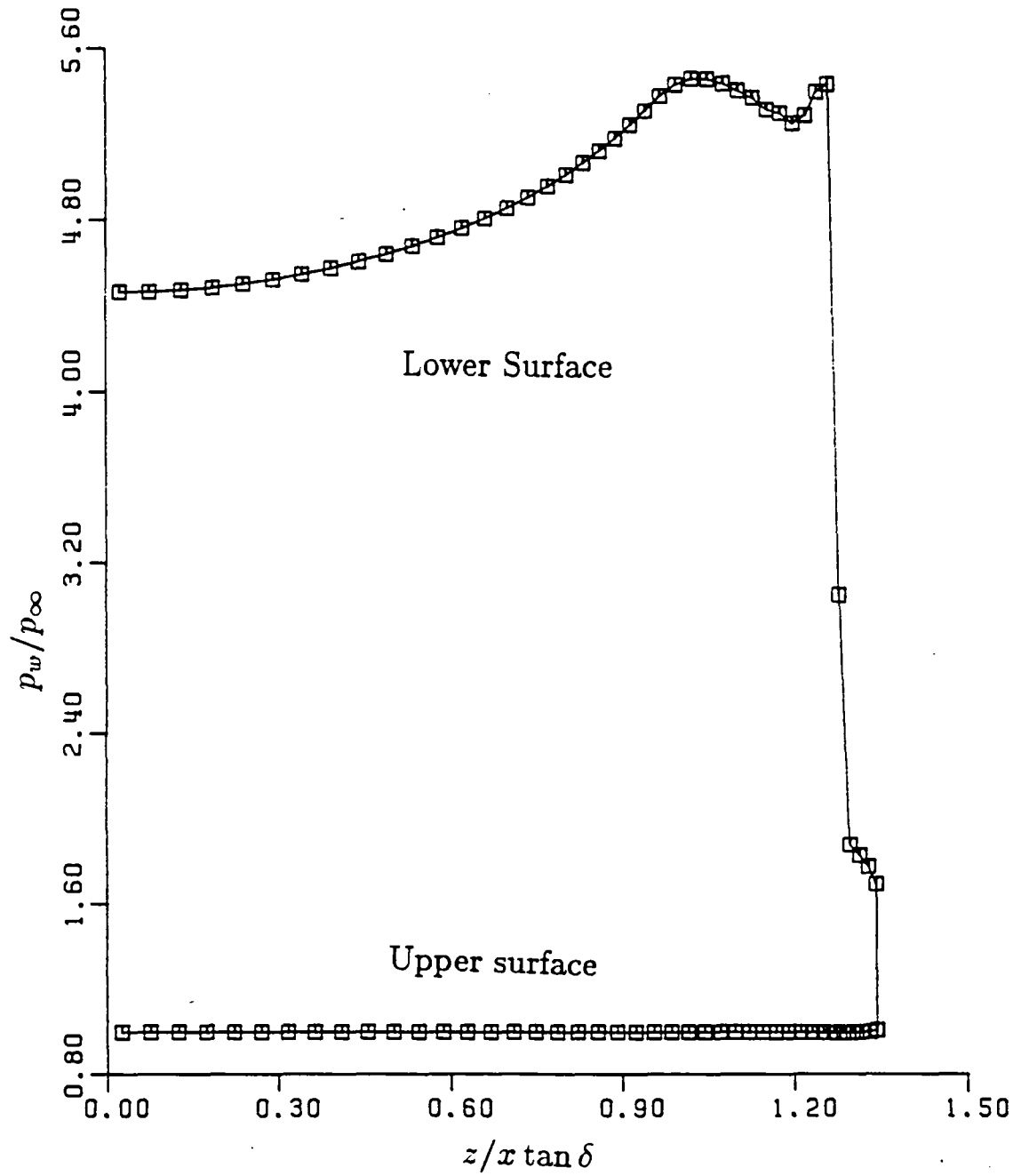


Fig. (7-9d) Wall Pressure Distribution

$$(M_\infty = 5, \quad \alpha = 0^\circ)$$

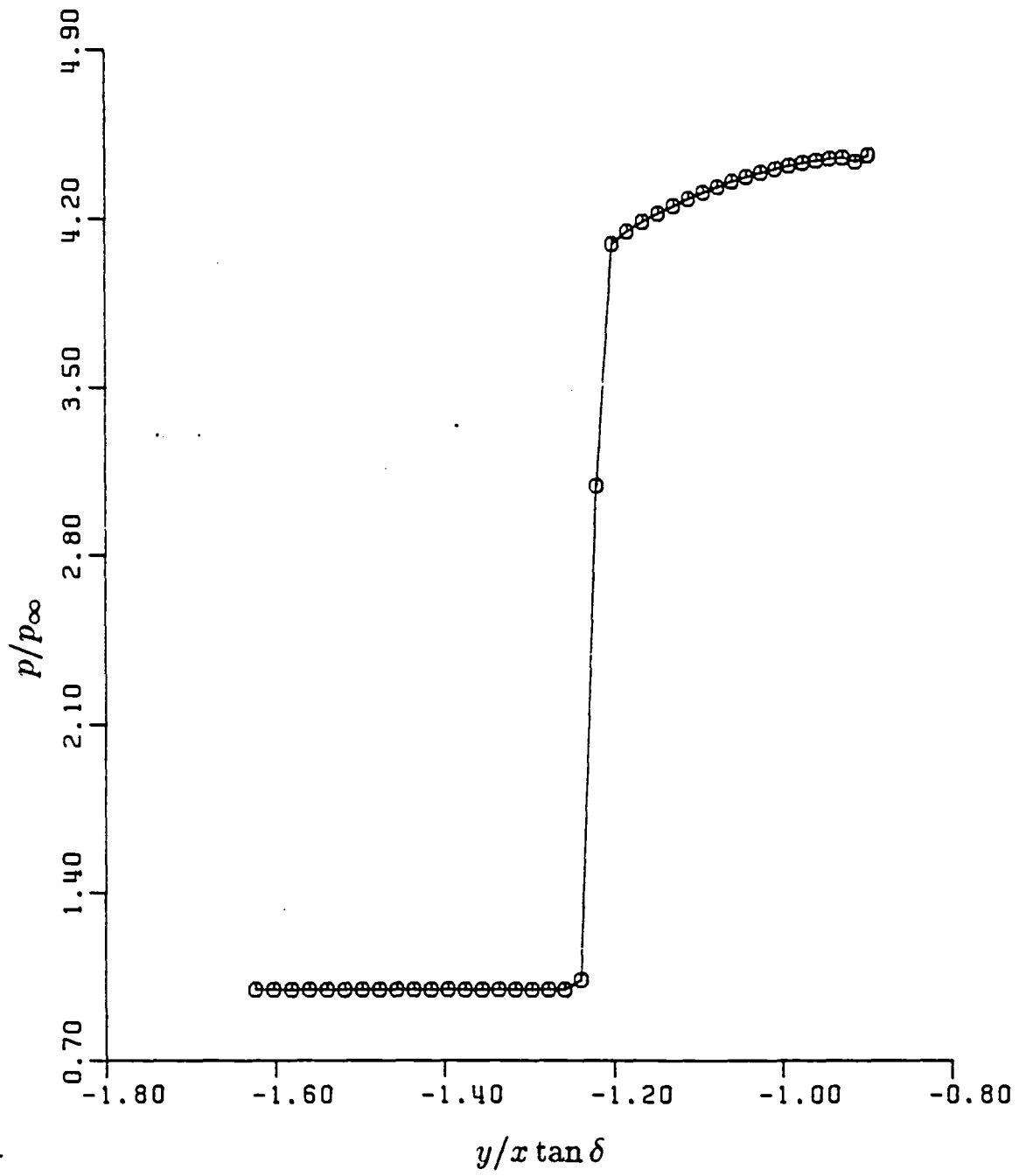


Fig. (7-9e) Pressure near Lower Symmetry Plane

$$(M_\infty = 5, \quad \alpha = 0^\circ)$$

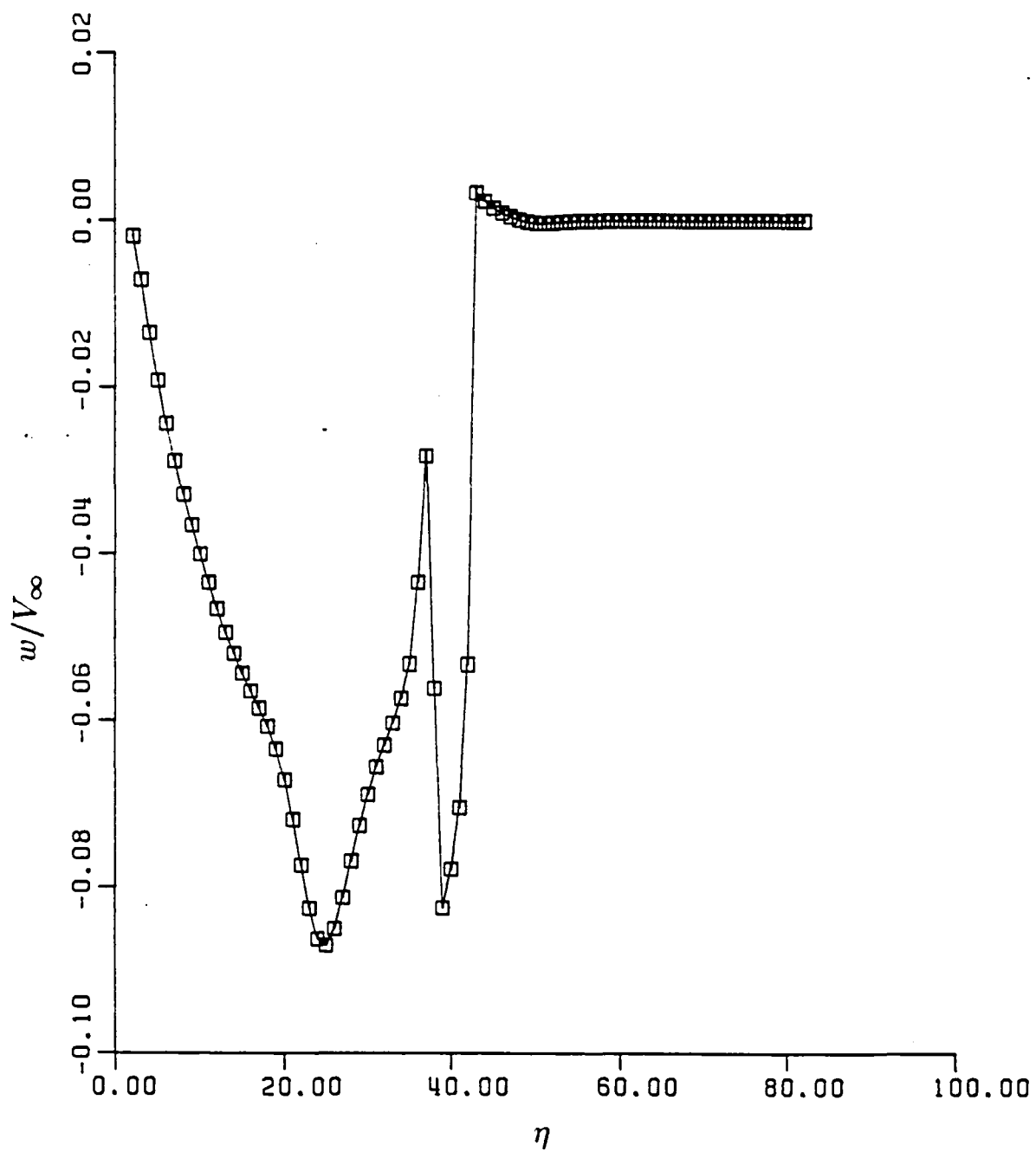


Fig. (7-9f) Azimuthal Velocity Component
($M_\infty = 5$, $\alpha = 0^\circ$)

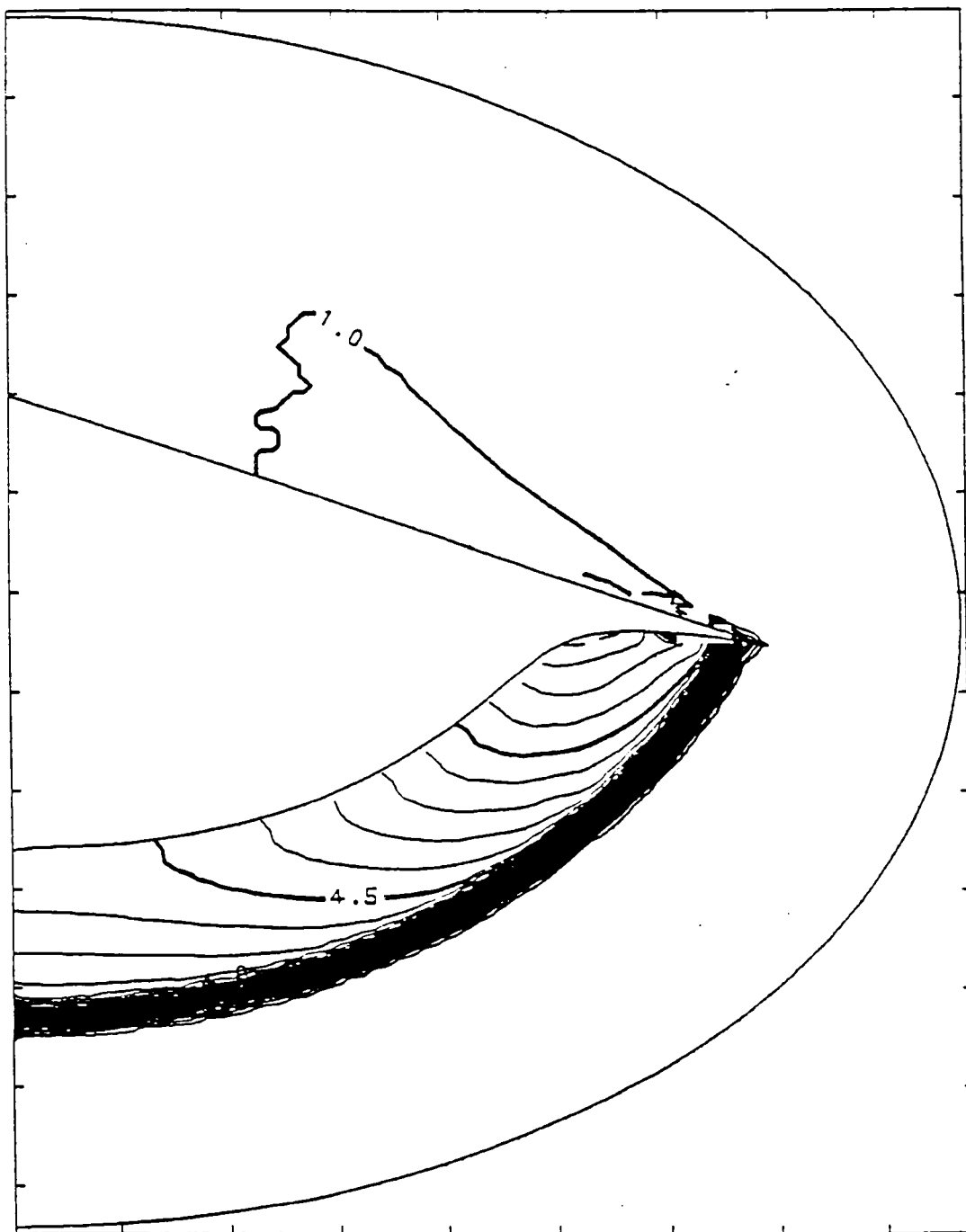


Fig. (7-9g) Pressure Contours
($M_{\infty} = 5$, $\alpha = 0^{\circ}$)

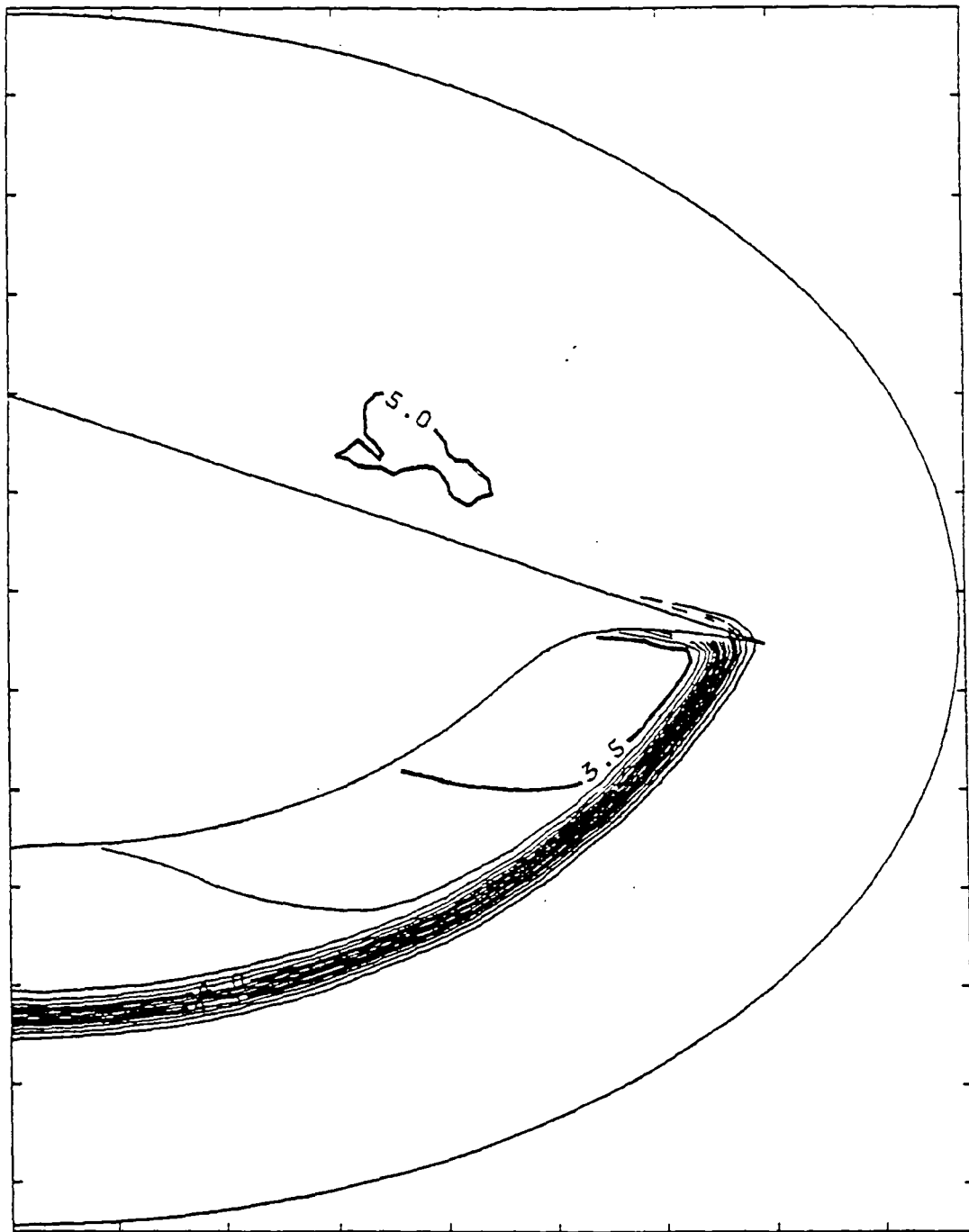


Fig. (7-9h) Mach Number Contours

$$(M_{\infty} = 5, \quad \alpha = 0^{\circ})$$

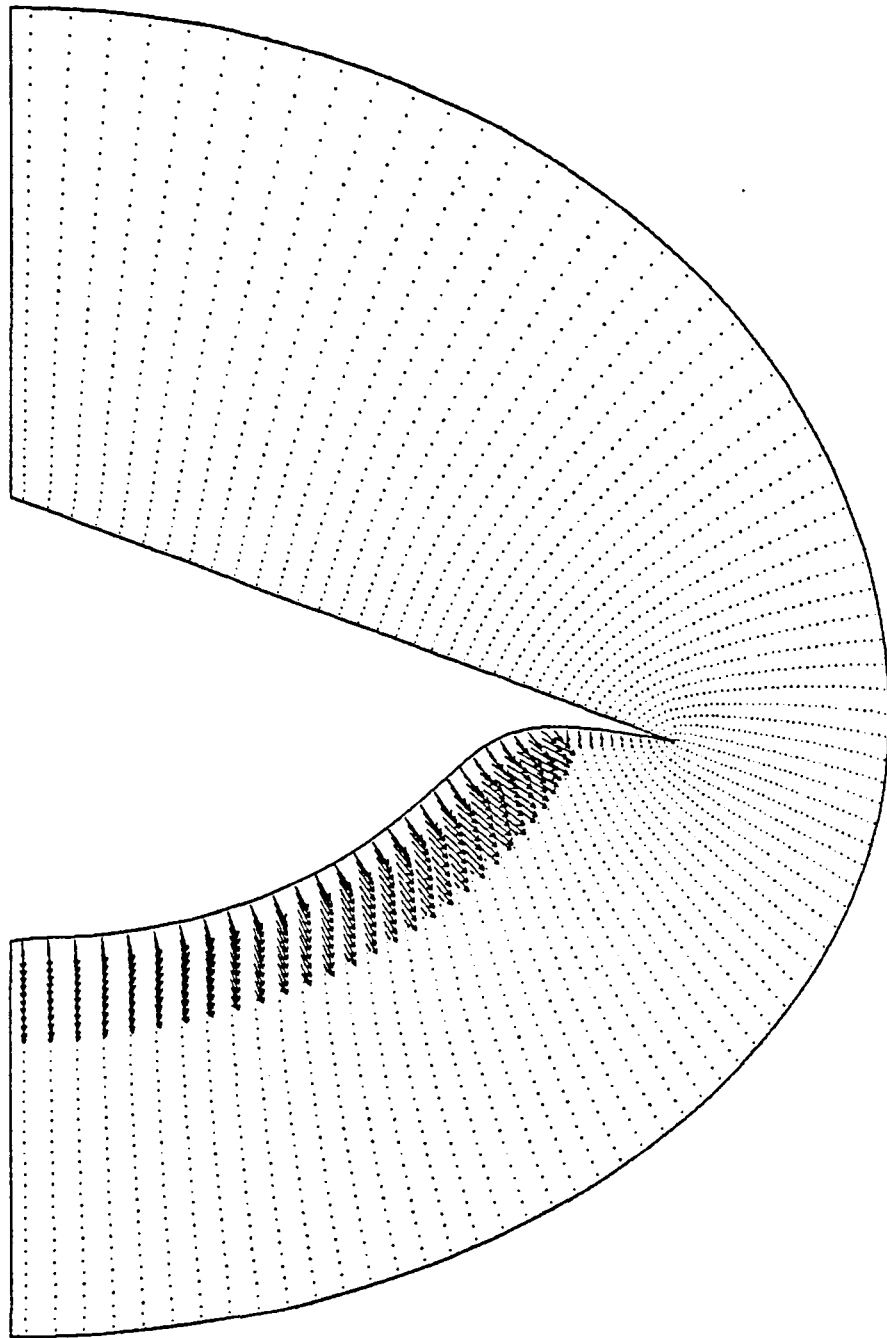


Fig. (7-10a) Cross-Plane Velocity Distribution

$$(M_{\infty} = 10, \quad \alpha = 0^{\circ})$$

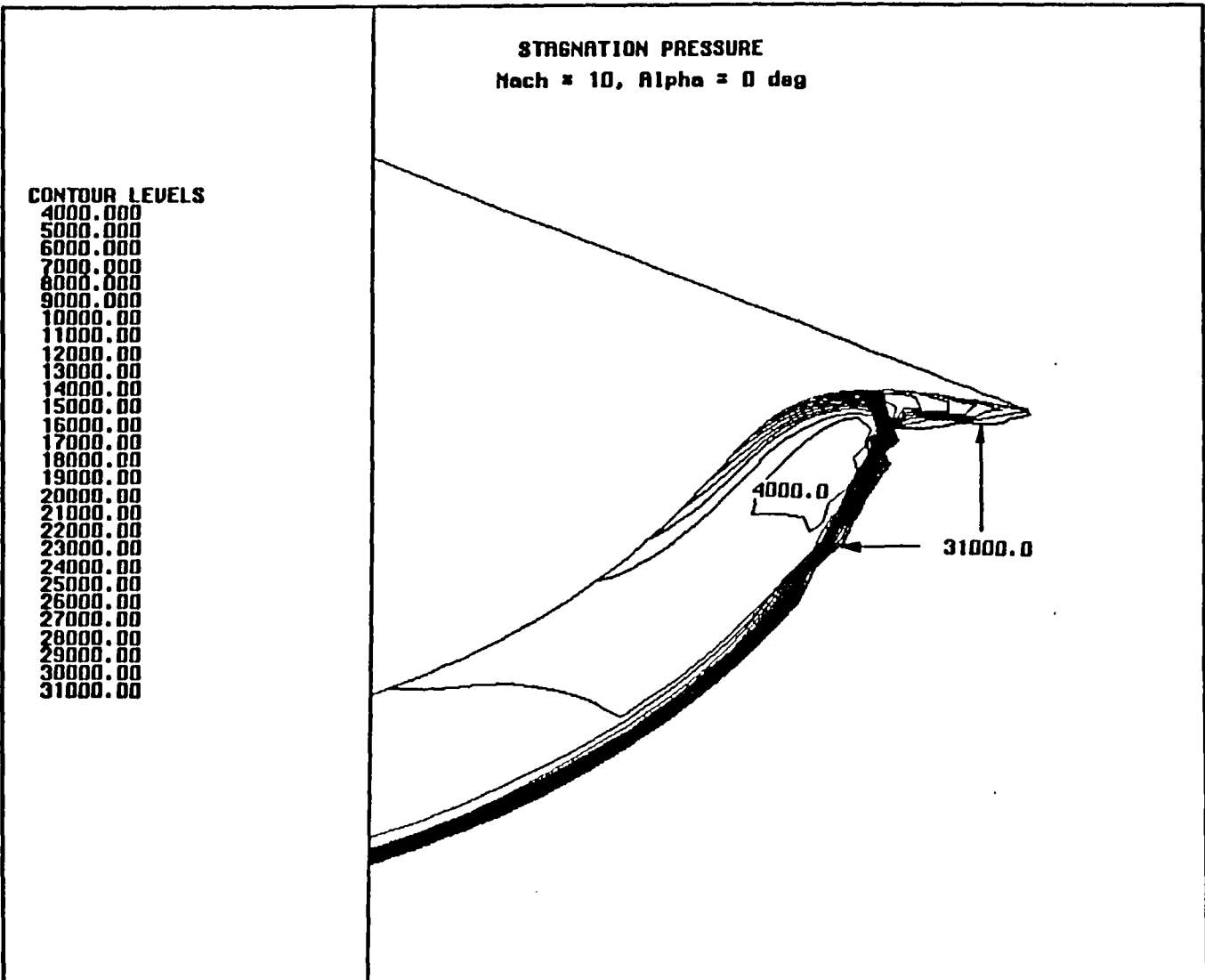


Fig. (7-10b) Total Pressure Contours

(M_∞ = 10, α = 0°)

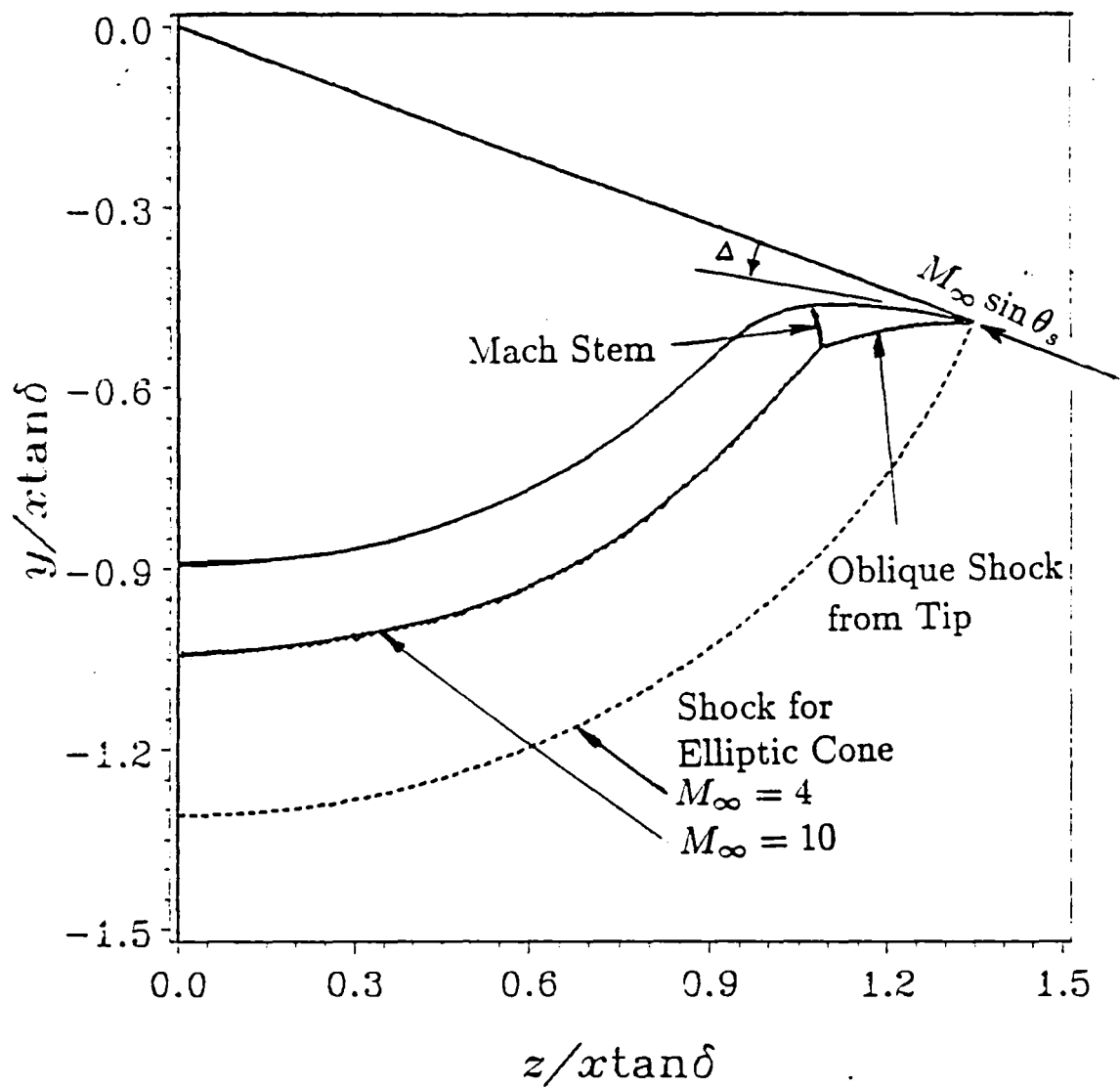


Fig. (7-10c) Schematic Diagram of Lambda Shock

$$(M_\infty = 10, \quad \alpha = 0^\circ)$$

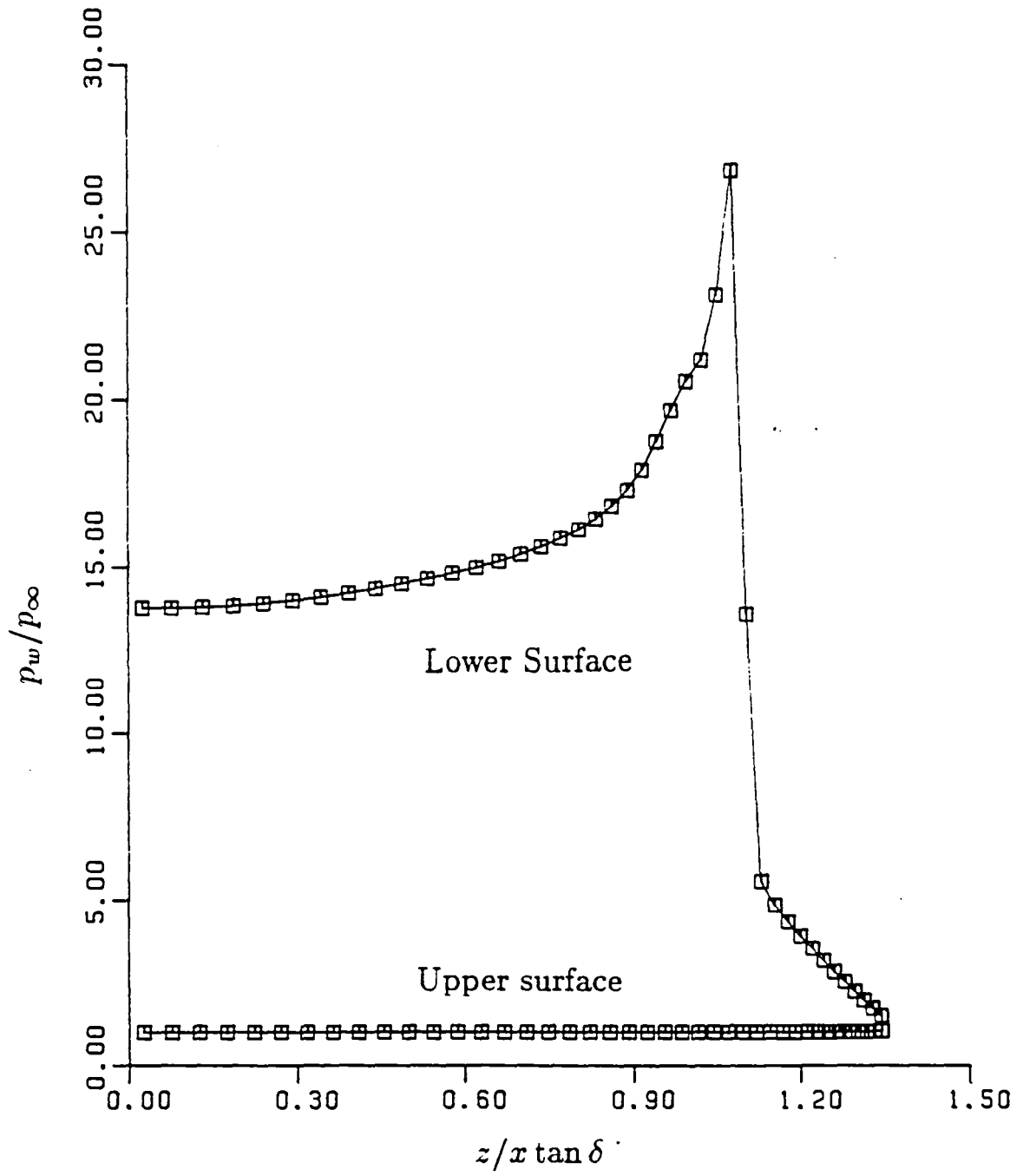


Fig. (7-10d) Wall Pressure Distribution

 $(M_\infty = 10, \alpha = 0^\circ)$

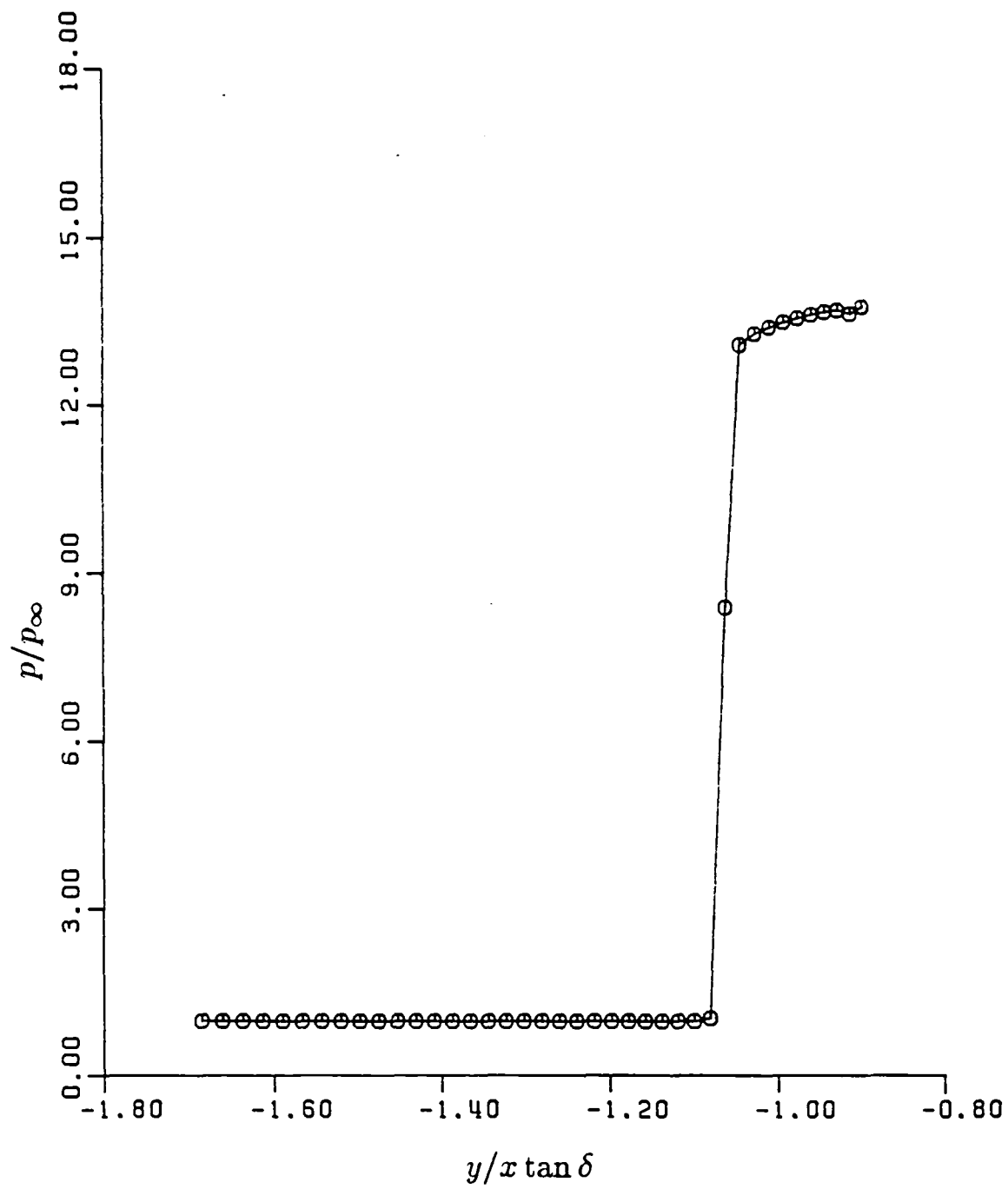


Fig. (7-10e) Pressure near Lower Symmetry Plane

$$(M_\infty = 10, \quad \alpha = 0^\circ)$$

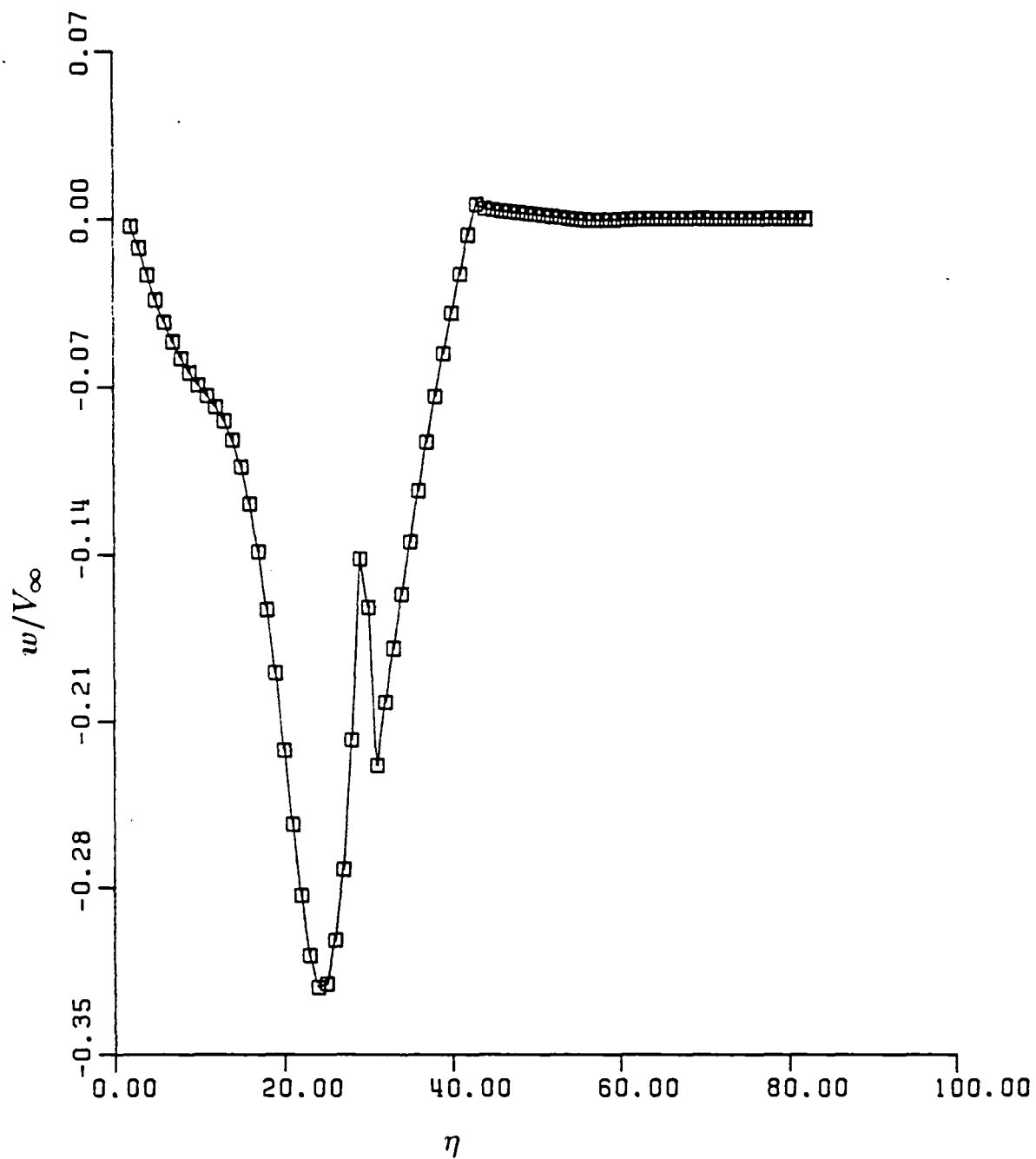


Fig. (7-10f) Azimuthal Velocity Component

$$(M_\infty = 10, \quad \alpha = 0^\circ)$$

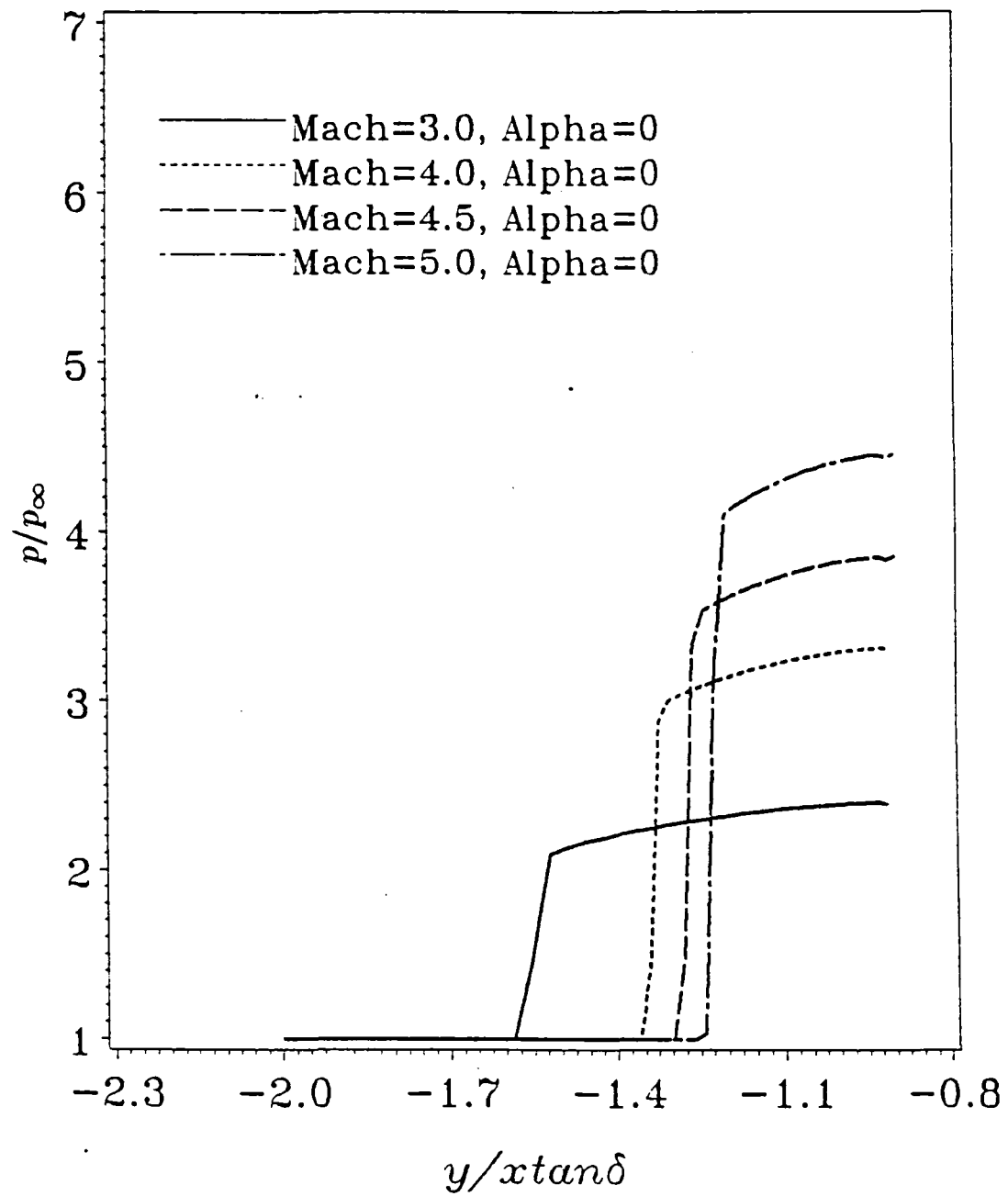


Fig. (7-11a) Pressure near Lower Symmetry Plane

$$(M_\infty \neq 4, \quad \alpha = 0^\circ)$$

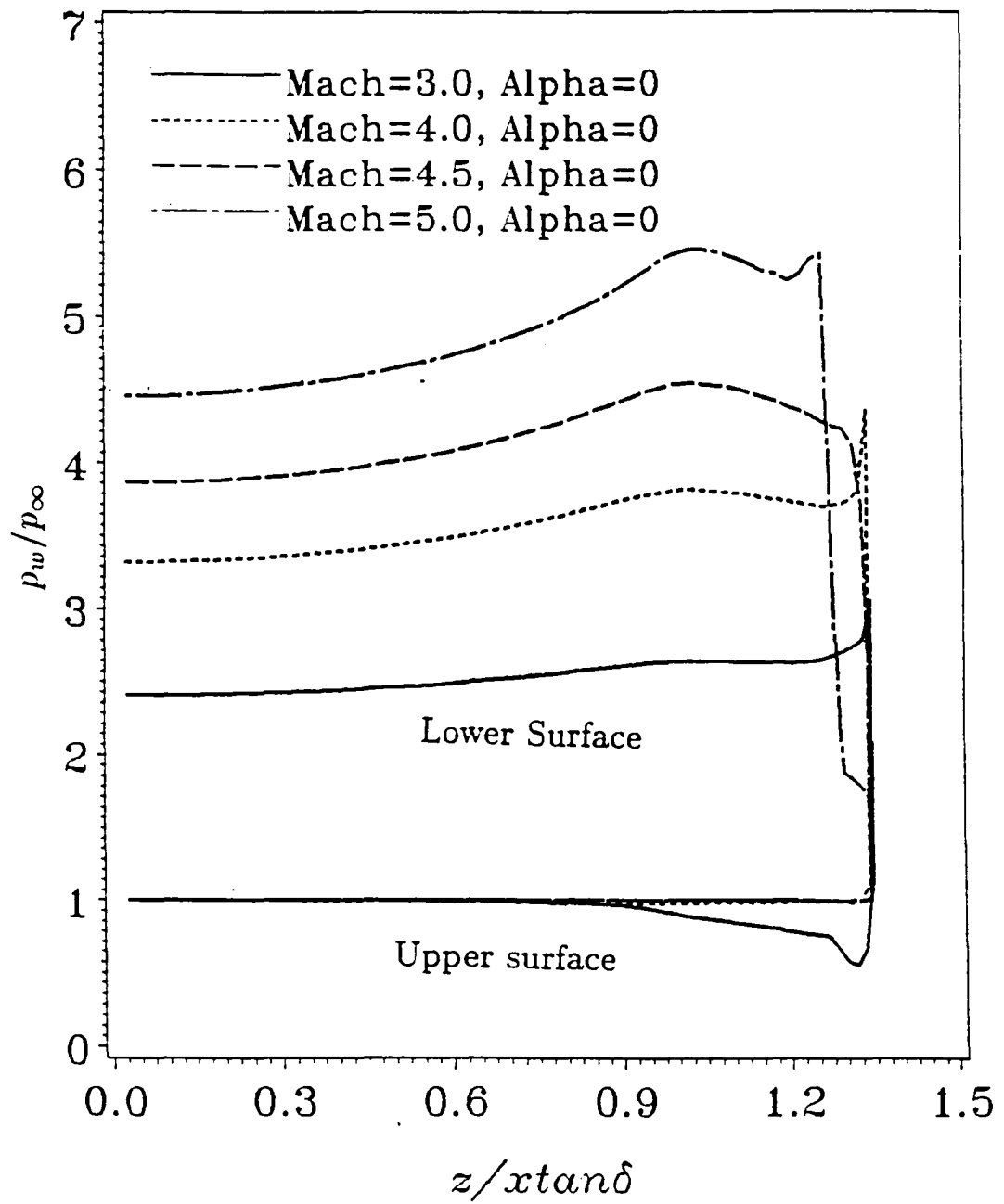


Fig. (7-11b) Wall Pressure
 $(M_\infty \neq 4, \alpha = 0^\circ)$

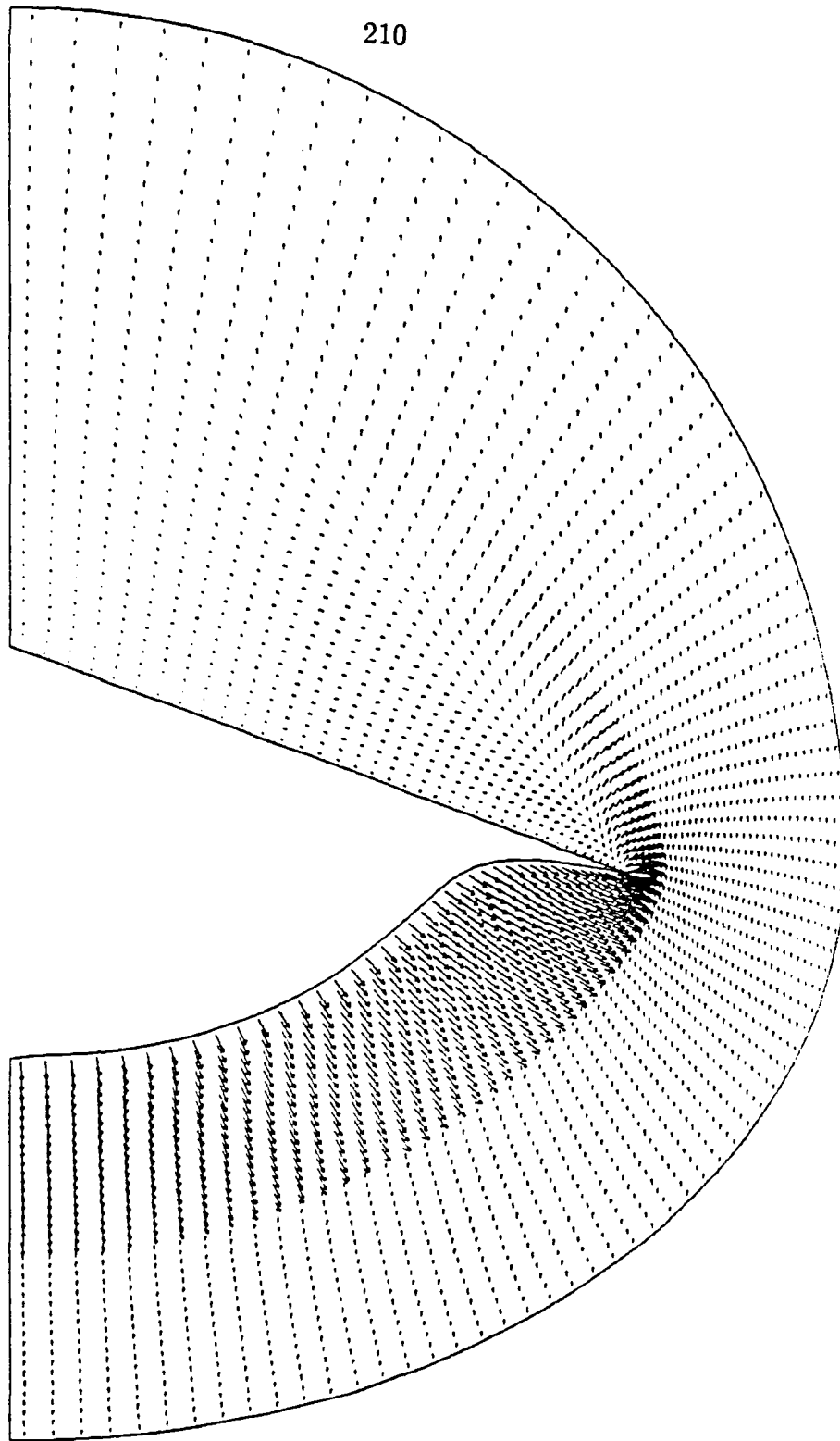


Fig. (7-12a) Cross-Plane Velocity Distribution
($M_{\infty} = 4$, $\alpha = +3^{\circ}$)

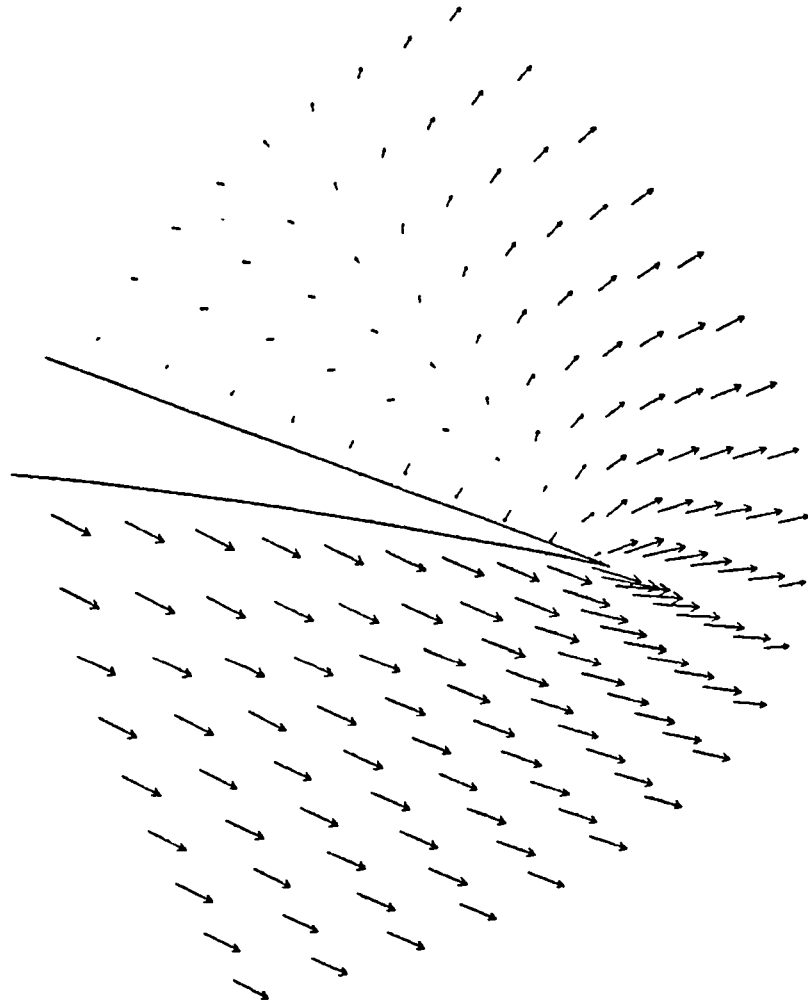


Fig. (7-12b) Magnified Cross-Plane Velocity near Tip

$$(M_{\infty} = 4, \quad \alpha = +3^{\circ})$$

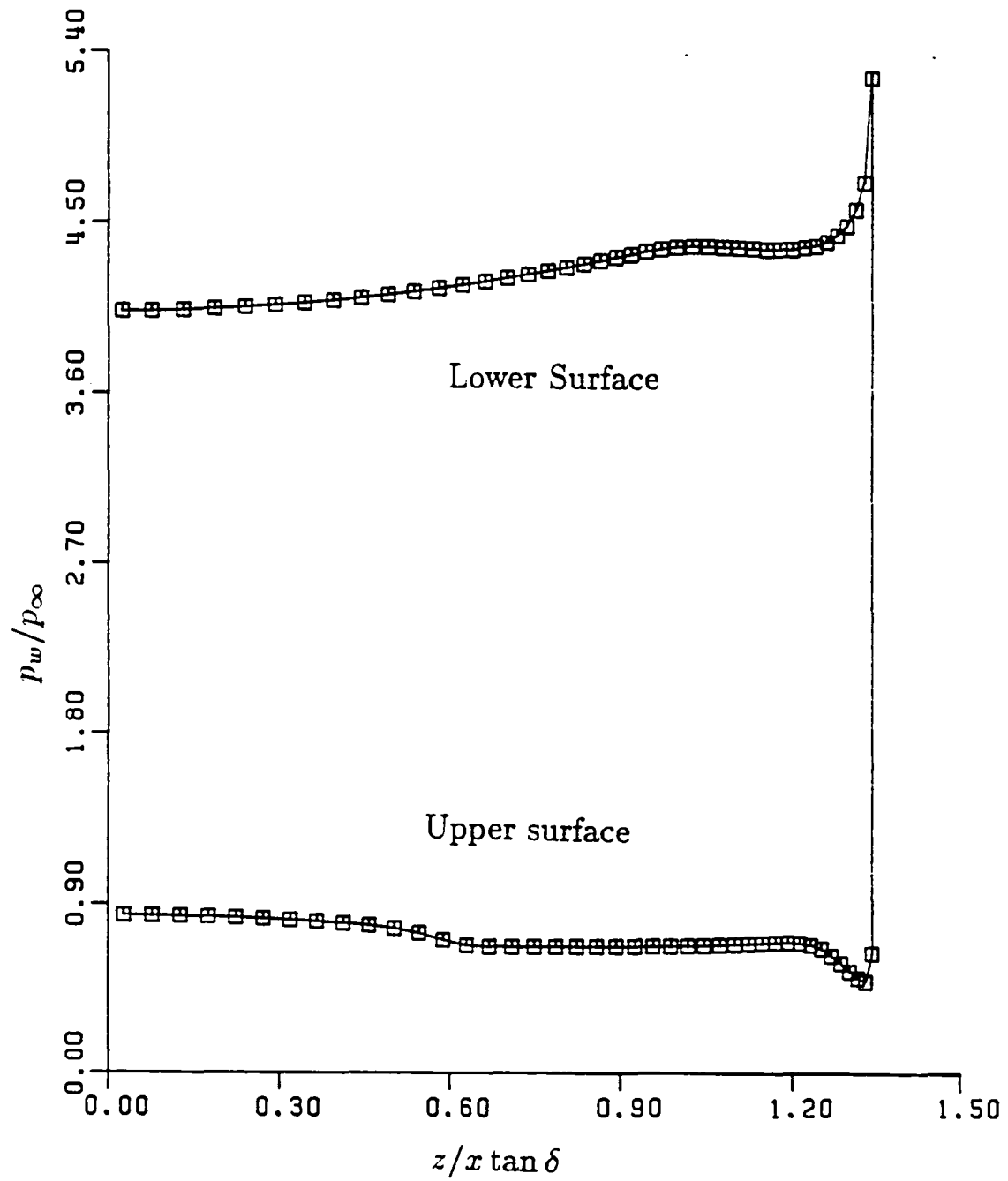


Fig. (7-12c) Wall Pressure Distribution
($M_\infty = 4$, $\alpha = +3^\circ$)

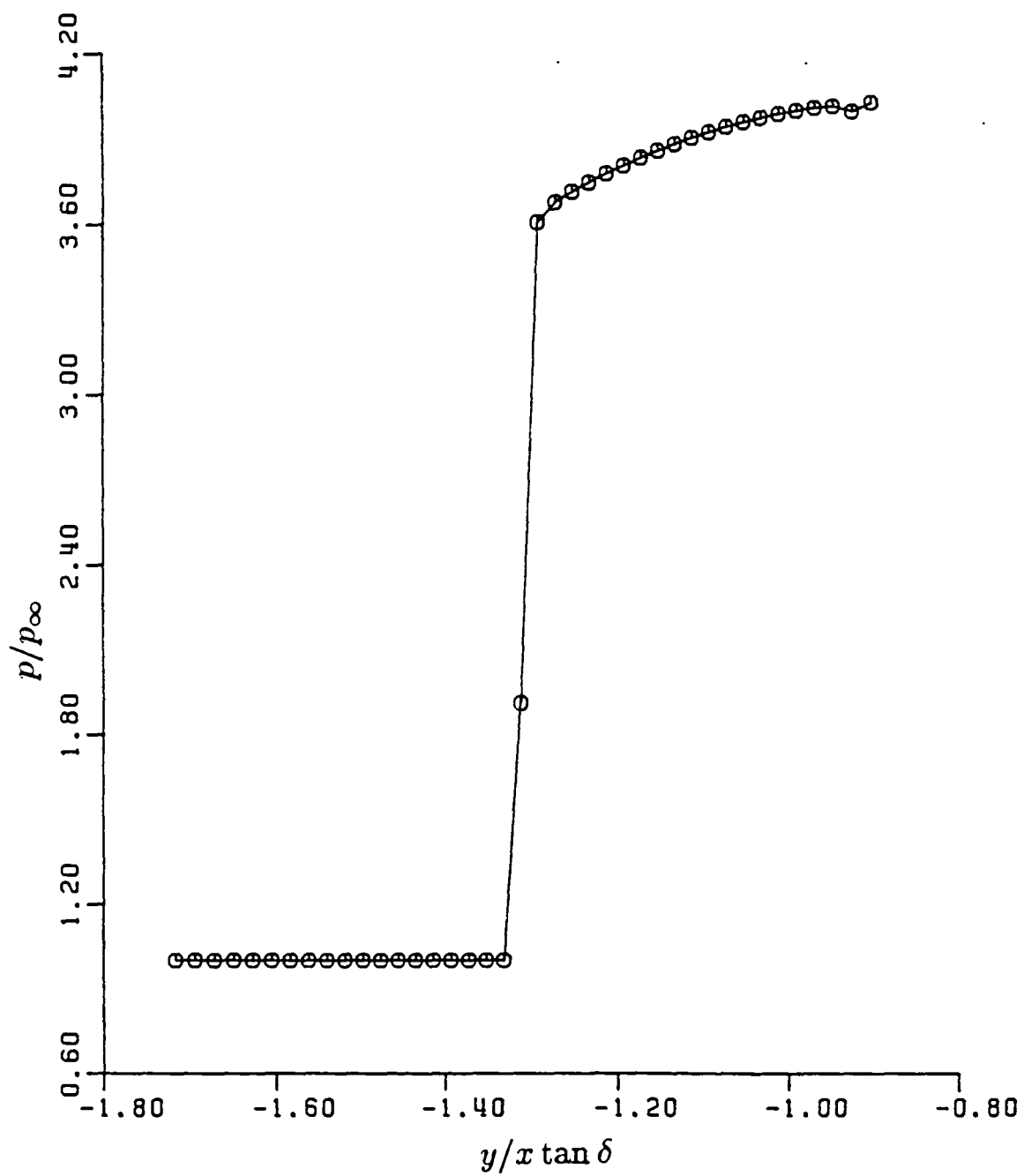


Fig. (7-12d) Pressure near Lower Symmetry Plane

$$(M_\infty = 4, \quad \alpha = +3^\circ)$$

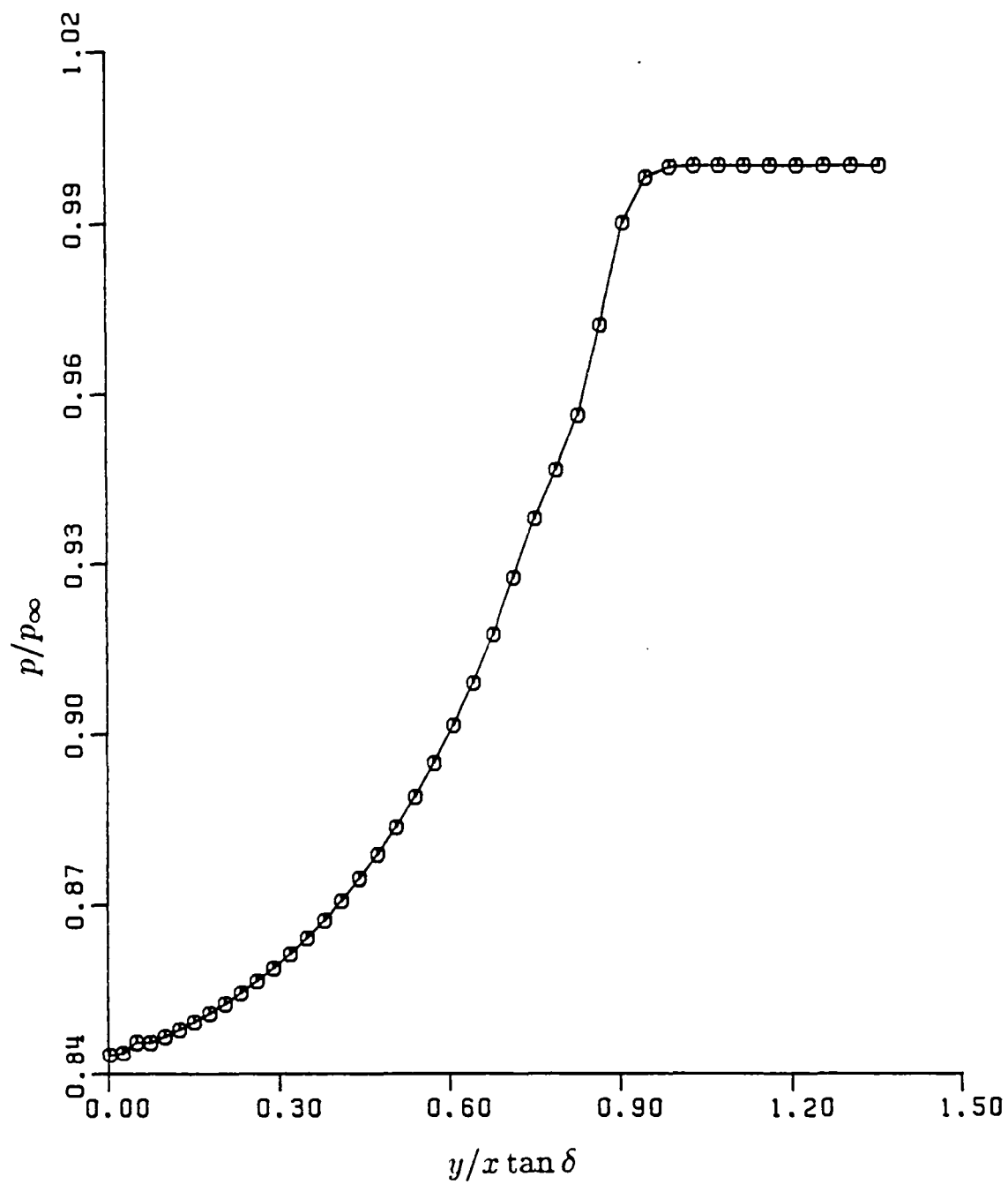


Fig. (7-12e) Pressure near Upper Symmetry Plane

$$(M_\infty = 4, \quad \alpha = +3^\circ)$$

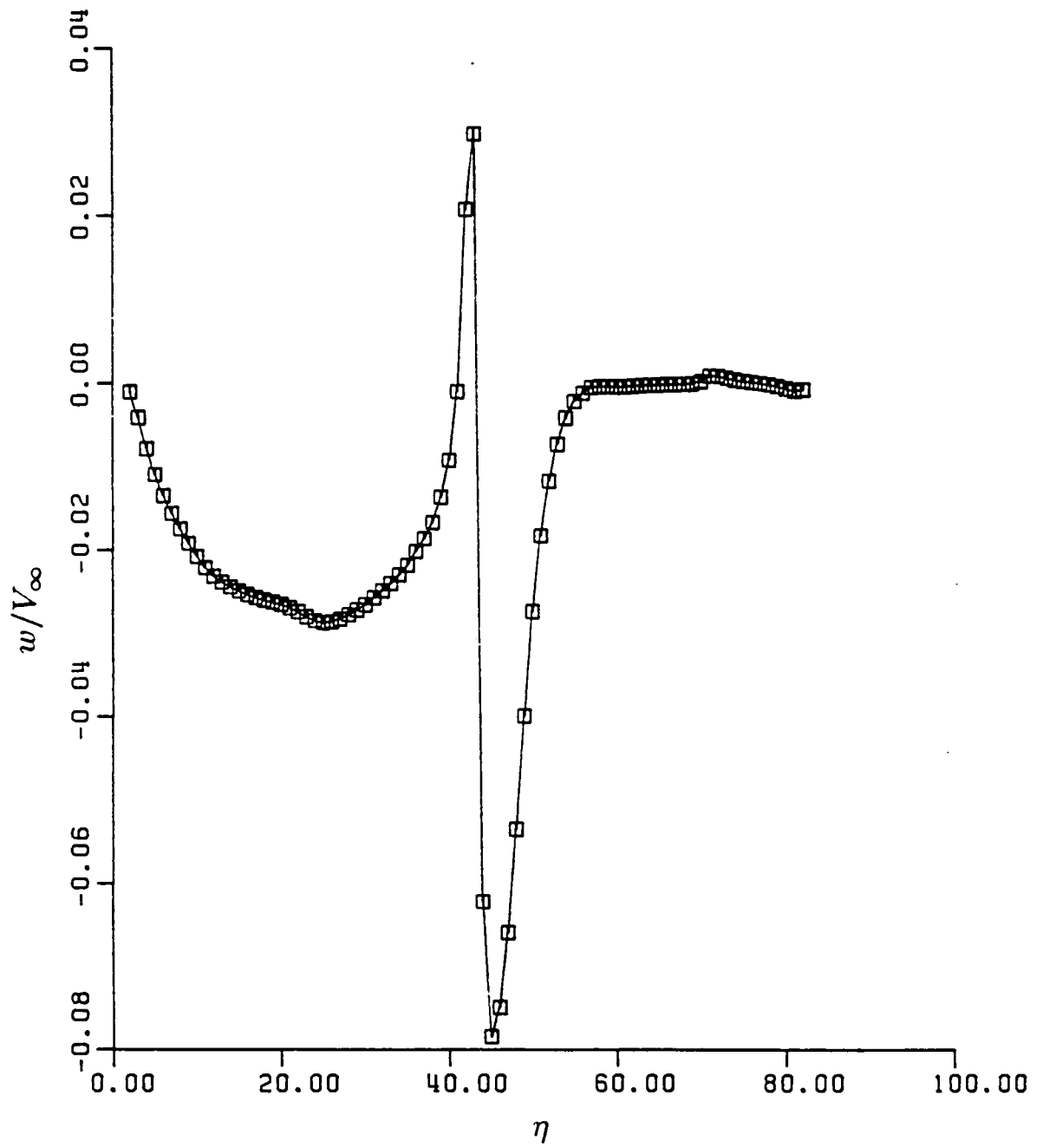


Fig. (7-12f) Azimuthal Velocity Componen

$$(M_\infty = 4, \quad \alpha = +3^\circ)$$

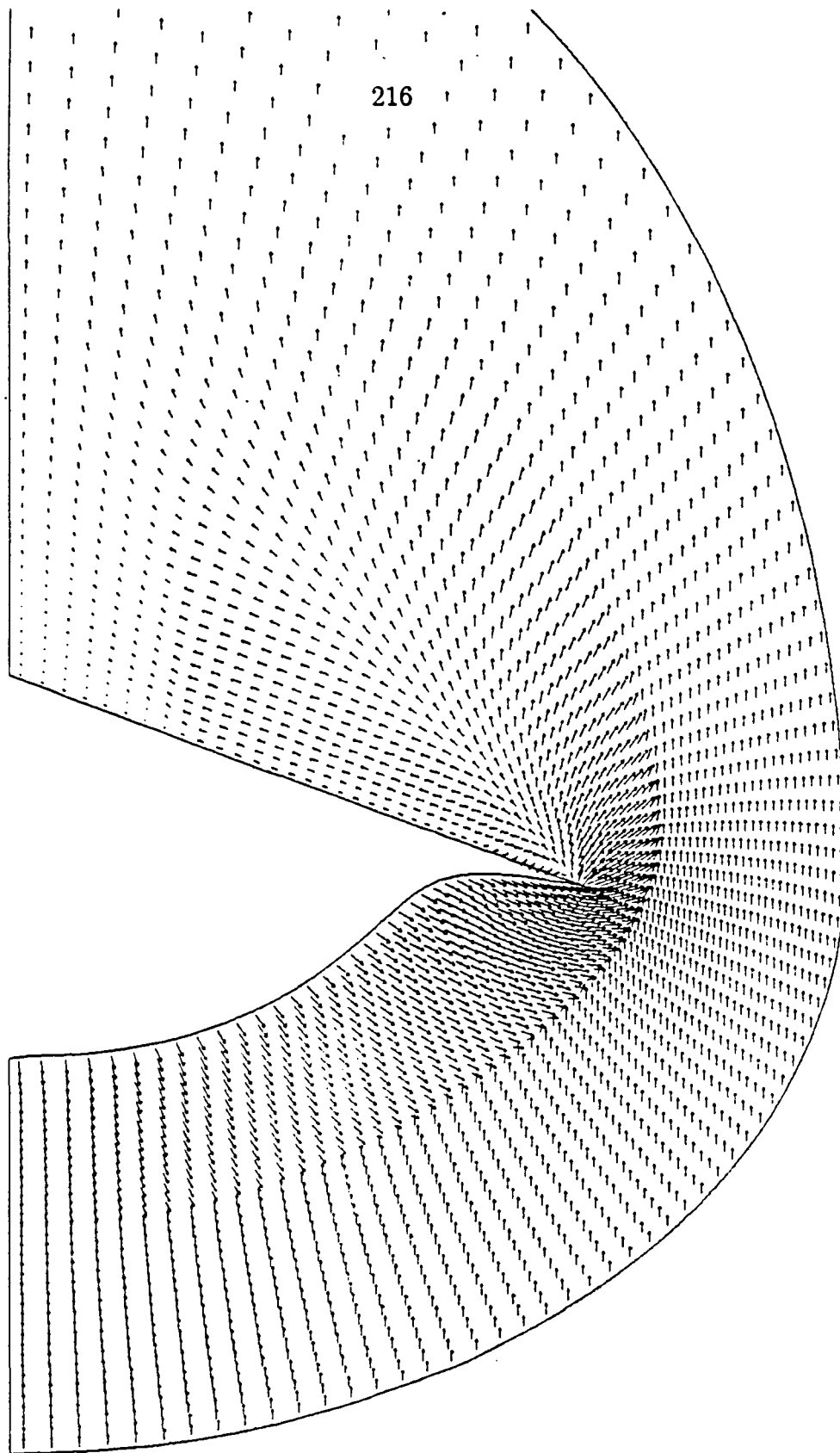


Fig. (7-13a) Cross-Plane Velocity Distribution

$$(M_{\infty} = 4, \quad \alpha = +10^{\circ})$$

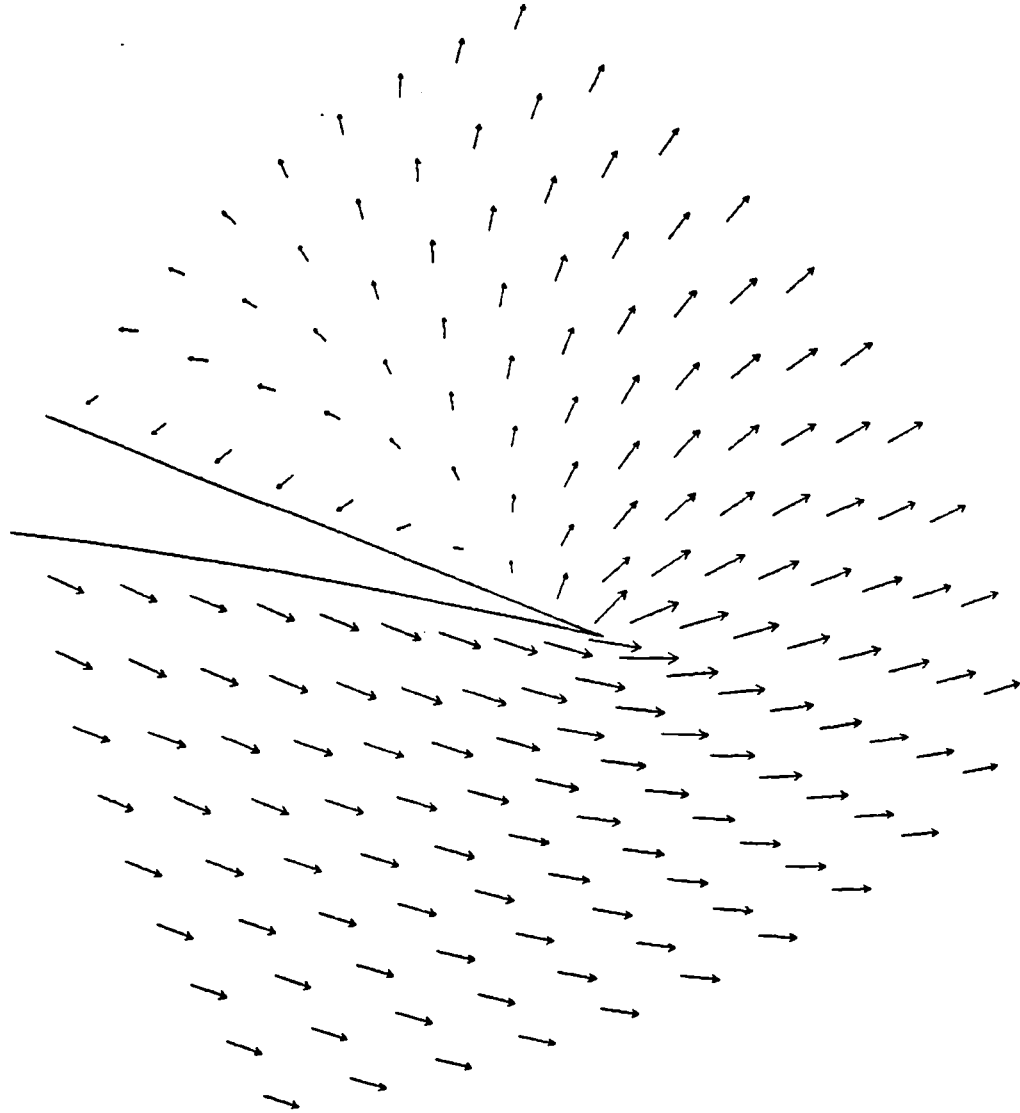


Fig. (7-13b) Magnified Cross-Plane Velocity near Tip
($M_\infty = 4$, $\alpha = +10^\circ$)

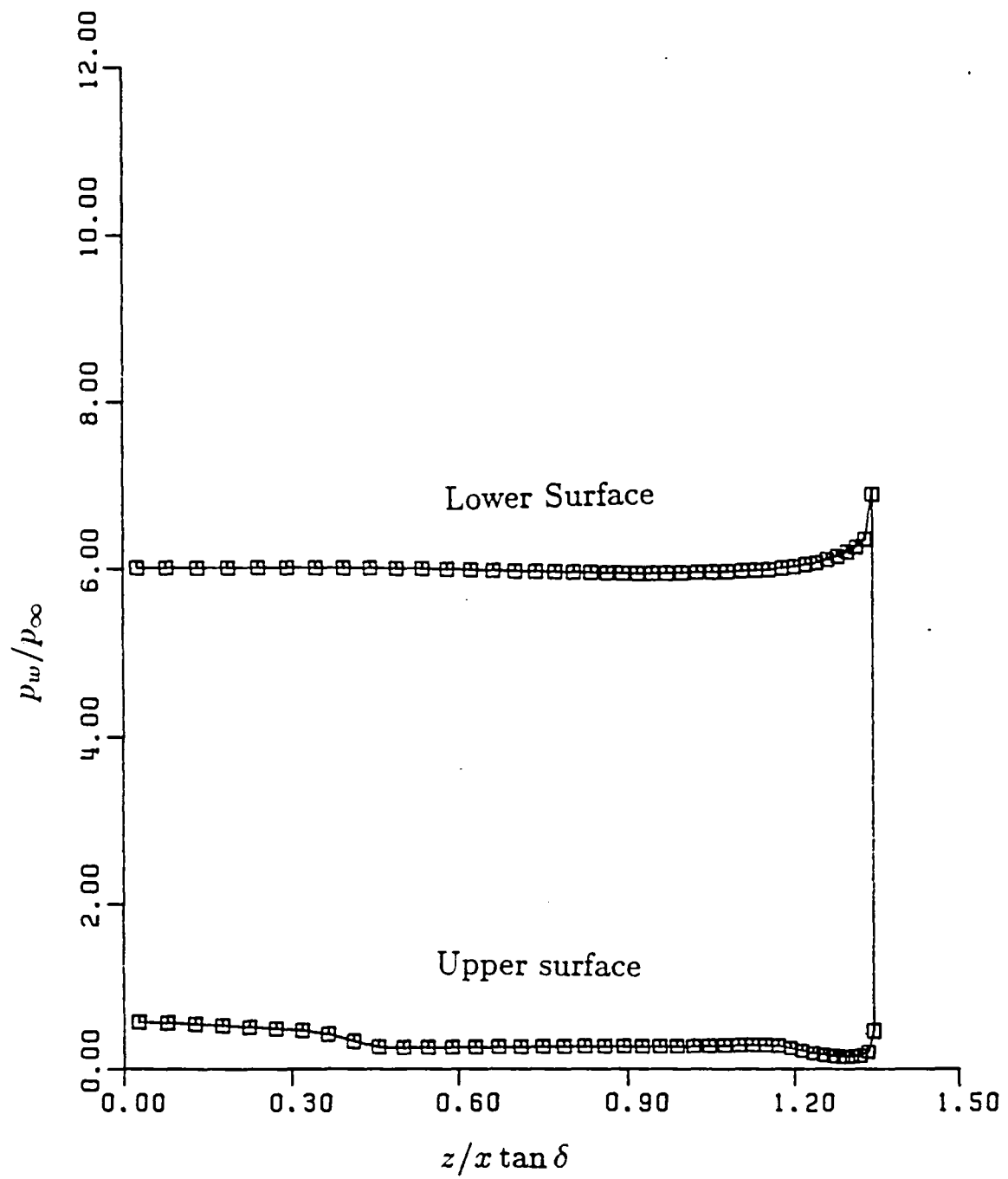


Fig. (7-13c) Wall Pressure Distribution

$$(M_\infty = 4, \quad \alpha = +10^\circ)$$

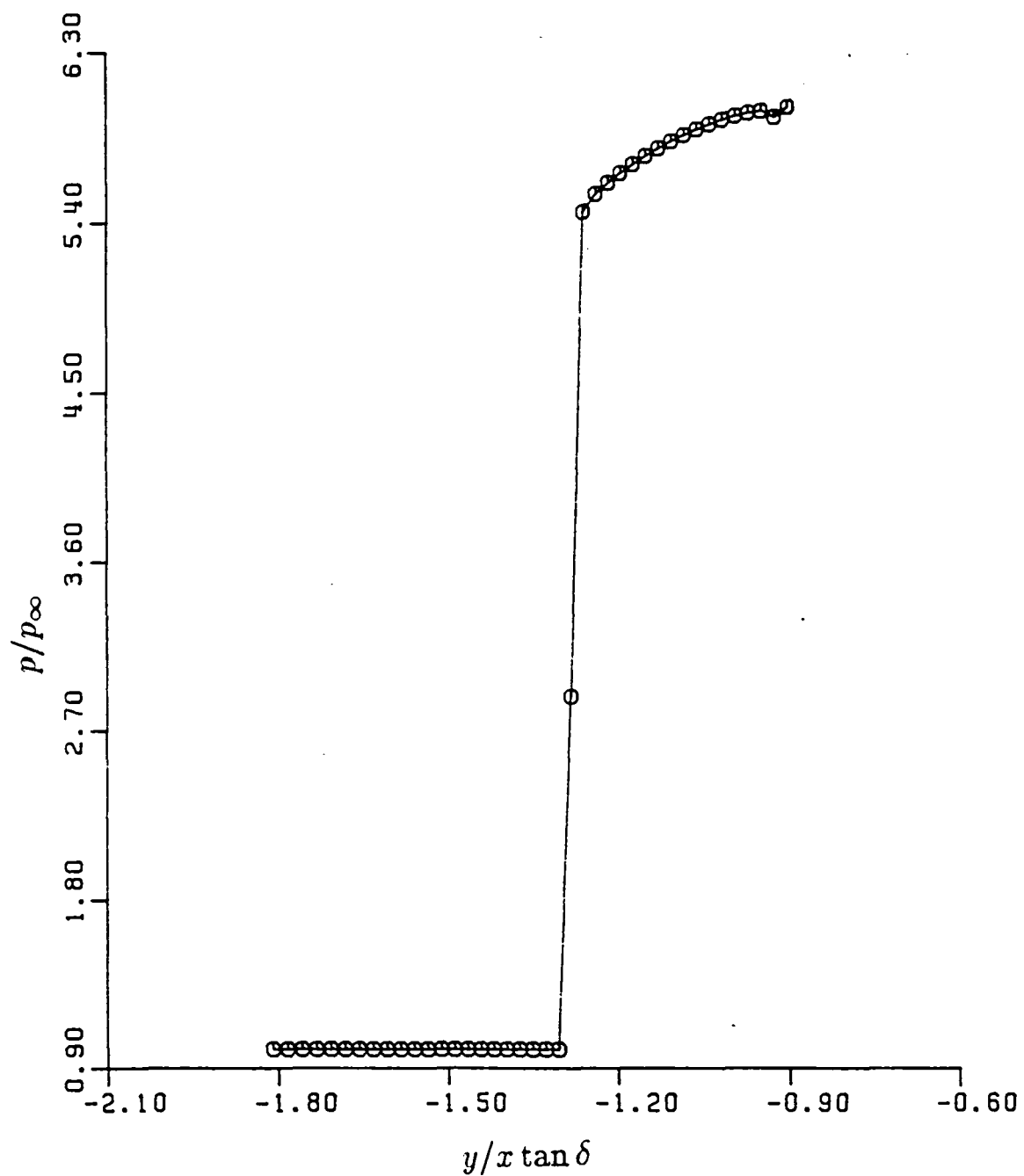


Fig. (7-13d) Pressure near Lower Symmetry Plane

($M_\infty = 4$, $\alpha = +10^\circ$)

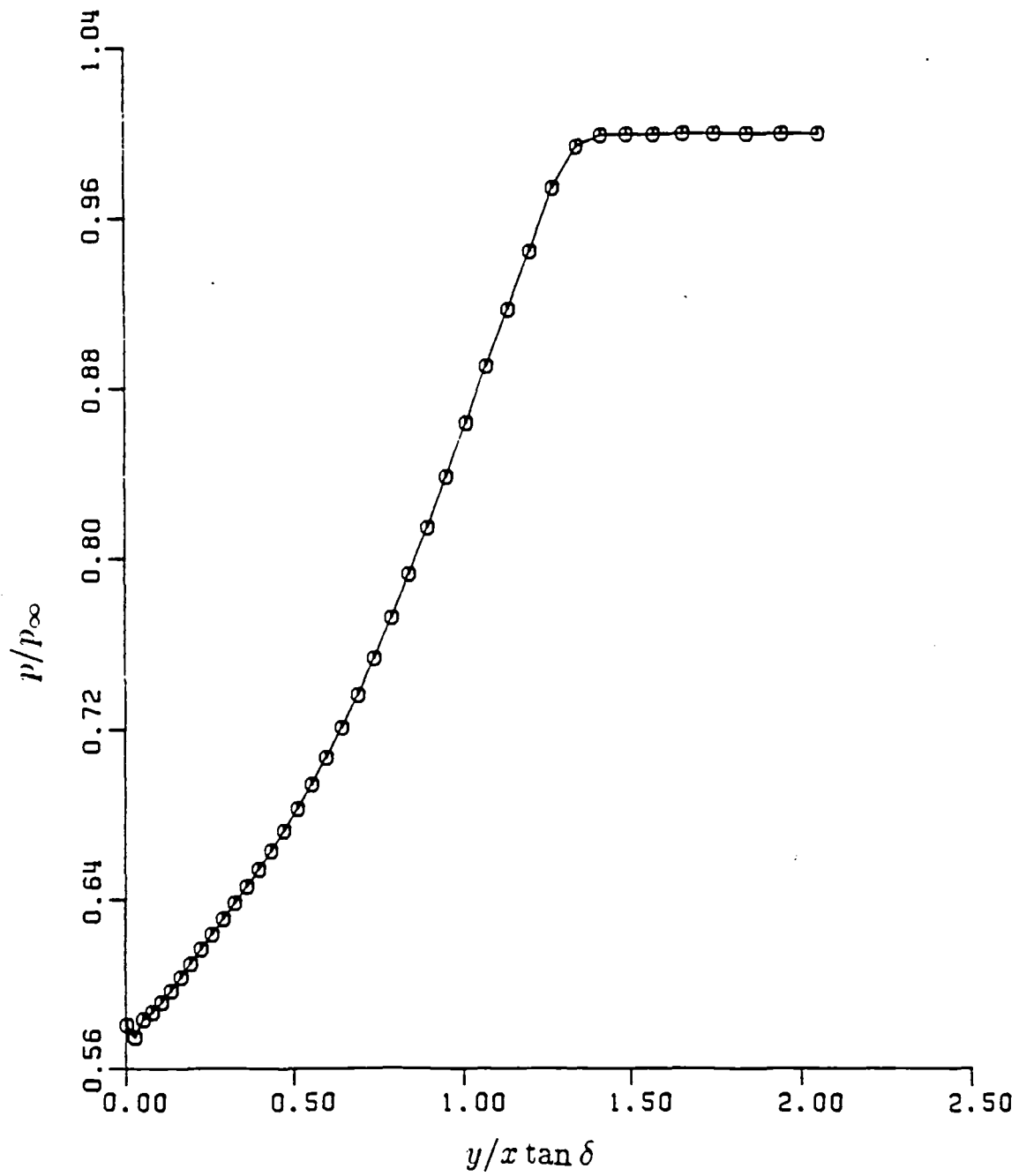


Fig. (7-13e) Pressure near Upper Symmetry Plane

$$(M_\infty = 4, \quad \alpha = +10^\circ)$$

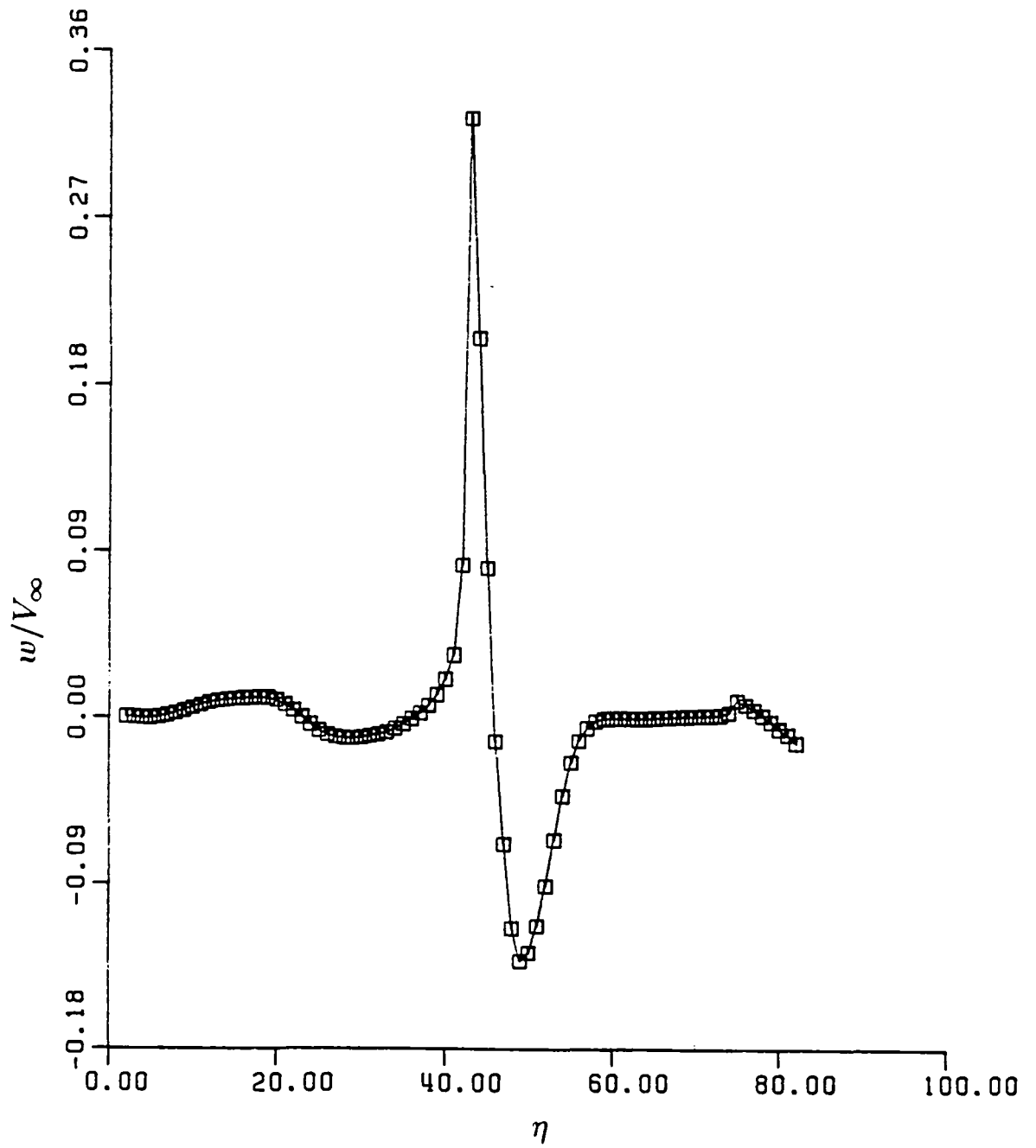


Fig. (7-13f) Azimuthal Velocity Component
($M_\infty = 4$, $\alpha = +10^\circ$)

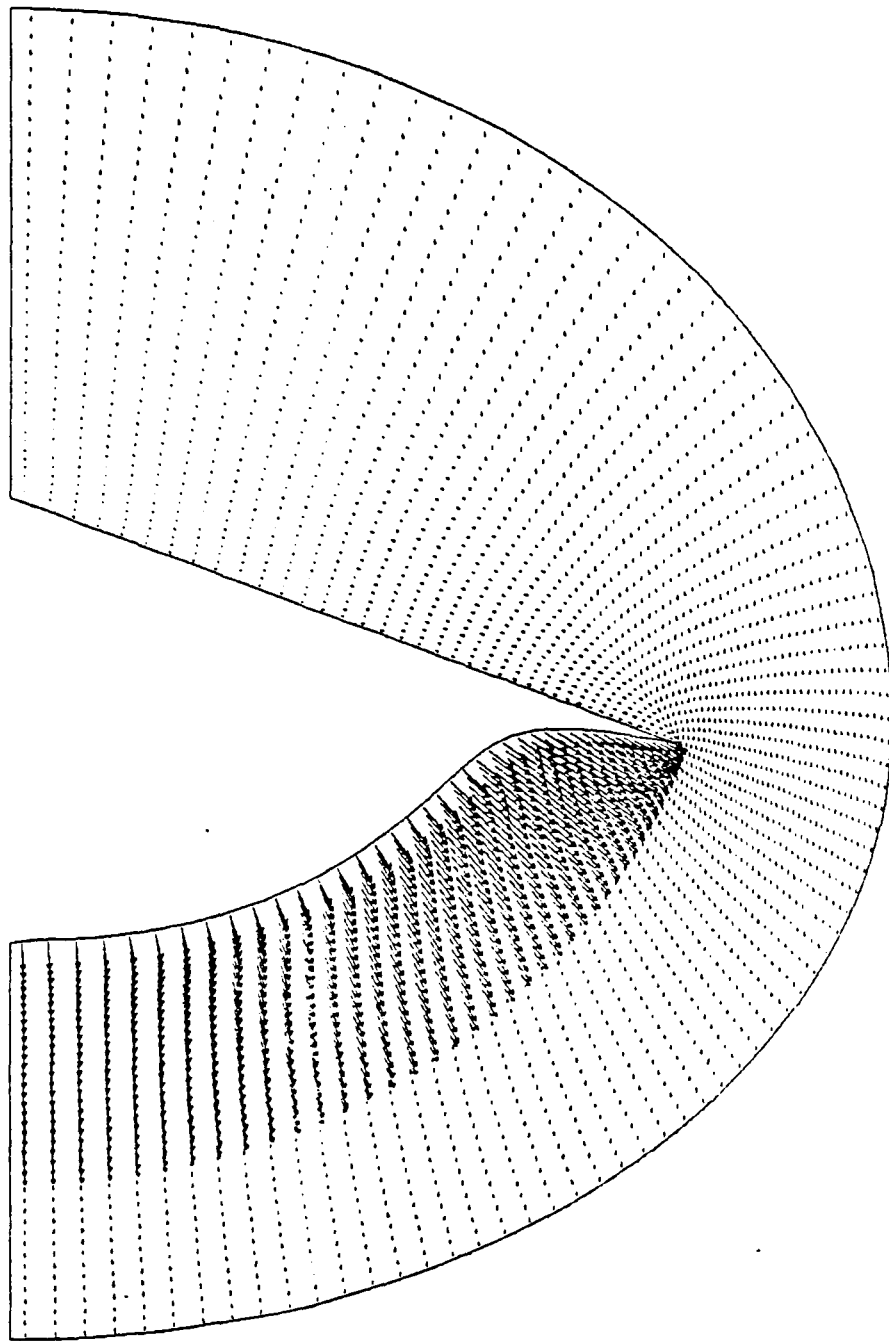


Fig. (7-14a) Cross-Plane Velocity Distribution

$$(M_{\infty} = 4, \quad \alpha = -2^{\circ})$$

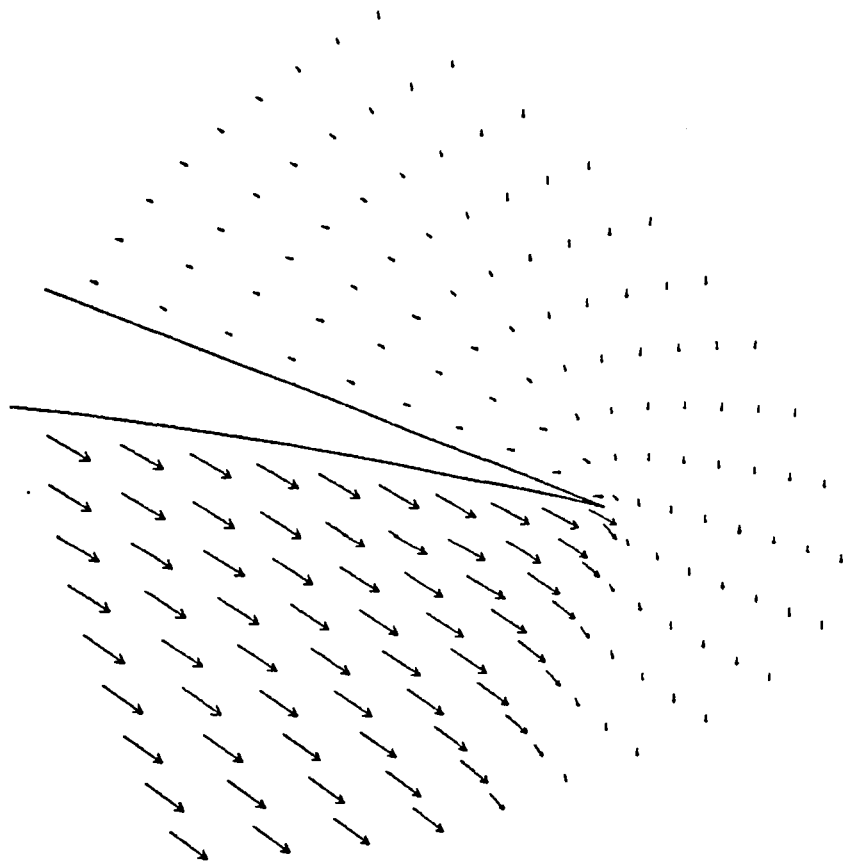


Fig. (7-14b) Magnified Cross-Plane Velocity near Tip
($M_{\infty} = 4$, $\alpha = -2^{\circ}$)

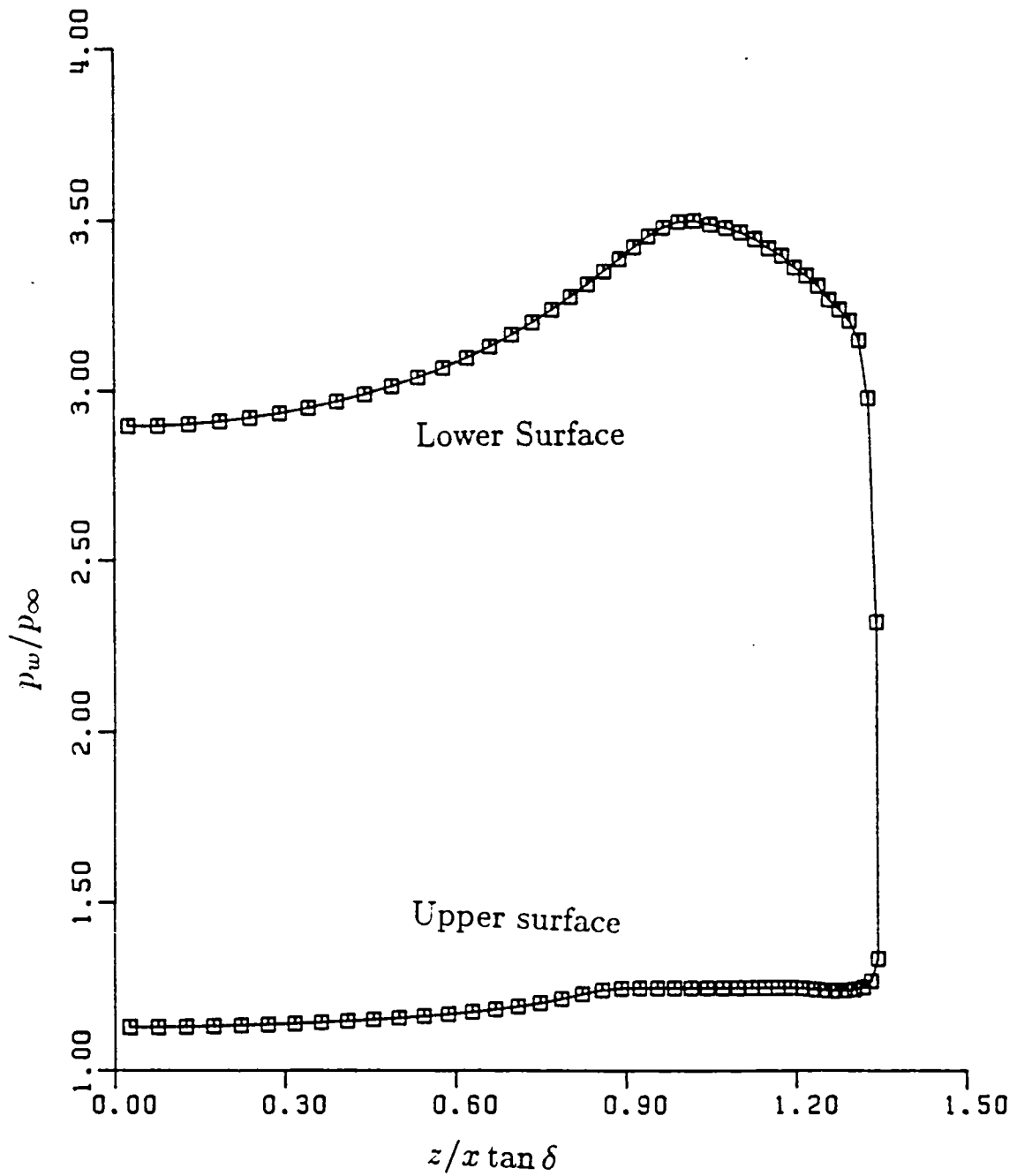


Fig. (7-14c) Wall Pressure Distribution
($M_\infty = 4$, $\alpha = -2^\circ$)

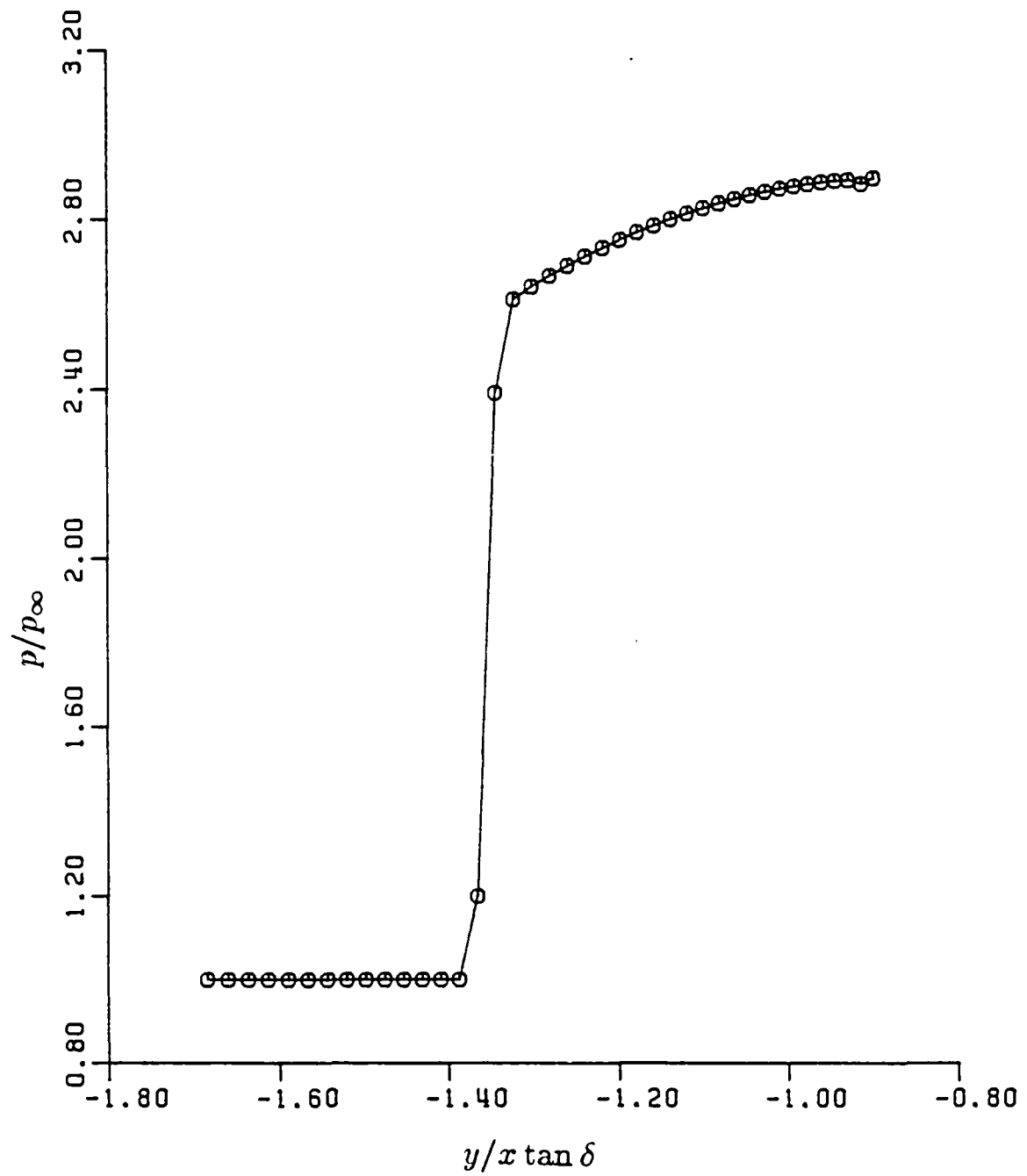


Fig. (7-14d) Pressure near Lower Symmetry Plane
($M_\infty = 4$, $\alpha = -2^\circ$)

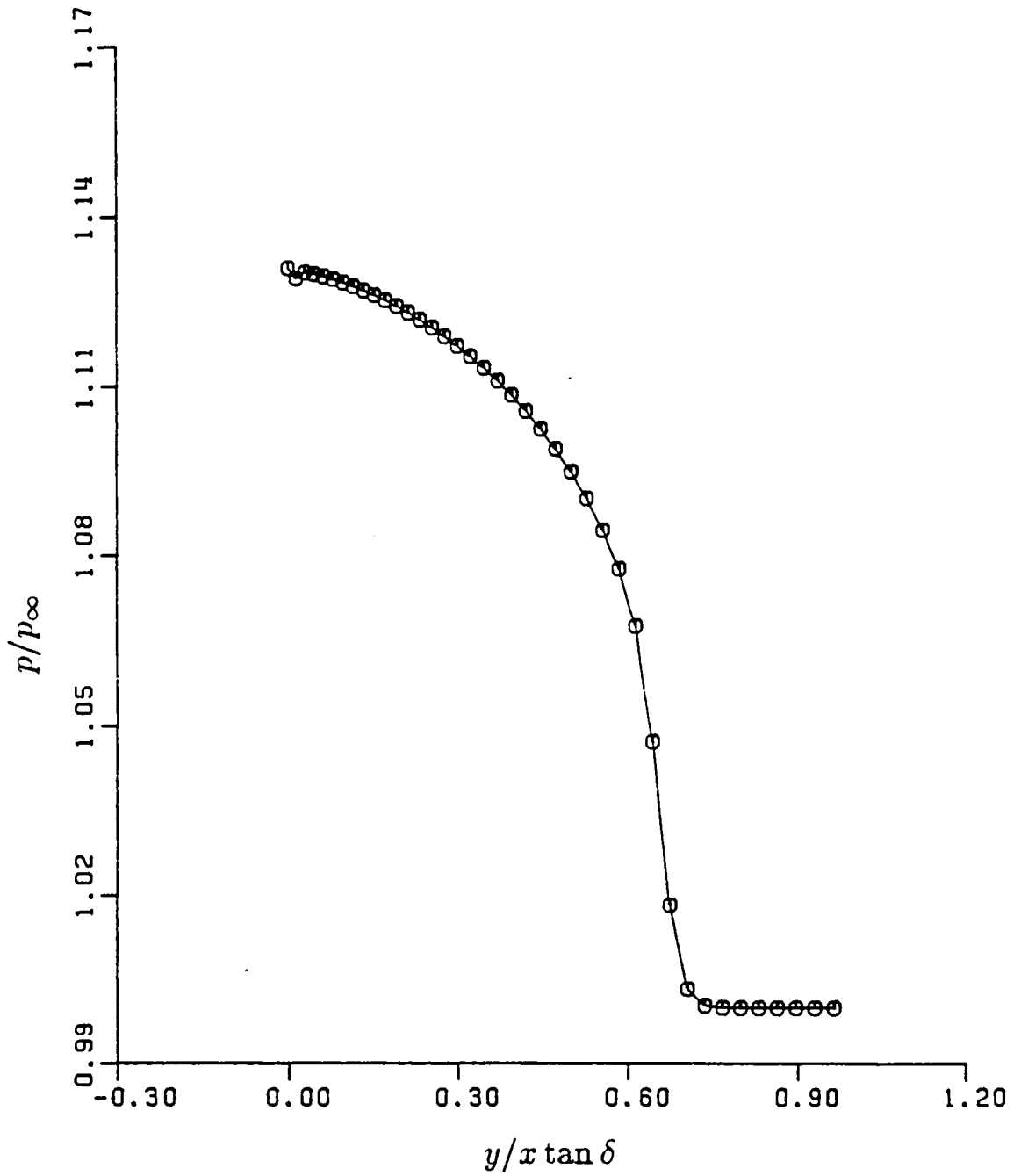


Fig. (7-14e) Pressure near Upper Symmetry Plane

$$(M_\infty = 4, \quad \alpha = -2^\circ)$$

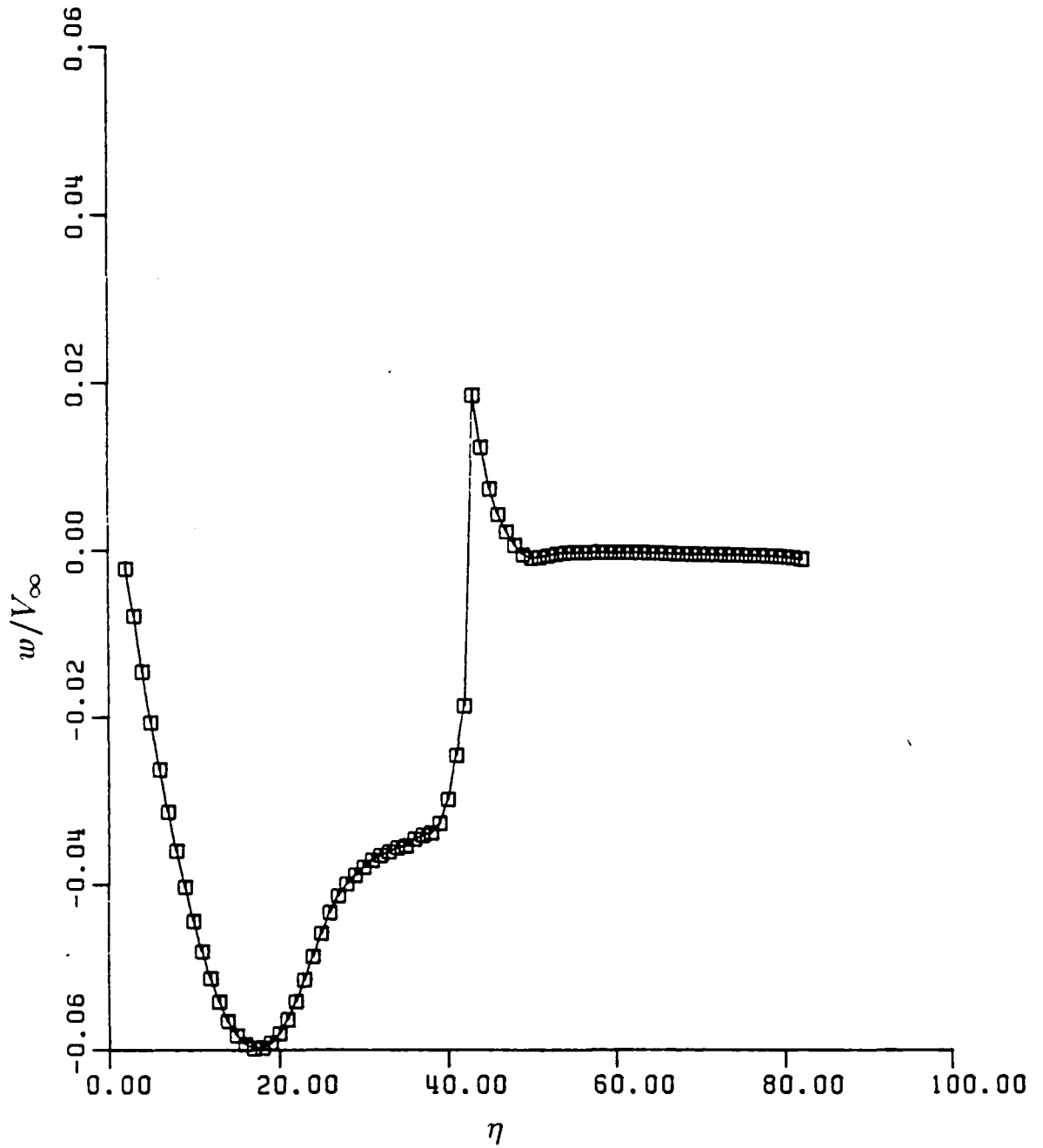


Fig. (7-14f) Azimuthal Velocity Component

$$(M_\infty = 4, \quad \alpha = -2^\circ)$$

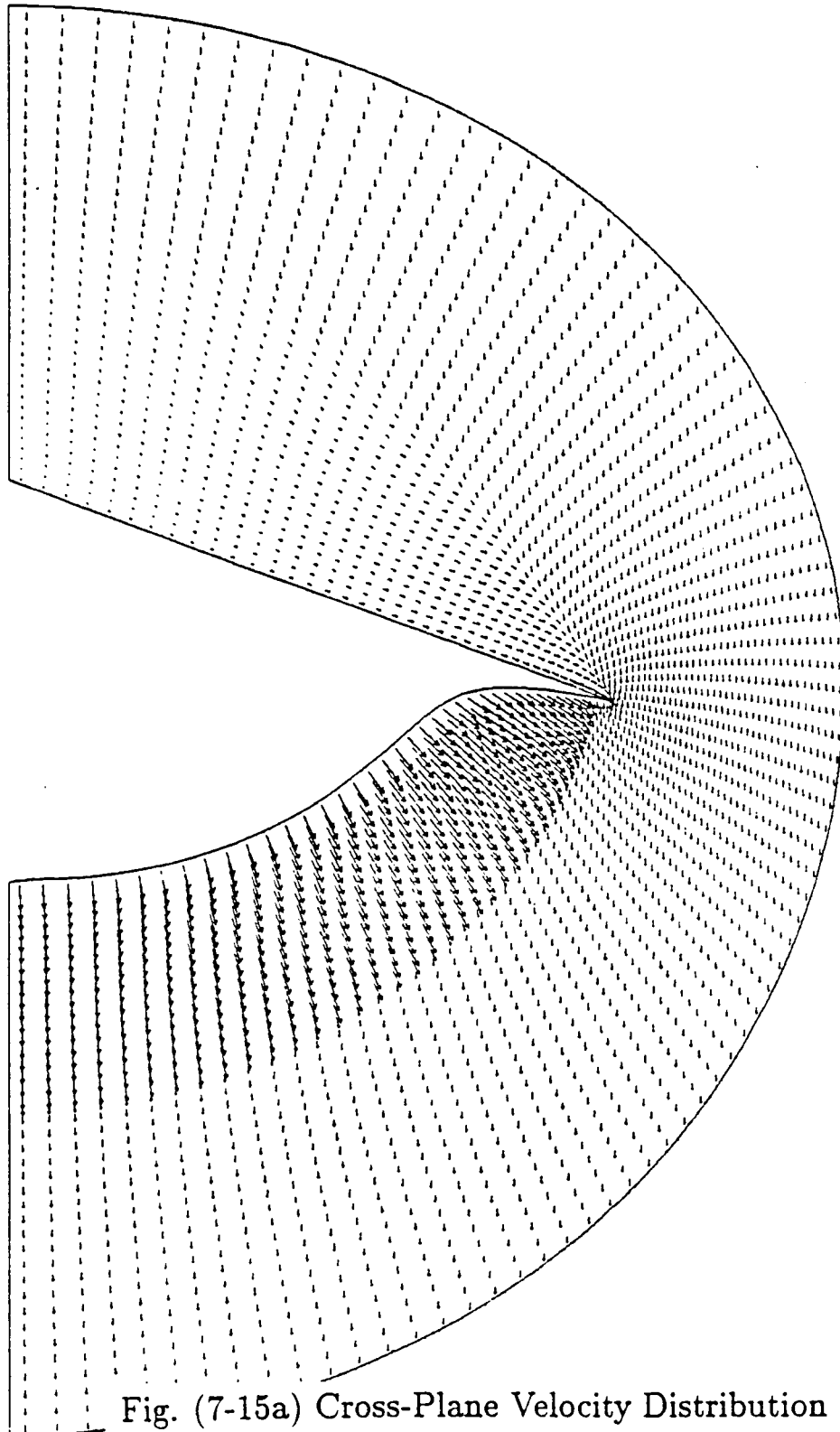


Fig. (7-15a) Cross-Plane Velocity Distribution
($M_{\infty} = 4$, $\alpha = -4^{\circ}$)

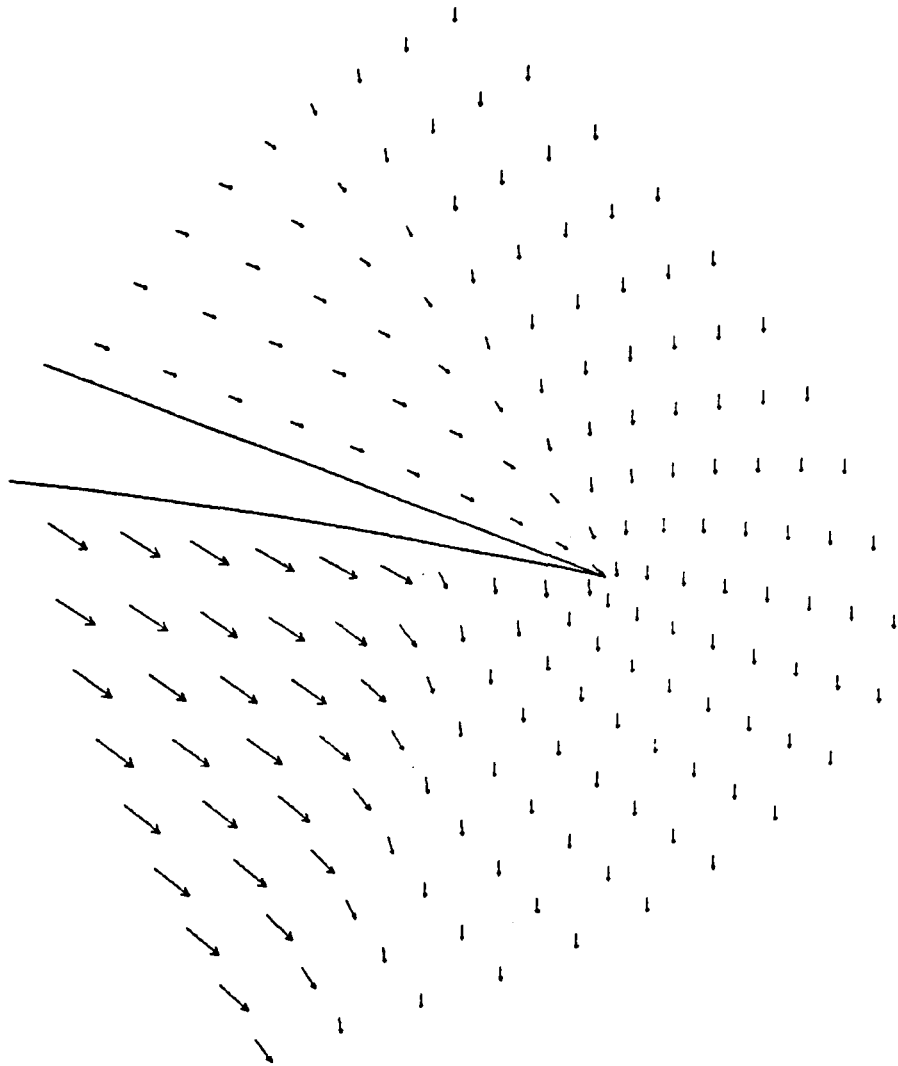


Fig. (7-15b) Magnified Cross-Plane Velocity near Tip

$$(M_{\infty} = 4, \quad \alpha = -4^{\circ})$$

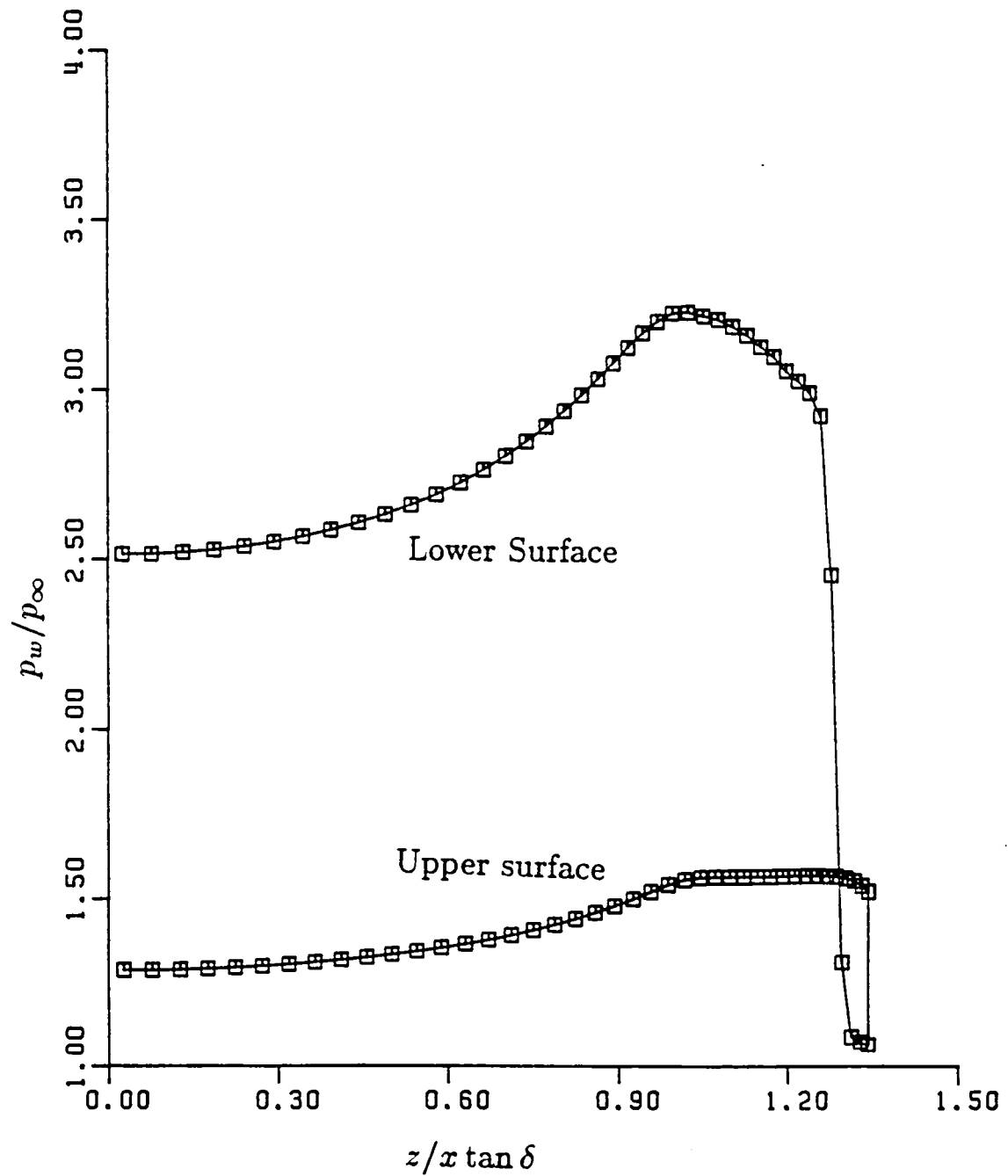


Fig. (7-15c) Wall Pressure Distribution

$$(M_\infty = 4, \quad \alpha = -4^\circ)$$

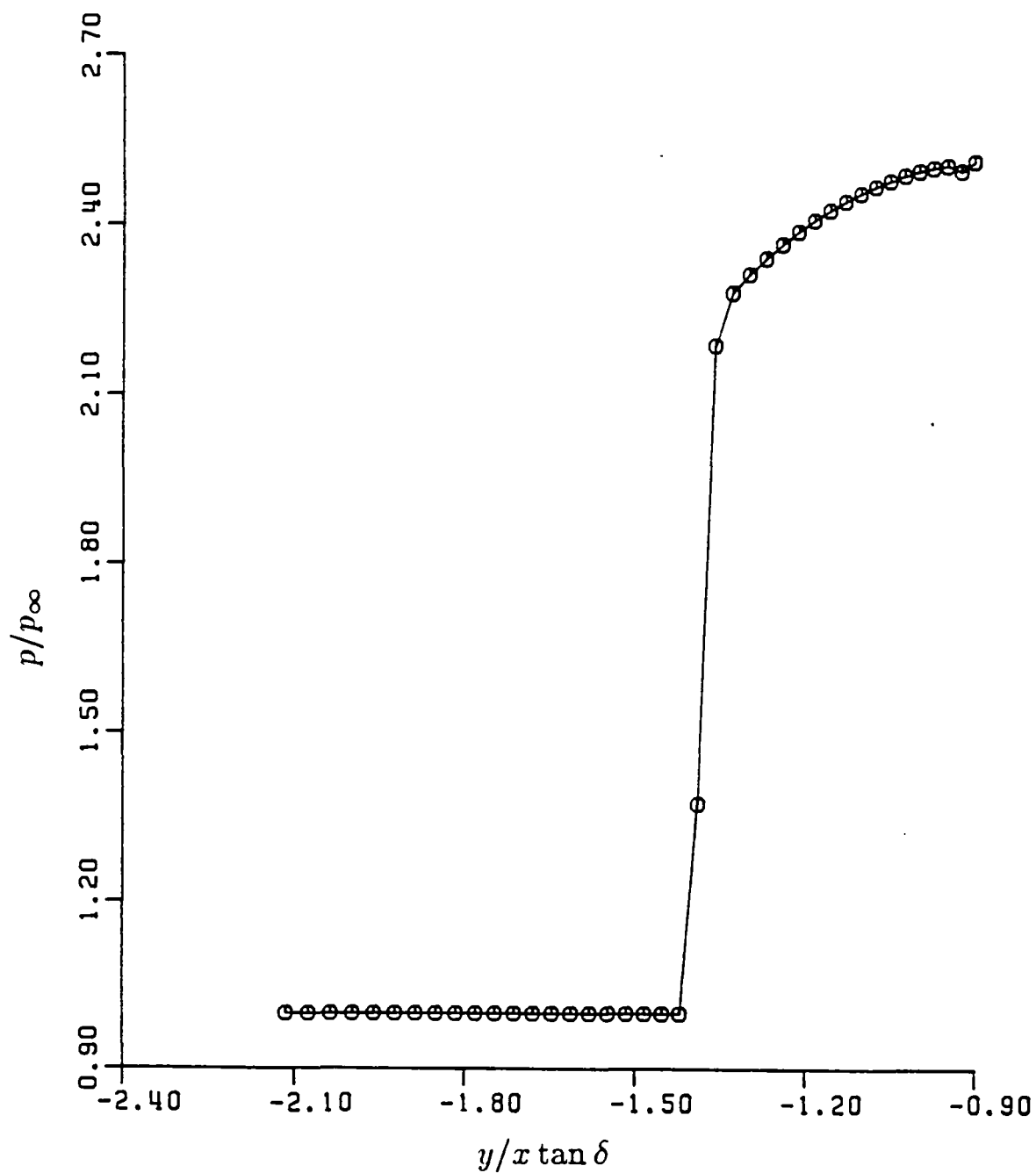


Fig. (7-15d) Pressure near Lower Symmetry Plane

$$(M_\infty = 4, \quad \alpha = -4^\circ)$$

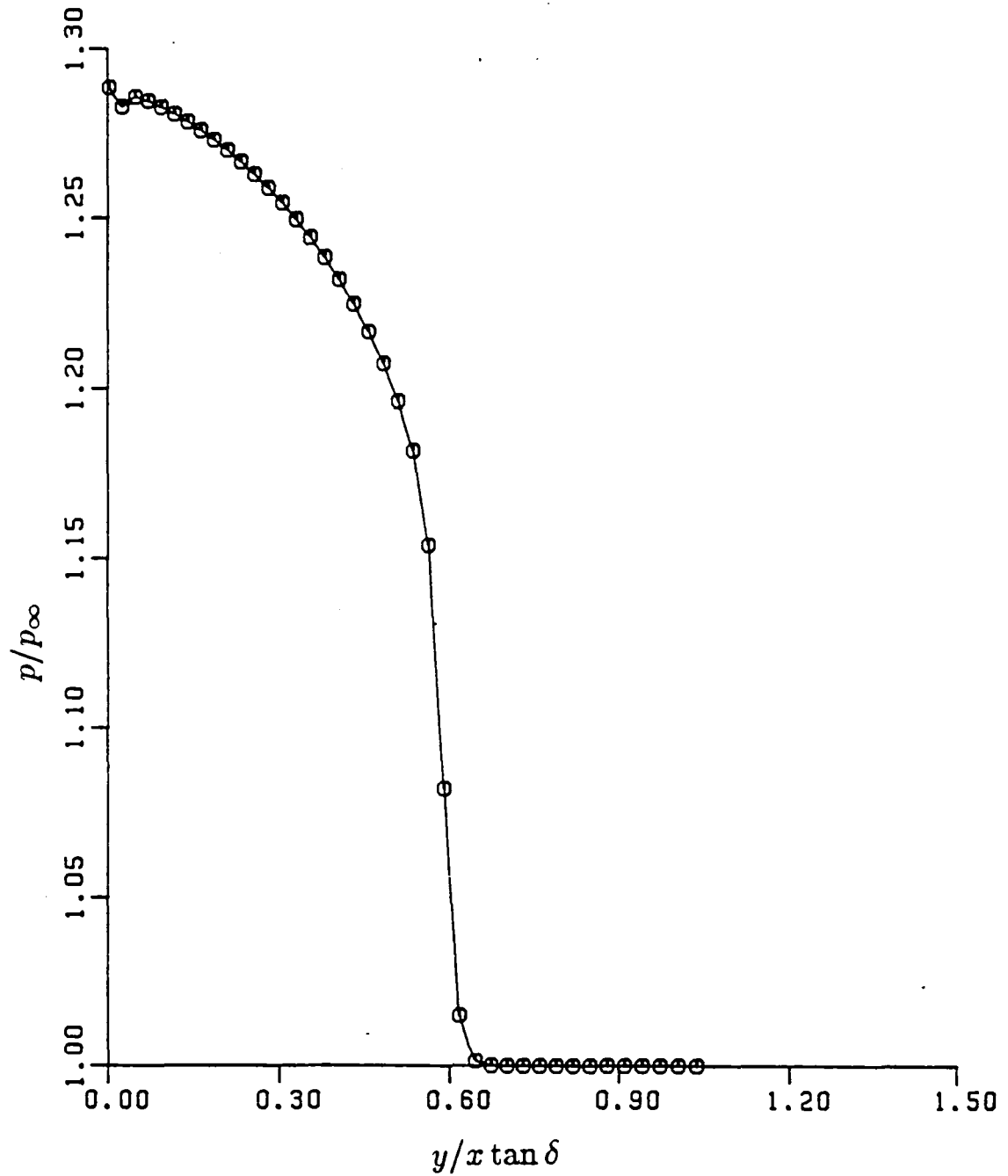


Fig. (7-15e) Pressure near Upper Symmetry Plane

$$(M_\infty = 4, \quad \alpha = -4^\circ)$$

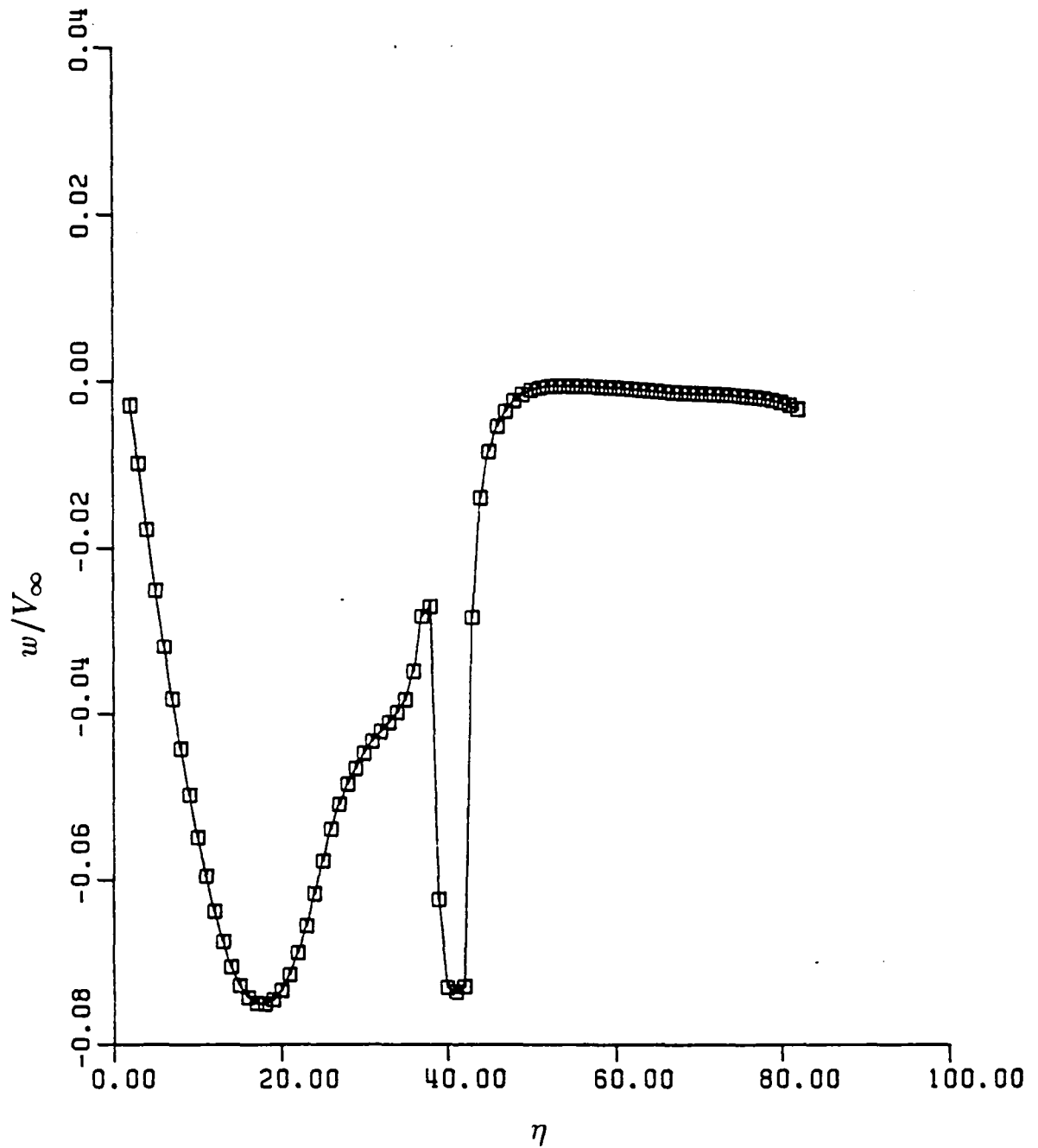
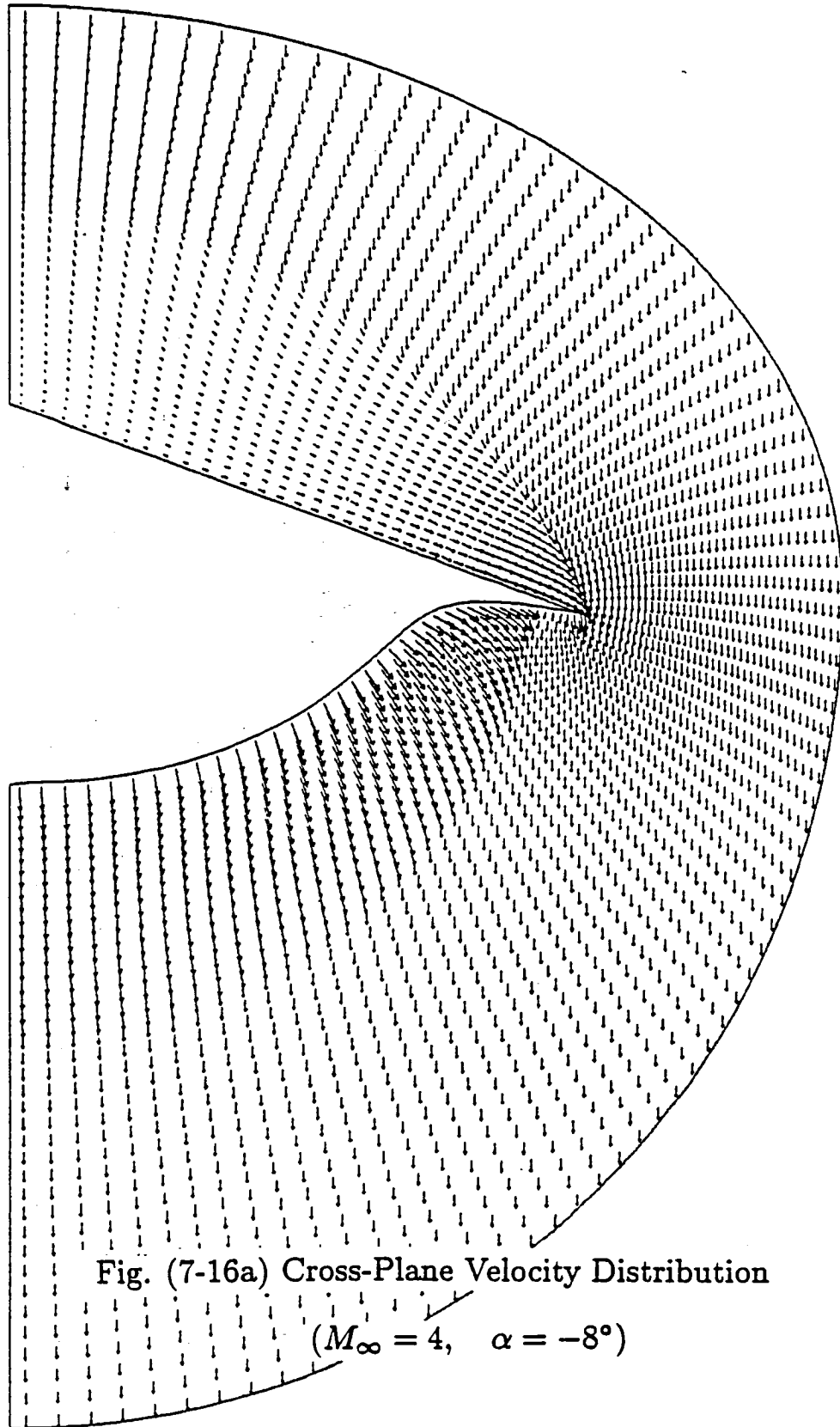


Fig. (7-15f) Azimuthal Velocity Component

$$(M_\infty = 4, \quad \alpha = -4^\circ)$$



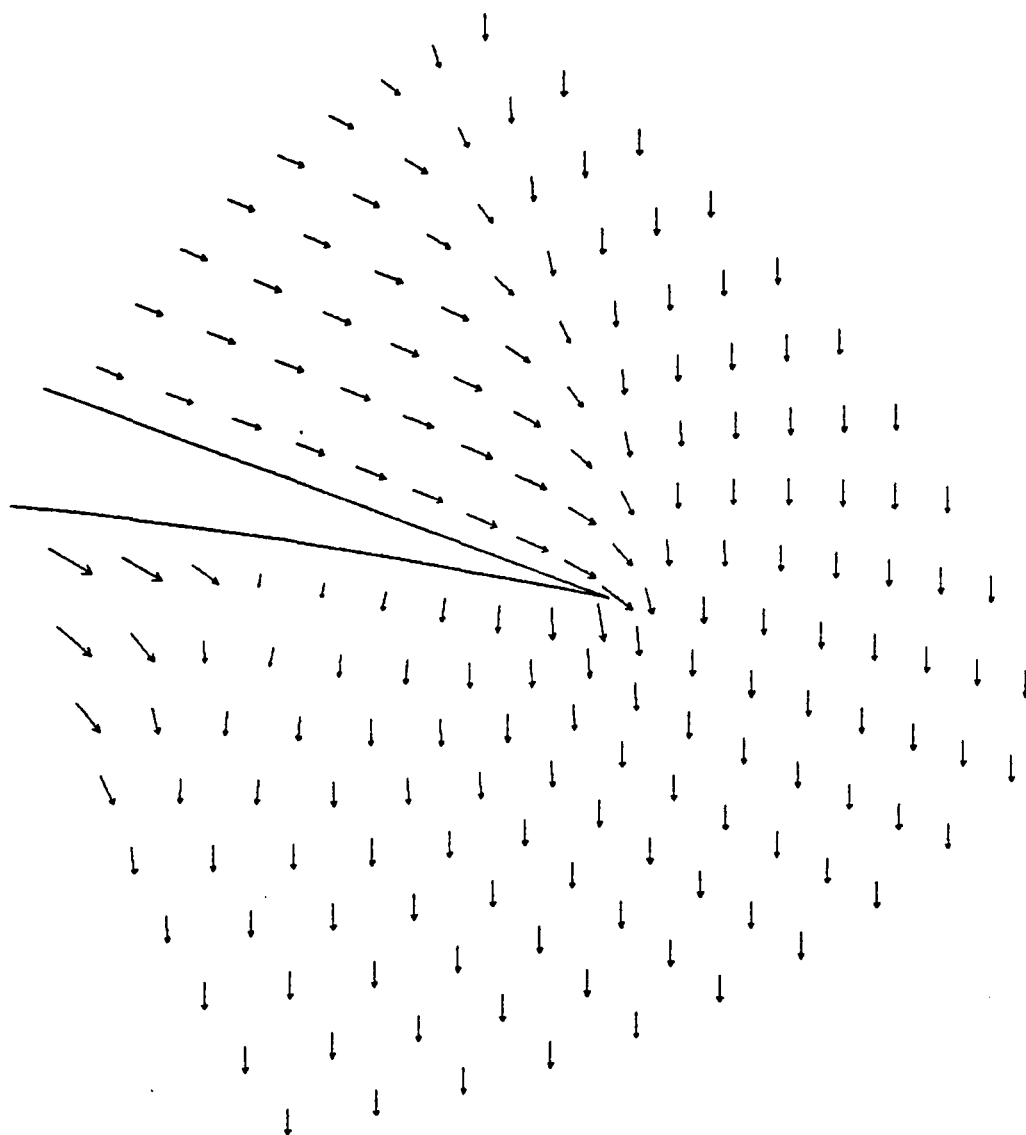


Fig. (7-16b) Magnified Cross-Plane Velocity near Tip

$$(M_{\infty} = 4, \quad \alpha = -8^{\circ})$$

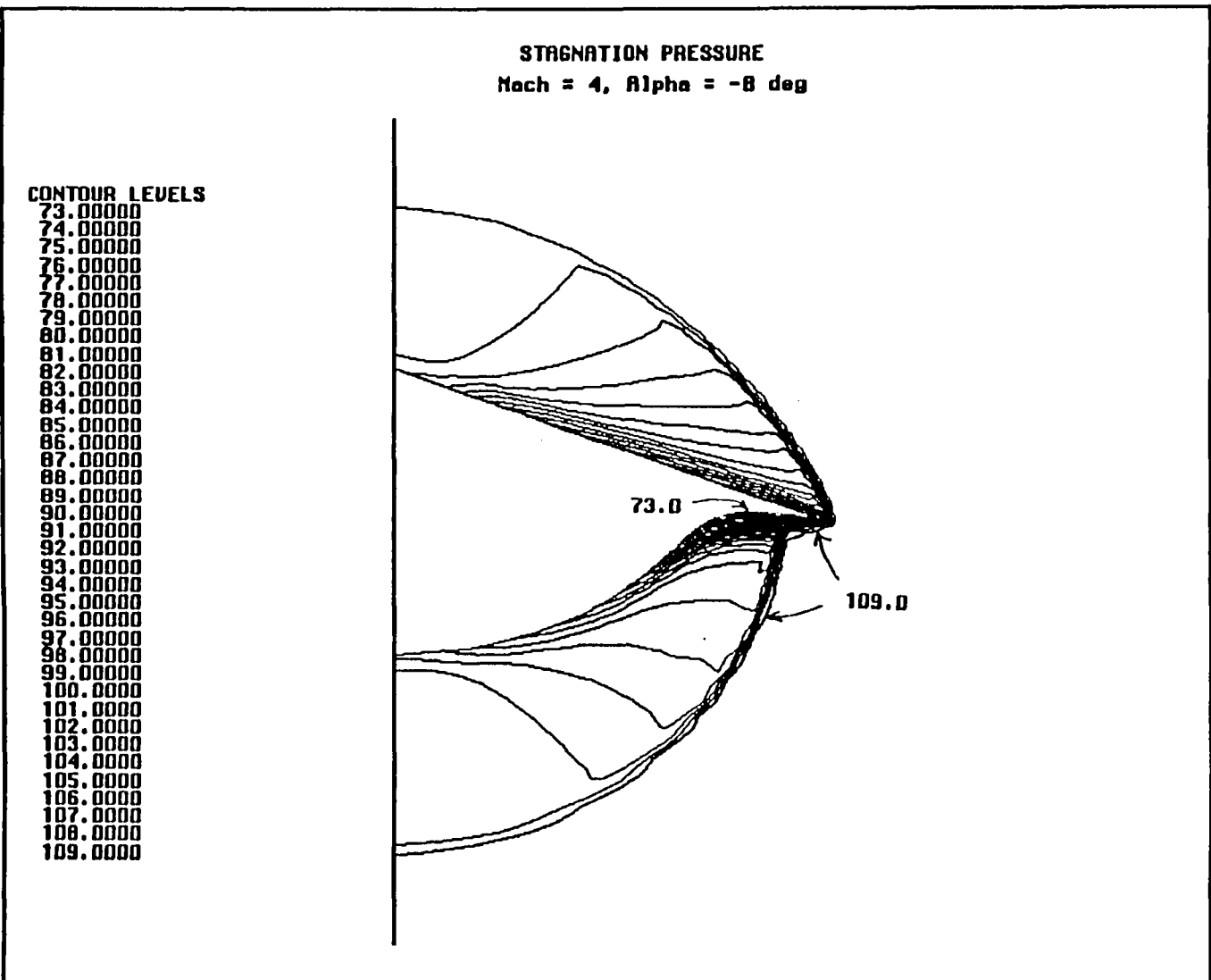


Fig. (7-16c) Total Pressure Contours

$$(M_{\infty} = 4, \alpha = -8^{\circ})$$

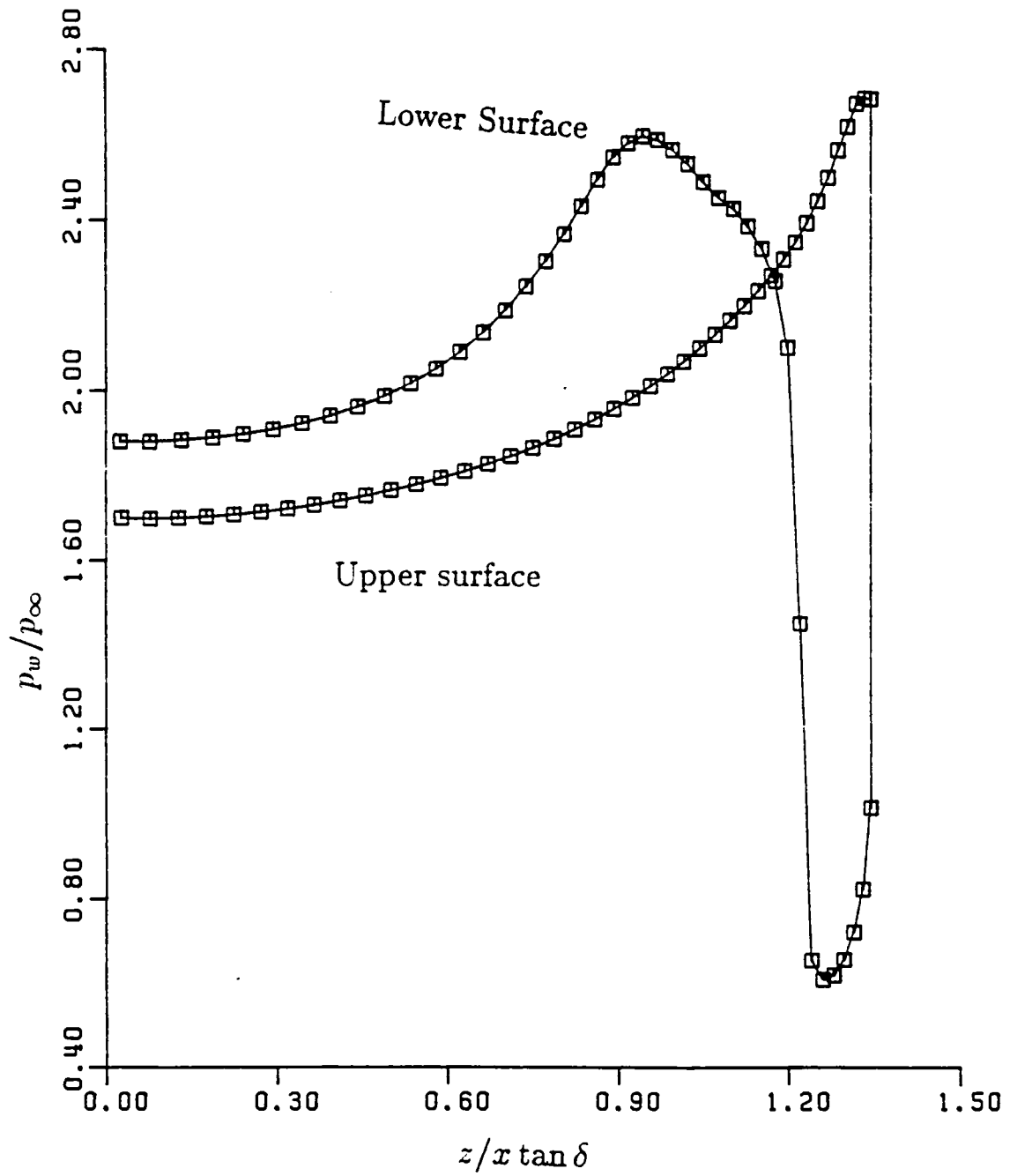


Fig. (7-16d) Wall Pressure Distribution

$$(M_\infty = 4, \quad \alpha = -8^\circ)$$

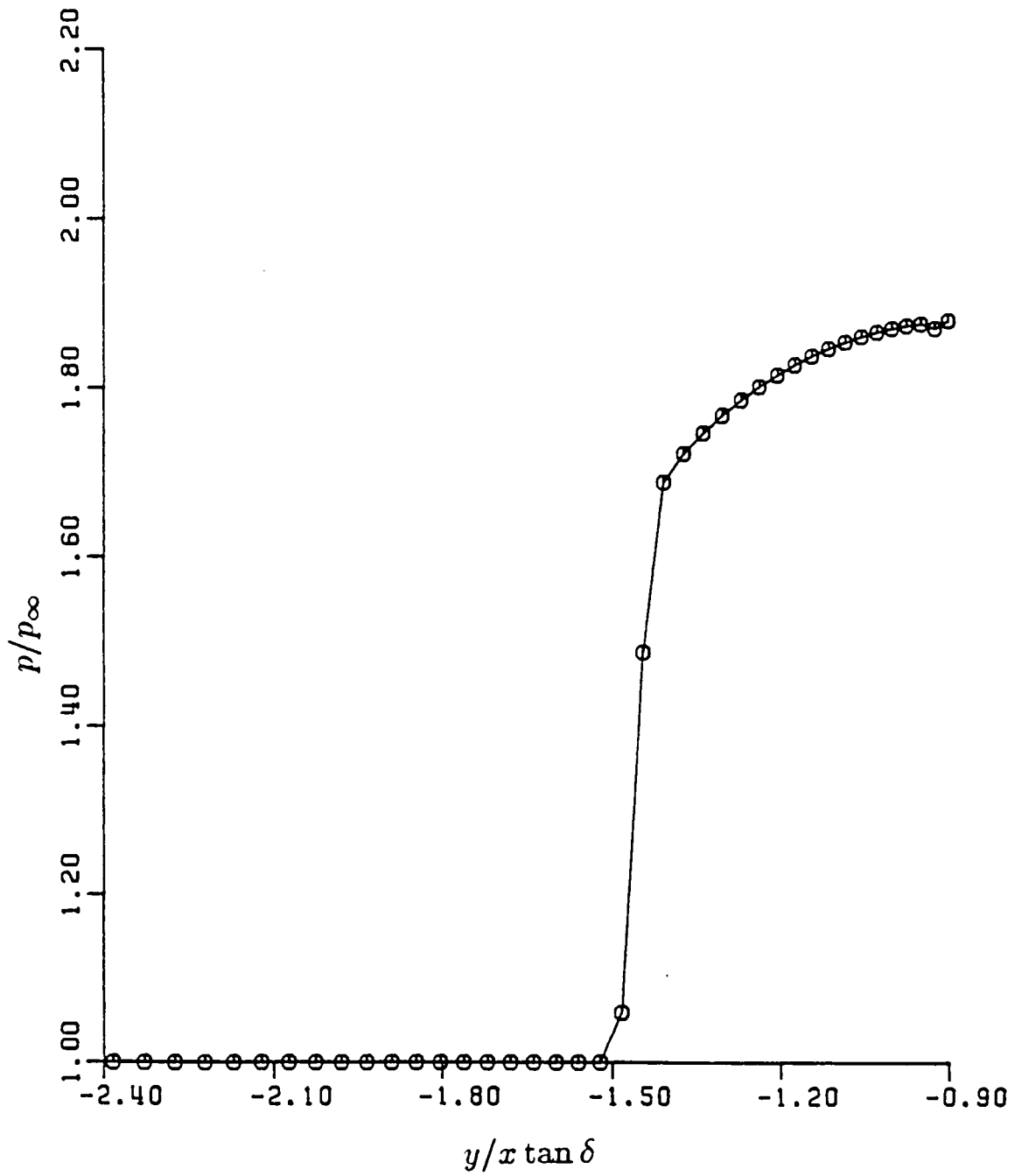


Fig. (7-16e) Pressure near Lower Symmetry Plane

$$(M_\infty = 4, \quad \alpha = -8^\circ)$$

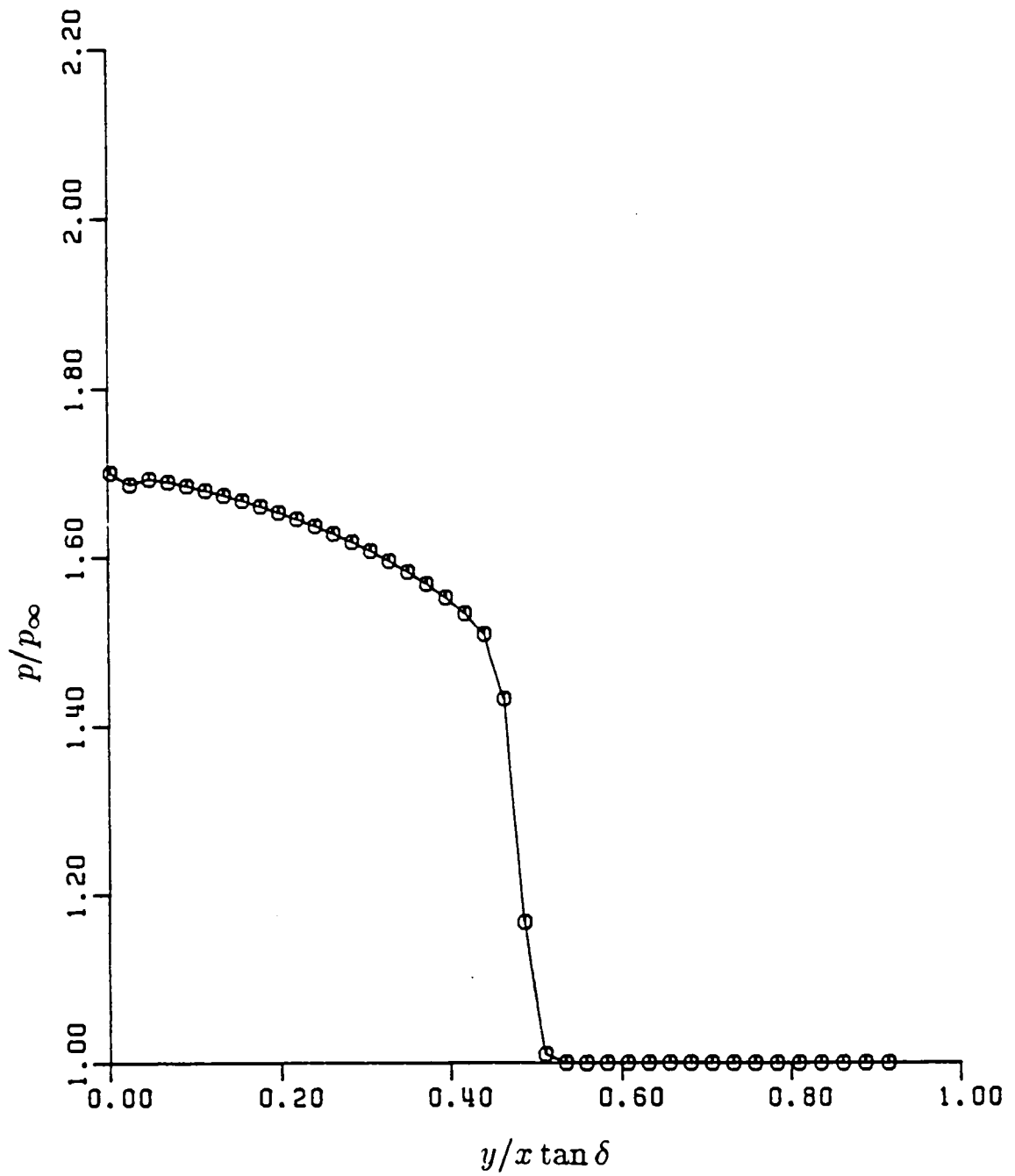


Fig. (7-16f) Pressure near Upper Symmetry Plan

$$(M_\infty = 4, \quad \alpha = -8^\circ)$$

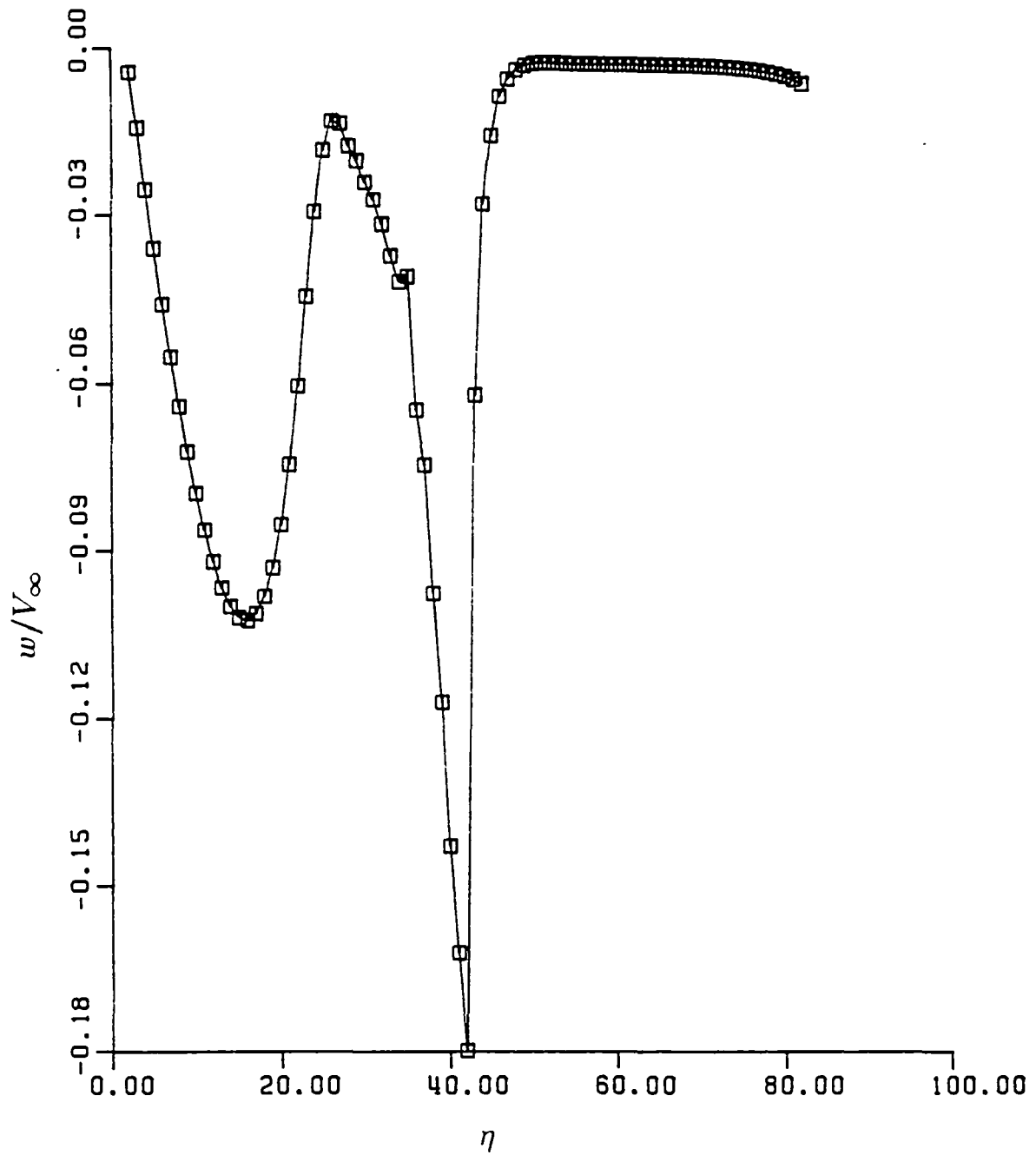


Fig. (7-16g) Azimuthal Velocity Component

$$(M_\infty = 4, \quad \alpha = -8^\circ)$$

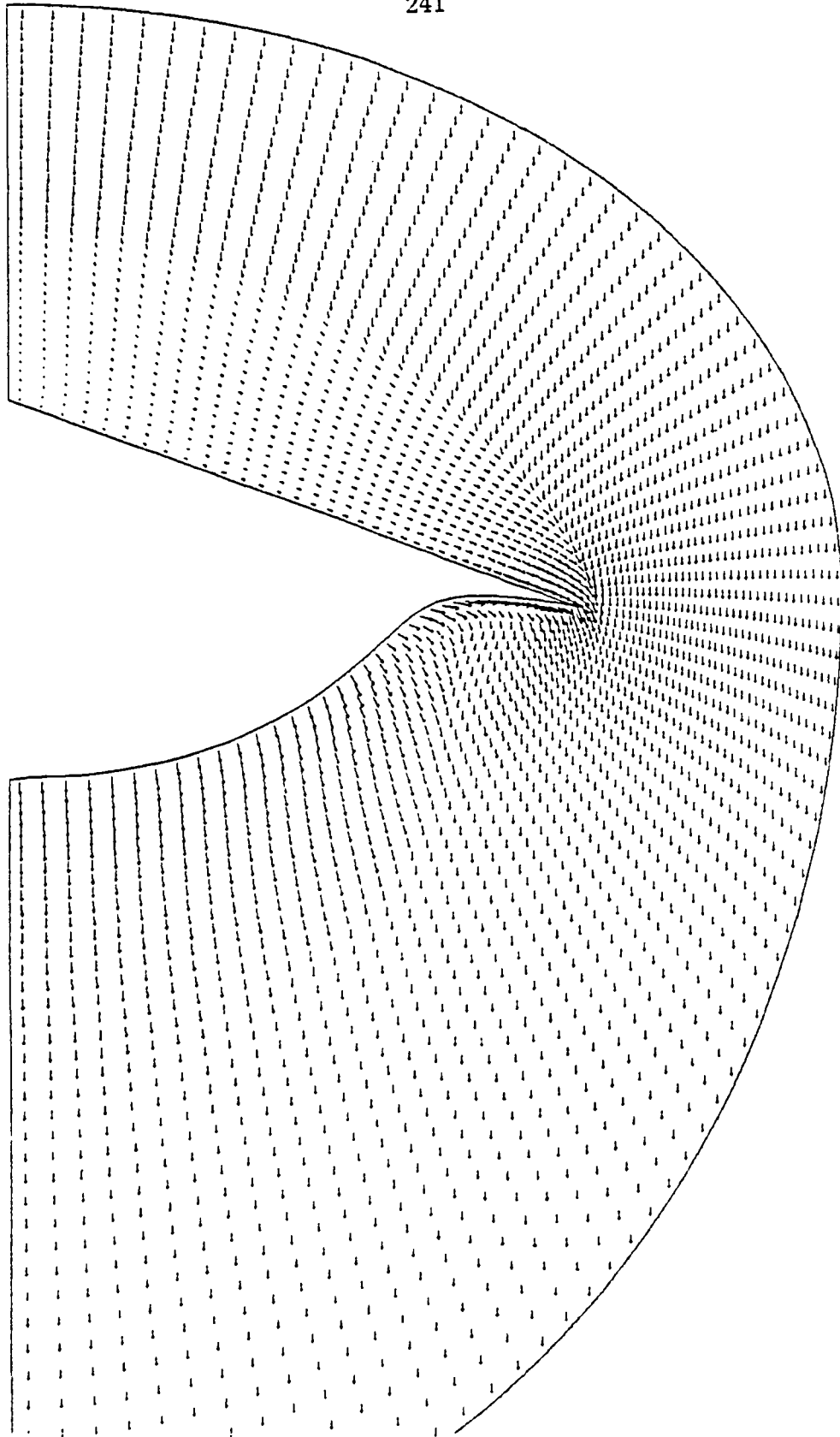


Fig. (7-17a) Cross-Plane Velocity Distribution

$$(M_{\infty} = 4, \quad \alpha = -12^{\circ})$$

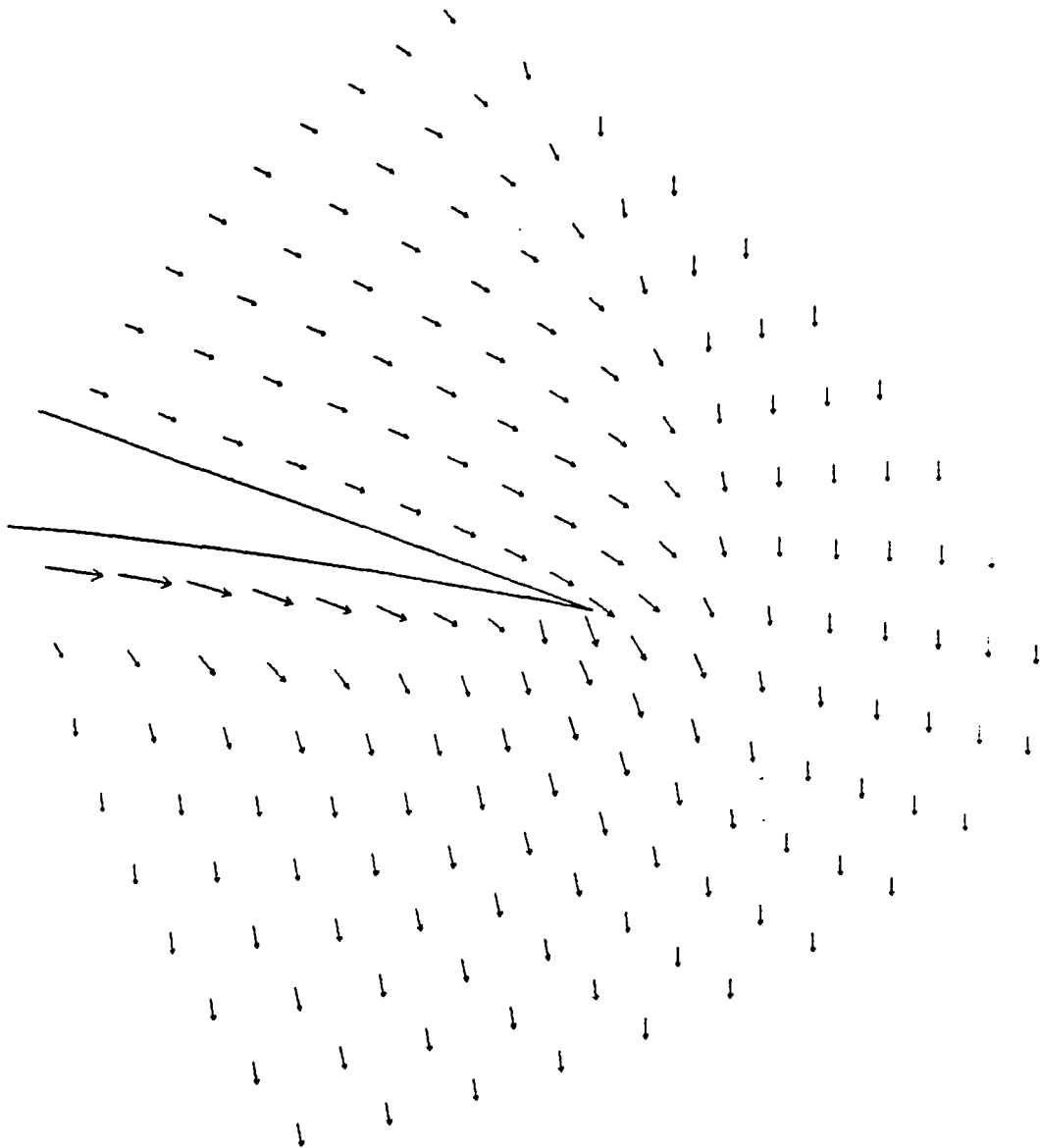


Fig. (7-17b) Magnified Cross-Plane Velocity near Tip

$$(M_{\infty} = 4, \quad \alpha = -12^{\circ})$$

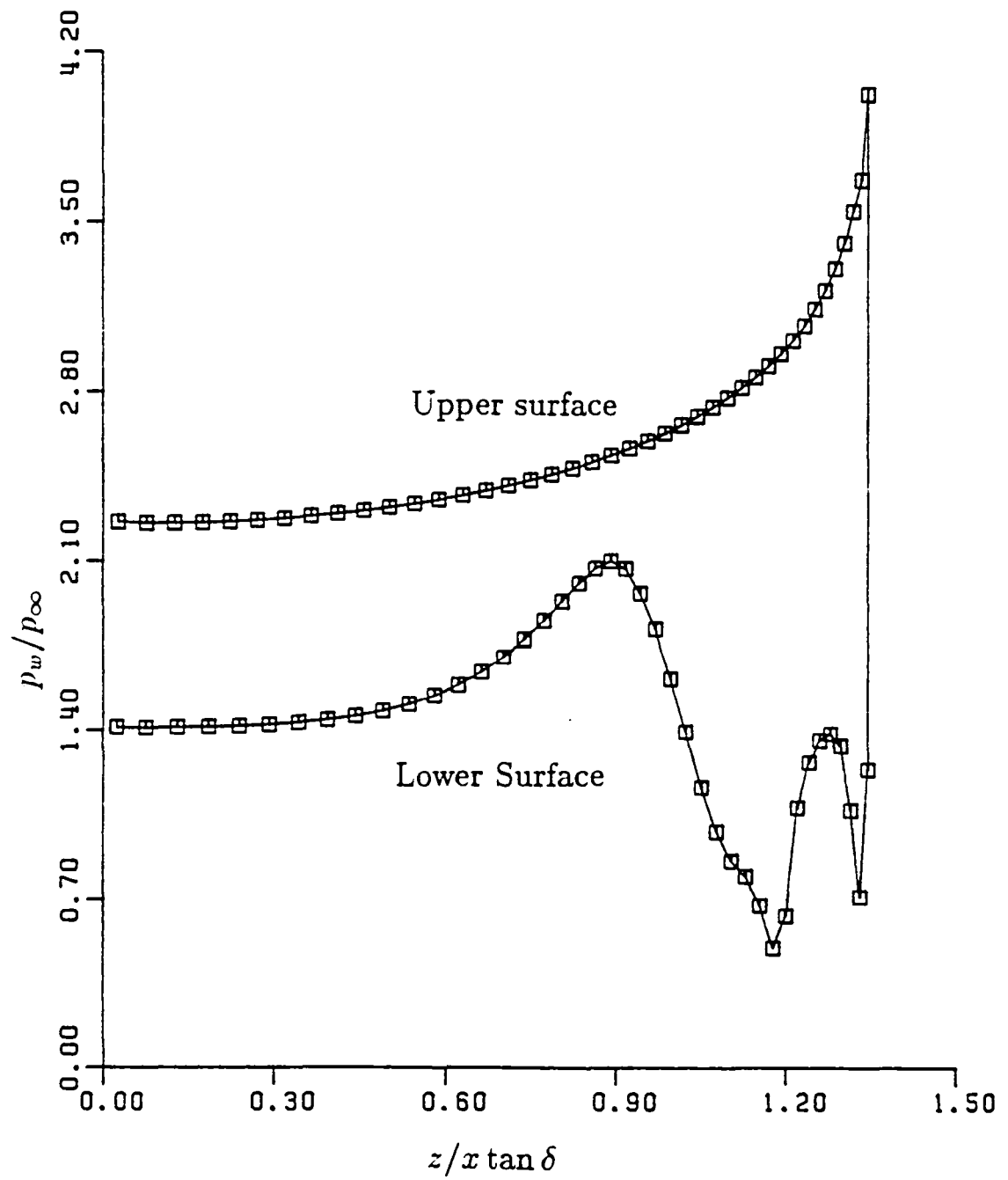


Fig. (7-17c) Wall Pressure Distribution
($M_\infty = 4$, $\alpha = -12^\circ$)

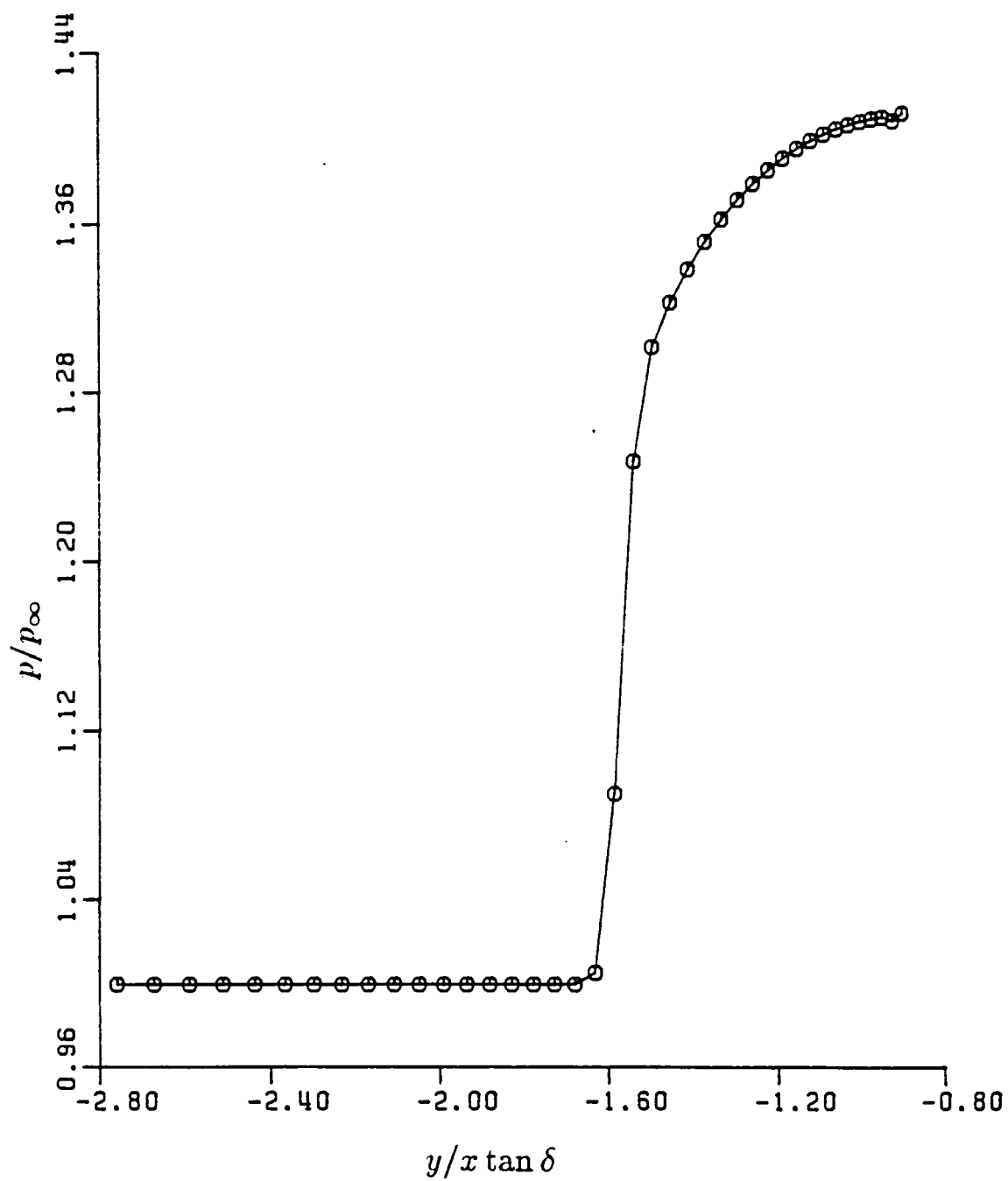


Fig. (7-17d) Pressure near Lower Symmetry Plane

$$(M_\infty = 4, \quad \alpha = -12^\circ)$$

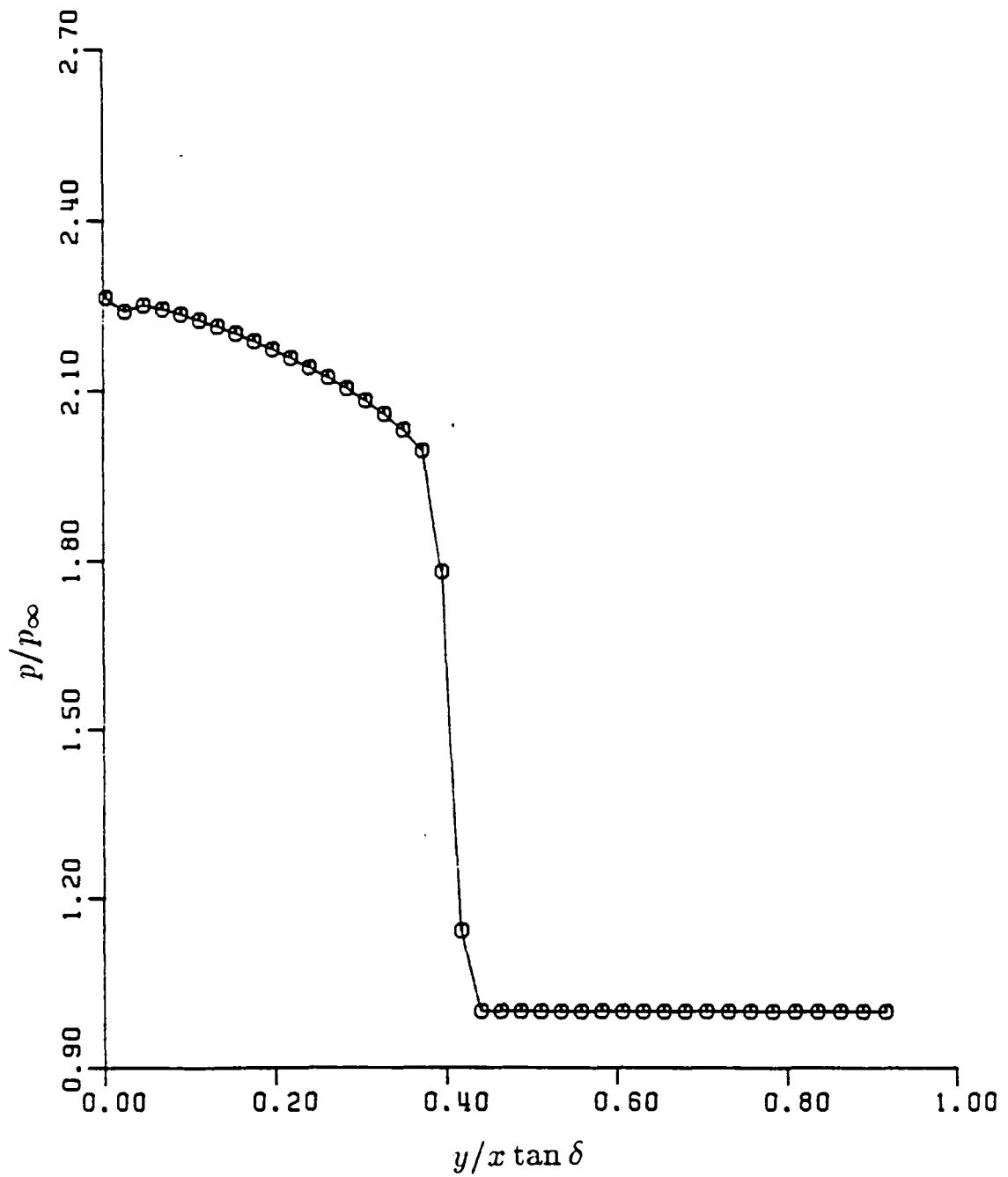


Fig. (7-17e) Pressure near Upper Symmetry Plane

$$(M_\infty = 4, \quad \alpha = -12^\circ)$$

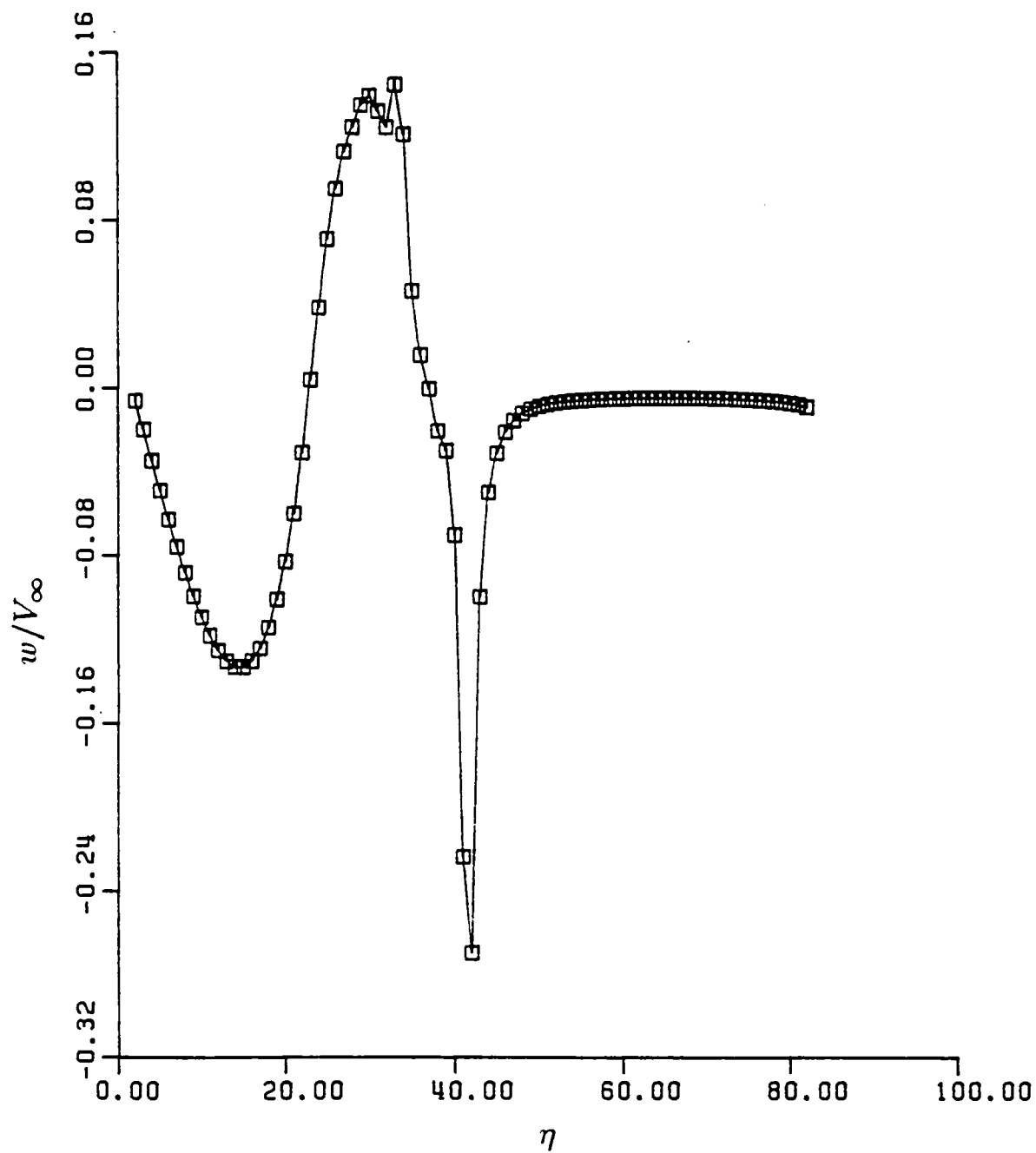


Fig. (7-17f) Azimuthal Velocity Component
($M_\infty = 4$, $\alpha = -12^\circ$)

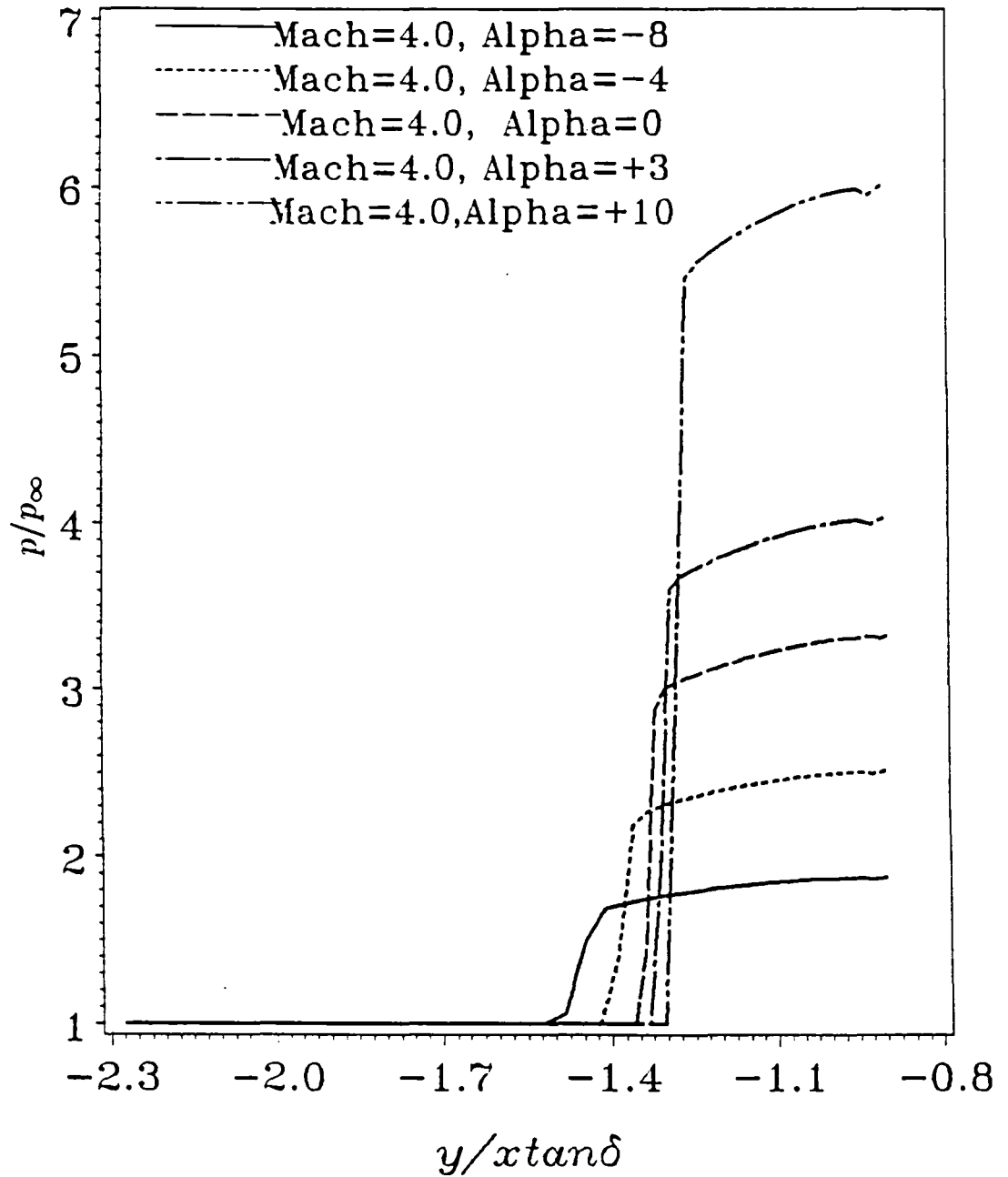


Fig. (7-18a) Pressure near Lower Symmetry Plane

$$(M_\infty = 4, \quad \alpha \neq 0^\circ)$$

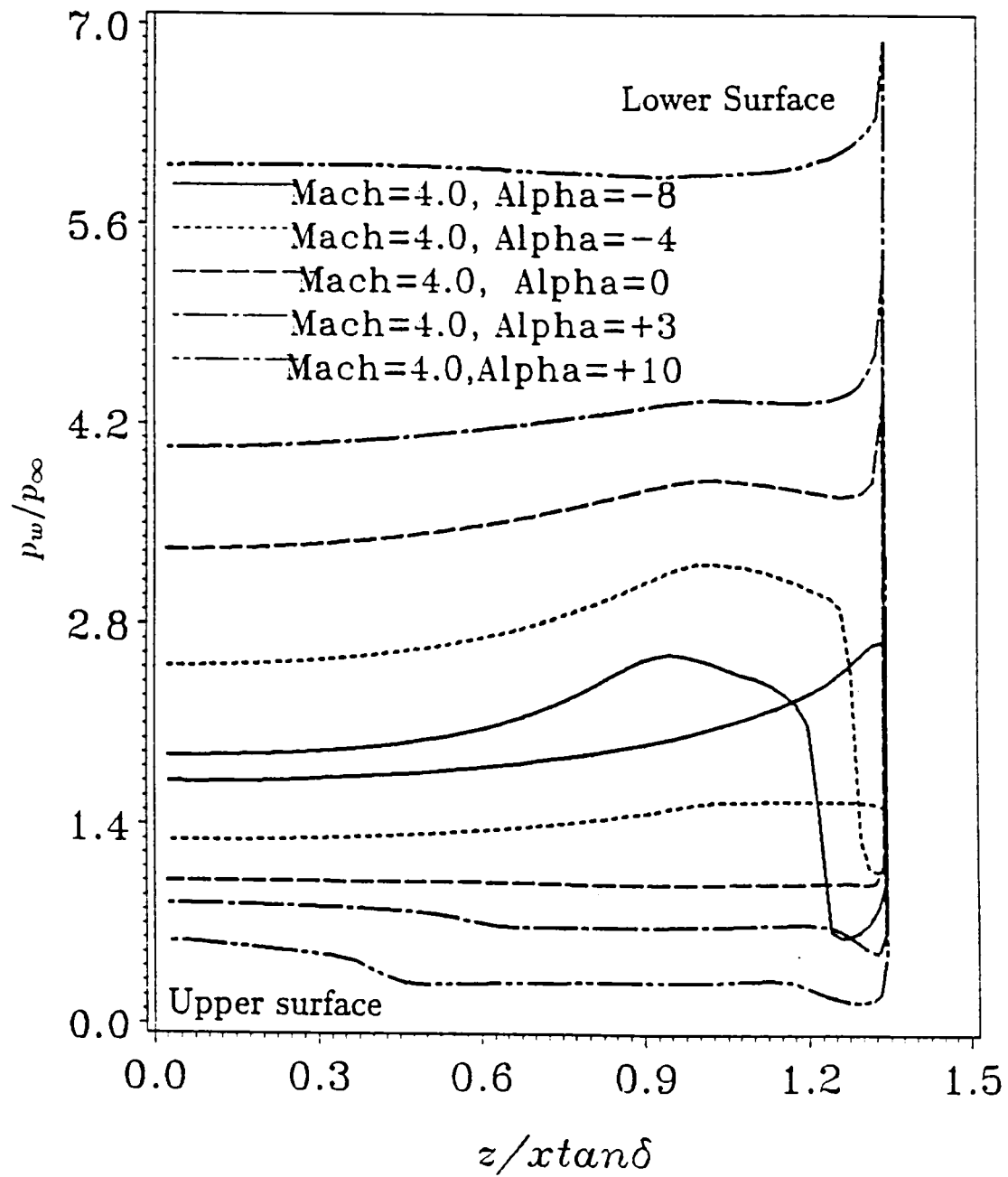


Fig. (7-18b) Wall Pressure

$$(M_\infty = 4, \quad \alpha \neq 0^\circ)$$

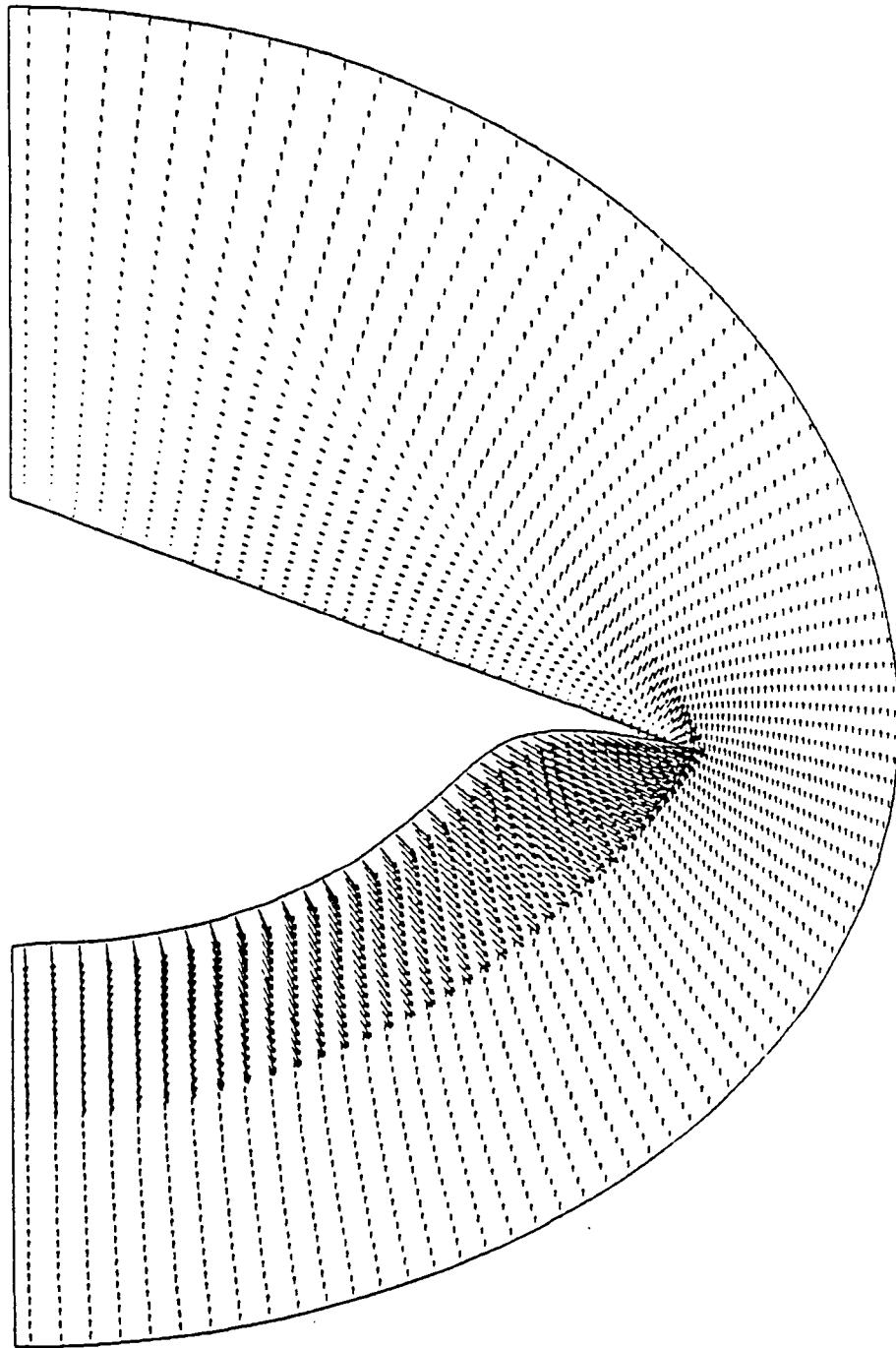


Fig. (7-19a) Cross-Plane Velocity Distribution

$$(M_{\infty} = 5, \quad \alpha = +4^{\circ})$$

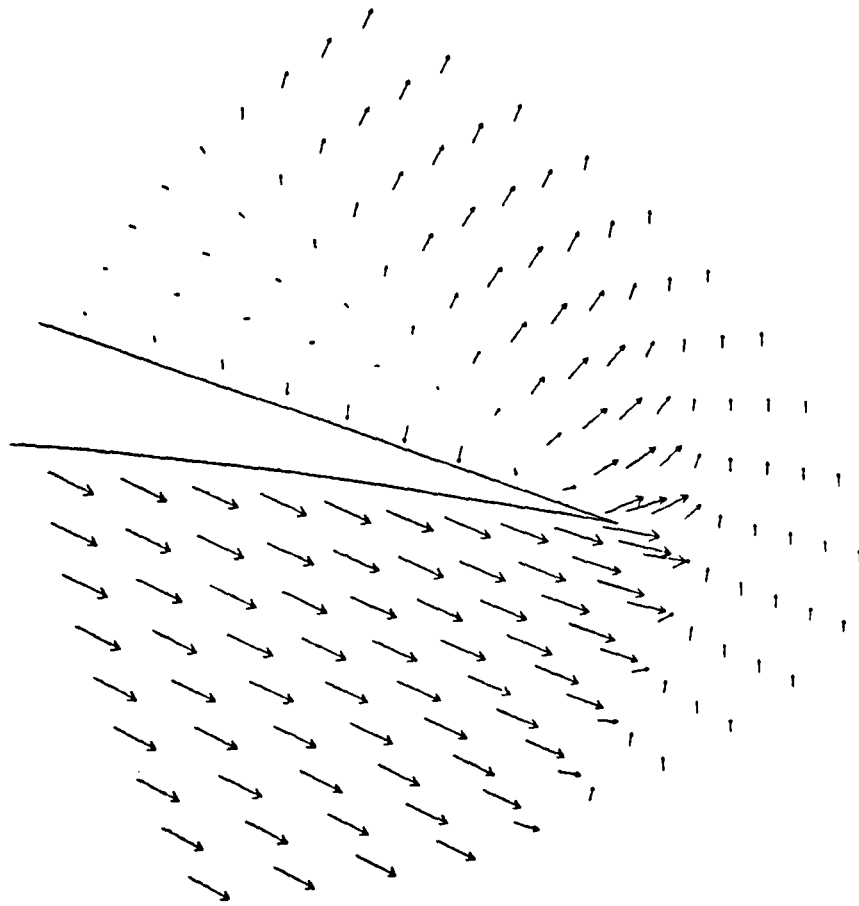


Fig. (7-19b) Magnified Cross-Plane Velocity near Tip

$$(M_{\infty} = 5, \quad \alpha = +4^{\circ})$$

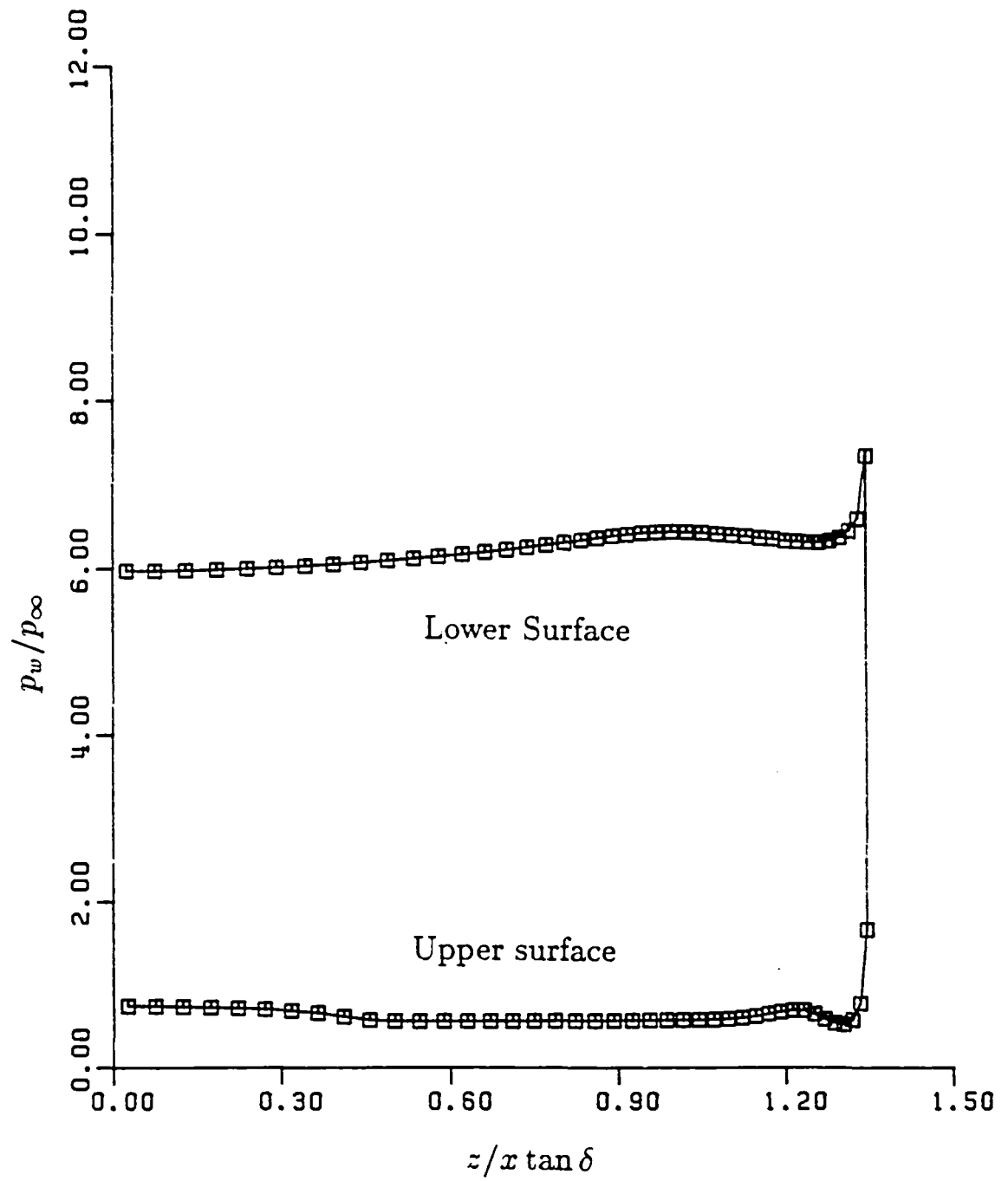


Fig. (7-19c) Wall Pressure Distribution

$$(M_\infty = 5, \quad \alpha = +4^\circ)$$

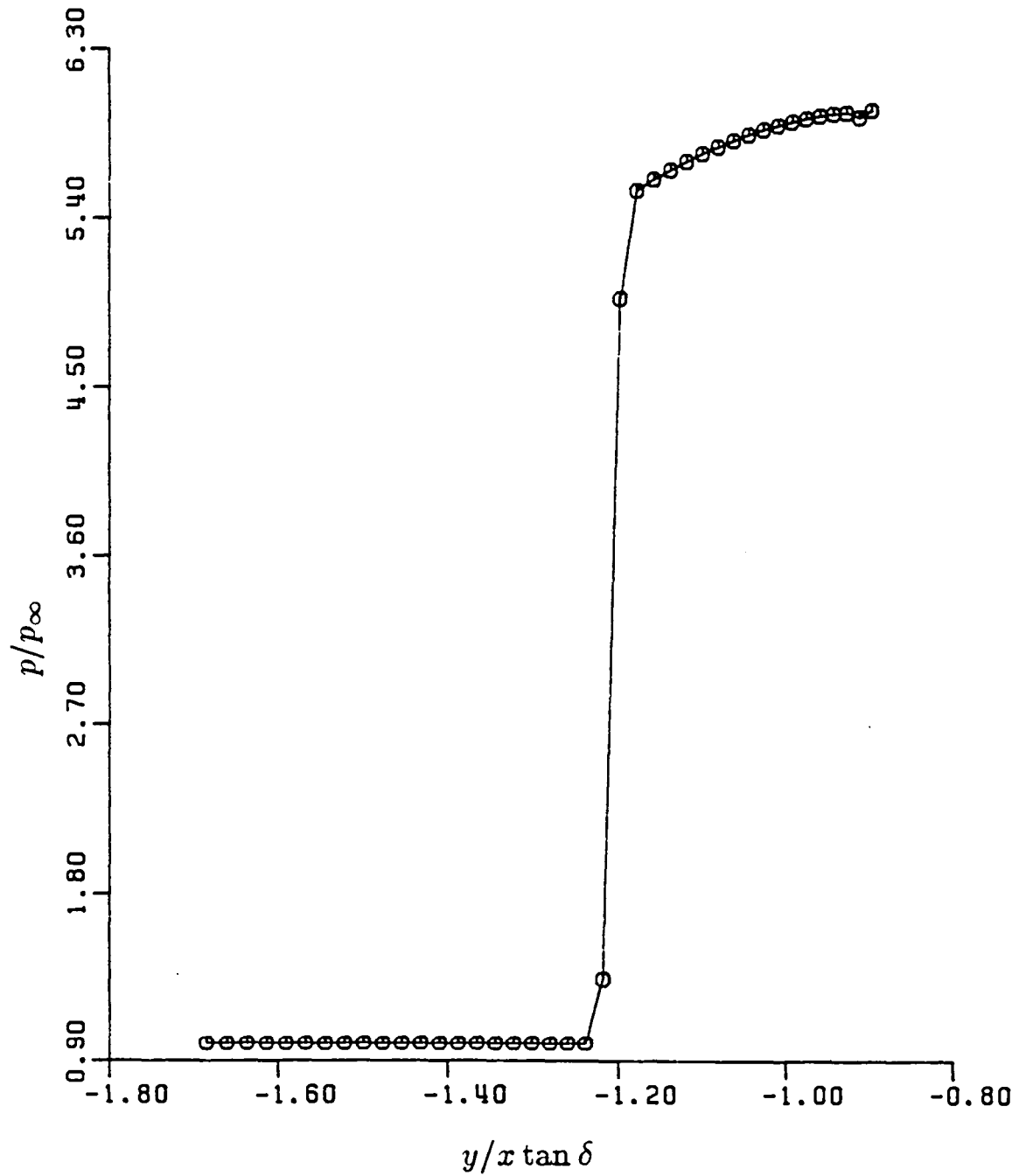


Fig. (7-19d) Pressure near Lower Symmetry Plane

$$(M_\infty = 5, \quad \alpha = +4^\circ)$$

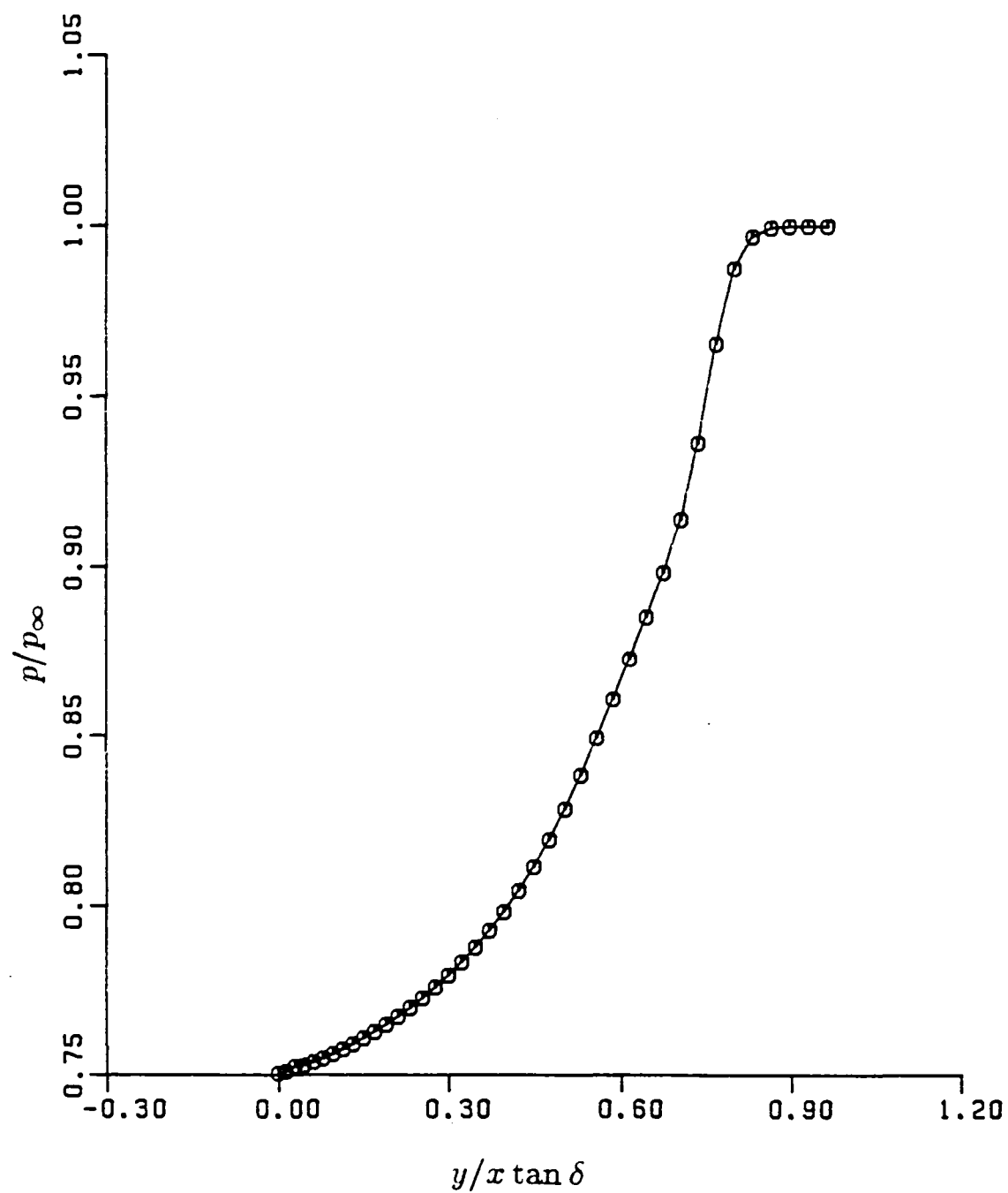


Fig. (7-19e) Pressure near Upper Symmetry Plane
($M_\infty = 5$, $\alpha = +4^\circ$)

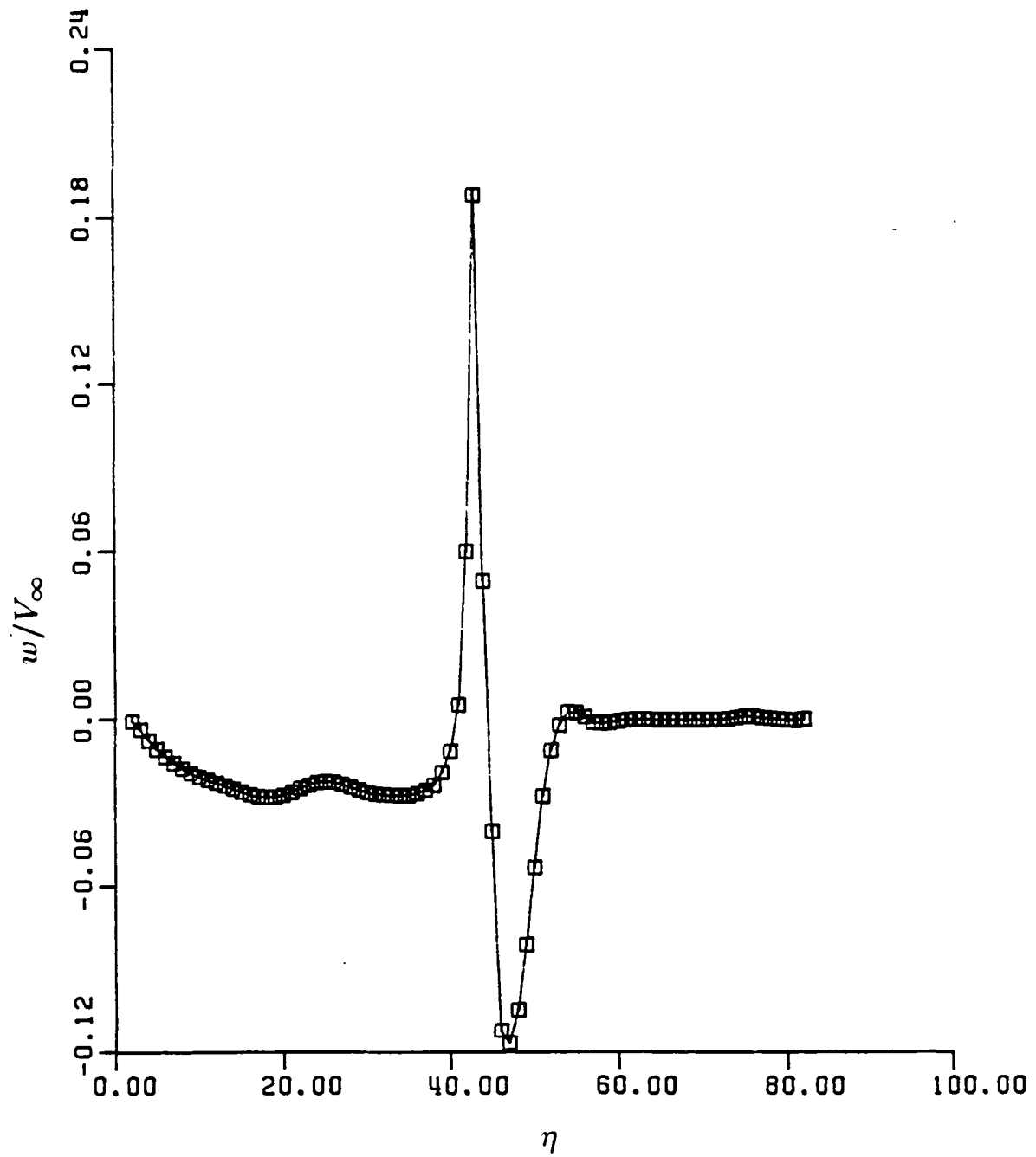


Fig. (7-19f) Azimuthal Velocity Component

$$(M_\infty = 5, \quad \alpha = +4^\circ)$$

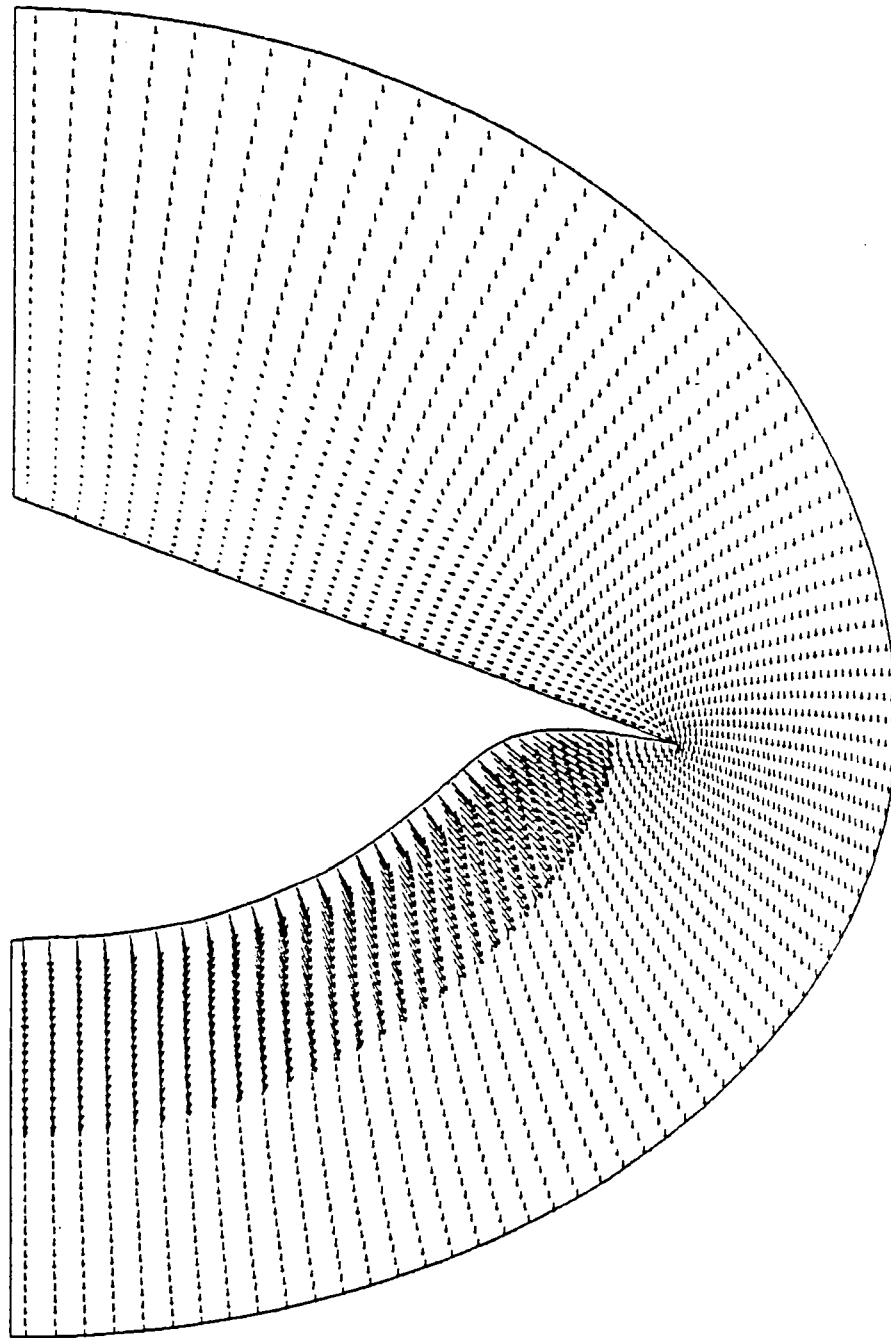


Fig. (7-20a) Cross-Plane Velocity Distribution

$$(M_{\infty} = 5, \quad \alpha = -4^{\circ})$$

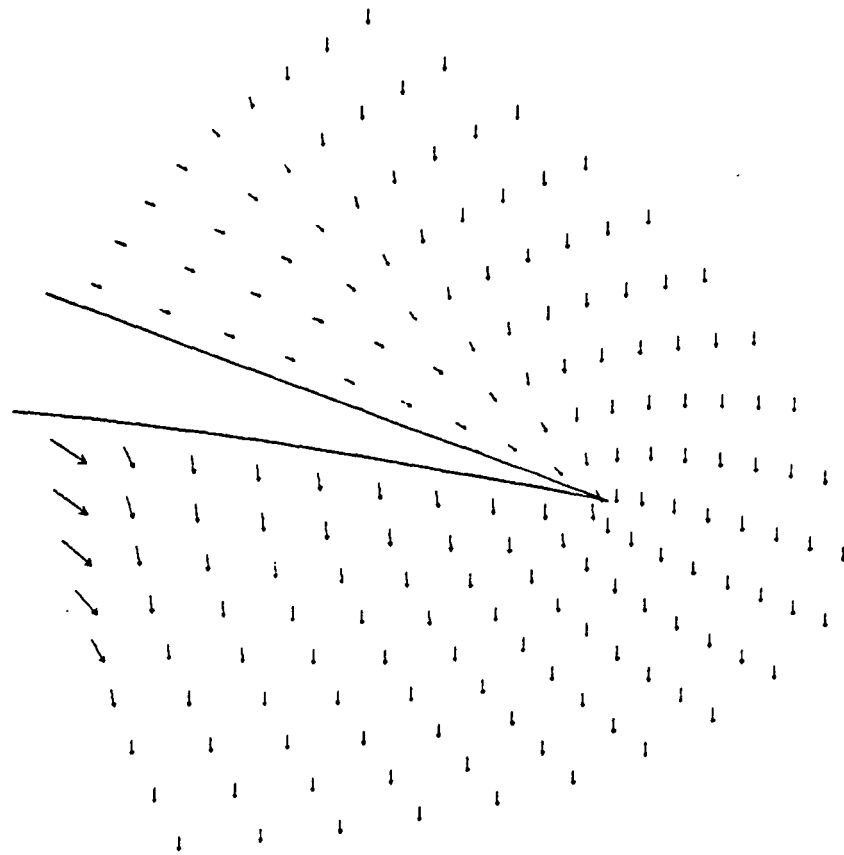


Fig. (7-20b) Magnified Cross-Plane Velocity near Tip

$$(M_{\infty} = 5, \quad \alpha = -4^{\circ})$$

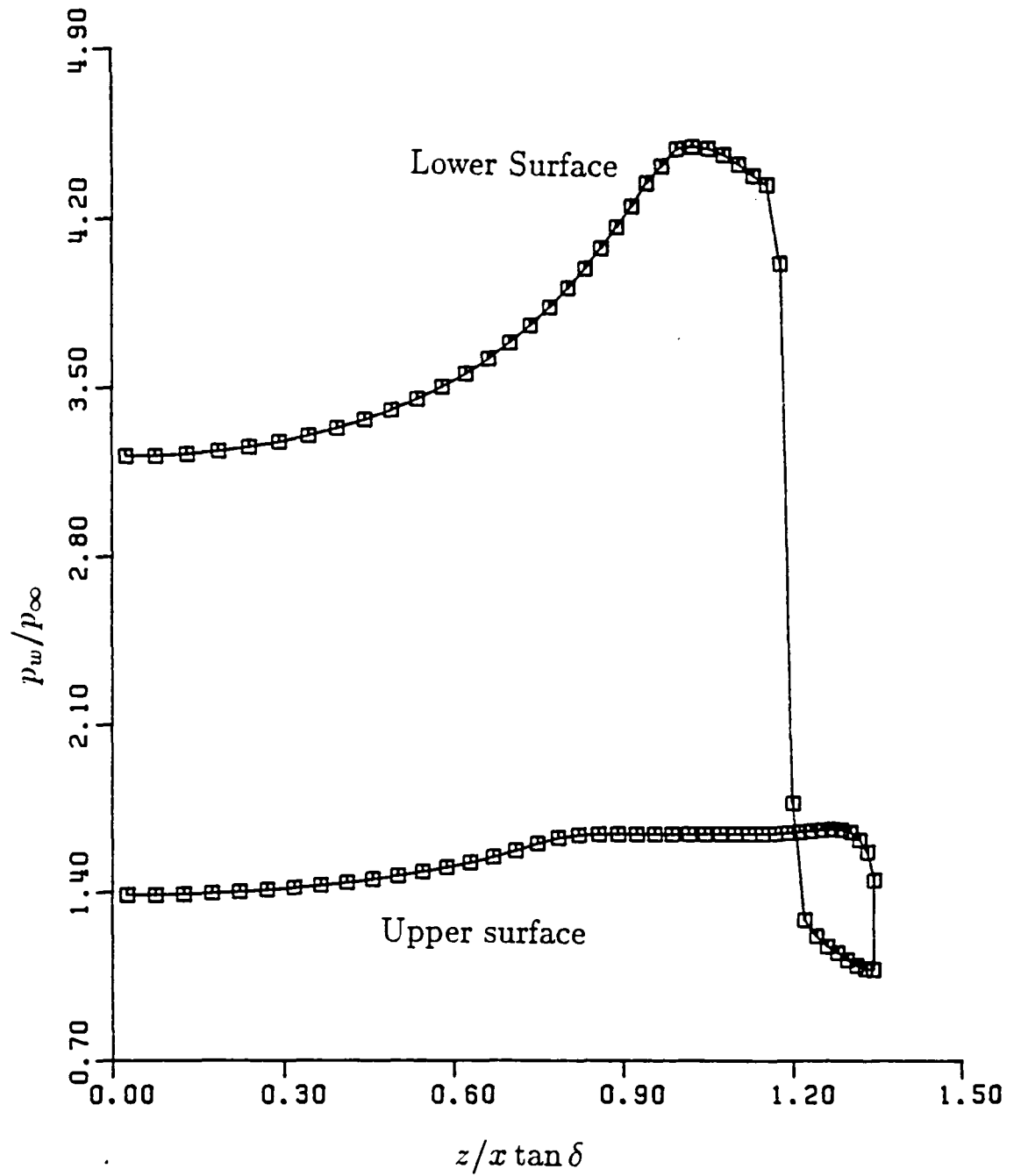


Fig. (7-20c) Wall Pressure Distribution

$$(M_\infty = 5, \quad \alpha = -4^\circ)$$

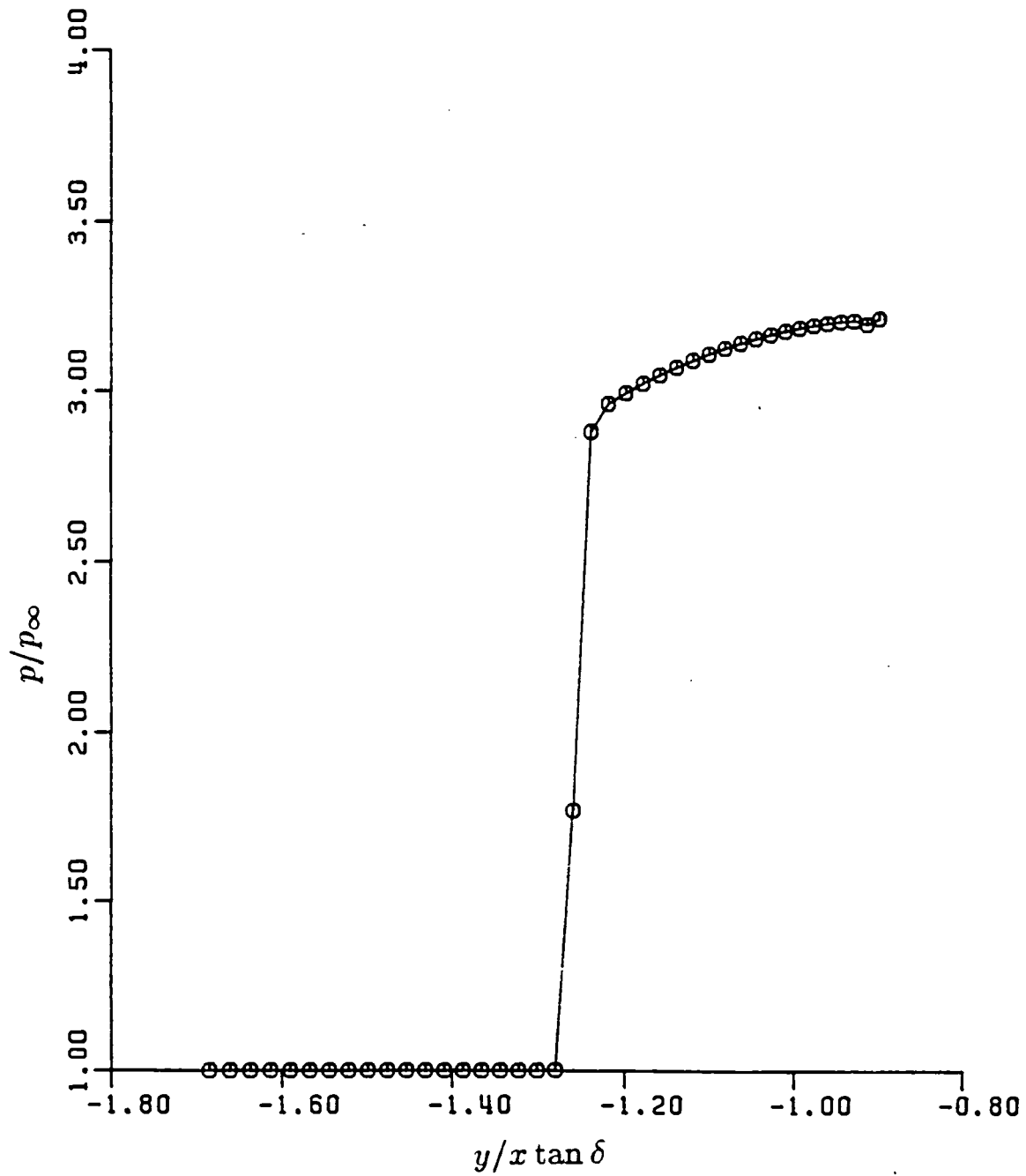


Fig. (7-20d) Pressure near Lower Symmetry Plane

$$(M_\infty = 5, \quad \alpha = -4^\circ)$$

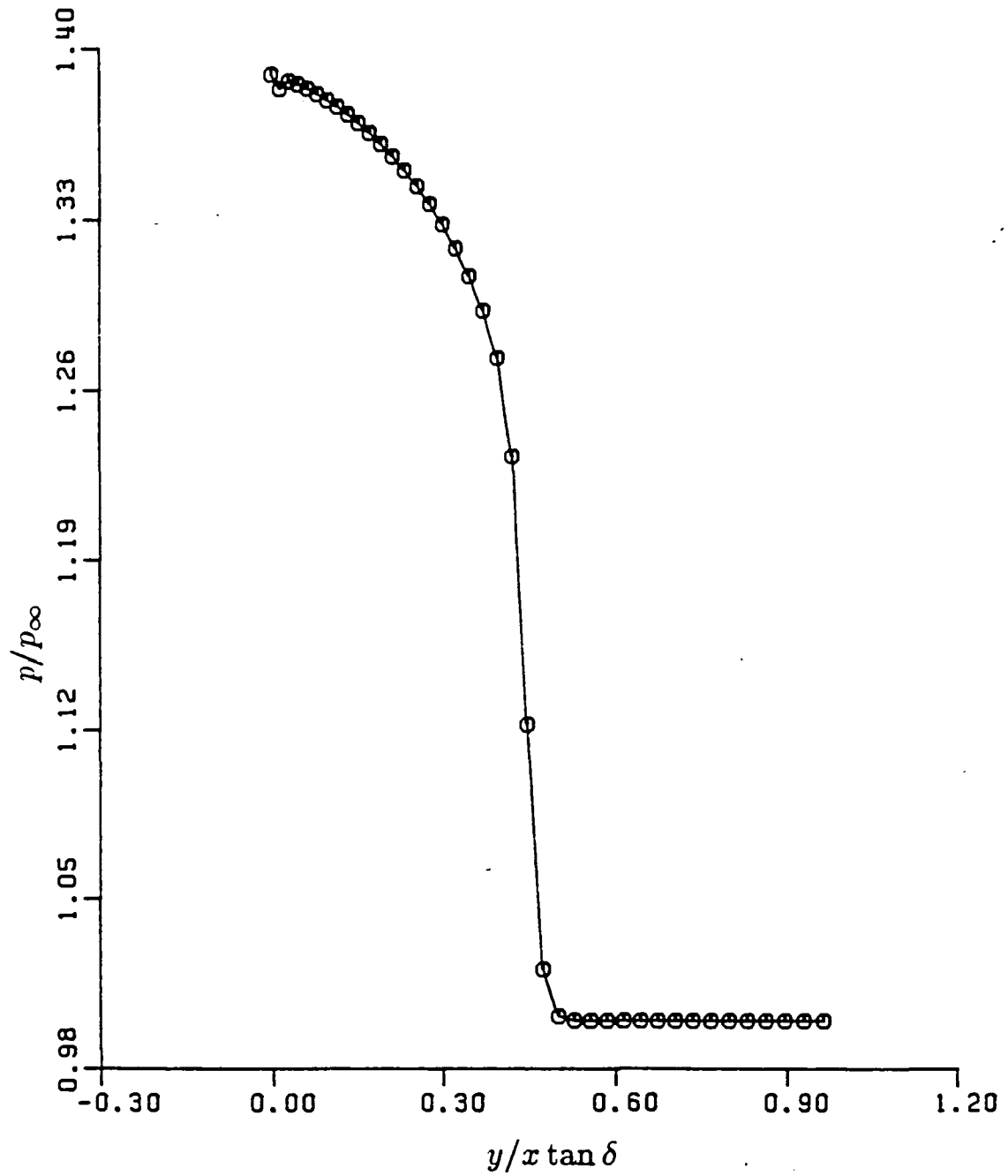


Fig. (7-20e) Pressure near Upper Symmetry Plane

$$(M_\infty = 5, \quad \alpha = -4^\circ)$$

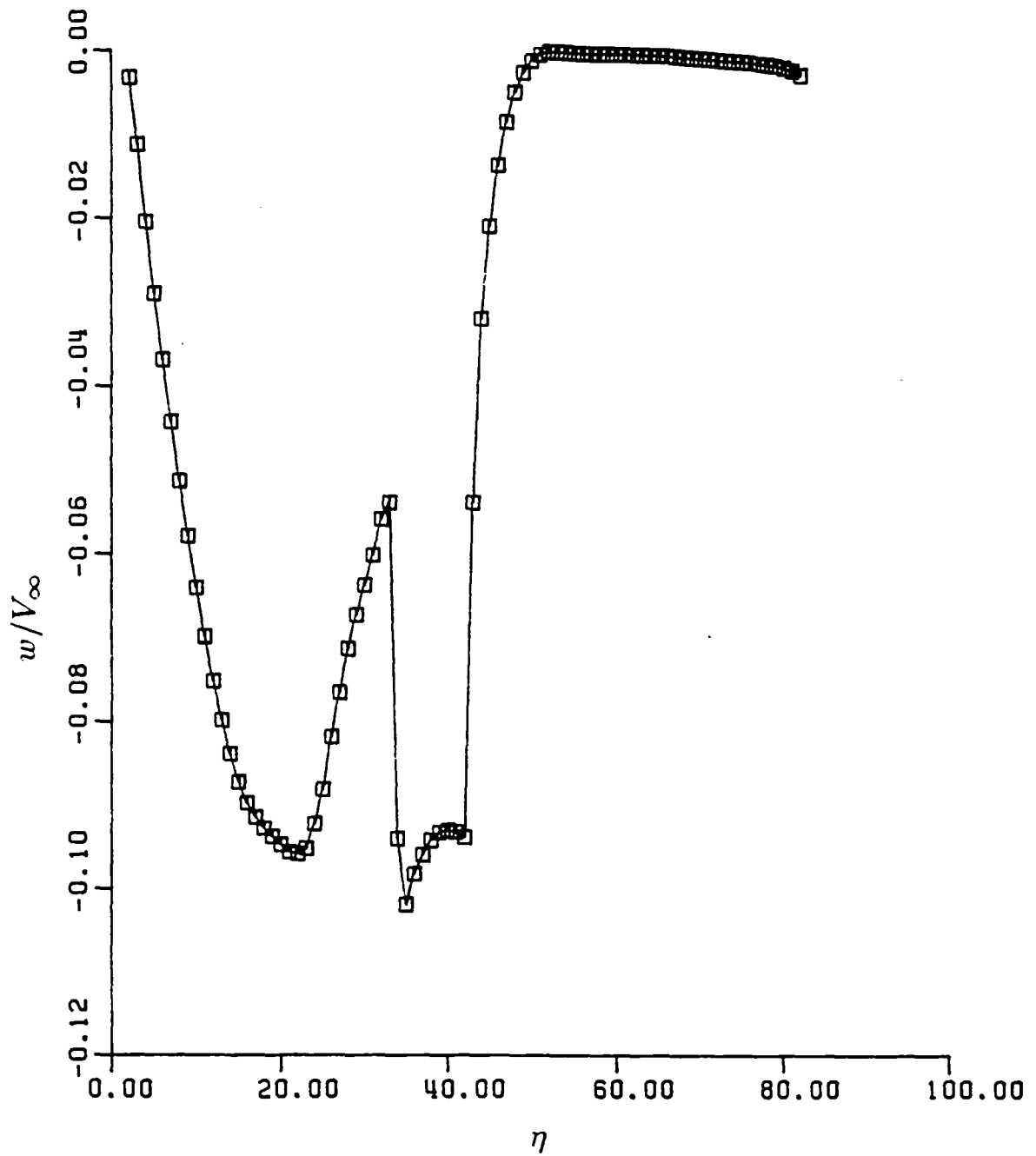


Fig. (7-20f) Azimuthal Velocity Component

$$(M_\infty = 5, \quad \alpha = -4^\circ)$$

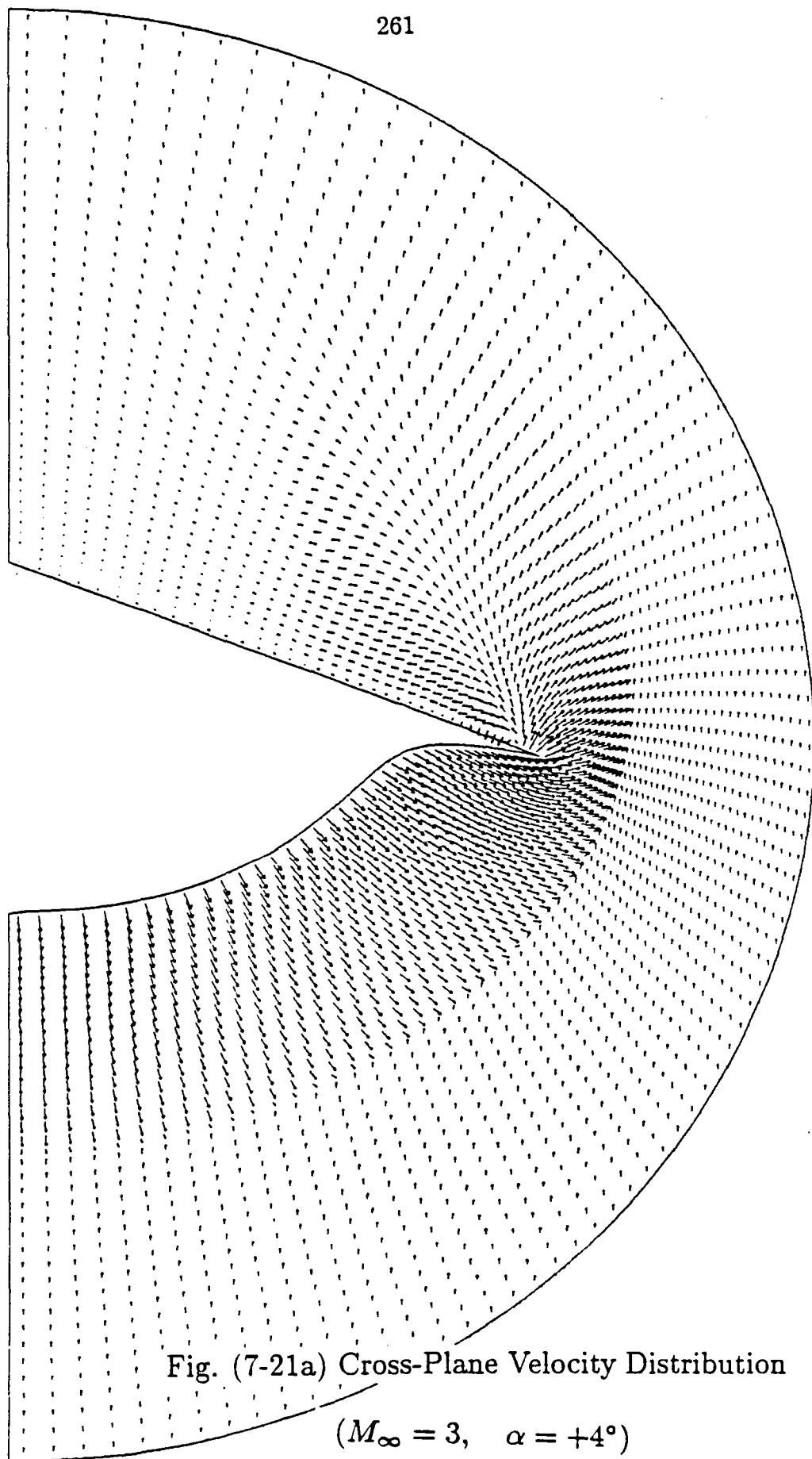


Fig. (7-21a) Cross-Plane Velocity Distribution
($M_\infty = 3$, $\alpha = +4^\circ$)

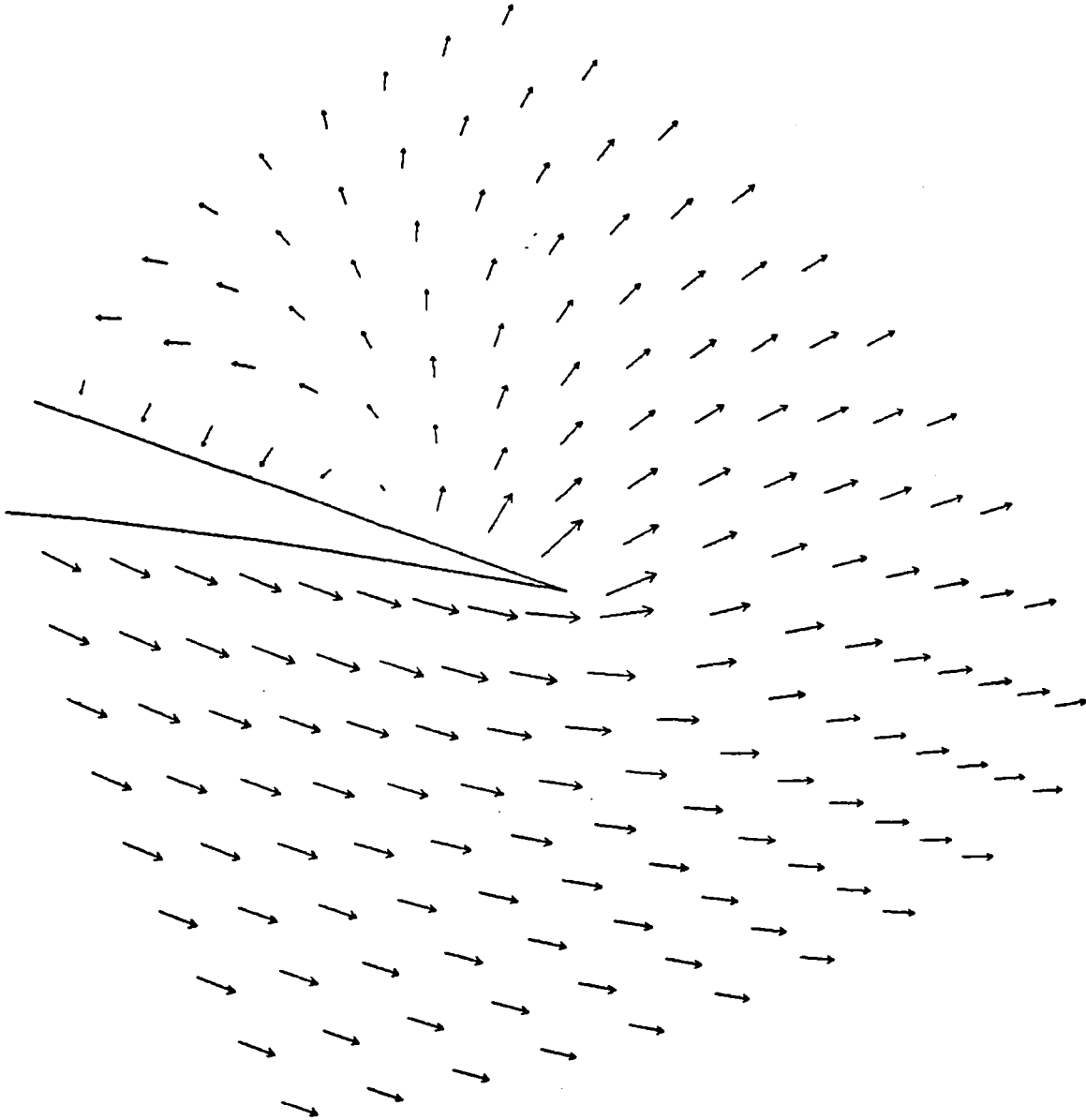


Fig. (7-21b) Magnified Cross-Plane Velocity near Tip

$$(M_{\infty} = 3, \quad \alpha = +4^{\circ})$$

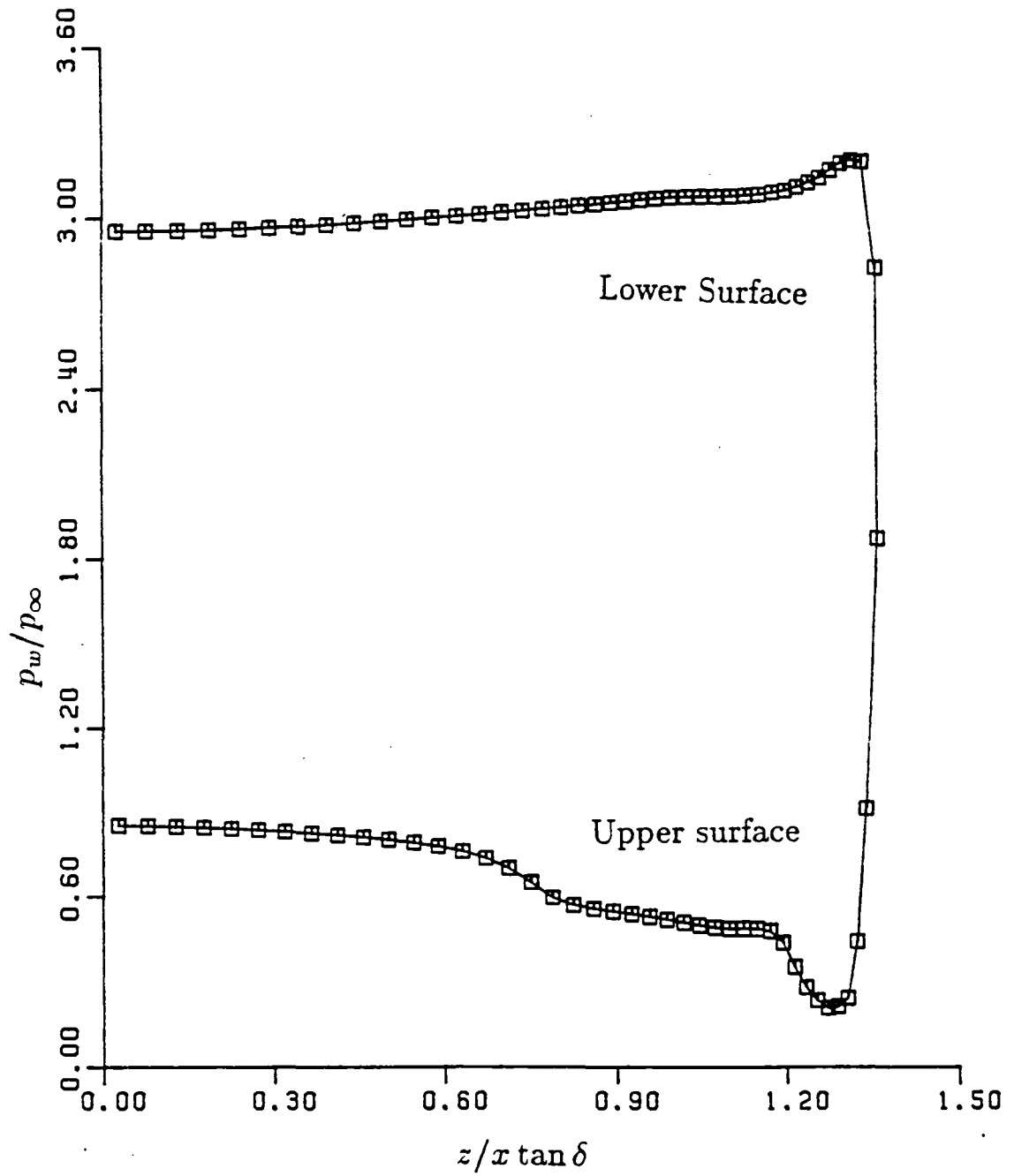


Fig. (7-21c) Wall Pressure Distribution

$$(M_\infty = 3, \quad \alpha = +4^\circ)$$

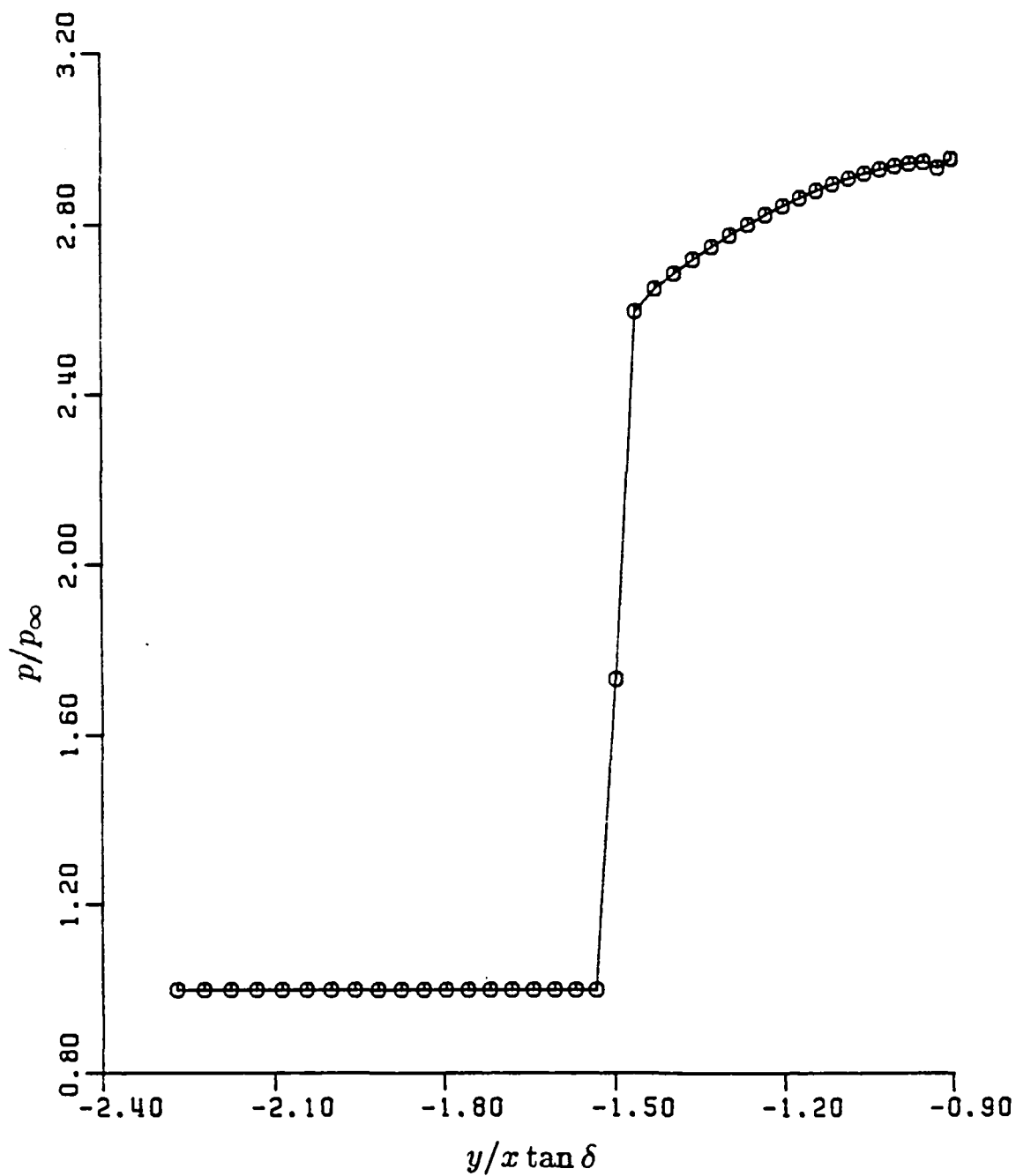


Fig. (7-21d) Pressure near Lower Symmetry Plane

$$(M_\infty = 3, \quad \alpha = +4^\circ)$$

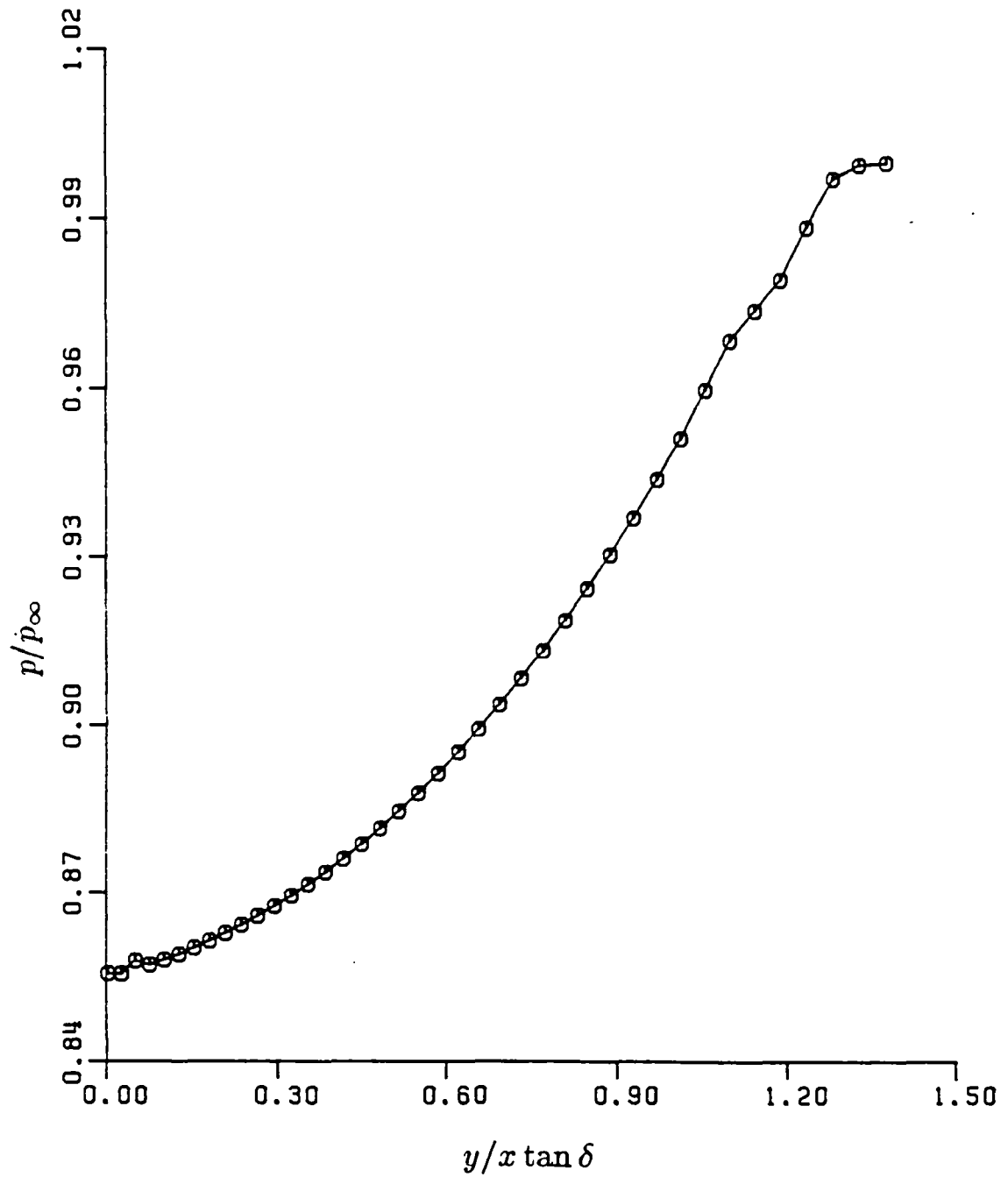


Fig. (7-21e) Pressure near Upper Symmetry Plane

$$(M_\infty = 3, \quad \alpha = +4^\circ)$$

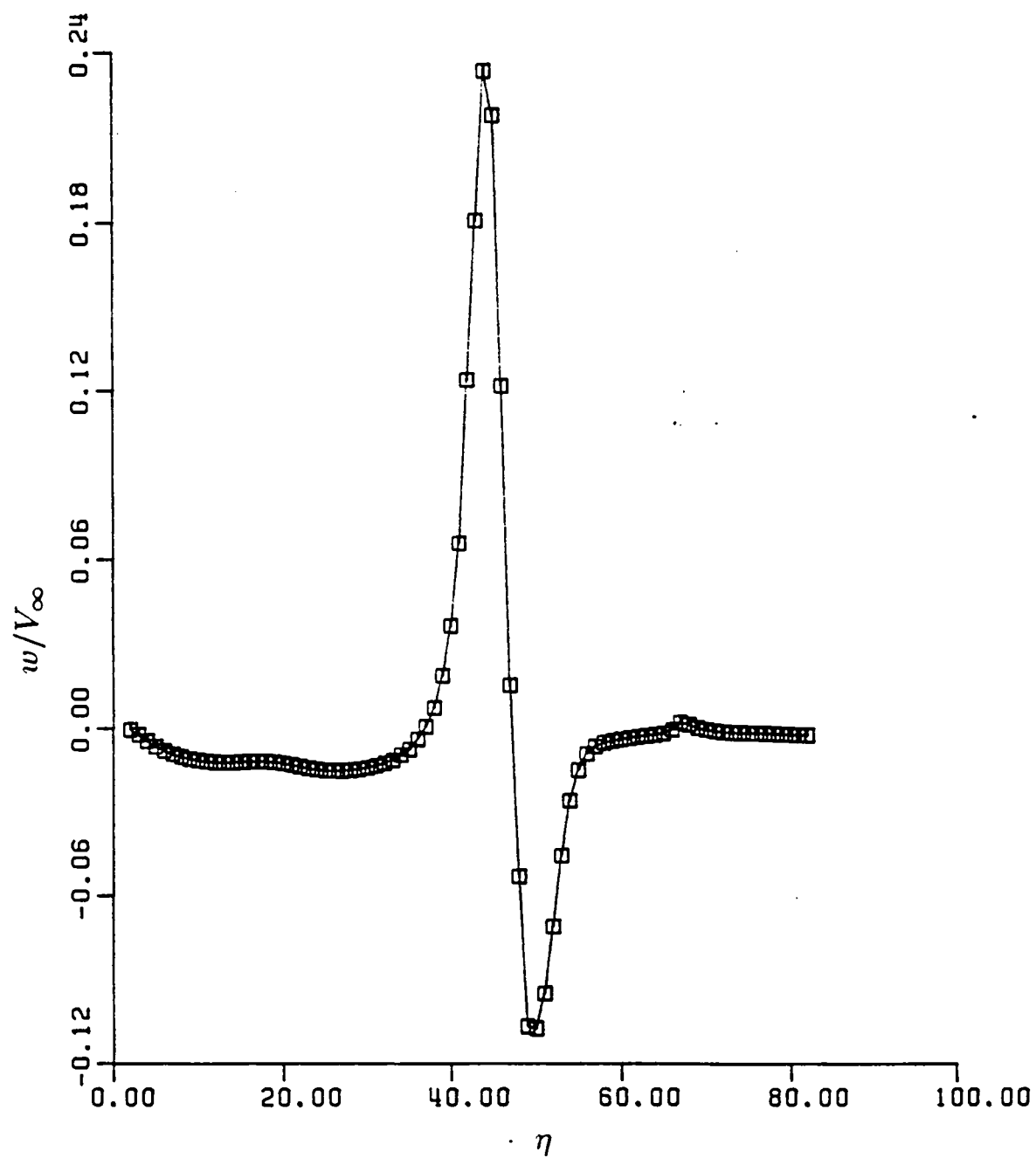


Fig. (7-21f) Azimuthal Velocity Component

 $(M_\infty = 3, \quad \alpha = +4^\circ)$

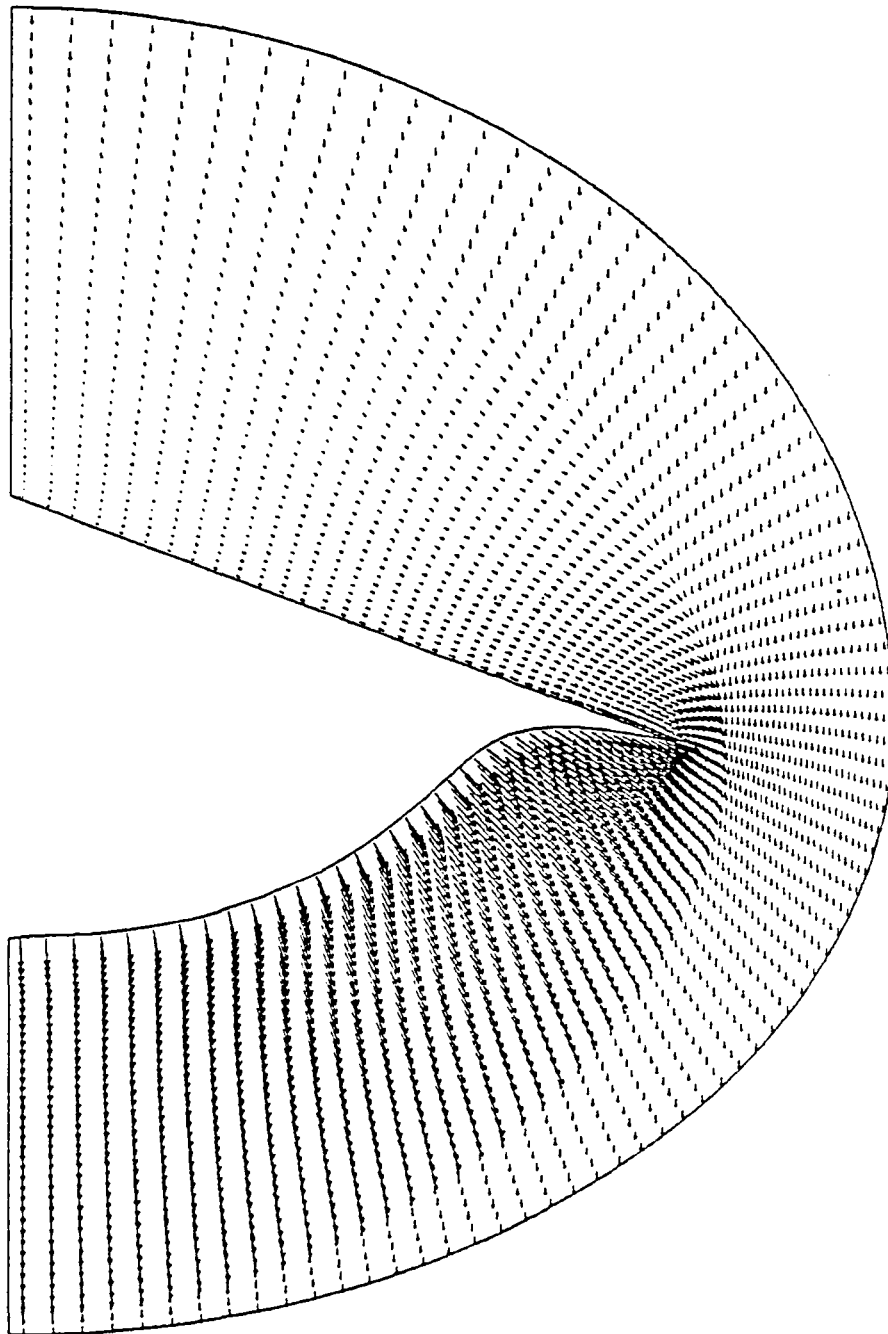


Fig. (7-22a) Cross-Plane Velocity Distribution

$$(M_{\infty} = 3, \quad \alpha = -4^{\circ})$$

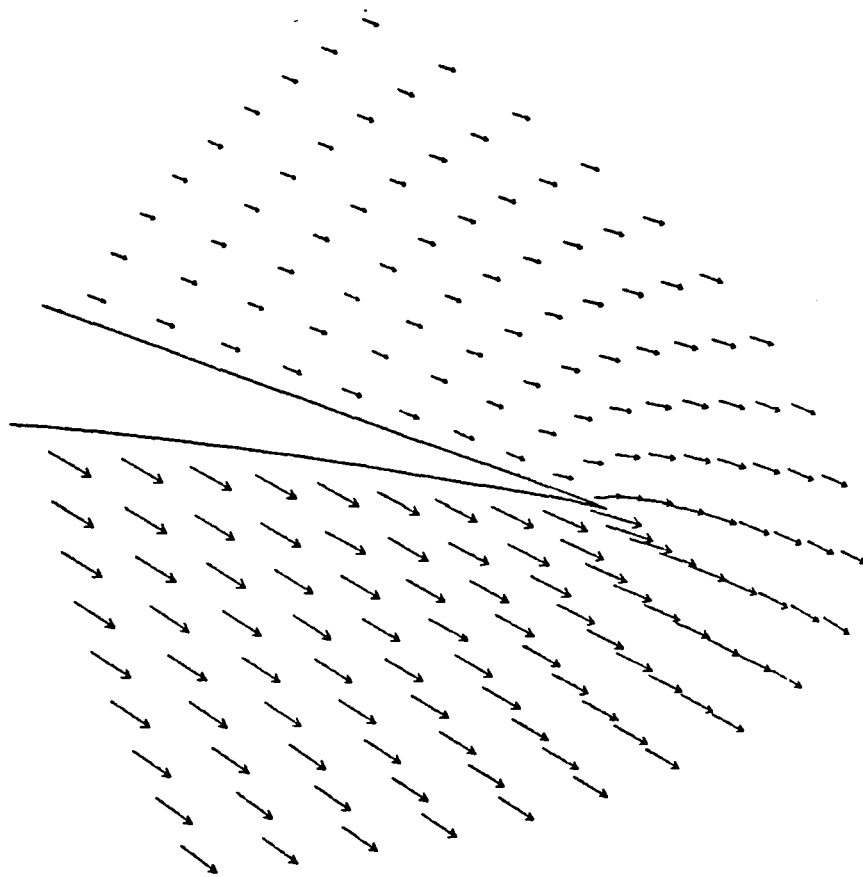


Fig. (7-22b) Magnified Cross-Plane Velocity near Tip

$$(M_{\infty} = 3, \quad \alpha = -4^{\circ})$$

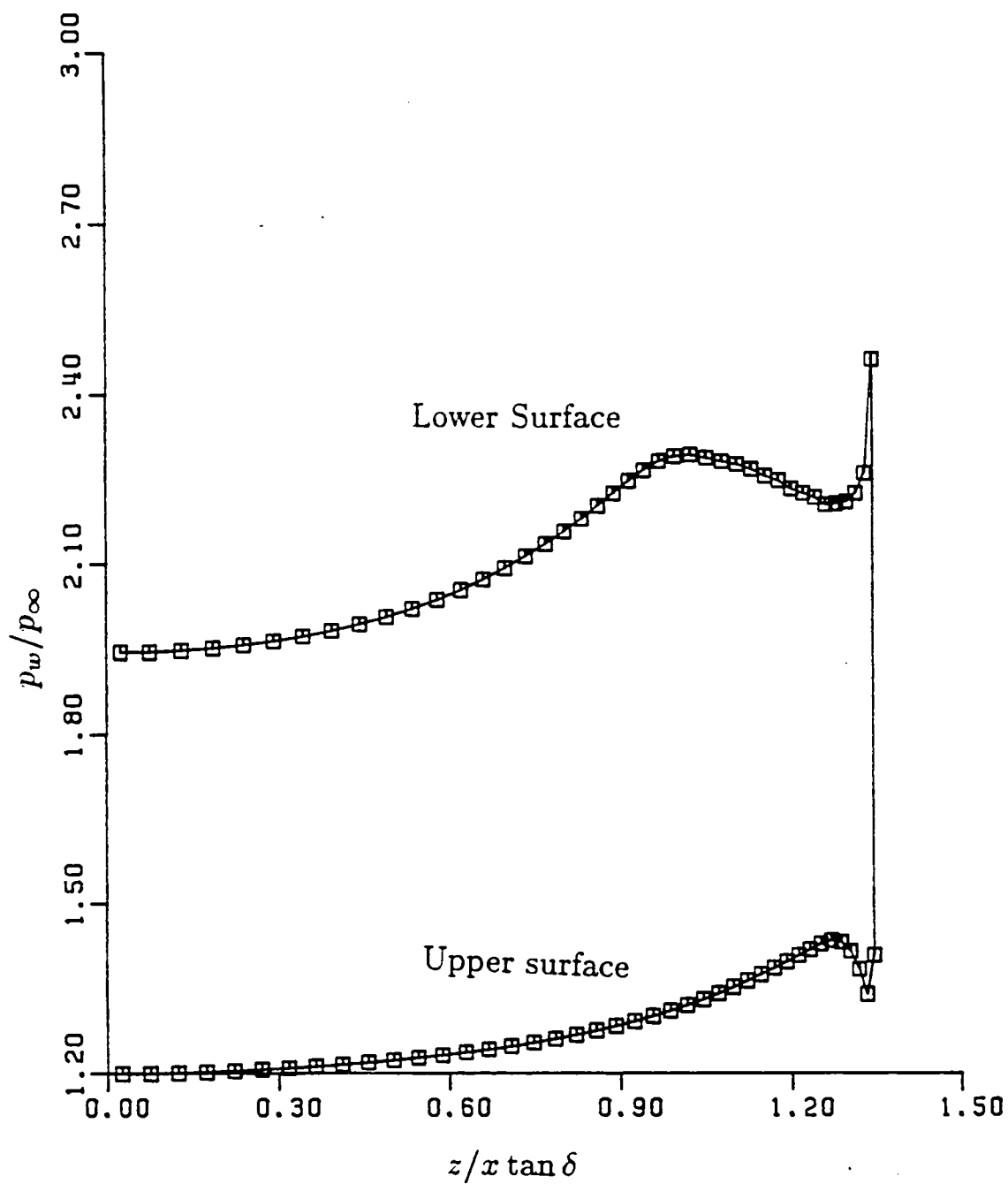


Fig. (7-22c) Wall Pressure Distribution

$$(M_\infty = 3, \quad \alpha = -4^\circ)$$

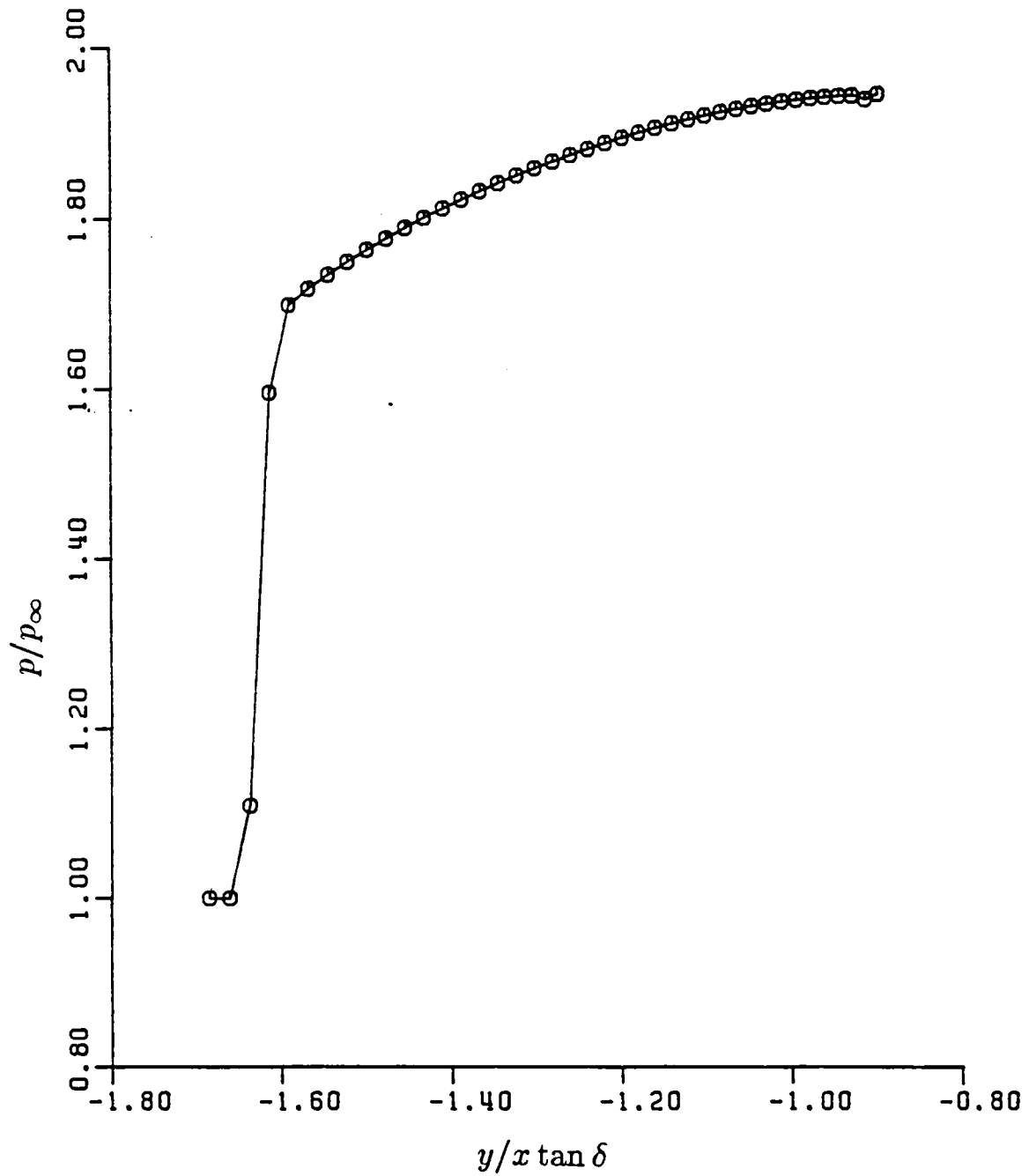


Fig. (7-22d) Pressure near Lower Symmetry Plane

($M_\infty = 3$, $\alpha = -4^\circ$)

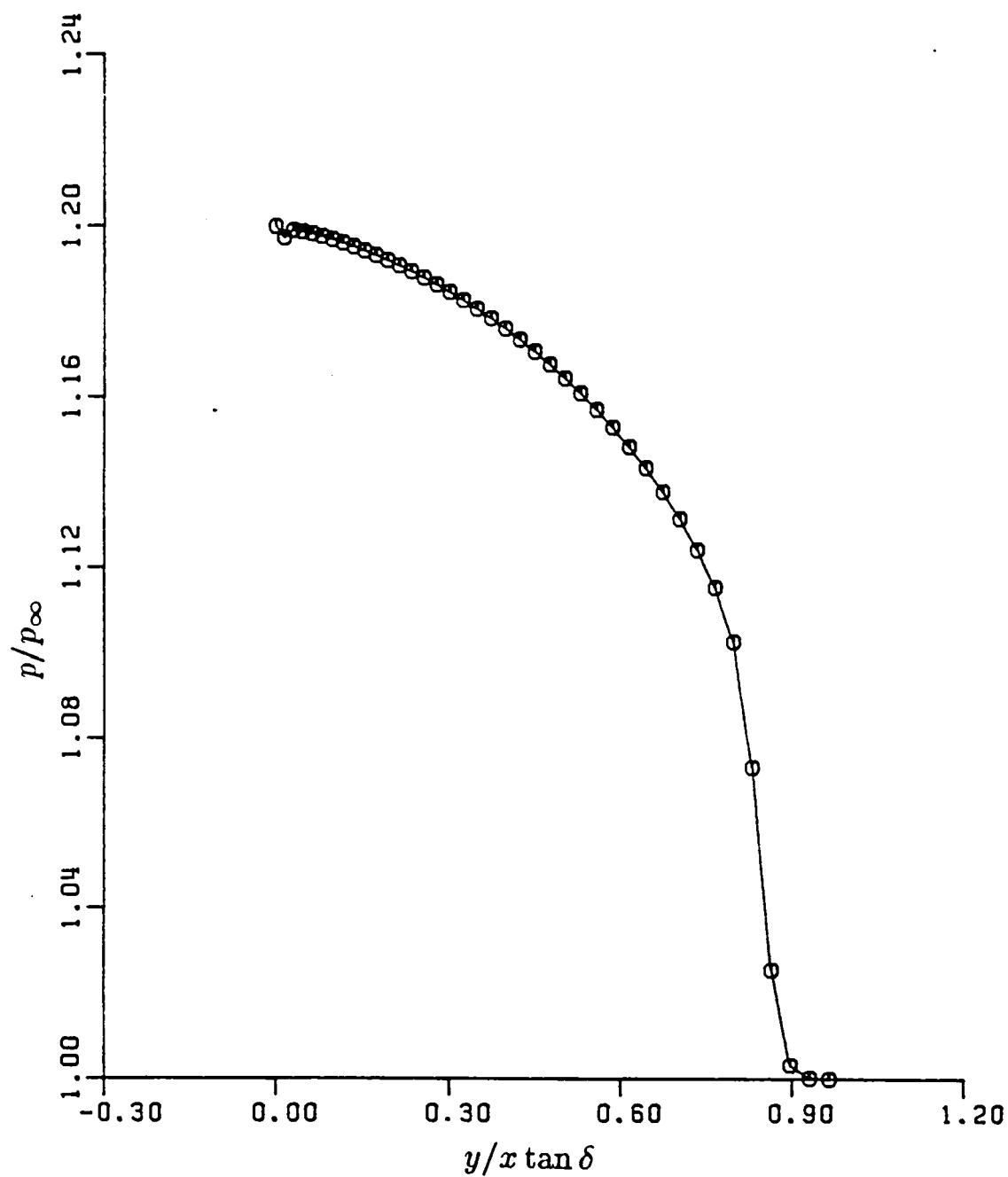


Fig. (7-22e) Pressure near Upper Symmetry Plane

$$(M_\infty = 3, \quad \alpha = -4^\circ)$$

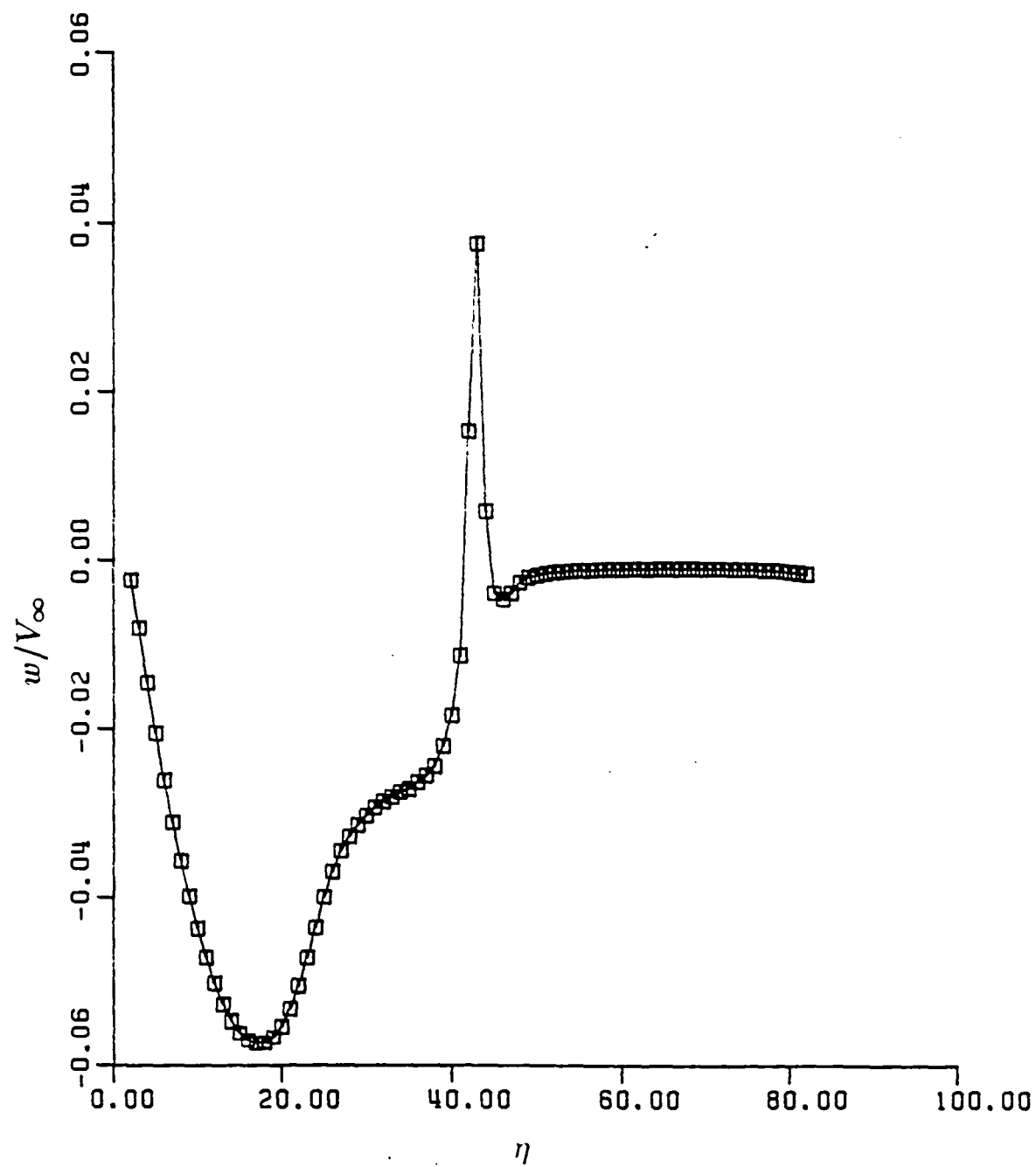


Fig. (7-22f) Azimuthal Velocity Component

$$(M_\infty = 3, \quad \alpha = -4^\circ)$$

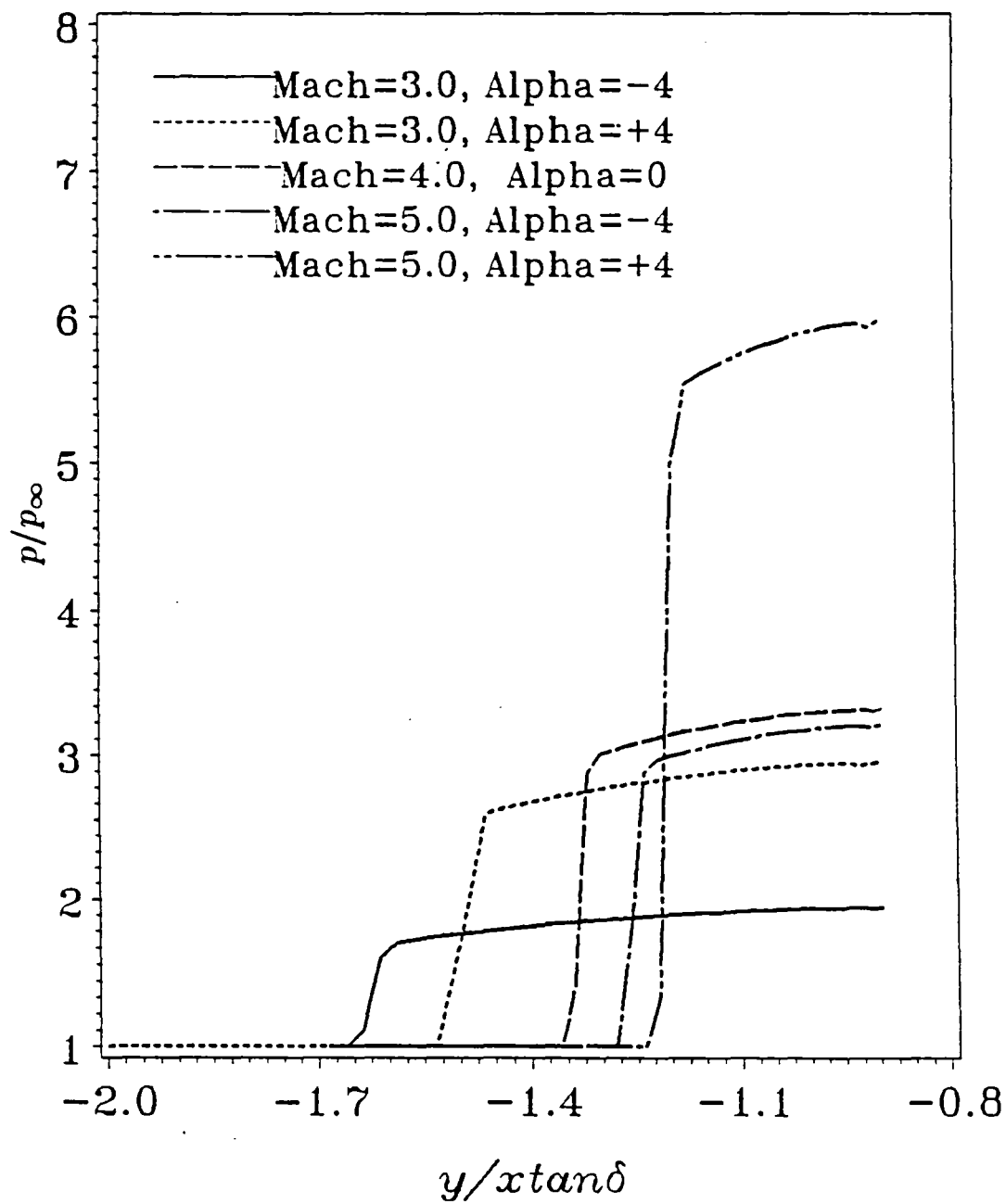


Fig. (7-23a) Pressure near Lower Symmetry Plane

 $(M_\infty \neq 4, \quad \alpha \neq 0^\circ)$

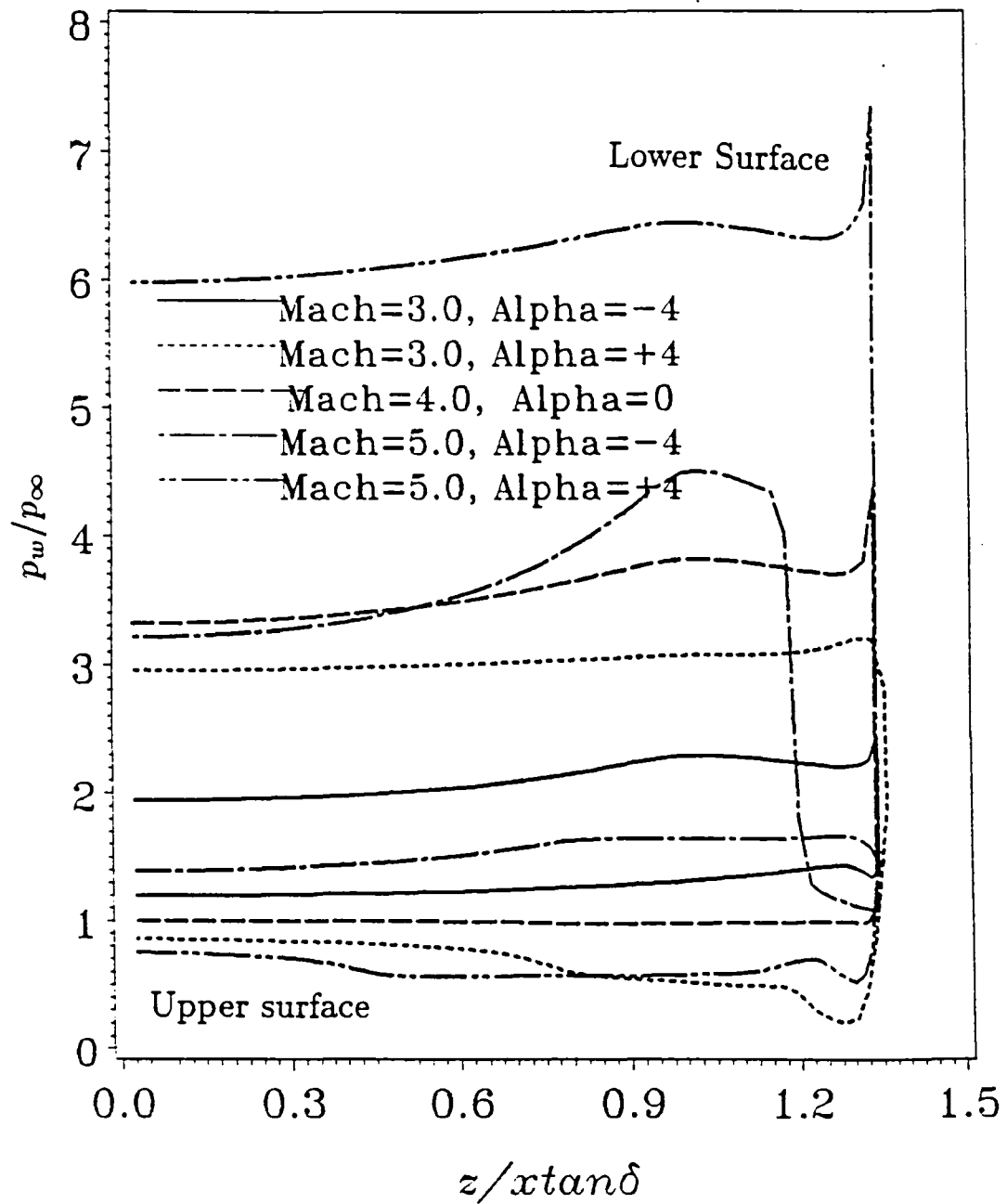


Fig. (7-23b) Wall Pressure

$$(M_\infty \neq 4, \quad \alpha \neq 0^\circ)$$

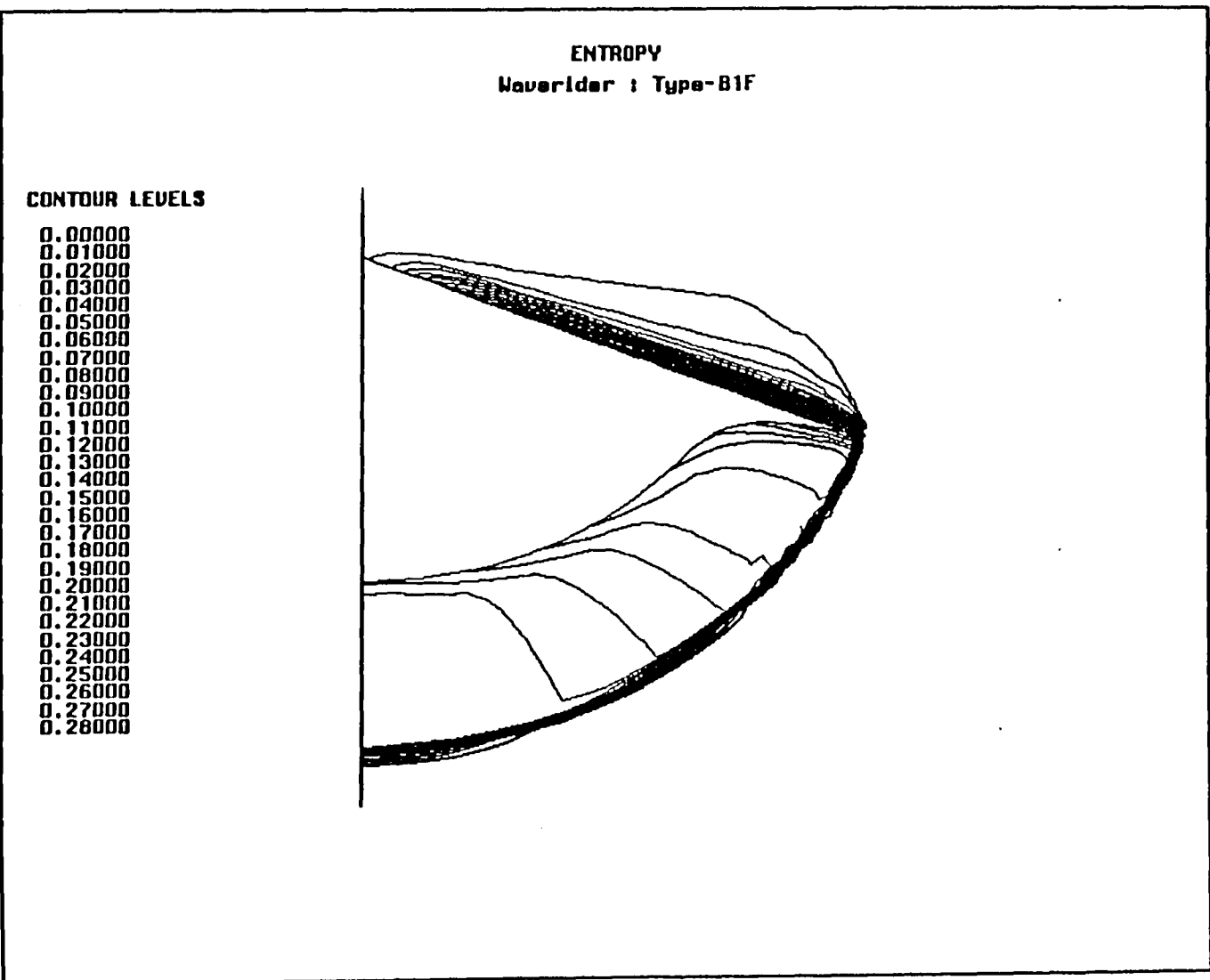


Fig. (7-24a) Entropy Contours for Waverider Type-B1F

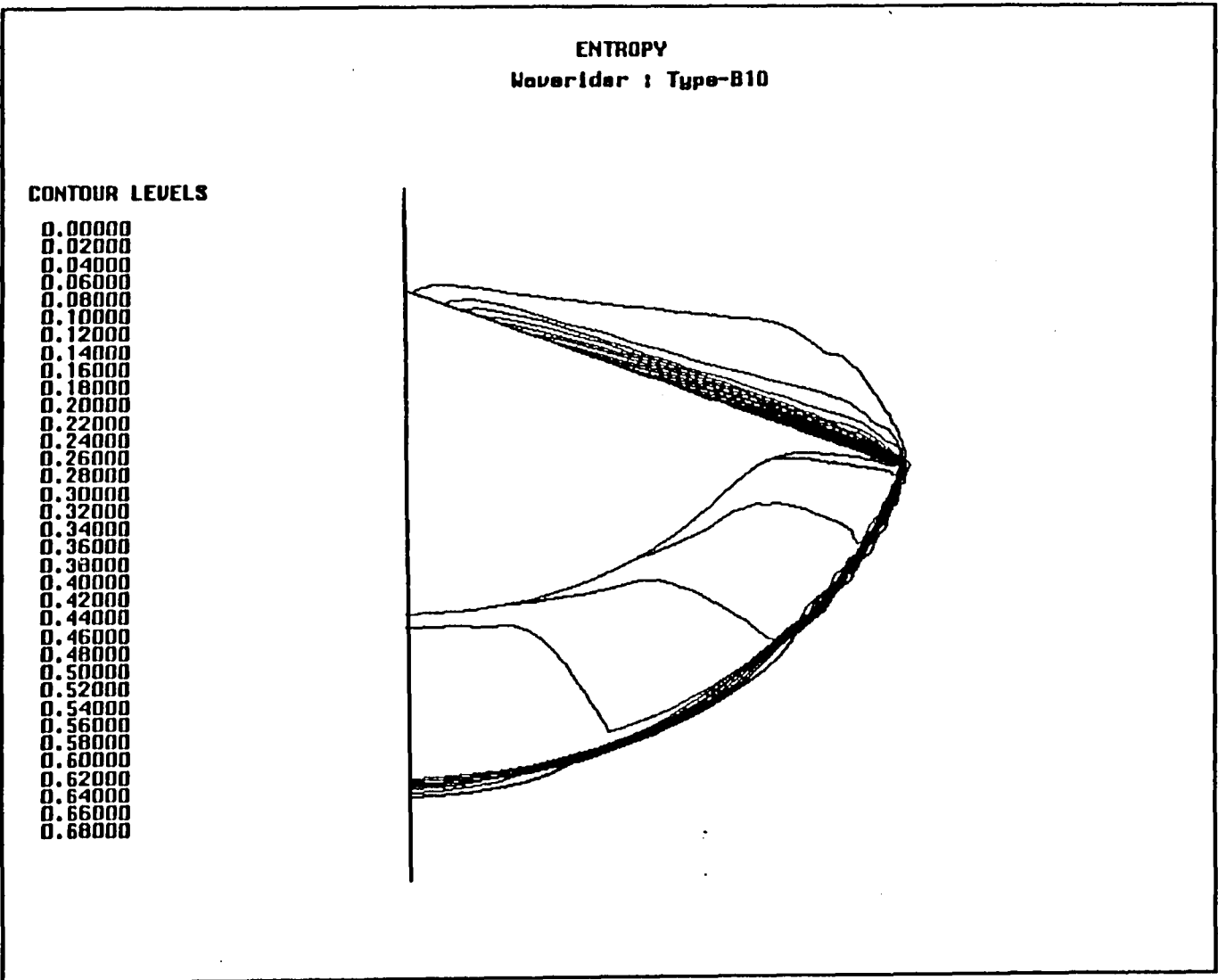
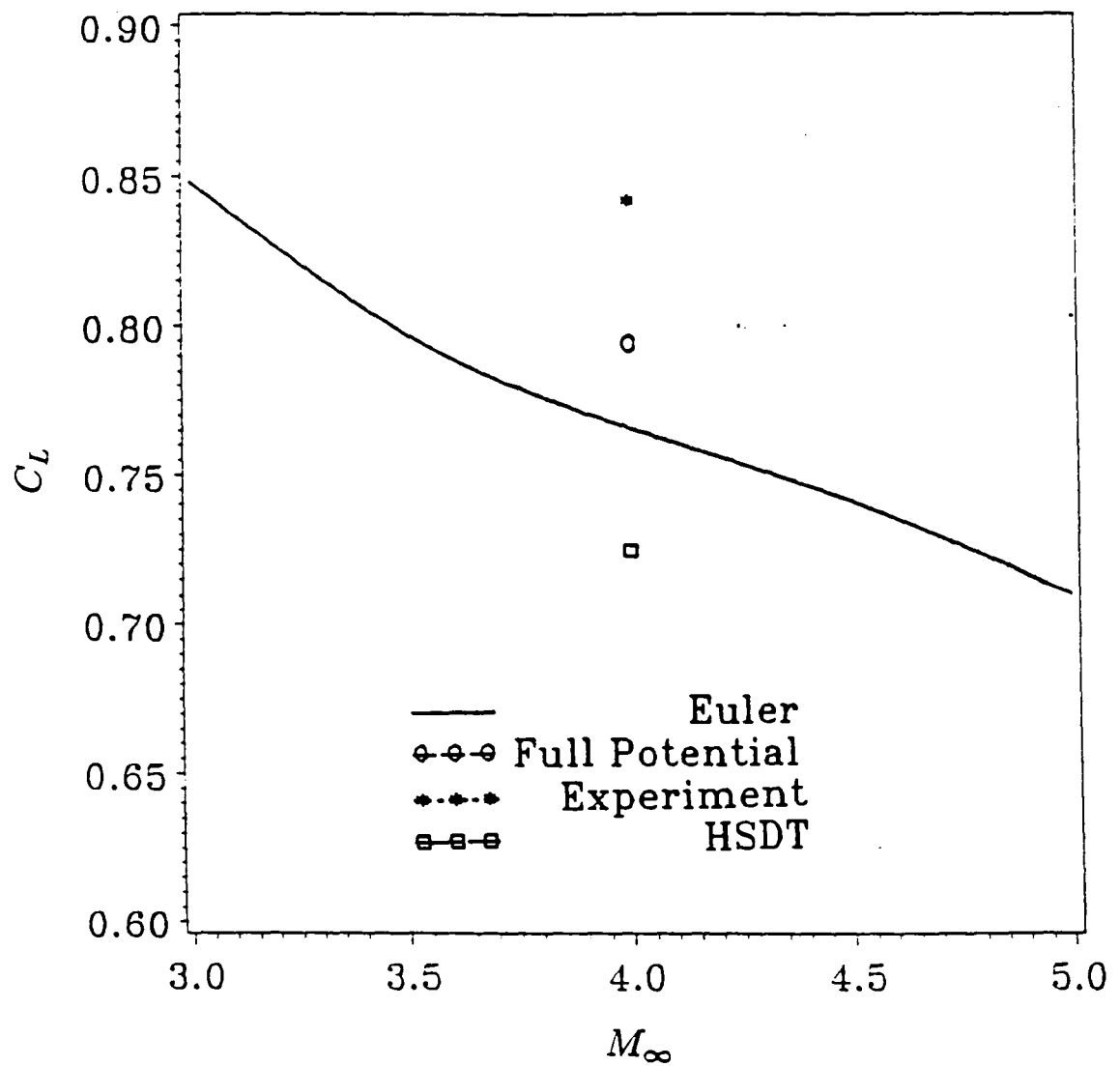
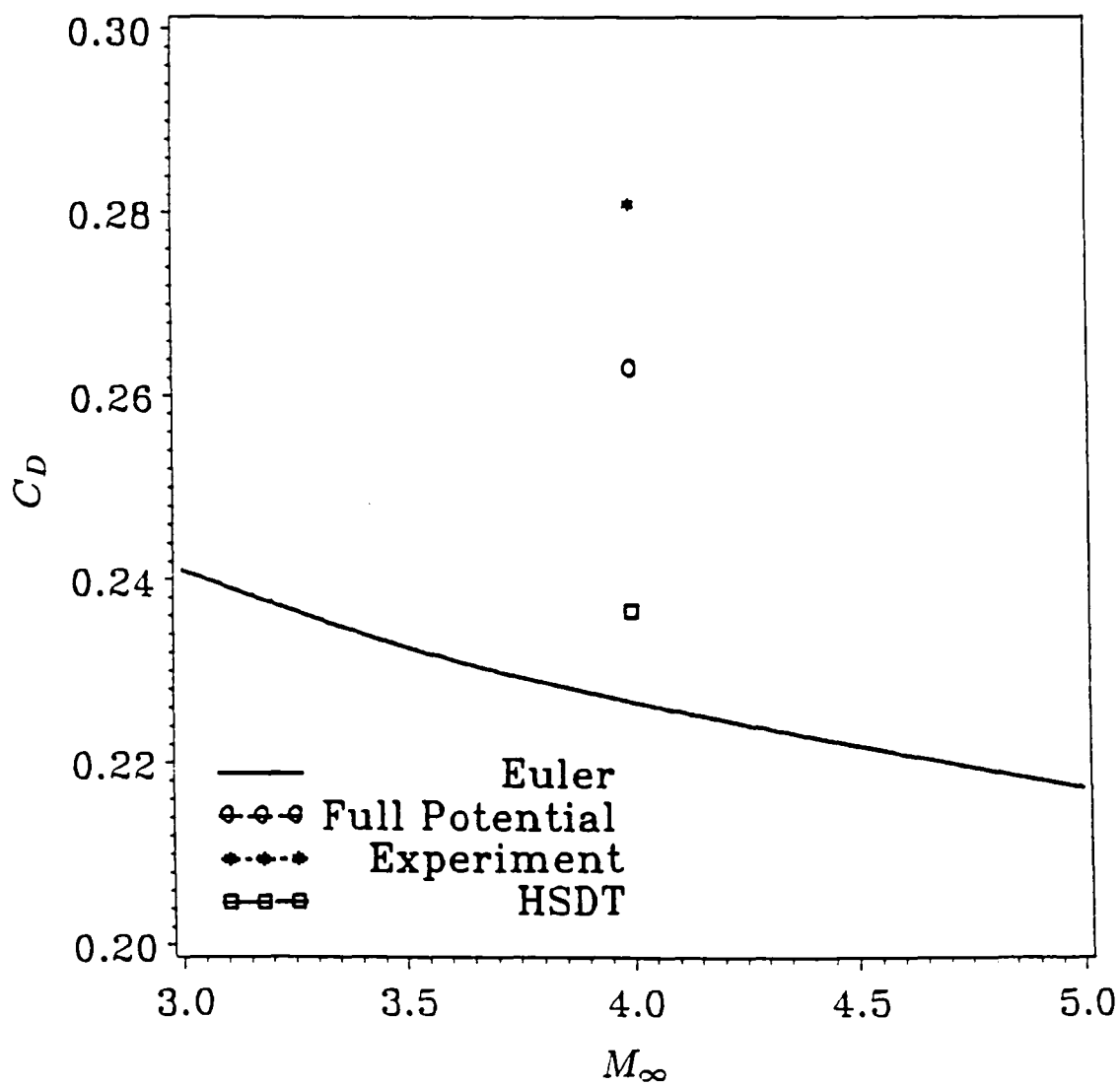


Fig. (7-24b) Entropy Contours for Waverider Type-B10

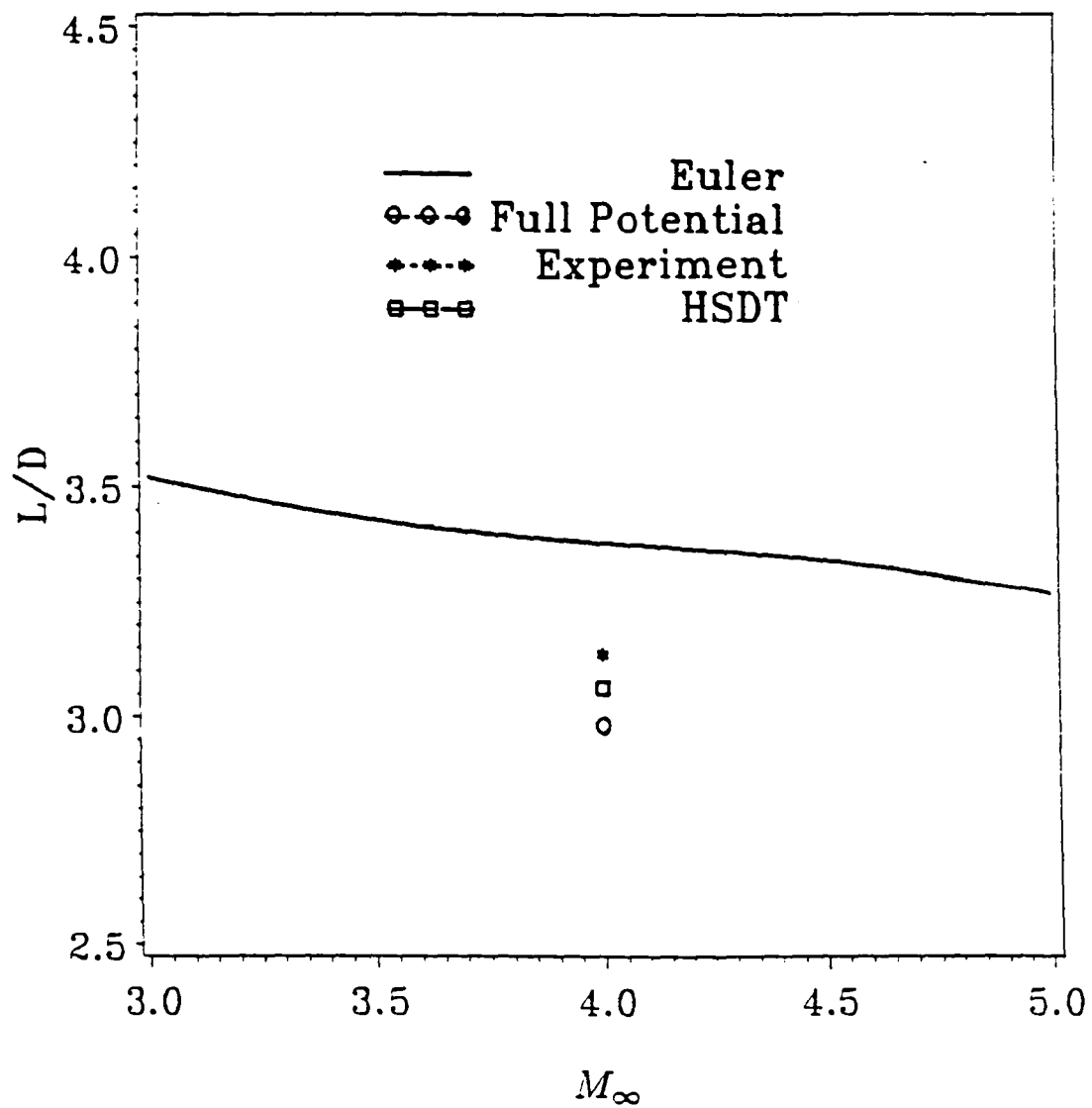
Waverider Type-B10

Fig. (7-25a) Lift Coefficient vs. M_∞

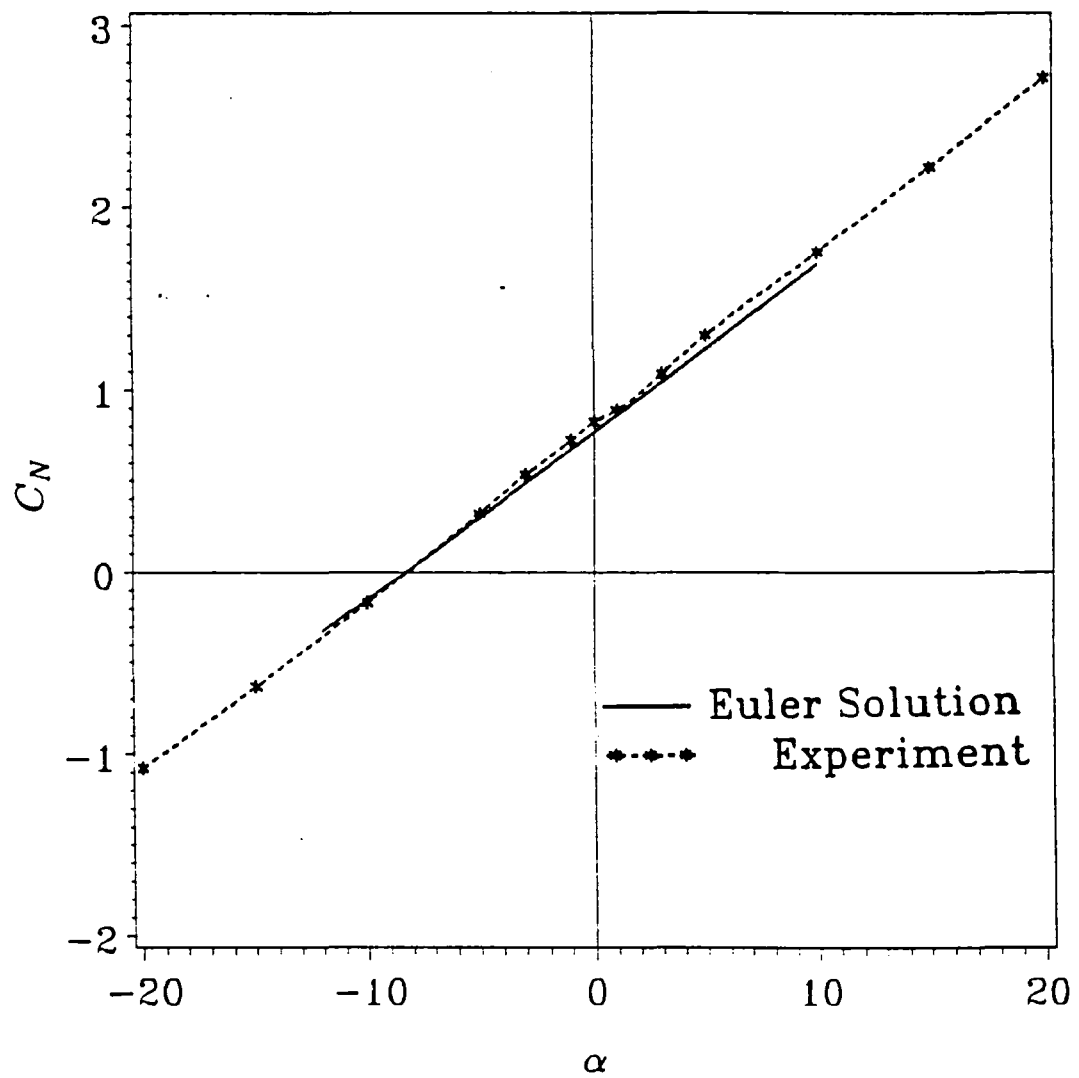
Waverider Type-B10

Fig. (7-25b) Drag Coefficient vs. M_∞

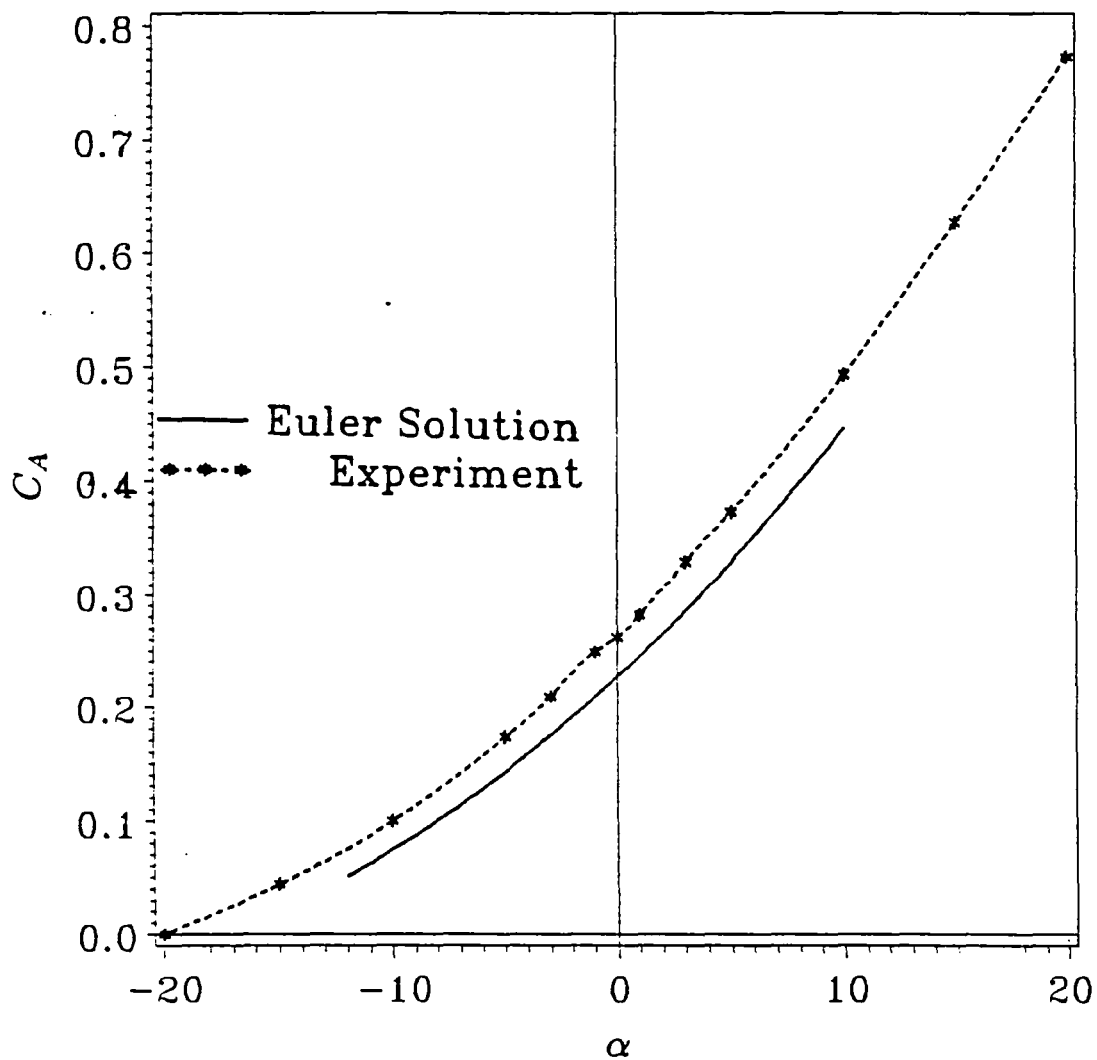
Waverider Type-B10

Fig. (7-25c) Lift/Drag Ratio vs. M_∞

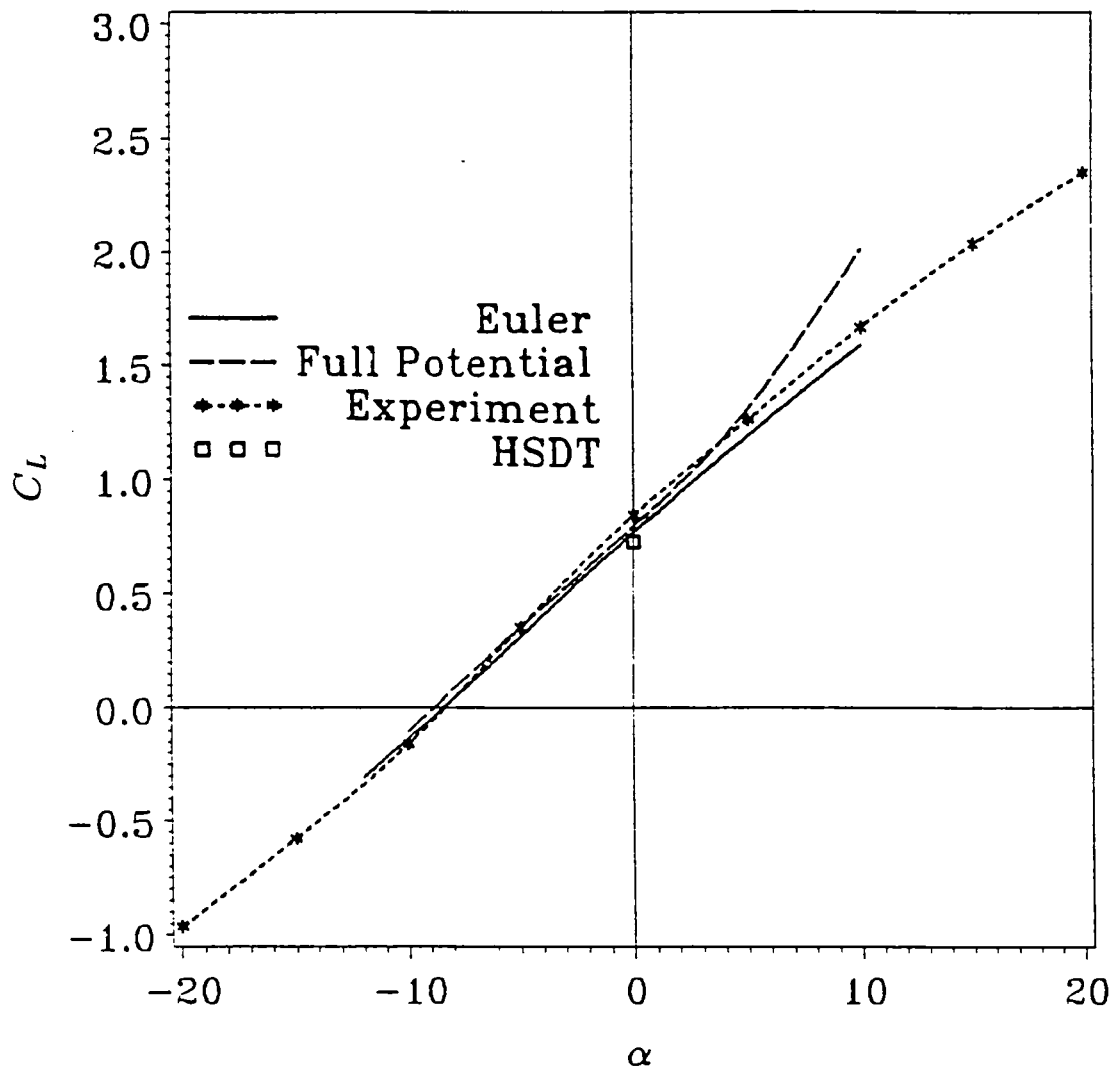
Waverider Type-B10

Fig. (7-25d) Normal-force Coefficient vs. α

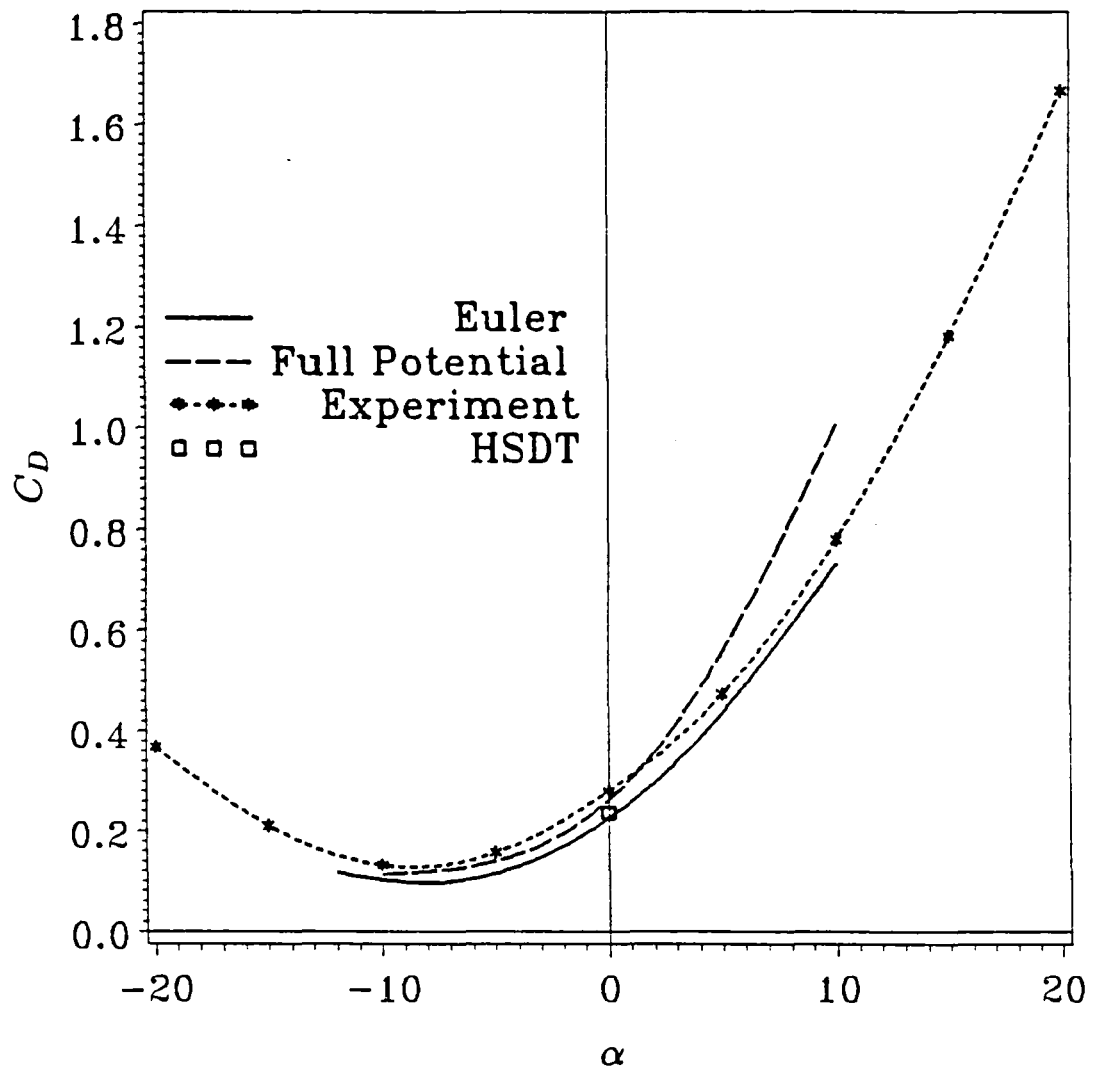
Waverider Type-B10

Fig. (7-25e) Axial-force Coefficient vs. α

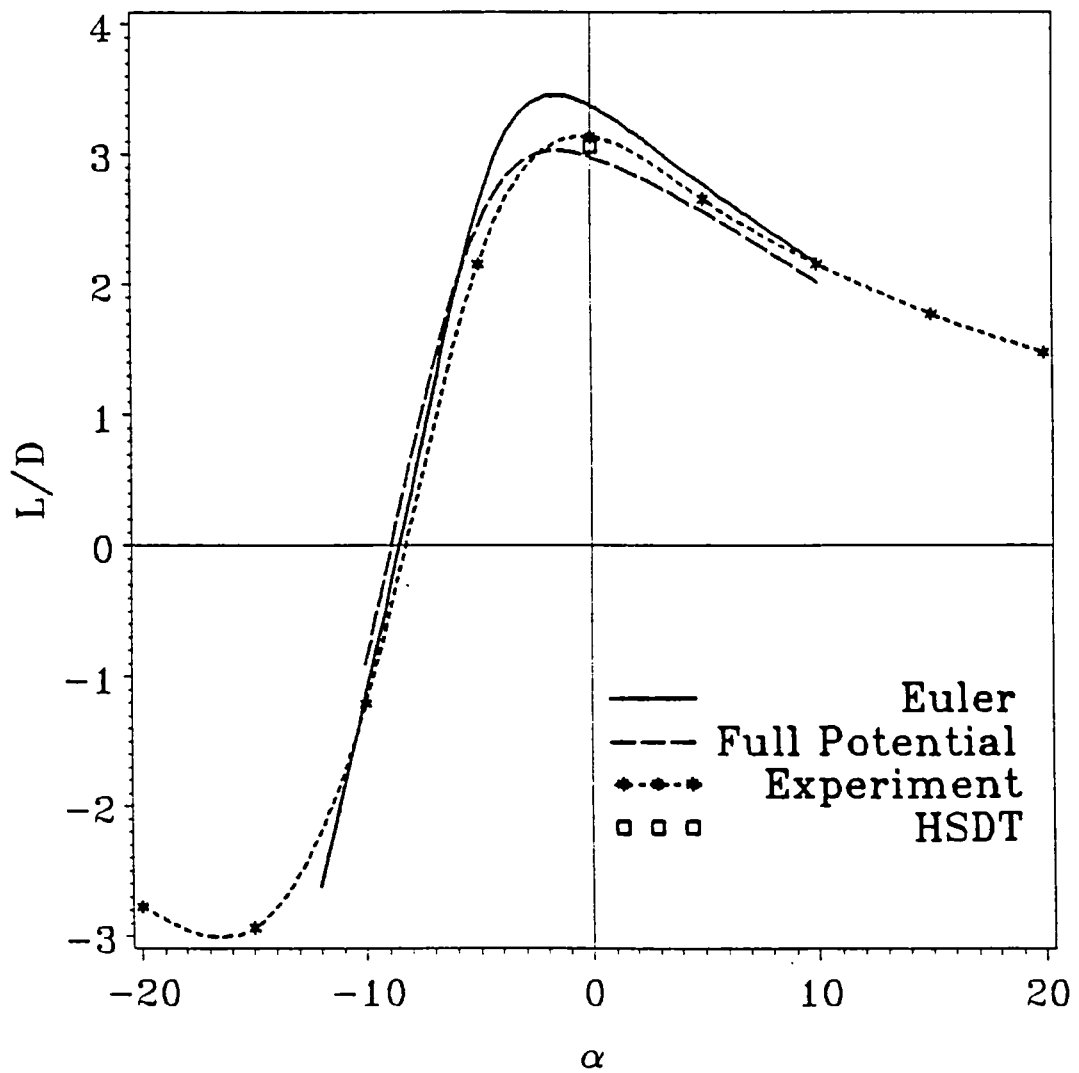
Waverider Type-B10

Fig. (7-25f) Lift Coefficient vs) α

Waverider Type-B10

Fig. (7-25g) Drag Coefficient vs. α

Waverider Type-B10

Fig. (7-25h) Lift/Drag Ratio vs. α

